UNCLASSIFIED

AD NUMBER
AD355561

CLASSIFICATION CHANGES

TO: **unclassified**

FROM: **confidential**

LIMITATION CHANGES

TO:

Approved for public release, distribution unlimited

FROM:

Distribution authorized to U.S. Gov't. agencies and their contractors; Administrative/Operational Use; 31 AUG 1960. Other requests shall be referred to Defense Atomic Support Agency, Washington, DC.

AUTHORITY
DNA ltr, 10 Oct 1979; DNA ltr, 8 Nov 1979

THIS PAGE IS UNCLASSIFIED

AD- 355561

SECURITY REMARKING REQUIREMENTS

DOD 5200.1-R, DEC 78

REVIEW ON 31 AUG 80

UNCLASSIFIED

AD 355 561

CLASSIFICATION CHANGED
TO: UNCLASSIFIED
FROM: CONFIDENTIAL
AUTHORITY:

chief, OAIS, DNA 1tr, 10 OCT79

OPERATION
PLUMBBOB
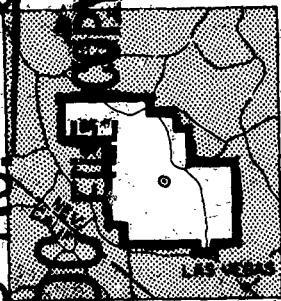
NEVADA TEST SITE
MAY-OCTOBER 1957
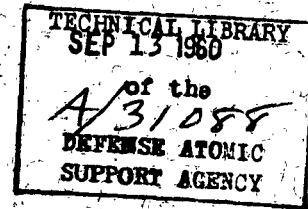
Project 3.6
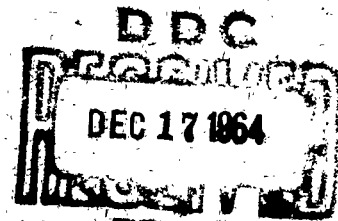
FULL-SCALE FIELD TESTS of DOME and ARCH STRUCTURES (U)

HEADQUARTERS FIELD COMMAND
DEFENSE ATOMIC SUPPORT AGENCY
SANDIA BASE, ALBUQUERQUE, NEW MEXICO

DDC
DEC 17 1964

Inquiries relative to this report may be made to

Chief, Defense Atomic Support Agency
Washington 25, D. C.

When no longer required, this document may be
destroyed in accordance with applicable security
regulations.

U.S. Military Agencies may obtain copies of this

report directly from DDC. Other qualified users shall

request through Director, Defense Atomic Support

Agency.

MRD Div., General American Transportation Corp., Niles, Ill.

DASA

WT-1425

Report on

OPERATION PLUMBBOB — PROJECT 3.6 [U]

(upper case)

FULL-SCALE FIELD TESTS of DOME and ARCH STRUCTURES (U)

by E.H. Bultmann, Jr., Capt, USAF, Project Officer
T.G. Morrison and
M.R. Johnson

Mechanics Research Division
American Machine and Foundry Company
Niles, Illinois

Air Force Special Weapons Center
Kirtland Air Force Base
Albuquerque, New Mexico

3

WIB

FOREWORD

This report presents the final results of one of the 46 projects comprising the military-effects progr?..a of Operation Plumbbob, which included 24 test detonations at the Nevada Test Site in 1957.

For overall Plumbbob military-effects information, the reader is referred to the "Summary Report of the Director, DOD Test Group (Programs 1–9)," ITR–1445, which includes: (1) a description of each detonation, including yield, zero-point location and environment, type of device, ambient atmospheric conditions, etc.; (2) a discussion of project results; (3) a summary of the objectives and results of each project; and (4) a listing of project reports for the military-effects program.

Tests are described for

ABSTRACT

~~This report describes tests on~~ dome and arch structures, sponsored by the Air Force Project 3.6 and the Office of Civil and Defense Mobilization (OCDM) Project 30.1 during Operation Plumbbob. The primary objectives of the test were to determine the blast-wave loading on dome and arch structures, determine the response motions of domes subjected to blast-wave forces, and check the performance of a large blast door after being subjected to blast-wave forces.

A total of ten structures were used: three 50-foot-diameter, reinforced-concrete, 6-inch-thick, responding domes; two 50-foot-diameter, reinforced-concrete, 24-inch-thick, non-responding domes; two 20-foot-diameter, responding aluminum domes; two 35-foot-span, 90-foot-long, reinforced-concrete nonresponding arches; and one 7-by-10-foot drawbridge-type door. The nonresponding structures were instrumented to determine pressure as a function of time, and the responding structures were instrumented to determine pressure and displacement as a function of time. A limited number of shear, strain, and ground acceleration measurements also were recorded on the responding domes.

The three 50-foot responding domes were identical as far as was practical to build them. They were placed in the 70-psi, 35-psi, and 20-psi regions and were designed to suffer slight damage at the 35-psi level. The aluminum domes were both placed in the 70-psi region. The shell of one was 1 inch thick, the other, $\frac{1}{2}$ inch thick. The nonresponding domes and arches were placed, one each, in the expected 70-psi and 35-psi regions. The nonresponding domes were self-supporting, while the nonresponding arches consisted of a 1-foot-thick slab poured on an earth mound. The drawbridge door was placed in the expected 35-psi region.

Actual overpressures developed in the predicted 70- and 20-psi regions were very close to the predicted overpressures. The actual overpressure at the expected 35-psi region was about 40 psi.

The responding reinforced-concrete dome in the high-pressure region suffered nearly total destruction. The windward side of the dome in the medium-pressure region was demolished. The responding dome in the low-pressure region was not damaged. No damage was suffered by any of the foundations.

Both aluminum domes suffered total destruction. The $\frac{1}{2}$-inch-thick shell was dished down into the foundation; the 1-inch-thick shell was crushed against the side of the foundation away from ground zero. No damage was suffered by the foundations for the aluminum domes.

The nonresponding domes and their foundations were not damaged by the blast.

The nonresponding arches suffered shear failure along the end walls and a slight displacement, about $2\frac{1}{2}$ inches, for the 70-psi arch, and 1 inch for the 35-psi arch. A tension crack appeared just beyond the crown of the 70-psi arch, the crack running the full length of the shell.

The test of the prototype door was also a success. It survived without significant permanent deformation. The only damage (around the edge of the door) was of minor nature and could be prevented by a slight change in design. The locking and hinge mechanisms functioned perfectly after the test.

Analysis of the loading data failed to disclose any reflected-pressure effects on the structures because of the lack of a classical type of shock front in the precursor blast wave at each of the structures. Enough loading information was obtained on the nonresponding structures at the 70-psi region to permit the computation of pressure coefficients as a function of time on these structures.

The dome-response measurements obtained on the tests generally confirmed the theory which was used for the design of the domes. Failure of certain response gages during the test, notably the strain gages, prevents a complete description of the manner in which the dome structures resisted the blast loading.

5

PREFACE

6

CONTENTS

CONFIDENTIAL

CONFIDENTIAL

CONFIDENTIAL

11

CONFIDENTIAL

CONFIDENTIAL

CONFIDENTIAL

Chapter I
INTRODUCTION

1.1 OBJECTIVES

The primary objectives of these tests were to: (1) determine the blast-wave loading on dome and arch structures; (2) determine the response motions of domes subjected to blast-wave forces; and (3) check the performance of a large blast door after subjection to blast-wave forces. A secondary objective of the test was to determine whether foundation soil-bearing pressures much higher than used in conventional practice could be used for carrying the transient blast loads on a dome structure.

The loading of a structure by a blast wave is a complex process which can be considered to occur in two phases. The first phase, called the diffraction phase, is defined as the period during which pressure distribution on the structure is governed by reflection and diffraction effects as the shock wave engulfs the structure. The peak reflected pressure, usually the maximum diffraction loading effect, is related to the blast-wave overpressure by the reflection coefficient. The second phase, called the drag phase, is the period during which the structure is immersed in the decaying flow field behind the shock front and the structure is loaded by the high-velocity air flow. The local pressure at a point on the structure during the drag phase is related to the dynamic pressure of the flow by the pressure coefficient. The objective of the loading measurements was to relate the pressures measured on the structures to the over-pressure and dynamic pressure of the free-field blast wave and thus obtain experimental values for reflection coefficients and pressure coefficients at various positions on the structures.

An array of ten test structures was required to fulfill the test objectives. The structures fall into two general categories: responding structures and nonresponding structures. The responding structures were used primarily to determine the response motions of the structure resulting from the blast load. The nonresponding structures were used principally to measure the distribution of the blast load over the surface of the structure. A brief description of each of the test structures and the specific objectives which were intended for each of the structures are included in the following paragraphs.

1.1.1 Nonresponding Concrete Arches (Test Structures F-3.6-9028.01 and F-3.6-9028.02).
These structures (Figure 3.32) consisted of arched concrete slabs laid on a compacted earth berm. They were 90 feet long, had a 35-foot span, and a 120-degree central angle.

The specific objectives of the test on these structures were to: (1) obtain pressure-time histories at a sufficient number of points on each arch to enable extrapolation of the data to all parts of the arch surface; (2) attempt to divide the pressure history into the diffraction and the drag phases; (3) attempt to determine the reflection coefficients and pressure coefficients as functions of position and time; and (4) compare the results with those of shock-tube tests on arch models.

1.1.2 Nonresponding Concrete Domes (Test Structures F-3.6-9027.01 and F-3.6-9027.02).
These test structures (Figures 3.39 and 3.40) were 50-foot-base diameter, 90-degree-central-angle, 24-inch-thick, reinforced-concrete domes.

The specific objectives of the test on these structures were the same as those given for the arch structures in Section 1.1.1. An additional objective was to determine the net permanent displacement of the domes with respect to the ground, if any.

1.1.3 Responding Concrete Domes (Test Structures F-30.1-8001.01, F-30.1-8001.02, and F-30.1-8001.03).

These test structures (Figures 3.36, 3.37 and 3.38) were 50-foot-base-diameter, 90-degree-central-angle, 6-inch-thick, reinforced-concrete domes.

The primary objectives of the test on these structures were to obtain: (1) the deflection of the shell as a function of time at a sufficient number of points on the shell to check analytical predictions; (2) the net pressure as a function of time on the shell at a sufficient number of points to extrapolate the results (guided by the more-extensive pressure records taken on the nonresponding dome) to obtain a good estimate of the pressure-versus-time record at any point on the dome; (3) the shear stress at the foundation in order to compare it with analytical predictions; (4) the ratio of bending-to-membrane stress at a single point on the shell in order to check with analytical predictions; (5) ground accelerations, both vertically and horizontally, inside and outside of the dome; and (6) insight into the nonelastic response of spherical domes.

The secondary objectives of the test on these structures were to determine: (1) character and degree of foundation movement; (2) accuracy of the overpressure surcharge theory of friction soils; (3) failure surface in the soil if failure occurred; (4) maximum changes in relative position of the dome shells and the earth floor; and (5) net permanent displacement of the domes with respect to the ground.

The three domes were placed in predicted overpressure regions of 70, 35, and 20 psi with the 35-psi blast overpressure expected to load the dome to the limit of elastic response. This gave a high probability of dome survival at 20-psi overpressure and dome destruction at 70-psi overpressure.

1.1.4 Responding Aluminum Domes (Test Structures F-3.6-9026.01 and F-3.6-9026.02).

These test structures (Figures 3.33 and 3.34) were 20-foot-diameter, 90-degree-central-angle, aluminum domes. One dome had a 1-inch metal thickness and the other a $\frac{1}{2}$-inch metal thickness.

The specific primary objectives of the test on these structures were the same as on responding concrete domes with the exception that no ground acceleration information was desired. An additional objective was the comparison of the dynamic behavior of the aluminum test domes as compared with the larger concrete test domes.

A secondary objective of the test on these structures was to determine the performance of the vertical foundations with hoop reinforcement, as used on the aluminum domes, and compare it with the inclined foundations used on the concrete domes.

1.1.5 Prototype Door (Structure F-30.1-8008).

This structure (Figure 3.35) was an 8-foot by 10-foot-7-inch drawbridge-type door made of steel.

The primary objectives of the test on this structure were to determine whether or not: (1) a door of the type tested could be opened easily after blast, and (2) the concrete tunnel entrance would be stable without the use of concrete aprons, piles, anchors, or other stabilizers.

A secondary objective of the test on this structure was to determine the effectiveness of the door seal in preventing the pressure from entering the interior of the structure.

1.2 BACKGROUND

Extensive theoretical analysis of the design of atomic blast-resistant shell structures was conducted by American Machine and Foundry Company (AMF) under Air Force Contract AF 33(616)-2522 (Reference 1). This investigation concluded that spherical dome and cylindrical arch shells are well suited for use as blast-resistant structures. They are especially desirable for resisting blast loads above 50-psi overpressure, since conventional rectangular structures become large and unwieldy when proportioned to resist these large blast loads.

16

CONFIDENTIAL

The theoretical analyses on which this conclusion was based depended on the solution of simultaneous, fourth-order, partial-differential equations. In order to solve the equations, certain simplifications were required. The fundamental equations were simplified by assumptions regarding structural behavior of the shell material and by neglecting minor inertia effects. The analytical work conducted with these assumptions was strictly applicable only to structures which remain elastic throughout their entire history of loading and response. More simplifying assumptions were necessary to extend the theory to nonelastic response.

This type approach is not unique. It follows the pattern of previous investigations of other structural configurations, both blast-resistant and conventional.

This full-scale test was part of a continuing theoretical and laboratory effort to determine the values of significant parameters used in the design of protective shelters.

During the preliminary planning stages for Projects 3.6 and 30.1 of Operation Plumbbob, it became evident that the best technical and economic interests would be served if the Air Force and the Office of Civil and Defense Mobilization (OCDM) programs were correlated closely with each other. This correlation was simplified because the same contractor (AMF) was designing the test structures for both the Air Force and OCDM. The test complex of arch, dome, and door structures, of interest to both agencies, was divided into DOD Project 3.6 and OCDM Project 30.1. This report covers both projects.

The following theoretically predicted conclusions and assumed input parameter magnitudes required verification and measurement:

1. The pressure-resisting mechanism of dome structures subjected to dynamic blast-wave loading departs considerably from the mechanism of static-load resistance.

2. The dynamically loaded dome is more sensitive to the distribution of pressure over its surface and the variation of this pressure with time than are most other structures, which are generally more sensitive to variations in average pressure than to pressure distribution.

3. Reflection coefficients and clearing times of reflected pressures vary from point to point on the dome surface. These factors have considerable effect on shell design. Due to the precursor developed in Nevada tests, it was believed unlikely that an accurate determination of reflection coefficients would be obtained. However, the possibility existed that if precursor waves having sharp overpressure rises were encountered at some of the test structures, reflection-coefficient data might be obtained.

4. Very little pressure-coefficient data for domes exists. Comparison and extrapolation of the limited data available indicated that the domes would not be severely loaded by the flow associated with the blast wave. More pressure-coefficient data is available for arches, but it is inadequate for blast-shelter design purposes. Arch shells are more sensitive to flow loading than domes, and therefore it was important that more arch-pressure-coefficient data be obtained. The high dynamic pressures usually encountered at the Nevada Test Site were believed to offer an excellent test for determining pressure coefficients.

5. If economical spread footings are to be used in blast-shelter construction, considerable reliance must be placed on the overpressure surcharge and triaxial resistance of the soil during the blast loading of the structure. The high internal friction soil at the Nevada Test Site is well suited for checking the theoretical increase in soil-bearing capacity developed when an increase in air pressure is applied to the surface of the ground.

A few field tests have been previously conducted on small dome and arch structures (References 2, 3, and 4). However, the test conditions differed greatly from those in the Operation Plumbbob test series. In one instance, the domes tested were externally ribbed; in another case, the structure used was only a polyhedral approximation of a dome (Reference 3). In general, the arches have been either completely buried or covered with a substantial earth berm.

None of the underground tests has much significance for designing above-ground structures. The results of shock-tube tests of models of the above-ground dome-shaped polyhedron (Reference 5) have been used for checking the extrapolated values of reflection coefficients used for dome design. These data are incomplete, obtained at an overpressure level below the level

17

CONFIDENTIAL

of current interest, and probably a poor approximation for dome design because of modifications introduced by vortex formation at the polyhedron edges.

A large personnel shelter (150 to 250 feet in diameter) will require many doors about the size of the prototype door structure. These doors will necessarily be ruggedly designed and must open easily after a blast. A door similar in design to the prototype door has been used for much larger Air Force structures (Reference 6) and has been found to operate efficiently under normal conditions. However, such a door never previously has been subjected to atomic blast.

The blast load acting on a closed prototype door structure would tend to cause large stresses in a tunnel behind the door if the direction of the tunnel changed from the direction of the applied blast load a short distance behind the door. Presumably, resistance could be built into the tunnel by the use of sufficient longitudinal reinforcing steel or by providing a heavy concrete apron ahead of the door, integral with the tunnel, to stabilize the entrance. These expedients would be expensive and unnecessary if the earth mound surrounding the entrance tunnel proved to be as effective as anticipated in resisting such tunnel bending. For the prototype door, the earth mound and tunnel continuation were approximated by an earth berm.

The ten structures tested by Projects 3.6 and 30.1 were designed on the basis of theoretical analysis, approximate wave-form data, and practically no applicable previous full-scale test data for similar structures. The structures were representative of types that may, in the future, be of considerable importance to both the Air Force and OCDM. Though all of the test structures, save the prototype door, were of much smaller dimensions than structures proposed to accomplish the contemplated civilian and military functions, they were not model structures. No modeling laws were used in their design. They were designed by the same methods proposed for use on much larger structures; the presumption was that if the design methods were successful for the small test structures, they could be applied with confidence to larger designs.

Chapter 2
THEORETICAL ASPECTS of EXPERIMENT DESIGN

2.1 DOME RESPONSE TO BLAST LOADING

The basic mathematical theory of the dynamic design of spherical dome shells is given in Reference 1. For purposes of the present project, the salient features of the theory and design methods will be presented here without the inclusion of the considerable analysis required to justify their validity.

The shell thickness required for a uniformly statically loaded, spherical dome is given by:

$$h_s = \frac{PR}{2\sigma} \qquad (2.1)$$

Where: h_s = shell thickness, inches

P = uniform static pressure, lb/in^2

R = spherical radius, inches

σ = design stress, lb/in^2

For a nonuniformly statically loaded spherical dome, the shell thickness required is given by:

$$h = \frac{k_s P_0 R}{2\sigma} \qquad (2.2)$$

Where: P_0 = a reference pressure, lb/in^2

k_s = a factor that is, in general, a function of load distribution and position on the dome (dimensionless)

In Formula 2.2 the thickness, h, is, in general, a function of position on the dome. This formula is deceptively simple in appearance. For nonsymmetrical loading, determination of the values of k_s at various points on the dome shell may be an extremely involved task. It should be noted that although static dome design has been the subject of serious investigation by several competent specialists since about the beginning of the present century, no concise engineering method for computation of k_s has yet been developed for nonpolar symmetrically distributed loading.

For dynamic, blast-resistant design, it is convenient for comparison purposes to define a dimensionless dynamic constant, k_d, such that the thickness required is given by:

$$h = \frac{k_d P_\sigma R}{2\sigma} \qquad (2.3)$$

Where: P_σ is the peak overpressure.

Much of the problem of blast-resistant dome design is directed toward determination of the appropriate values for k_d. Depending on the pressure-time history of the blast wave and the appropriate values for reflection and pressure coefficients, values for k_d can range between 1.6 and about 10.

In general, for a blast wave for which the rise time is on the order of a half period of the dome vibration, the factor k_d does not vary significantly from point to point on the dome, i.e.,

a uniformly thick shell design results. However, as the rise time decreases to essentially zero, the reflection coefficient becomes more significant, and the variation of k_d along a meridian increases from center to spring line by a factor of as much as 2.5. For a steep shock front, k_d at the crown of the dome is somewhat less than 4, depending to some extent on the duration of the wave.

Some discussion of the response of a dome shell to a blast wave is appropriate at this point. An ideal blast wave will be assumed. The essential method for handling a nonideal wave is identical, but the details of the computations are considerably more complicated.

The coordinate systems used for the dome analysis are shown in Figure 2.1. The dome itself is symmetrical about the ϕ, θ pole, while the blast wave is symmetrical about the α, β pole, i.e., at any particular instant the pressure on the dome along a parallel of constant α is independent of β, if ground effects are neglected. It is believed that these latter effects are small enough to be negligible. Any point on the dome shell can be specified by either a value of α and a value of β or a value of ϕ and a value of θ. Both systems are used in the analysis, use being made of the simpler system for any given element of the analysis.

The prime meridians for the two systems are coincident. The prime meridian joins the α, β pole with the ϕ, θ pole. The "leading edge" of the dome is the point where the prime meridian intersects the dome edge nearest to ground zero; the "trailing edge" is the point where the prime meridian intersects the dome edge farthest from ground zero.

The essential method followed for developing the design method for blast-loaded domes is outlined below:

1. The fundamental differential equations for dynamic response of the dome shell were set up. These accounted for displacements of a point on the shell in three dimensions, included both the bending and membrane resistance of the shell, and assumed no symmetry whatever in the time-and-position-varying loading function. Accelerations tangent to the dome surface were neglected.

2. A normal-mode solution of the fundamental equations was deduced. The normal modes were expressed in terms of the associated Legendre and trigonometric functions. The frequency spectrum of the normal modes was found to be extremely narrow. Further, it was found that a large number of modes (20 or more) would be required to adequately represent the deflection configuration. The normal-mode solution was concluded to be too cumbersome for practical design.

3. The fundamental equations were simplified to neglect the effects of bending. Their solution was carried as far as possible in terms of a general loading function. The equations did not admit solution explicitly for the deflection, w, in terms of a general loading function. However, they did admit an implicit dynamic solution in terms of a general loading function and yielded the remarkable result that, irrespective of the vibration geometry, the frequency of vibration of a membrane dome is single-valued. There does not exist a spectrum of mode frequencies for the membrane dome. Any arbitrary deflection configuration vibrates at the membrane frequency and the deflection geometry of the arbitrary deflection configuration is conserved.

4. A practical design method based on the equivalent-static-load concept was developed. In this approach the actual dynamic loading is replaced by a series of mathematically equivalent static loads and designs for these carried out by any appropriate static-dome-design method. The most severe of these controls dome-shell thickness and reinforcing.

The complete mathematical development of the dome-design method is given in Part III (Unclassified) of Reference 1. Essential elements of the development are given here, for convenience.

Notation:

∇^2 = Laplacian operator

$w(\alpha,\beta)$ = static displacement

$w(\alpha,\beta,t)$ = dynamic displacement

$P_s(\alpha,\beta)$ = static pressure

$P(\alpha,\beta,t)$ = time varying pressure

R = dome spherical radius

E = modulus of elasticity of dome-shell material

$$h = \text{dome-shell thickness}$$
$$\rho = \text{dome-shell material mass density}$$
$$\omega = \text{circular frequency of vibration of dome shell}$$
$$C = \text{sonic velocity in dome-shell material}$$
$$t = \text{time, variable}$$
$$t^* = \text{time, particular instant}$$
$$\tau = \text{dummy variable of integration}$$
$$\left.\begin{array}{l} H_S(\alpha,\beta) \\ H_D(\alpha,\beta,t) \end{array}\right\} = \text{harmonic functions}$$
$$F(\alpha,\beta;t^*) = \text{equivalent static load at instant } t^*$$

The relation between loading and radial displacement of a statically loaded dome is given by the equation:

$$\nabla^2 w(\alpha,\beta) = \frac{R^2}{Eh} \nabla^2 P_S(\alpha,\beta) \tag{2.4}$$

The solution of this is

$$w(\alpha,\beta) = \frac{R^2 P_S(\alpha,\beta)}{Eh} + H_S(\alpha,\beta) \tag{2.5}$$

Where: $\nabla^2 H_S(\alpha,\beta) = 0$

For dynamic loading, Equation 2.4 becomes

$$\nabla^2 w(\alpha,\beta,t) = \nabla^2 \int_0^t \frac{P(\alpha,\beta,\tau)}{\rho h \omega} \sin \omega(t-\tau)\, d\tau \tag{2.6}$$

Where: $\omega^2 = E/\rho R^2 = (C/R)^2$ (2.7)

The solution of this is

$$w(\alpha,\beta,t) = H_D(\alpha,\beta,t) + \int_0^t \frac{P(\alpha,\beta,\tau)}{\rho h \omega} \sin \omega(t-\tau)\, d\tau \tag{2.8}$$

Where: $\nabla^2 H_D(\alpha,\beta,t) = 0$ (2.9)

If at a particular instant of time, t^*, the equivalent static load $F(\alpha,\beta;t^*)$ is defined

$$F(\alpha,\beta;t^*) = \int_0^{t^*} \omega P(\alpha,\beta,\tau) \sin \omega(t^*-\tau)\, d\tau \tag{2.10}$$

then

$$w(\alpha,\beta,t^*) = \frac{R^2 F(\alpha,\beta;t^*)}{Eh} + H_D(\alpha,\beta,t^*) \tag{2.11}$$

Note that $F(\alpha,\beta;t^*)$ is a function of two variables, α and β, and that t^* indicates the particular instant of time at which it has been evaluated by the operation indicated by Equation 2.10.
Equation 2.5 can be rewritten:

$$H_S(\alpha,\beta) = w(\alpha,\beta) - \frac{R^2 P_S(\alpha,\beta)}{Eh} \tag{2.12}$$

21

CONFIDENTIAL

and, similarly, Equation 2.11 can be rewritten:

$$H_D(\alpha,\beta,t^*) = w(\alpha,\beta,t^*) - \frac{R^2 F(\alpha,\beta;t^*)}{Eh} \qquad (2.13)$$

It can be shown that if

$$F(\alpha,\beta;t^*) \equiv P_s(\alpha,\beta) \qquad (2.14)$$

then

$$H_D(\alpha,\beta,t^*) \equiv H_s(\alpha,\beta) \qquad (2.15)$$

and, therefore,

$$w(\alpha,\beta,t^*) \equiv w(\alpha,\beta) \qquad (2.16)$$

if $F(\alpha,\beta;t^*)$ is substituted for $P_s(\alpha,\beta)$ in Equation 2.4 or 2.5.

Thus, if the static equations are solved by any method, using for the static load the function $F(\alpha,\beta;t^*)$ defined by Equation 2.10, the computed deflections will be equal to the dynamic deflections due to the loading history $P(\alpha,\beta,t)$ between times zero and t^*. Of course, since the dynamic loading changes from instant to instant, the equivalent static load so computed is valid at a single instant only. A series of equivalent static loads must be computed for suitably spaced time intervals during the loading history of the dome.

5. To gain insight into the effects of bending, a traveling-elastic-wave analysis for a shell in the form of a spherical zone defined by 45 degrees $\leq \alpha \leq$ 135 degrees was carried out. In this analysis, the effects of both bending and membrane stresses were retained in the fundamental equations. However, to obtain a solution admitting simple, physical interpretation, the second term of the Laplacian operator expressed in spherical coordinates with radius held fixed was neglected.

$$\nabla^2 = \frac{1}{R^2}(1-X^2)\frac{\partial^2}{\partial X^2} - \frac{2X}{R^2}\frac{\partial}{\partial X} + \frac{1}{R^2(1-X^2)}\frac{\partial^2}{\partial \theta^2} \qquad (2.17)$$

Where: ∇^2 = Laplacian operator
    R = spherical radius, constant
    X = $\cos \phi$ (see Figure 2.1)

This simplification introduces negligible error near the crown of the dome where deflections are most severe. This analysis showed that the propagation velocity of bending waves is considerably less than the shock-front velocity and that behind the shock front the geometric character of the bending wave is identical to the deflection configuration of the membrane solution determined in Step 4. Further, the single frequency of vibration of a bending wave due to super-critical velocity of blast loading is identical with that found for the membrane shell in Step 3.

6. The contribution to external-pressure resistance of the bending wave of Step 5 was divided by the contribution to external-pressure resistance of the membrane solution of Step 4. The ratio was found to be about 6 percent maximum, justifying neglect of bending resistance in the determination of deflections in Step 4 (also see Step 8).

7. If the dynamic loading is assumed to be independent of β, then the equivalent static loads are independent of β. Such a set of loads was applied to the dome and the normal stresses along meridians of constant β, σ_α, approximated. These were found to be less than 10 percent of the normal stresses along small circles of constant α, σ_β, and in general, more nearly 6 percent of the latter at the points of maximum compression stress, for instantaneous rise shock wave.

22

CONFIDENTIAL

Therefore, to simplify the design procedure for short-rise-time shock wave, the normal stresses σ_α were neglected. This was tantamount to adopting a small safety factor inasmuch as neglect of the small value of σ_α increases the computed value of σ_β by an amount equal to the value of the stress neglected. For the dynamically loaded dome the membrane stresses at a point always have the same sense at any instant. For slow-rise-time compression wave, the stresses σ_α may be significant.

8. After computation of membrane stresses, the bending stresses can be computed and the concrete and steel stresses corrected, if necessary. Generally, the stresses due to bending are small enough to neglect.

The equivalent static loads were found in Step 4 to be given by an integral formula of the form of Duhamel's integral. Thus, if a traveling dynamic load in the form of a step function were to
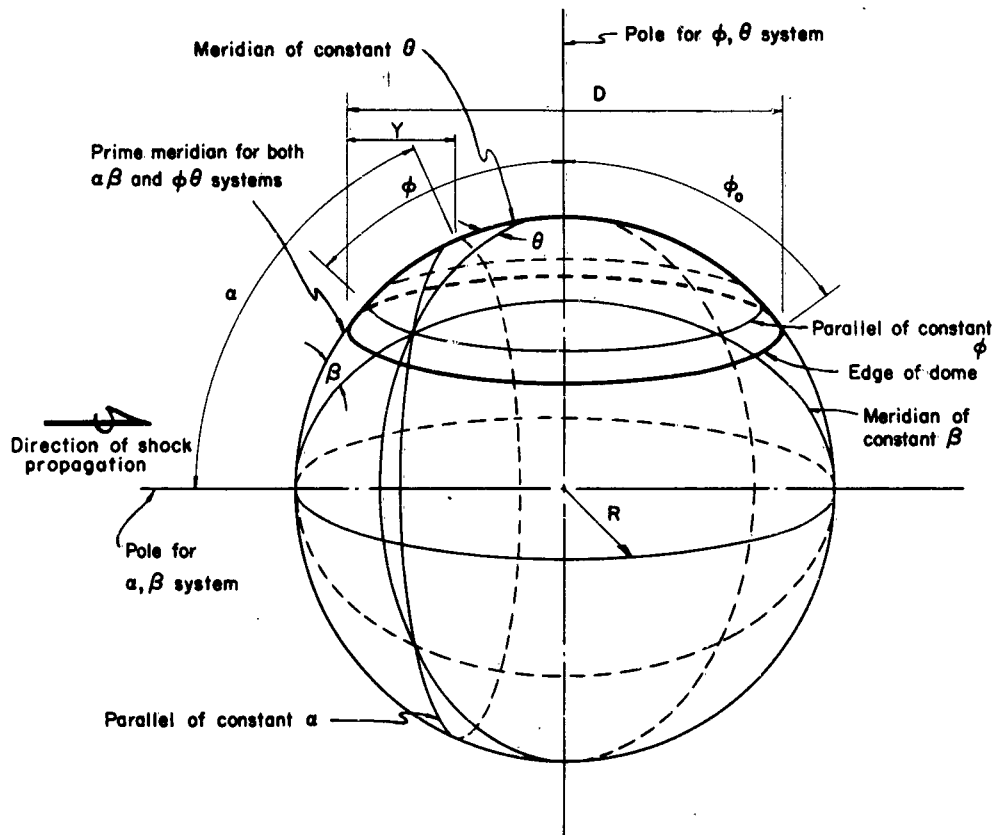
Figure 2.1 Coordinate system.

be applied to the dome, the peak value of equivalent static pressure would be twice the value of the step function. Another factor of two is introduced by the small value of the normal stress σ_α, because $\sigma_\alpha = 0$ implies that σ_β (and hence, the net thickness required) would be twice the value attained for $\sigma_\alpha = \sigma_\beta$, corresponding to uniform static load. Thus, for a step-function loading the value of k_d would be four. Reflection effects further increase this value by a factor approaching three. The factor k_d is also sensitive to the rise time of the blast wave. For instance, if the blast wave consists of a step function having a finite rise time equal to the half period of dome vibration, the peak intensity of the equivalent static load is equal to the intensity of the step function, rather than twice this value (as found for an infinitesimal rise time). Further, as the rise time increases, the stresses σ_α and σ_β at the instant of peak intensity of σ_β are more nearly equal, due to more-uniform distribution of pressure on the dome. When the

23

rise time of a step function is equal to one period of vibration of the dome, the net value of k_d is about 1.6. For peaked, irregular waves of the form encountered at the Nevada Test Site, the factors k_d are considerably larger.

Formula 2.10 gives the equivalent static loads at a point as a function of time. Cross plotting these values for several points at a particular time instant gives the distributed equivalent static loads at that time instant.

The value of this approach to the problem becomes evident, when it is recalled that in spite of the many investigations that have been undertaken in past years, the problem of an asymmet-
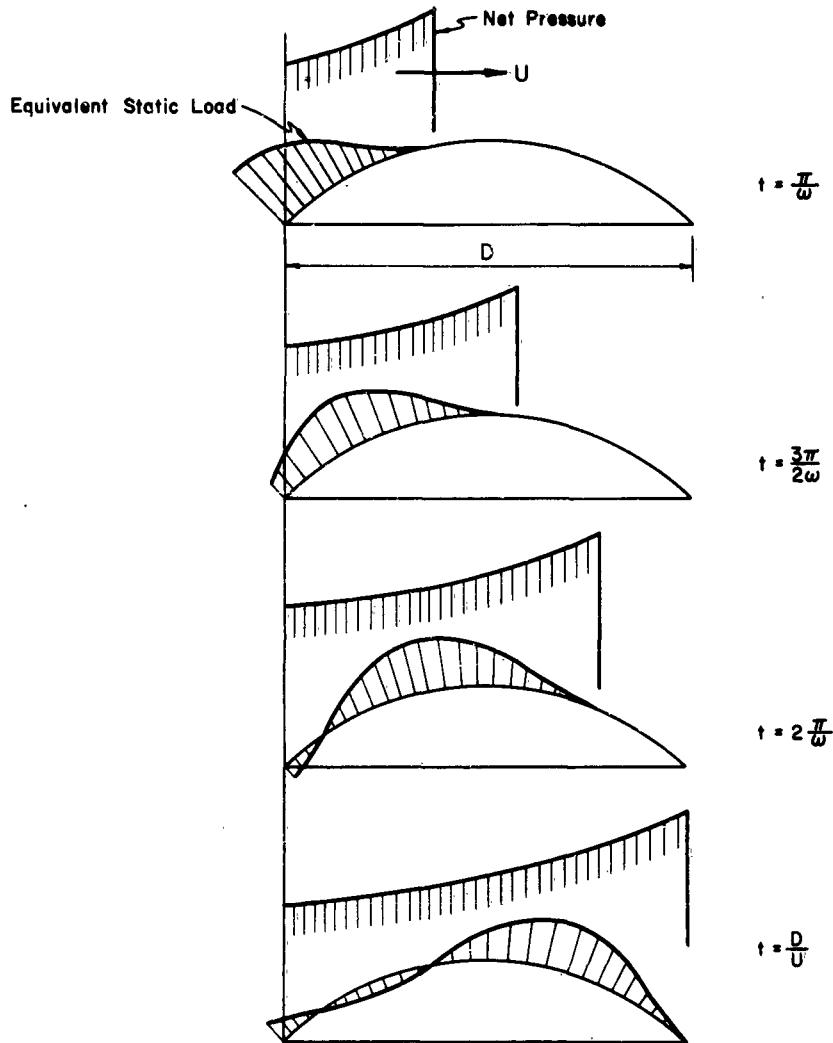
Figure 2.2 Equivalent static loads. t = time, ω = circular frequency of dome vibration, rad/sec, U = velocity of shock front.

rically statically loaded dome has not been solved in a form expeditious for numerical calcula-
tion. Reliance must yet be placed on approximate engineering methods based on a combination
of mathematical analysis, engineering insight, and judgment. Reduction of the dynamic problem
to a series of equivalent static problems enables the design engineer to employ the insight and
judgment developed in design of statically loaded domes and other shell structures.

The essential results of this analysis are presented graphically in Figures 2.2 through 2.4.
Figure 2.2 shows the net-pressure wave moving at velocity U at four selected instants of

24
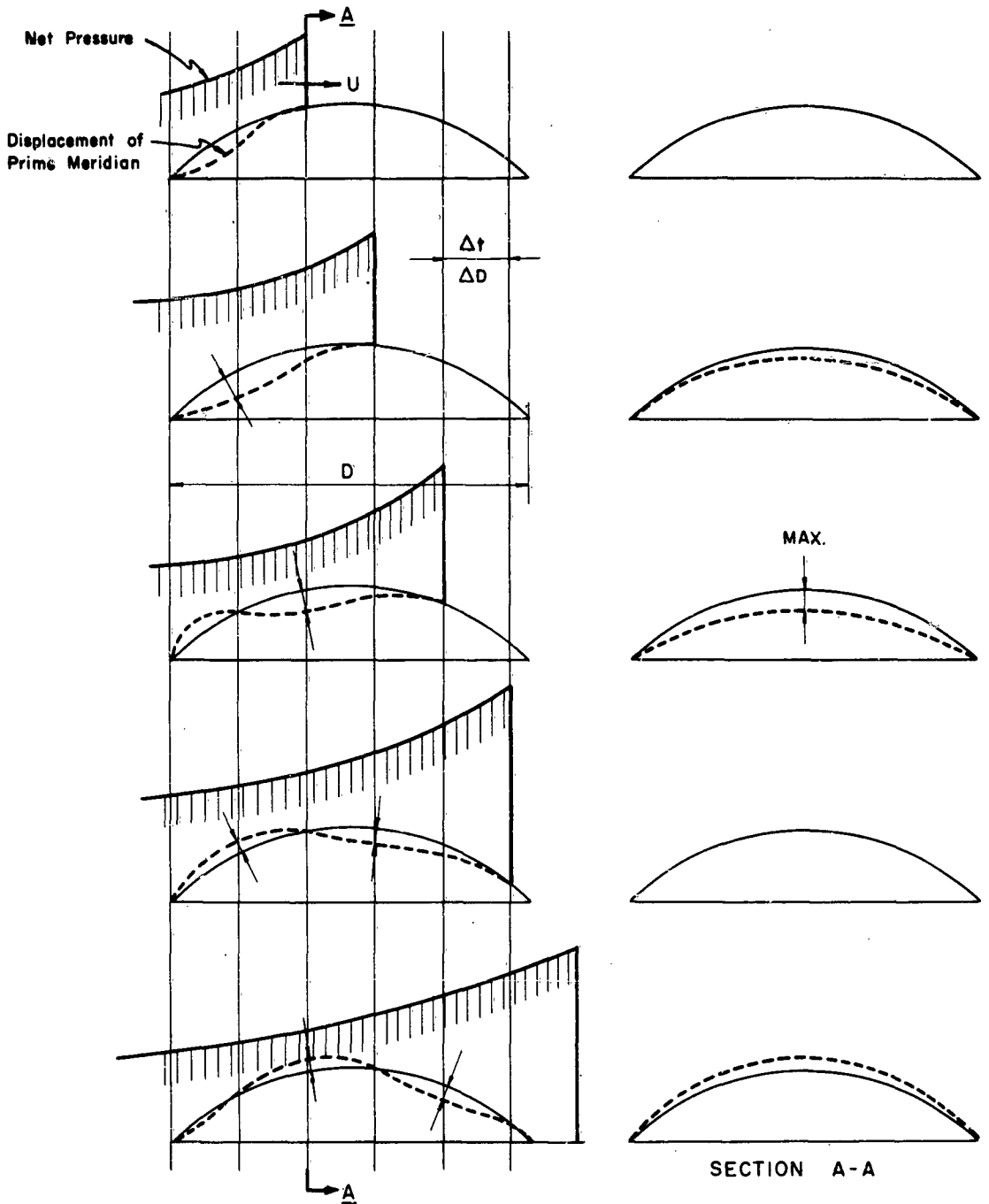
Figure 2.3 Dome deflection modes, ideal loading.

25

time t as it moves along the prime meridian. Beneath the net-pressure waves, the equivalent static pressure for each time instant is plotted on the prime meridian. Both pressure diagrams are symmetrical about the α axis; i.e., they are toroidal in shape.

Figure 2.3 shows the deflection of the prime meridian and one particular small circle arc of constant α for five successive positions of the shock front, spaced at intervals of $\frac{1}{4}$ wave length
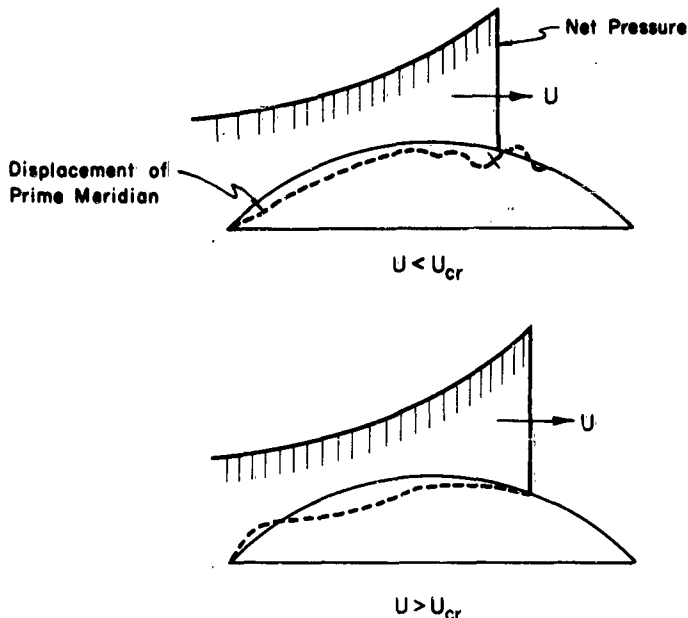
Figure 2.4 Comparison of bending waves.

for dome vibration. The time intervals, Δt, and corresponding distance intervals, ΔD, are given by the formulas (see also Equation 2.22):

$$\Delta t = \frac{\pi R}{2C} = \frac{T}{4} = \frac{1}{4}\left(\frac{2\pi}{\omega}\right) \tag{2.18}$$

$$\Delta D = \frac{U\pi D}{4C \sin \phi_0} = U(\Delta t) \tag{2.19}$$

Where: R = spherical radius of dome, ft
   C = velocity of sound in dome shell, ft/sec
   U = shock-front velocity, ft/sec
   D = dome diameter at spring line, ft
   ϕ_0 = half central angle of dome
   T = period of vibration of dome, sec/cycle

Figure 2.4 illustrates the difference between the geometric character of the bending wave due to a shock front crossing the dome at velocities below and above the critical velocity. For shock-front velocities, U, greater than critical, the deflection configuration of the prime meridian is identical with the deflection configuration of membrane stress shown in Figure 2.3. The shock-front velocity is always greater than critical.

The formula for the critical velocity is:

$$U_{cr} = 0.76C (h/R)^{1/2} \tag{2.20}$$

26

Where: C = velocity of sound in the shell, ft/sec
       h = shell thickness, ft
       R = shell spherical radius, ft

The factors k_d are useful more as a guide for judgment or comparison of designs than as working factors for design. The method of computation for the value of k_d is essentially the computation of the required shell thickness for the net pressure to be resisted and the division of this value by the shell thickness required to resist a uniformly distributed static load of the intensity of peak overpressure. This latter value is an arbitrarily established reference pressure chosen for convenience. Of course, if values of k_d were to be plotted against the significant parameters entering into their determination, the design effort for domes lying within the range of the parameters plotted would be greatly reduced.

The technique for computing k_d is as follows:

1. For several points along the prime meridian (the meridian joining the leading edge of the dome with the crown and trailing edge), net pressure versus time is determined. Here the expression "net pressure" is taken to include effects of reflection coefficient, pressure coefficient, clearing time, wave decay, overpressure, and dynamic pressure.

2. The net pressure $P_n(\phi,\theta,t)$ is transformed to equivalent static pressure $F(\phi,\theta;t^*)$ by the formula:

$$F(\phi,\theta;t^*) = \int_0^{t^*} \omega P_n(\phi,\theta,t)\ \sin\ \omega(t^*-\tau)\,d\tau \qquad (2.21)$$

Where: ϕ = colatitude angle of point on dome shell
      θ = longitude angle of point on dome shell
      ω = circular frequency of dome shell, rad/sec
      t^* = time, constant, instant at which equivalent static load is computed, sec
      τ = time, variable, past history from impingement of blast wave to time t^*, sec

The circular frequency is given by:

$$\omega = \frac{1}{R}\sqrt{\frac{E}{\rho}}$$
$$\qquad (2.22)$$
$$\omega = \frac{C}{R}$$

Where: R = spherical radius of dome, inches
      E = modulus of elasticity of dome material, lb/in^2
      ρ = density of dome material, lb-sec^2/in^4
      C = velocity of sound in dome material, in/sec

The first form of Formula 2.22 neglects the effects of Poisson's ratio; the second is accurate for any material.

It should be noted that in Equation 2.21 both ϕ and θ are constant during integration. Also, it should be noted that Equation 2.21 is of the same functional form as the Duhamel integral solution of a mass-spring system driven by a force of the pressure-versus-time history of $P_n(\phi,\theta,t)$. Therefore, the considerable body of graphical methods for integrating the Duhamel integral solution are immediately applicable to Equation 2.21. Solution of Equation 2.21 is simplified if the pressure function $P_n(\phi,\theta,\tau)$ is expressed in the α,β, system (see Figure 2.1). Then due to the symmetry of the loading function, $P_n(\phi,\theta,t)$ becomes $P(\alpha,t)$, i.e., it is independent of β.

3. For various fixed instants of time, t^*, the values of $F(\alpha,t^*)$ are plotted against α; these are the equivalent distributed static loads for the time instants t^*.

4. Each equivalent distributed static load $F(\alpha,t^*)$ is applied to the dome and the static normal forces N_α and N_β along the prime meridian are computed by static analysis. (The normal

CONFIDENTIAL

forces N are equal to the unit stress times shell thickness.) These are tabulated for the various values of t*.

5. The largest values at each small circle, α, of the tabulated normal forces of Step 4 are divided by the unit normal force N_0 defined by:

$$N_0 = (P_\sigma R)/2 \qquad (2.23)$$

Where: P_σ = peak overpressure, lb/in^2
R = spherical radius, inches

The resulting ratios are values of k_d. Thus:

$$k_d(\alpha) = \frac{N_{\alpha/\beta}(\alpha)\,max}{N_0} \qquad (2.24)$$

Where: $N_{\alpha/\beta}(\alpha)\,max$ represents the largest value of N_α or N_β occurring on the prime meridian at small circle α

Then the shell thickness can be computed for each small circle, α, from Equation 2.3.

Determination of the steel required for elastic reinforced-concrete shells follows the identical procedure, except that in Step 5 the largest negative value (tension) of N_α or N_β at each small circle α is chosen. If a limited amount of plastic deformation is allowable, the strain energy in the steel that would be necessary to maintain the dome elastic is computed, and sufficient steel is provided to accommodate this strain energy by both elastic and plastic deformation.

2.2 FOUNDATION DESIGN

The concrete dome and arch foundations were analyzed and designed as inclined foundations; the axis of the foundation was given the same slope as the tangent to the middle surface of the shell, at the springing. Preliminary design estimates indicated two factors of importance that stopped further consideration of the more conventional, vertical foundations: (1) the greater probability that significant bending stresses would be introduced into the shells at the discontinuity of the springing if vertical foundations were used and (2) the amount of tensile-stress-resistive material (probably steel) required to resist the horizontal component of thrust would be excessive, substantially exceeding the total reinforcement required in the shell itself. The inclined foundation more directly and efficiently delivers the thrust load to the supporting soil.

The initial foundation investigations under Contract AF 33(616)-2522 showed the need for extending and generalizing the studies of Terzaghi (References 7 and 8) and Meyerhof (References 9 and 10). The unique properties of the foundation problem, which were not adequately handled by the literature, became apparent when it was realized that there was little justification for assuming, in a continuous structure such as a dome, that the foundation movements would be oriented in directions perpendicular to the base of the foundation. Also, in the foundation studies of Terzaghi and Meyerhof, the literature shows a difference of opinion in the assumptions regarding the geometry of the zone of plastic equilibrium immediately adjacent to the foundation surface.

Terzaghi states in Reference 7, Page 122, that angles α_o and α_i should be equal to the angle of internal friction, ϕ (see Figure B.1). Thus β would be 180 degrees $- 2\phi$. The reason given is that the resultant of P_n and τ_n must be perpendicular to the foundation base. This reason does not seem valid. For centrally loaded foundations ($\Gamma = 0$) the resultant force on the base is perpendicular to the base regardless of the value of β.

Meyerhof states in Reference 9, Page 303, and Reference 10, Page 442, that the wedge below the footing is a passive wedge and that the angle β is 90 degrees $- \phi$. This view is confirmed by Figure 26 of Reference 11, which shows flow lines in sand under a centrally loaded footing model. The edges of the wedge under the footing are well defined in the photograph, and the angle β appears to be about 90 degrees, minus a reasonable value of ϕ.

28

However, Meyerhof makes the tacit assumption that the angle Γ (Figure B.1) is zero. If the thrust, T, is applied to the footing at angle Γ which may be small, the resultant angle δ is relatively large.

In the analysis of Appendix B, the relation between P_b, P_σ, and Γ is determined without regard for the weight of the soil and its cohesion, both conservative simplifications. The analysis is made for an infinitely long, straight footing. The bearing values obtained are so high that it has not been considered necessary to take into account the curvature of the footings.

The results obtained in Appendix B are plotted in Figure 2.5 for three values of ϵ, the angle of inclination of the footing base with respect to the ground surface for an angle of internal fric-
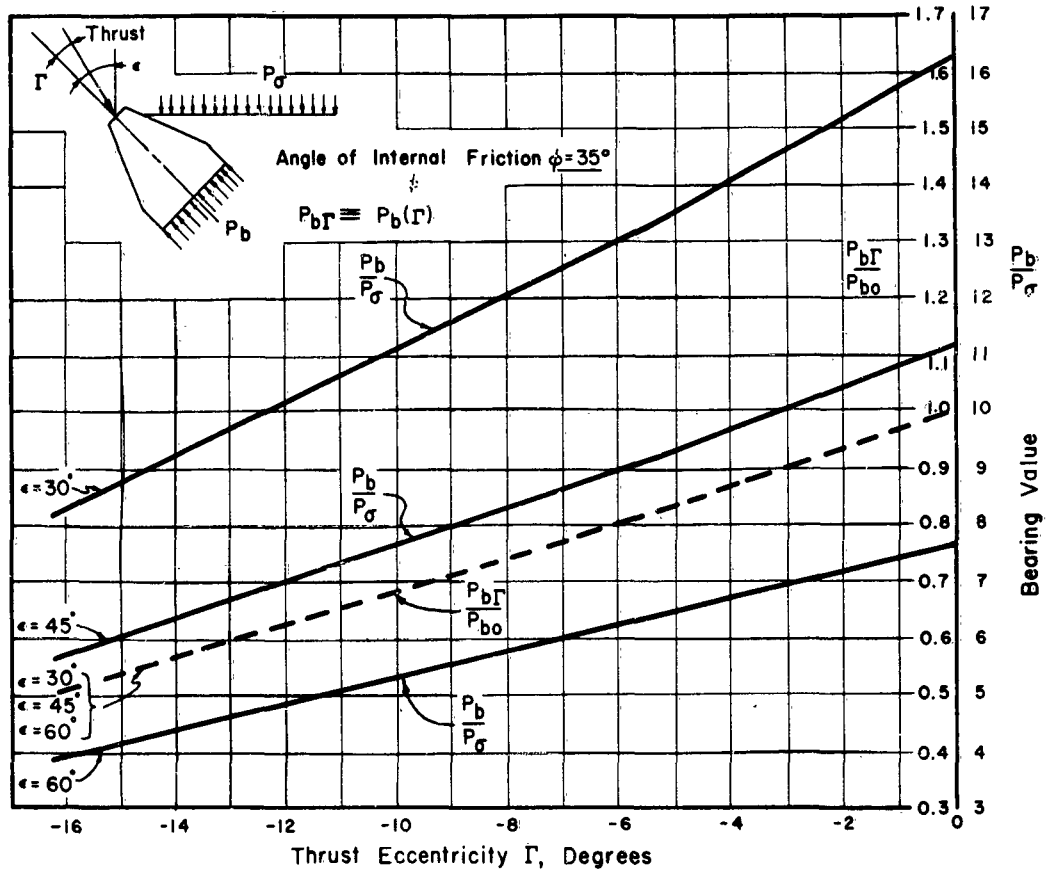
Figure 2.5 Foundation bearing value versus thrust eccentricity.

tion, ϕ', of 35 degrees. Results are presented in the form of the dimensionless ratio P_b/P_σ versus Γ where P_b is the ultimate bearing pressure and P_σ is the side-on pressure on the surface.

A ratio $P_{b\Gamma}/P_{bo}$ is also presented in Figure 2.5. This factor is defined:

$$\frac{P_{b\Gamma}}{P_{bo}} = \frac{P_b(\Gamma)/P_\sigma}{P_b(0)/P_\sigma} \tag{2.25}$$

Thus $P_{b\Gamma}/P_{bo}$ is an index of the sensitivity of ultimate bearing capacity of the foundation to fortuitous variations in the direction of the action line of the foundation thrust. $P_{b\Gamma}/P_{bo}$ is independent of ϵ.

29

CONFIDENTIAL

It had been intended to design the foundations for the domes on the basis of a conservative assumption for Γ, say 10 degrees. However, it developed during design that the foundation required to resist uplift was larger than would be dictated by any reasonable value of Γ.

Design of the domes for Nevada tests sharpened awareness of the lack of basic knowledge of inclined-foundation design, overpressure (massless) effects, and dynamic soil resistance. More investigation into these promising fields is indicated.

Negative-Phase Uplift of Foundations. The maximum negative pressure to be expected was checked with Dr. H. L. Brode, who provided points plotted in Figure 2.6. At the time the tests were planned Dr. Brode's computations had not been carried beyond a shock
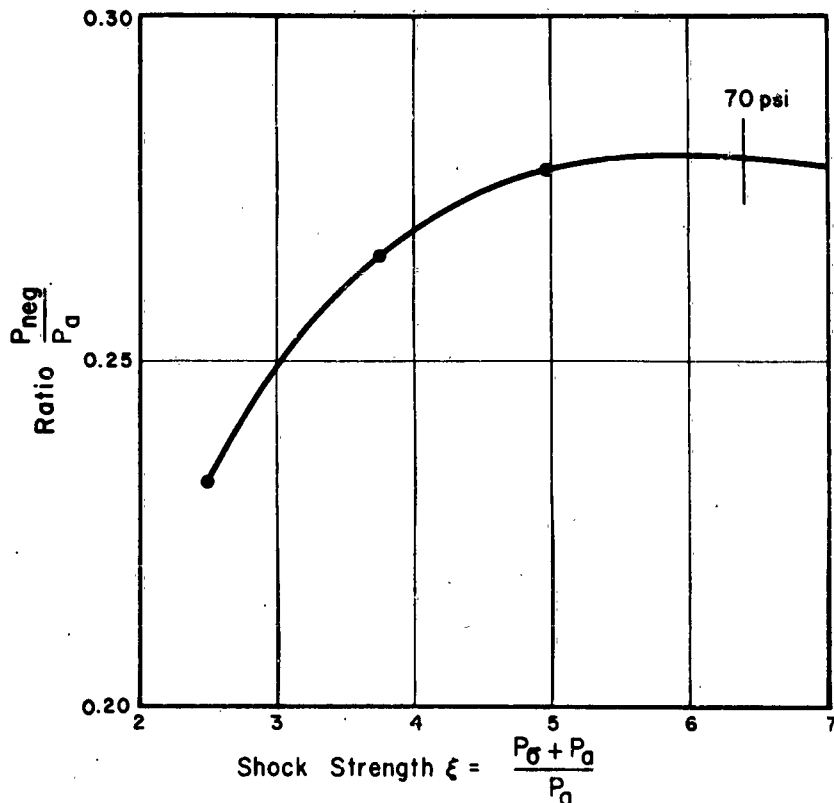
Figure 2.6 Ratio of peak negative pressure to atmospheric pressure, as a function of shock strength. P_σ = peak overpressure, P_a = ambient atmospheric pressure, P_{neg} = peak negative overpressure.

strength of five but Dr. Brode expressed the opinion that the curve would level off at higher shock strengths. From the graph constructed on the basis of these data, it was concluded that in the 70-psi region the ratio of peak negative pressure to ambient pressure would be about 0.28. For ambient pressure of 13 psi at the site, this yields a peak negative pressure of 3.64 psi which, when applied to the plan area of the dome, yielded the total uplift force. This figure controlled the mass of concrete required for all dome foundations.

Upward Flow of Soil to Inside of Structures. The possibility that the air pressure on the soil outside of the dome foundations would force the soil beneath the foundations and up into the domes was investigated. The problem was simplified, for sake of analysis, by a consideration of the foundation as an infinitely long rigid wall of negligible thickness buried to a depth h below the surface. The failure surfaces at incipient failure assumed are shown in Figure 2.7.

30

CONFIDENTIAL
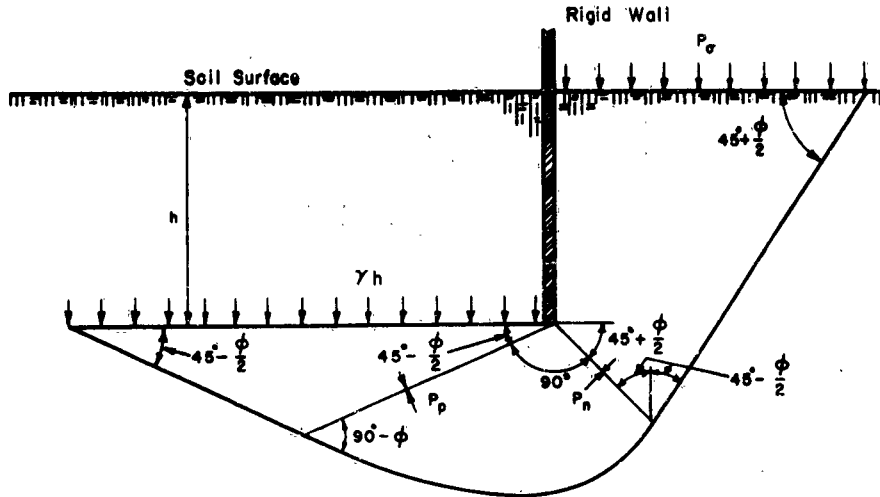
Figure 2.7 Flow of soil beneath rigid wall.

The soil density (lb/ft^3) is taken as γ, the angle of internal friction as ϕ, and the external static pressure as P_σ. Other quantities are defined by Figure 2.7. Cohesion was neglected.

Then: $P_p = \gamma h(1 + \sin \phi)$ (2.26)

$P_n = P_p \, e^{\pi \tan \phi}$ (2.27)

$= P_\sigma(1 - \sin \phi)$ (2.28)

Therefore: $h = \dfrac{P_\sigma}{\gamma} \dfrac{(1 - \sin \phi) e^{-\pi \tan \phi}}{(1 + \sin \phi)}$ (2.29)

For values of $P_\sigma = 70$ psi, $\gamma = 90$ lb/ft^3, and $\phi = 35$ degrees, h should be about $3\frac{1}{2}$ feet to prevent failure. It was concluded that upward flow would not be a determining factor in foundation design.

31

Chapter 3
PROCEDURE

3.1 TEST PLAN

3.1.1 Arrangement of Structures. The 70-psi overpressure region was selected for one group of structures so that they would be tested in the supersonic flow region. Since peak overpressure varies rapidly with ground range at the higher overpressures the likelihood of experimental error was less than it would have been had a higher overpressure level been chosen.

The 35-psi region was chosen for the second group of test structures because this was a region of considerable interest to OCDM and was near the lower limit of regions of interest to the Air Force.

Therefore, the location of the test structures was centered around the 70- and 35-psi overpressure regions.

For brevity the word "overpressure" is omitted in certain portions of the rest of this report when referring to the test structures. Thus, the term "70-psi arch" refers to an arch located at the region where 70-psi overpressure was expected.

Two concrete domes and both of the arch structures were designed to resist the blast loading and located at the expected 70- and 35-psi regions. These structures contained extensive pressure instrumentation and were designated as nonresponding structures.

Three additional dome structures, with the same external dimensions as the nonresponding domes but with thinner shell, were located at the expected 70-, 35-, and 20-psi overpressure regions and designated responding domes. The intent with these domes was to bracket the failure condition; that is, the 35-psi dome was designed for incipient failure resulting in expected survival of the dome at 20 psi and expected failure of the dome at 70 psi. This was done to establish the accuracy of the design procedure and also to ensure the placing of one dome near the incipient failure conditions if the actual weapon yield should vary significantly from its rated value. In addition, the correlation of dome loading with shell deformations and the determination of the mechanism of dome failure were intended to be made on the responding concrete domes.

Two additional smaller aluminum domes were located at the 70-psi region. Response data of these thin-shell structures to the blast loading were desired. Also, a comparison was intended of the behavior of these domes with the concrete domes to examine the possibility of using smaller and less-costly aluminum domes instead of concrete domes in future field-test programs. Aluminum was chosen for the construction because, based on limited information, it was believed to have stress-strain curves similar to those of concrete in compression.

The prototype-door structure was located at the 35-psi overpressure level.

A diagram showing the location of the test structures with respect to the ground zero of the blast is shown in Figure 3.1. Table 3.1 summarizes the important features of each of the structures and their division between Projects 3.6 and 30.1.

3.1.2 Blast Loads on Structures. It was originally believed that the nuclear detonation for the test subjecting the structures to blast loads would be a 30- or 40-kt device exploded on a 500-foot tower. A study of blast data from previous tests showed that the results from Operation Teapot, Shot 12 (Reference 4) could be scaled to the expected blast conditions. Blast loads were predicted from the free-field static and dynamic pressures measured in the Teapot shot. At a later date the burst condition was changed to a 700-foot, 39.5-kt balloon shot. Shot 10 of Operation Upshot-Knothole (Reference 13) was found to scale almost exactly to the revised con-

CONFIDENTIAL
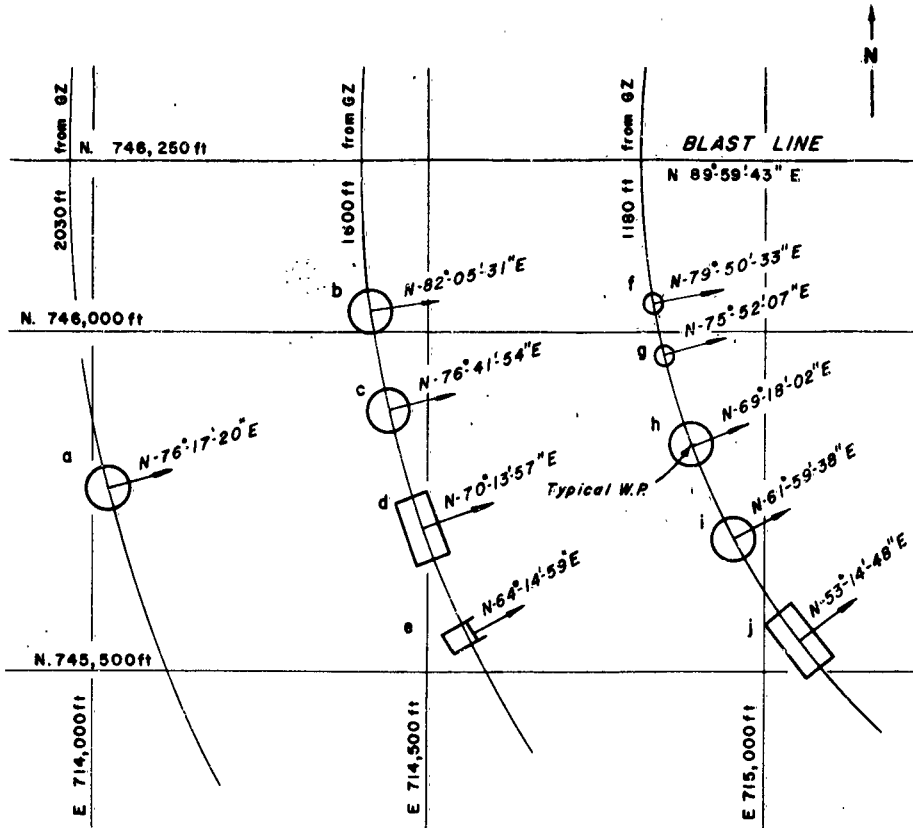
PLOT PLAN

Location of Structure at Work Point

Mark	Project	To Ground Zero	Location		To Blast Line	Structure
		feet	feet		feet	
a	30.1-8001.03	2,030	N-745,766.94	E-714,028.64	481	Concrete Dome
b	30.1-8001.02	1,600	N-746,029.90	E-714,416.90	220	Concrete Dome
c	3.6-9027.02	1,600	N-745,881.95	E-714,443.61	368	Concrete Dome
d	3.6-9028.02	1,600	N-745,708.02	E-714,494.96	541	Concrete Arch
e	30.1-8006.00	1,600	N-745,555.04	E-714,559.55	695	Prototype Door
f	3.6-9026.01	1,180	N-746,041.93	E-714,839.08	208	Aluminum Dome ($\frac{1}{2}$-inch)
g	3.6-9026.02	1,180	N-745,961.96	E-714,856.39	288	Aluminum Dome (1-inch)
h	3.6-9027.01	1,180	N-745,833.00	E-714,896.75	417	Concrete Dome
i	30.1-8001.01	1,180	N-745,696.03	E-714,958.74	554	Concrete Dome
j	3.6-9028.01	1,180	N-745,544.06	E-715,055.09	706	Concrete Arch

Figure 3.1 Layout of test complex.

ditions. Pressure measurements obtained on this test were compared with the predictions which had been made for the expected free-field blast conditions and found to require no significant change in the estimate of the blast loads.

Figures 3.2 through 3.4 show the assumed overpressure-versus-time curves used for the design of the structures in the 70-, 35-, and 20-psi regions. An estimated dynamic-pressure-versus-time curve for the 35-psi region is shown in Figure 3.5. The peak values of dynamic pressure at the 70- and 20-psi regions were estimated by appropriate scaling of the peak values of Figure 3.5. Data from Operation Upshot-Knothole Shot 10 was used to construct the curves.

The reflection coefficients used in predicting the peak diffraction loads on the concrete domes are shown in Figure 3.6. They were estimated from shock-tube tests on half-cylinders reported in Reference 1. It is probable that in the region 30 degrees $< \alpha <$ 60 degrees they are slightly conservative.

The reflection coefficient concept has been extended in Figure 3.6 to include angles of α greater than 90 degrees. For these values of α, the reflection coefficient (or, more properly,

TABLE 3.1 SUMMARY OF TEST STRUCTURES

NTS Structure Number	Type of Structure	Primary Study	Peak Overpressure Expected	Construction Material	Diameter or Span	Length	Height	Shell Thickness	Distance from Ground Zero	Midsurface Radius
			psi		ft	ft	ft	in	ft	ft
FCDA Project 30.1										
F-30.1-8001.01	dome	responding	70	reinforced concrete	50	—	10.7	6	1,180	35.75
F-30.1-8001.02	dome	responding	35	reinforced concrete	50	—	10.7	6	1,600	35.75
F-30.1-8001.03	dome	responding	20	reinforced concrete	50	—	10.7	6	2,030	35.75
F-30.1-8006	prototype door	responding	35	structural steel	*	—	*	*	1,600	*.
USAF Project 3.6										
F-3.6-9027.01	dome	loading	70	reinforced concrete	50	—	11.67	24	1,180	36.5
F-3.6-9027.02	dome	loading	35	reinforced concrete	50	—	11.67	24	1,600	36.5
F-3.6-9026.02	dome	responding	70	aluminum	20	—	4.13	1	1,180	14.14
F-3.6-9026.01	dome	responding	70	aluminum	20	—	4.13	¼	1,180	14.14
F-3.6-9028.01	arch	loading	70	reinforced concrete	34	90	10.25	12	1,180	19.5
F-3.6-9028.02	arch	loading	35	reinforced concrete	34	90	10.25	12	1,600	19.5

* Dimensions of the Prototype door structure were: 21 feet 3 inches long by 12 feet wide by 9 feet 4 inches high. Dimensions of Steel Door were: 10 feet 7 inches wide by 8 feet 3½ inches high.

diffraction coefficient) is the ratio of the initial pressure felt by the dome to the shock-front overpressure. For values of α greater than 90 degrees, the initial pressure increases to the overpressure during the interval corresponding to the clearing time on the front face.

The curves shown in Figure 3.6 are for blast waves with a zero rise time. The peak reflected pressures for blast waves having a finite rise time, like the ones shown in Figures 3.2 through 3.4, are estimated by a method which is discussed in Appendix C.

The determination of the pressure coefficients to be used in estimating the drag loads acting on the dome during the drag phase of the blast load was a problem of considerable magnitude. Three factors contributed to the difficulty:

1. The available data on pressure coefficients from shock-tube and field tests of dome and dome-like models was limited. Most tests had been concerned principally with the diffraction phase of loading and were conducted at pressures so low that accurate determination of the pressure coefficients was not possible.

2. The dynamic pressures measured at the NTS are greater than ideal by a factor of four to six. A significant part of the abnormal dynamic pressure is due to entrained dust. It is questionable that the drag characteristics of entrained dust are even reasonably analogous to the drag characteristics of air.

3. The many wind-tunnel and shock-tube tests previously conducted on complete spheres have demonstrated that the drag of spherical models is sensitive to turbulence in the air stream (Reference 14, Pages 31, 32, and 33).

Therefore, it was concluded that, for the responding dome tests, the best that could be done was to adopt reasonable (but not too conservative) values for the pressure coefficients, based on educated guesses as to which of the widely varying available data most nearly matched NTS conditions.

34

CONFIDENTIAL
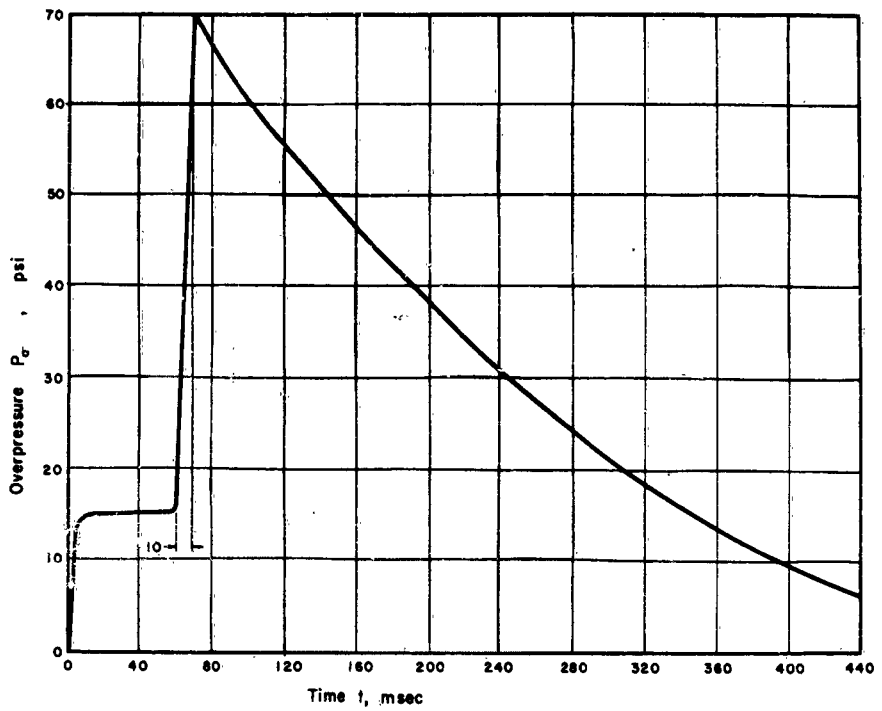
Figure 3.2 Assumed overpressure versus time in the 70-psi overpressure region.
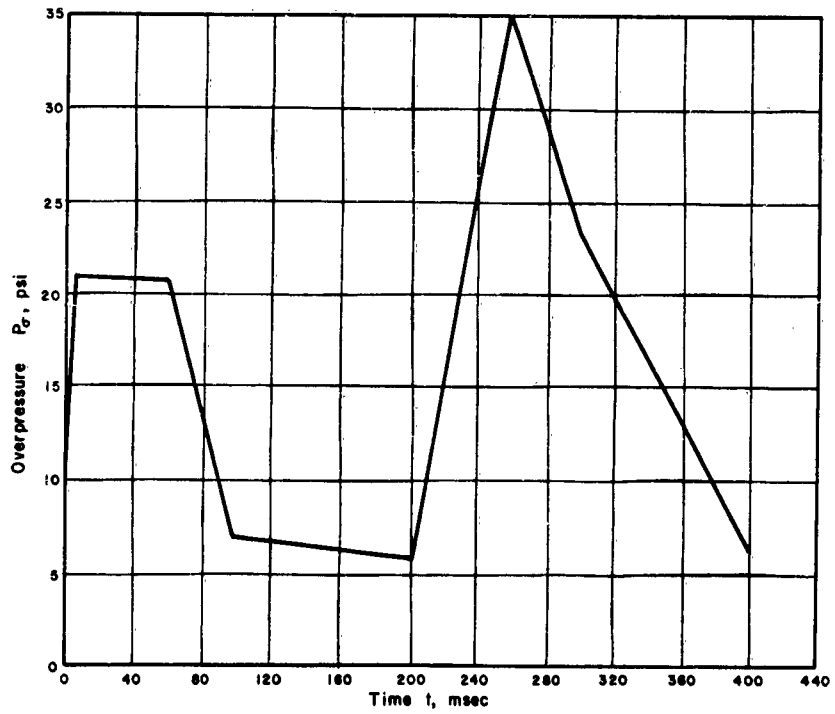
Figure 3.3 Assumed overpressure versus time in the 35-psi overpressure region.

35
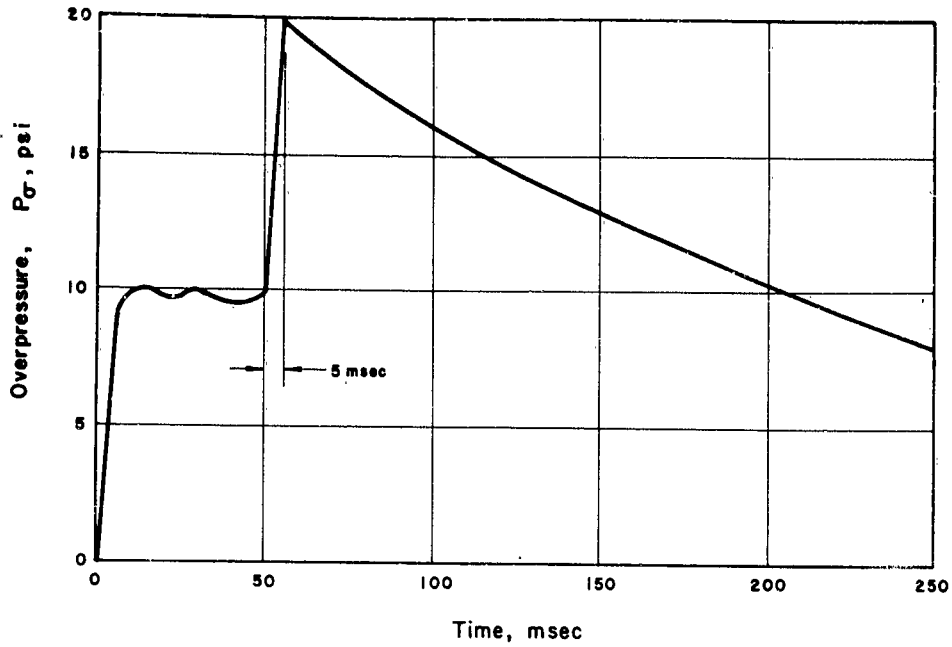
Figure 3.4 Assumed overpressure versus time in the 20-psi overpressure region.
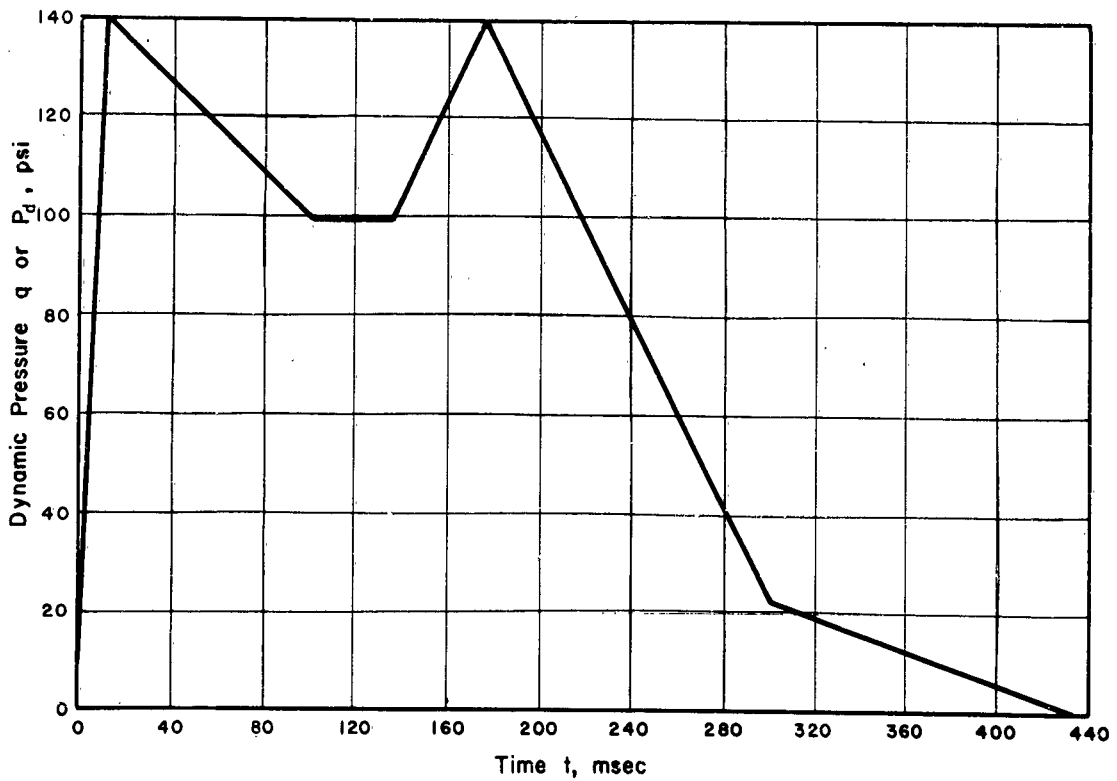
Figure 3.5 Assumed dynamic pressure versus time in the 35-psi overpressure region.

36

CONFIDENTIAL

The principal authority relied upon in choosing the drag and pressure coefficients was Hoerner (Reference 15). The Reynolds number for both the concrete and aluminum domes was on the order of 10^6 to 10^8, both figures well above the critical value of 4.6×10^5. Figure 3.2 of Reference 15, gives the pressure distribution on a complete sphere for values of the Reynolds number, both above and below critical, for subsonic flow.

Figure 3.5 of Reference 15 gives the value of the drag coefficients for complete spheres plotted against Reynolds number, n_r. In the range n_r from 10^6 to 10^8 the drag coefficient, C_d,
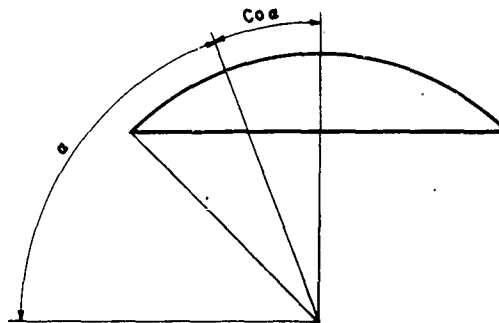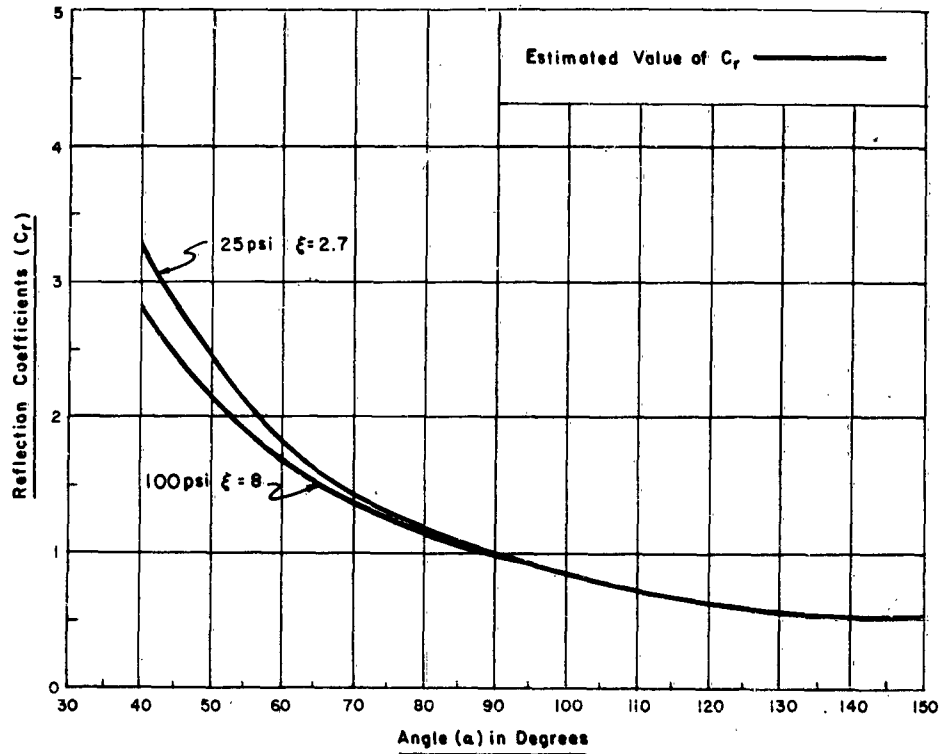
Figure 3.6 Assumed reflection coefficients for domes versus elevation angle, α.

rises from 0.1 at 10^6 to 0.15 at 10^7 and drops again to 0.1 at an n_r of 10^8. These data were obtained in liquids and wind tunnels and are, therefore, applicable to subsonic flow.

Figure 4.16 of Reference 15 gives the steady-state drag on dome-like rivet heads in a turbulent boundary layer as a function of both the height-to-diameter ratio (h/d) and the ratio of height to distance beyond the leading edge of an airplane wing (h/x). For h/d of 0.2 (about the value for the domes), the drag coefficient is less than 0.1 for all values of h/x except within the internal

CONFIDENTIAL

$0.004 < h/x < 0.60$. Within this internal the drag coefficient has a maximum of 0.14. For the domes the h/x parameter is not strictly valid but might reasonably be taken as the height divided by the distance between the 70-psi line (previous disturbance to flow) and the 35-psi line, or about 0.02.

Thus, since the precursor blast wave is certainly turbulent, the 0.1 figure would seem to be a reasonable value for the 35-psi region, where the air flow is subsonic, ideally at least, though actually the particle velocity is undoubtedly higher than ideal.

The flow at the 70-psi region was expected to be greater than Mach 1.0. Figure 12.10 of Reference 15 shows the drag coefficient for complete spheres as a function of Mach number. The coefficient at Mach 0.6 is about 0.5, rising irregularly to 0.8 at Mach 1.0 and continuing more smoothly to 1.0 at Mach 1.4. The value of 0.5 at Mach 0.6 implies that the models used were so small that at 0.6 the Reynolds number was still below the critical value of 4.6×10^5. How the drag coefficient of spheres varies at both supercritical Reynolds number and supersonic Mach number is not given.

In Reference 16, Figure B.22, a graph of drag coefficients for spheres plotted against both Mach and Reynolds numbers is reproduced. Unfortunately, this graph does not extend to the range of Reynolds numbers of interest. It would appear from extrapolation that at Mach 1 and Reynolds number of 10^7 the drag coefficient would be about 0.6 or 0.8.

Thus, the drag coefficient of the dome at the 70-psi region was expected to be higher during the initial high-velocity flow than the 0.1 value assumed for the 35-psi dome. It was decided, however, to use the 0.1 drag coefficient for estimating the loads on the 70-psi dome because it was expected that the supersonic flow would last for a very short period of time and because a slightly nonconservative design approach was desired on the 70-psi dome to ensure severe response to the blast loading.

In order to design the domes it was necessary to know the local pressures due to the flow rather than the total force given by the drag coefficient. Therefore, it was necessary to estimate the local pressure coefficients on the dome from the assumed drag coefficient. The assumptions were made that the normal pressure on the front of the dome varied as $\cos^2 \alpha$, the negative drag on the rear side of the dome was 30 percent of the total drag, and the total drag coefficient had a value of 0.1. Then it was shown that the maximum pressure coefficient on the dome, at α equals 45 degrees, was equal to 0.17. The corresponding drag coefficient on a complete sphere would be 0.25. To bring this value more in line with the values of drag coefficients for spheres presented in Figure 3.5 of Reference 15, it was reduced by a factor of two. The resulting pressure coefficients used for the design of the domes were then found by assuming a maximum pressure coefficient of 0.085 at $\alpha = 45$ degrees and assuming a $\cos^2 \alpha$ distribution of the values of pressure coefficients at other points on the front face of the dome. Pressure coefficients obtained from net pressure measurements made in the test, which are described later in this report, showed significant divergence from the assumed values, especially in the early stages of the blast loading.

For design of the arches, the pressure coefficients were taken from Reference 16, Figure B.3, which reproduced them from NACA Technical Note 2960.

Figure 3.7 reproduces the curve for a Mach number of 2.0 only. According to Figure B.3 of Reference 16, the entire curve is displaced downward an amount equal to a change of C_p (the pressure coefficient) of between 0.15 and 0.2 by a decrease of Mach number to 1.5. However, Figure B.5 of Reference 16 (also reproduced from NACA TN 2960) shows an estimated sharp rise of about 50 percent in the drag coefficient in the vicinity of Mach 1.0. Had the arches been designed as self-supporting structures, this variation in drag coefficient would have required considerable further consideration. However, it turned out that for even the Mach 2.0 pressure coefficients, self-supporting arches could not be built economically. No further investigation was devoted to the variation of arch-pressure coefficients with Mach number.

3.2 DESIGN OF STRUCTURES

3.2.1 Responding Concrete Domes. It was desired to place one identical responding concrete dome in each of three pressure regions. It was intended that the medium-pressure dome would

CONFIDENTIAL

suffer slight damage from the blast, while the high- and low-pressure domes would suffer extensive damage and survive the blast undamaged, respectively.

The medium-pressure level was established at 35 psi, and preliminary designs were made for the expected blast wave. For the low-pressure dome, the most-severe loading conditions (no precursor, short rise time) were assumed, and the pressure resistance was computed at about 20-psi overpressure. For the high-pressure region, the least-severe loading conditions
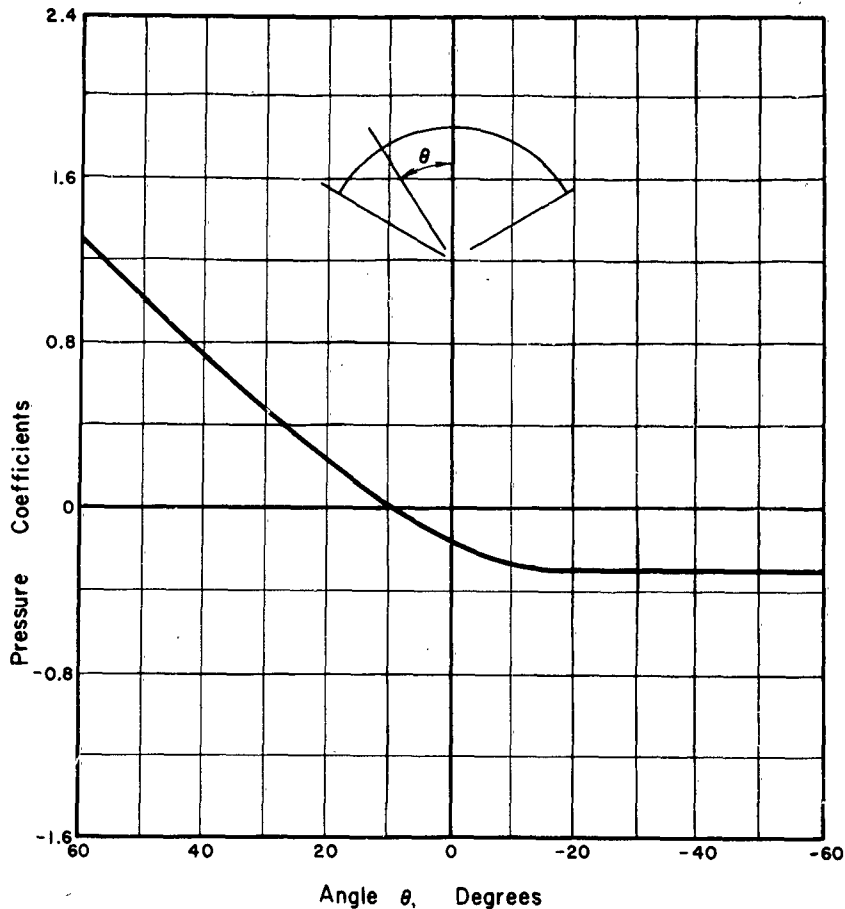
Figure 3.7 Pressure coefficients for arch. Data
obtained from NACA TN 2960; Mach number equals 2.

were assumed (rounded precursor, long rise time), and the dome resistance was computed to be about 70 psi.

The actual blast waves encountered at NTS diverge so greatly from ideal that it was considered impossible to design the domes for precise, assumed test conditions. However, it was necessary to bracket the range of possible conditions with the three domes, so that the desired response information would be obtained. This was attempted as follows:

1. For the two lower-pressure domes, extreme values of the factor k_d were computed; for the high-pressure dome, only the lower value of k_d was computed. Some judgment was exercised in setting the limits on k_d for the 35-psi dome, so that the range of values would not be so great that the design method would be defeated. Values of k_d were computed at $\alpha = 50$ degrees, which is 5 degrees or about 3 feet above the spring lines of the domes. (It was believed that the restraint of the foundation would effectively strengthen the outer few thicknesses of the dome shells.)

39

CONFIDENTIAL

2. A plot was made (Figure 3.8) of the maximum membrane unit force, N (shell thickness, h, times allowable unit stress, σ), versus overpressure for the several values of k_d.

3. The range of k_d at each overpressure level was plotted in Figure 3.8, and the effects of 10 percent increase or decrease in pressure was plotted.

4. A design value of $h\sigma$ was chosen so that the low-pressure dome would probably survive undamaged, the medium-pressure dome would probably suffer some damage, and the high-pressure dome would certainly be damaged. The value chosen was $h\sigma$ = 22,000 lb/inch.

5. The value of σ corresponding to several assumed values of h was computed. For a 6-inch-thick shell, the concrete stress was computed to be 3,670 psi. This value was considered
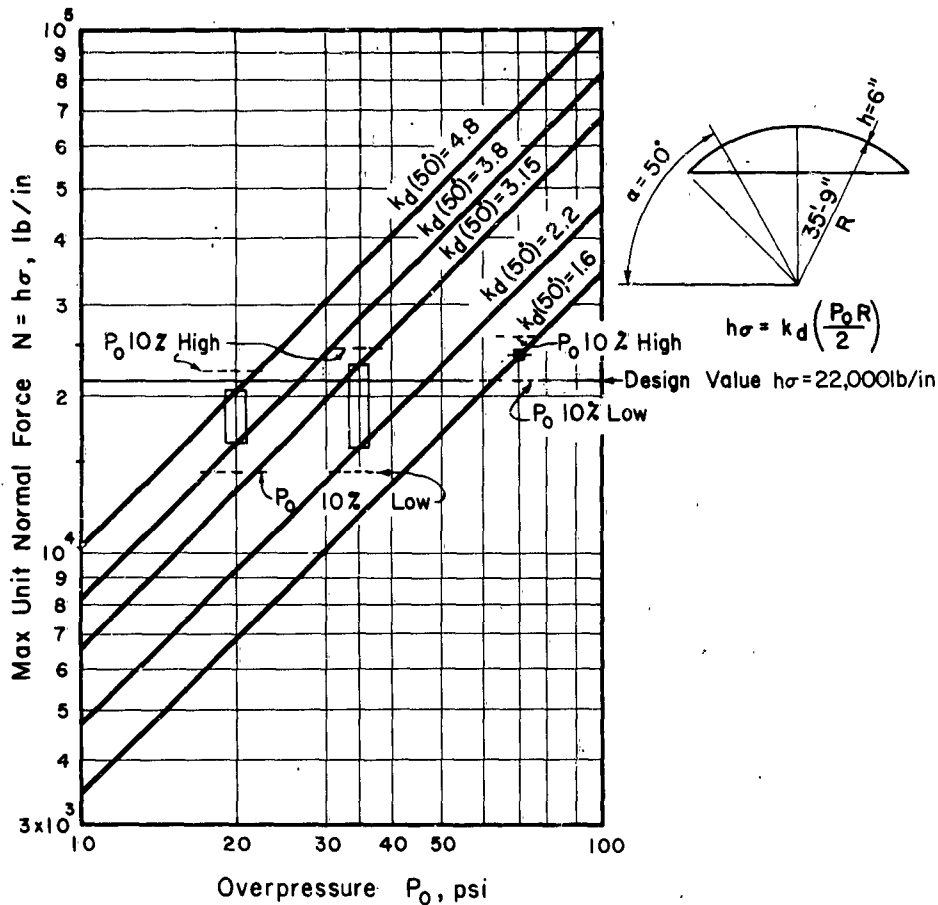
Figure 3.8 Maximum unit normal force in spherical dome
as a function of peak overpressure.

to be reasonable for the average ultimate value of compression stress for the 4,500-psi concrete specified, considering the adverse curing conditions at the test site and the inevitable construction deficiencies.

The 6-inch-thick shell was adopted.

Reinforcing of the responding dome shells was designed to resist: (1) rebound of the shell during the second half cycle of vibration; (2) membrane tension in the leeward half of the shell during the loading phase; (3) shear and diagonal tension; (4) negative pressure; and (5) shrinkage stresses during curing.

At peak rebound, the strain energy in the shell is equal to the strain energy at peak compression stress minus the energy returned to the blast wave by the shell moving outwardly against

40

the blast pressure. For shell materials having the same mechanical properties in tension and compression the peak tension stresses developed during rebound can be computed from the formulas

$$\sigma_t = k_{dt} (P_\sigma - R)/2h \qquad (3.1)$$

Where σ_t is the maximum tension unit stress in the shell and k_{dt} is an appropriately determined dynamic factor.

For long-duration blast waves having short rise time k_{dt} is given with good accuracy by

$$k_{dt} = (k_d - 4) \qquad (3.2)$$

For sharply decaying or irregular waves k_{dt} is more difficult to obtain. If we denote by F_t the equivalent static pressure for tension stress and by r_β the fraction of external load resisted by stress along small circles of constant α then k_{dt} is given by

$$k_{dt} = 2r_\beta (F_t/P_\sigma) \qquad (3.3)$$

The gyrogram method (see Appendix C) can be used to determine F_t, the value of F_t being that corresponding to the second crossing of the vertical axis (F axis) by the gyrogram. For the 20-psi dome, F_t was found to be 14 psi. Estimating that 90 percent of the external pressure is resisted by the σ_β stresses and 10 percent by the σ_α stresses, k_{dt} was computed to be

$$k_{dt} = 2 \times 0.9 \times (14/20) = 1.25$$

The reinforced-concrete domes did not have the same mechanical properties in tension and compression. Also, the blast waves to which they were subjected had significant decay rates. The technique used was to compute the strain energy that would exist in the shell at maximum rebound during the first cycle of vibration if the shell had identical tension and compression properties. Then sufficient steel was provided to accommodate this strain energy. It was assumed that the development of cracks in the concrete during the tension regime, and slight yielding of the steel would provide damping sufficient to reduce peak tension stresses at the peak of the second cycle of rebound to values below those developed during the first rebound cycle.

The 20-psi dome was critical for rebound. For a fictitious concrete having identical tension and compression properties, the peak tension stress would be

$$\sigma_t = \frac{1.25 \times 20 \times 429}{2 \times 6} = 890 \text{ psi}$$

and at a modulus of elasticity of 4×10^6 psi the unit strain energy would be 0.099 lb-in/in^3.

At an assumed yield point stress of 4.5×10^4 psi the unit strain energy capacity of the reinforcing steel was computed to be 33.7 lb-in/in^3.

Then the percent steel required to resist rebound was computed to be

$$\frac{100 \times 0.099}{33.7} = 0.293 \text{ percent}$$

This value is approximately the steel ratio usually provided to resist shrinkage and temperature stresses. Rebound was not critical for tension-steel design.

The maximum negative pressure expected was less than 4 psi. Therefore, negative pressure did not control design of reinforcing steel.

If the blast wave has a short rise time most of the equivalent static load is resisted by the σ_β stresses. However, even though the σ_α compression stress is small it is propagated ahead of the wave front into the portion of the dome not engulfed by the blast. Velocity of propagation is

CONFIDENTIAL

approximately the sonic velocity of the shell material, about 11 feet per msec for the concrete domes. A true shock of the dome is under no external pressure at this time, so an equal and opposite tension stress is developed in the σ_β direction. If steel is not provided to resist this stress the shell will crack somewhat and relieve both the σ_α and σ_β stresses on the leeward side, the windward side then carrying the entire equivalent static load by σ_β compression stresses. A short time later, when the entire dome is engulfed by the blast wave, the previously opened cracks on the leeward side are closed. For the test structures, if the tension steel undergoes inelastic yielding equal to the yield-point strain, cracks (having an aggregate width of about $\frac{3}{4}$ inch) will appear in the leeward sides of the domes. Cracking of this magnitude, it was believed, might introduce difficulties in interpretation of the instrumentation; also, it was desired that the 20-psi dome survive undamaged. Therefore, the tension steel was designed to remain elastic.

For the 35-psi dome the maximum expected value of k_d was 3.15. Assuming that 90 percent of the equivalent static load was resisted by the σ_β stress, the k_{dt} factor was computed to be

$$k_{dt} = 3.15 \times (0.1/0.9) = 0.35$$

The unit stress in a fictitious concrete having identical tension-and-compression mechanical properties was computed to be

$$\sigma_t = \frac{0.35 \times 35 \times 429}{2 \times 6} = 438 \text{ psi}$$

At 45,000-psi yield point the steel percentage required to resist this stress was computed to be

$$\frac{100 \times 438}{45,000} = 0.98 \text{ percent}$$

At 40,000-psi yield point the steel percentage required was computed to be 1.1 percent. Half-inch bars at 6-inch centers in each face provided 1.05 percent steel. This spacing was used.

In order for reinforcing steel design to be influenced by shear or diagonal tension, a set of biaxial stresses of opposite sign has to be developed in the shell. This situation does not occur in blast-loaded domes.

Shear, diagonal tension, negative pressure and shrinkage were checked for the domes and found to require less steel than had been provided for rebound.

The refinement of varying the thickness of dome shells was not considered desirable. This conclusion was considerably influenced by the factors that the uniform shell is easier to build and would probably be easier to analyze, though deflections might be somewhat less than would be obtained with nonuniform shells.

The uniform shells required design at only one specific point, that of maximum stress. This was estimated to be at $\alpha = 50$ degrees on the prime meridian.

The design method used was based on the presumption that the entire net pressure is resisted by uniaxial stress. Use was also made of the fact that (for membranes) the sum of the two normal stresses is always proportional to the net pressure. Therefore, in plotting the net-pressure waves, components resisted by equal biaxial stress were halved. Thus, half of such a component, when treated as though resisted by uniaxial stress, yielded the same result as the entire component resisted by biaxial stress.

The design procedure was further simplified by making three assumptions regarding stress distribution in the dome shell: (1) An overpressure wave having a rise distance (rise time × wave velocity) less than two thirds of the dome diameter is resisted by biaxial stresses (σ_α and σ_β), the σ_β stress being at least 90 percent of the total stress ($\sigma_\alpha + \sigma_\beta$) and the σ_α stress being less 10 percent of the total stress. (2) A pressure wave component completely engulfing the dome is resisted by equal biaxial stresses. (3) Dynamic pressure, being positive on the ground-zero side of the dome and negative on the other, is resisted by uniaxial stress.

The above assumptions result in a conservative design yielding a shell thickness no more than 20 percent thicker than would result from a more accurate analysis.

One further assumption was required. During the diffraction phase of loading which controlled design, dynamic pressure is conventionally included in the reflection coefficient. However, the high dynamic pressures of hot, dust-laden air encountered at NTS are not accounted for by shock-tube-determined reflection coefficients. For these designs, dynamic pressure was assumed to be six times the ideal. Therefore, the effect of the excess five sixths of the total was accounted for by adding to the reflected overpressure. The low-pressure coefficient used for these designs reduced the local drag pressure to a value so low that this component was not a large factor in the determination of k_d. This assumption was used only for the combination of rapid overpressure rise and slow dynamic-pressure rise (Computations 3, 5, and 6 of Table 3.2).

The following characteristics of the 50-foot diameter concrete domes were computed and used in the computation of k_d.

> Circular frequency, $\omega = 302$ rad/sec
> Period, $T = 21$ msec/cycle
> Reflection coefficient at $\alpha = 50$ degrees, $C_r(50) = 2.4$
> Shock-front velocity, U:
>   20-psi dome, $U = 1.7$ ft/msec
>   35-psi dome, $U = 2.0$ ft/msec
>   70-psi dome, $U = 2.65$ ft/msec

The clearing time was taken to be the time required for the shock front to pass from the point $\alpha = 50$ degrees on the prime meridian to the crown of the dome. This value is admittedly only an educated guess. However, examination of the records reproduced in Reference 5 indicated that this was a reasonable approximation. The clearing times computed were:

> 20-psi dome, $t_c = 13.5$ msec
> 35-psi dome, $t_c = 11.6$ msec
> 70-psi dome, $t_c = 8.8$ msec

Table 3.2 summarizes the values of $k_d(50$ degrees) computed for the 50-foot-diameter concrete responding domes and the values of parameters assumed for their computation. The method for determining the peak value of the equivalent static load is illustrated in Appendix C.

For a rapid rise, 90 percent of the equivalent static load was assumed resisted by uniaxial stress. Therefore, for rapid-rise loading, the peak equivalent static load was multiplied by 1.8 before division by the nominal peak overpressure to obtain $k_d(50$ degrees).

The slow-rise equivalent static pressures (Computations 1 and 4, Table 3.2) were multiplied by two before being divided by the nominal peak overpressure. This was done to correct for the step in the design procedure (see Appendix C) in which pressures resisted by biaxial stress are divided by two for reduction to a common base for addition to pressures resisted by uniaxial stress.

Foundations for the responding concrete domes were designed in the following manner. The mass of the foundations provided was found to be controlled by resistance to uplift at a negative pressure of 3.64 psi. Steel was arbitrarily established at 0.5 percent of the gross area. This is greater than the 0.3 percent required for shrinkage, but it was believed to be justified as insurance against an outward-moving foundation failure in the event that significant compression of the surrounding soil would be necessary before the bearing values predicted by theory could be developed. For the same reason, the foundation was poured against a shotcrete pad placed on undisturbed soil.

During the transit time of the blast wave, local bearing pressures on the foundation could have exceeded the average design value by a factor of 60 percent. This situation would have had two significant effects: (1) The foundation, to remain intact, would have to function as a beam having small span-to-depth ratio for short sections of its length. (2) Some of the high local shear would be transmitted to the dome shell.

43

CONFIDENTIAL

These factors were provided for by the use of a system of inclined stirrups for the foundation, as is recommended for deep concrete beams. The dowels joining the shell to the foundation were inclined also and designed for a low stress, about 16,000 psi, for the expected maximum shear in the 35-psi shell. Thus, the foundation-shell interface could resist local values of shear three times as great as the expected maximum values. At the entrance doors, which were placed on the less-severely loaded side of the foundations (away from ground zero), the upper or lower

TABLE 3.2 SUMMARY OF VALUES OF k_d COMPUTED FOR 50-FOOT-DIAMETER RESPONDING DOMES

Number	psi	Loading Condition	Uniform Over-pressure Component	Uniform Dynamic Pressure Component	Overpressure Rise		Dynamic Pressure Rise		Local Drag Pressure	α = 50° β = 0°	% Drag Pressure	Uniform Load Component (Fig. C.2)	Peak Reflected Pressure (zero rise)	Clearing Time	Peak Value Equivalent Static Load (Fig. C.3)	180 pct Equivalent Static Load	200 pct Equivalent Static Load	k_d (50°)
					psi	msec	psi	msec	uniform	fast rise	%							
1	70	Slow rise assumed	70	300	70	QS*	300	QS*	20.6	—	NA†	56	—	8.8	56	—	112	1.6
2	35	Initial precursor plus steep dynamic	0	0	21*	10*	140	10	—	9.6	NA†	—	60	11.6	83	150	—	4.3
3	35	Initial precursor slow dynamic rise	0	140	21	10	140	QS*	9.6	—	8	7	50	11.6	61	110	—	3.15
4	35	Slow main-wave rise, slow dynamic rise	6	140	29	58	140	QS*	9.6	—	8	11	70	11.6	31	—	62	2.2
5	20	Main wave, Figure 3.4	10	53	10	5	53	QS*	3.6	—	3	8	24	13.5	48.5	87.5	—	4.35
6	20	Main wave, no precursor	—	53	20	5	53	QS*	3.6	—	3	3	48	13.5	53	96	—	4.8

* Zero rise time for pressure rise from 0 to 13 psi.
  10 msec rise time for pressure rise from 13 to 21 psi.
† Quasi-static.

jambs were curved to provide local concrete arches sufficient to carry the transverse stress around the door.

3.2.2 Responding Aluminum Domes. Shells. The circular frequency was computed to be $\omega = 1,160$ rad/sec. The period was computed to be $T = 5.4$ msec/cycle. Clearing time at $\alpha = 50$ degrees was then taken as $t_c(50 \text{ degrees}) = 3.5$ msec.

The main wave was assumed to rise from 15 psi to 70 psi in 10 msec. This rise was so long with respect to the clearing time that diffraction effects were considered negligible. During $\frac{1}{2}$ cycle of vibration, the rise in overpressure would be about 15 psi. The static pressure corresponding to the dynamic overshoot of a single-degree-of-freedom system loaded by a linearly rising forcing function is equal to the pressure rise during $\frac{1}{2}$ cycle divided by π. This component of pressure was assumed resisted by substantially uniaxial stress. When added to a pressure component resisted by biaxial stress, it was doubled.

For design of the aluminum domes, the dynamic pressure was assumed to be about six times ideal, or 410 psi. This value is about 100 psi higher than used for the 70-psi responding concrete dome. However, the aluminum domes were designed to bracket the pressure developed, rather than to suffer severe damage. Therefore, the higher dynamic pressure, which was the best estimate of the actual pressure to be expected, was used. At $\alpha = 50$ degrees, the local drag pressure due to this would be about 29 psi. This, also, is resisted substantially by uniaxial stress.

Thus, the total equivalent static load at $\alpha = 50$ degrees, converted to pressures resisted by biaxial stress, was computed to be:

CONFIDENTIAL

Precursor pressure	15 psi
Rise to main overpressure peak	55 psi
Overshoot pressure (times two)	9 psi
Drag pressure at α = 50 degrees (times two)	58 psi
Equivalent Static Load	137 psi

Thus, k_d(50 degrees) was computed to be 1.9.

So that the as-welded properties of the aluminum domes would be nearly the same as the parent metal, it was necessary to employ a low-strength alloy. The alloy selected, 5052-0, was listed (Reference 17) as having an ultimate strength of 28,000 psi and a yield strength of 13,000 psi.

Two domes were provided, one expected to remain elastic at computed pressure and the other expected to be driven far into the plastic region. Basing the design on the yield-point stress would have required a thickness of $7/8$ inch. Therefore, the two domes were made 1 inch and $1/2$ inch thick, respectively.

The $1/2$-inch-thick dome was checked for stability. Reference 18 lists the formula for critical pressure for a spherical shell as:

$$P_{cr} = \frac{2E(h/R)^2}{\sqrt{3(1-\nu^2)}}$$

Where: P_{cr} = critical pressure, lb/in^2

E = modulus of elasticity, lb/in^2

ν = Poisson's ratio

For the $1/2$-inch-thick aluminum dome, P_{cr} was computed to be 104 psi. Since buckling takes some time and since this value is based on a uniformly distributed pressure and the value computed was 50 percent higher than the nominal peak pressure, the $1/2$-inch aluminum dome was presumed to be safe against buckling.

Foundations. In order to prevent uplift during the negative phase of the blast, the mass of the concrete provided was required. Therefore, advantage was taken of the situation to run a qualitative test of the behavior of a combination of tie ring and vertical foundation. For design purposes, the horizontal component of thrust distributed around the foundation top was divided into an average uniform component and a nonuniform component. The nonuniform component was approximated for design purposes by a load proportional to cos 2 θ as shown in Figure 3.9. The foundation steel was designed to carry the uniform component in hoop tension and the sinusoidal component in bending.

Thermal Protection. It was estimated from the curves in Reference 19 that the incident thermal energy would be about 1,000 cal/cm^2, with 80 percent of the total energy delivered in 900 msec.

Assuming a reflectivity of 60 percent for the fabricated aluminum, the average temperature rise for the $1/2$-inch dome would have been about 540 C, or 970 F. This implied that the surface of the aluminum domes required thermal protection. For this purpose, a special coating, consisting of a $2\frac{1}{2}$-lb/yd^2 asbestos cloth with a highly reflective 0.001-inch-thick aluminum foil bonded to its surface, was cemented to the dome surface. It was assumed that the foil would reflect 80 to 90 percent of the incident thermal energy and be melted or vaporized by the rest, while the asbestos (due to its low conduction coefficient) would shield the aluminum shell from the heat developed during the interval of interest.

3.2.3 Nonresponding Concrete Domes. Design of the 50-foot-diameter, nonresponding concrete domes closely followed the design for the responding domes except that more severe loading conditions were assumed to increase the probability of survival of the 70-psi dome. Inspection of the Teapot Shot 12 data (Reference 4) disclosed that even at the 160-psi region for this shot a significant precursor existed and that the rise time of the main blast wave was of the order of

45

10 msec or $\frac{1}{2}$ cycle of dome vibration (Reference 4, Figure 2.6). The precursor and rise time at the 70-psi region for the proposed shot were anticipated as being at least as large. Then, assuming a 15-psi precursor of 25 msec duration, a 10-msec rise from 15 psi to 70 psi and a dynamic pressure of 410 psi (six times ideal), k_d(50 degrees) was computed to be about 4.2. At a concrete stress of 3,500 psi, the required shell thickness would have been about 18 inches.

Actual Horizontal Component of Thrust
from Aluminum Dome

$$T_u = \frac{1}{\pi}\int_0^\pi T(\theta)d\theta$$

Uniform Component of Thrust

$$T_n(\theta) = T(\theta) - T(u)$$

Nonuniform
Component of Thrust

$$T_b(\theta) = T_b(0)\cos 2\theta$$

$$T_b(0) = \int_0^{\theta_i} T_n(\theta)d\theta$$

Component of Thrust
Assumed for Bending Design
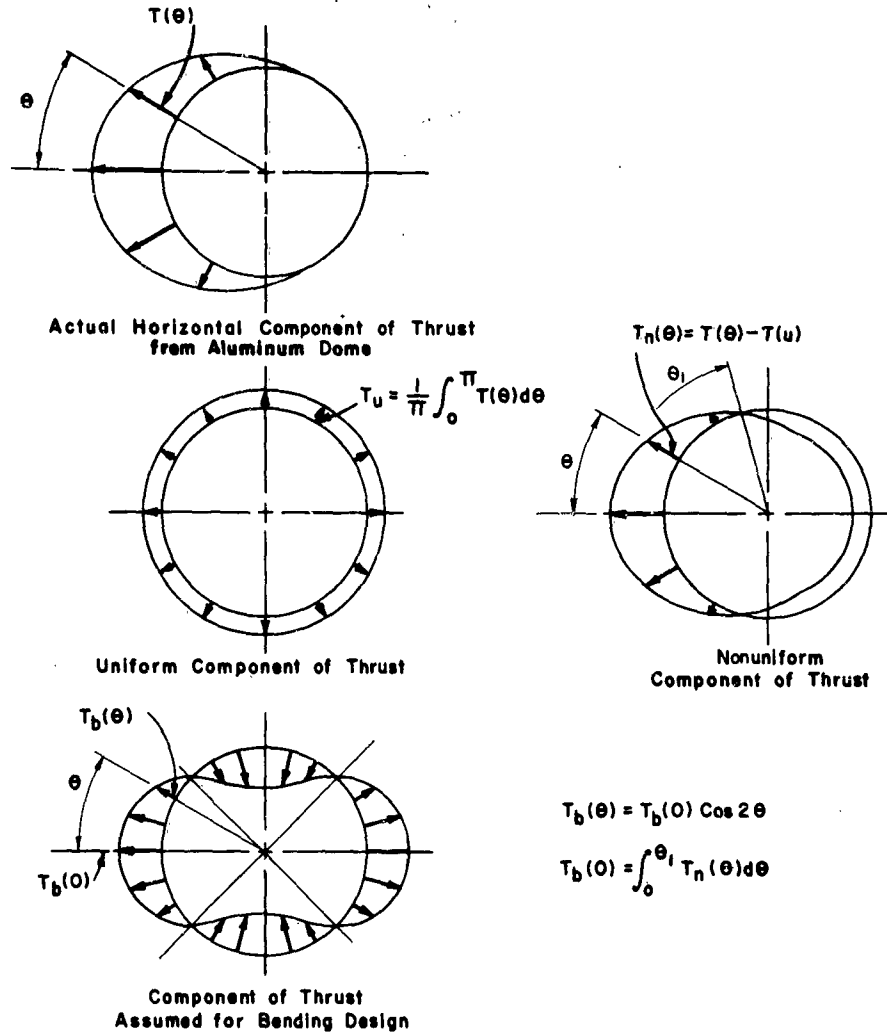
Figure 3.9 Design assumptions for aluminum dome foundations.

This was increased to 24 inches to allow some safety factor for pressures higher than expected and possible deficiencies in concrete strength.

A shrinkage allowance of 0.3 percent required the steel provided. This was checked for adequacy in resisting diagonal tension due to shear. The drag coefficient for the domes was taken at 0.1; the peak dynamic pressure at 410 psi. Shear distribution around the dome on small circles of constant ϕ was taken to be proportional to $\sin \theta$ and tangent to the shell. On these assumptions the unit shear at the spring line was computed to be 1,700 lb/in. If, at the instant of peak dynamic pressure, the overpressure was low (as, for instance, at time 173 msec of Figures 3.3 and 3.5), diagonal tension could approach this value. Adding 50 percent for a safety factor, this required No. 4 bars ($\frac{1}{2}$ inch) spaced in pairs on 7-inch centers at a unit stress of 45,000 psi. The shell reinforcing and dowels provided were more than required for shear.

46

3.2.4 Nonresponding Arches. Originally it was intended to make the nonresponding arch shells self supporting (as was done with the nonresponding domes) and have them double as instrument shelters. However, the high dynamic pressures encountered at the Nevada Test Site necessitated such a thick, heavily reinforced shell (about 54 inches thick with a total of about 6 percent of steel) that the bermed shell was substituted.

Evidently, if the berm could be thoroughly compacted and relied upon to support the entire inside surface of the shell, a nominal concrete cover would have been all that was required.
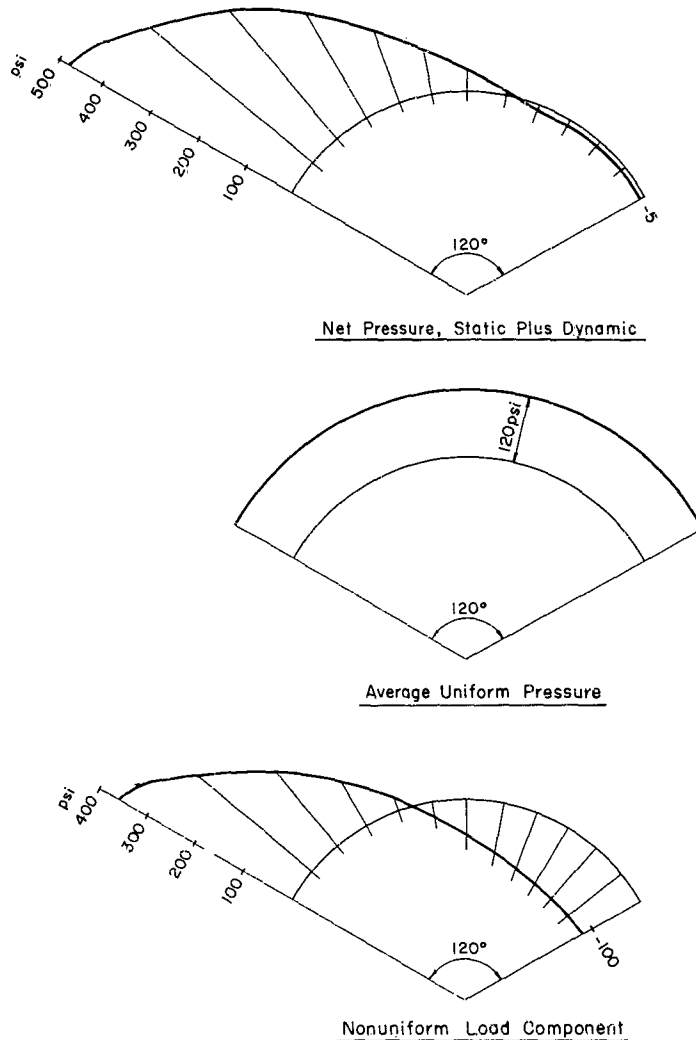
Figure 3.10 Net pressure on arch in 70-psi overpressure region.

However, such perfection of construction seemed grossly overoptimistic, so an arbitrary design criteria was adopted.

The nonresponding arches were designed for an overpressure of 70 psi and a simultaneous dynamic pressure of 310 psi, both applied as static loads. Based on the pressure coefficients of Figure 3.7, the net positive pressure as a function of position was estimated as plotted in Figure 3.10; the absolute values of negative pressure obtained were greater than atmospheric pressure. Therefore, a constant value of −5 psi was assumed on the rear half of the arch.

The uniform load component was assumed carried by the concrete shell and foundation; the nonuniform component by the berm. Actually, this partition of the resistance was open to ques-

47

CONFIDENTIAL

tion: Evidently the berm cannot develop the negative pressure assumed on the side of the structure away from ground zero. In fact, if there was some small shifting and compaction of the soil comprising the berm, the soil on the side away from the detonation might exert an outwardly directed pressure against the arch shell. The average net horizontal force against the arch was computed as 17,000 lb/in of arch, the average net vertical force as 65,000 lb/in. Thus, at an internal friction angle of 16 degrees or greater, the soil mass should be stable except for compaction movements.

Longitudinal steel in the arch was provided for shrinkage, 0.3 percent. The circumferential steel was arbitrarily doubled, thereby providing for about 10 percent of the negative component of the nonsymmetrical load.

The end walls of the arch were designed to resist half of the peak overpressure at the yield point of the steel and at full negative overpressure.
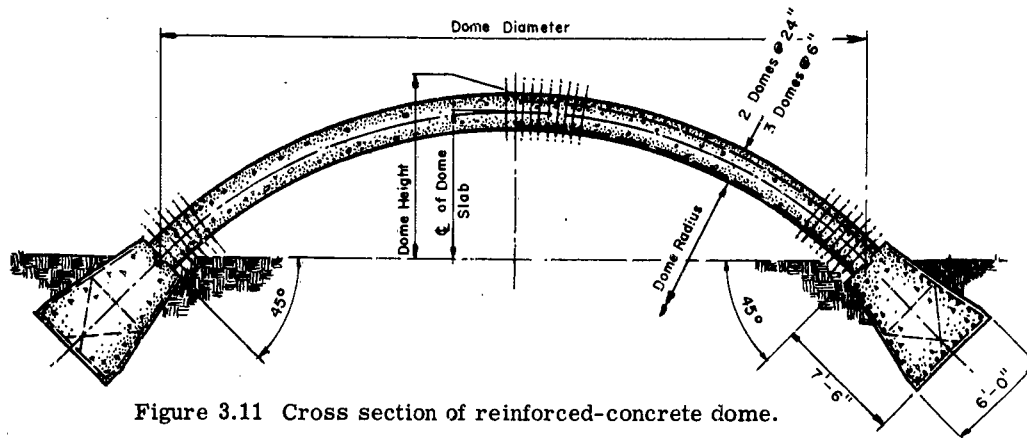
Figure 3.11 Cross section of reinforced-concrete dome.

3.2.5 Prototype Door at 35 psi. The period of vibration of the prototype door was estimated to be about 6 msec; clearing time was estimated to be about 7.5 msec. Assuming a peak reflection coefficient of 3.7, the peak reflected pressure was computed to be 130 psi. The average pressure coefficient on the door was taken from Reference 16, Figures A.20 and A.24. A value of 1.2 seemed reasonable but not excessively conservative in the light of the data. (There was no rear-face negative component acting on the door.) Then an average value of freestream dynamic pressure of 125 psi was assumed, the peaks of the curve being neglected (see Figure 3.5). This yielded a design pressure of 185 psi. This value was considerably higher than the peak reflected overpressure. Thus, the drag phase of the loading was assumed to be critical, so the door was designed for a long-duration load of 185 psi. The structure provided could resist this pressure at a stress of 45,000 psi. Web shear in the beams was computed to be 26,700 psi at this pressure.

The concrete portions of the structure were designed conventionally, except that yield-point stress was used for steel design.

3.3 DESIGN DETAILS

A generalized cross section of the reinforced-concrete domes is shown in Figure 3.11. The height and midsurface radius of each dome is given in Table 3.1. Different midsurface radii were used for the 6- and 24-inch-thick domes to make the inside dome radius the same on each shell. It was intended that a single reusable steel form would be used for the construction of all domes, but difficulties in obtaining steel prevented the use of this system for building the domes. The width of the foundation was 36.5 inches on the 24-inch-thick domes and 20 inches on the 6-inch-thick domes.

The placement of the shell reinforcing on the concrete domes is illustrated in Figure 3.12. The details of the reinforcing are listed in Table 3.3.

48

A cross section of the aluminum domes showing the shell and foundation is presented in Figure 3.13. One dome shell was $\frac{1}{2}$-inch thick and the other, 1-inch thick. The midsurface spherical radii of these domes was 14.14 feet. Foundation reinforcing data are listed in Table 3.3.

Details of the two nonresponding arches are shown in Figure 3.14. Both arches were identical in construction. The midsurface radius was 19.5 feet and the structures were 90 feet long. Foundation reinforcing data are contained in Table 3.3.

Drawings of the prototype door located at the 35-psi region are shown in Figure 3.15.

3.4 INSTRUMENTATION PLAN

A number of types of instrumentation were used to achieve the objectives of the test. Since one of the important objectives of the test was the study of the blast-wave loading on dome and

TABLE 3.3 REINFORCING OF SHELL STRUCTURES

Structure	Shell	Main Reinforcing		
		Foundations		
		Longitudinal	Stirrups	Dowels
50-foot-diameter responding domes	No. 4 Bars at 6-inch centers each face each way	39 No. 6 Bars	No. 4 Bars at 3-foot centers inclined 45° both ways	No. 4 Bars at 6-inch centers inclined 45° both faces both ways
50-foot-diameter nonresponding domes	No. 4 Bars at 6-inch centers each face each way	39 No. 6 Bars	No. 4 Bars at 3-foot centers inclined 45° both ways	No. 4 Bars at 6-inch centers inclined 45° both faces both ways
34-foot by 90-foot nonresponding arches	Transverse: No. 4 Bars at 6-inch centers each face Longitudinal: No. 4 Bars at 12-inch centers each face	5 No. 8 Bars 16 No. 5 Bars	No. 5 Bars at 6-inch centers	No. 6 Bars at 12-inch centers both faces
20-foot-diameter responding domes	—	18 No. 11 Bars 10 No. 6 Bars	No. 7 Bars at 10-inch centers vertical	—

arch surfaces, extensive pressure instrumentation which measured pressure as a function of time was required on the exposed structural surfaces. A second important objective, that of determining the response motions of the dome shell as a function of time during the blast loading, required instruments which would measure the deflection as a function of time at a number of points on the shell. Other instruments, such as mechanical maximum and minimum displacement gages, scratch gages, cameras, accelerometers, and soil test holes were used to provide additional information to satisfy secondary objectives of the test and aid in the interpretation of the test results.

The instrumentation was installed and calibrated, and the data were recorded by two agencies, Armour Research Foundation of Chicago, Illinois, (ARF), and the Ballistic Research Laboratories of Aberdeen Proving Ground, Maryland, (BRL).

The complete structure instrumentation plan is given in Table 3.4. The locations of the instruments on each structure are shown in Figures 3.16 to 3.21. A brief description of the various types of instruments used in the test and their functions are given in the following paragraphs.

3.4.1 Electronic Pressure Gages. The electronic pressure gages were installed by BRL. This type of gage (see Reference 25), used extensively on the dome and arch structures, consisted of a twisted bourdon-tube sensing element attached to an armature in a magnetic field which gave a variable-differential-inductance type of output when pressure was applied to the gage. The output of the gage was recorded on an electronic recorder. The use of this type of gage has the advantage that all records are recorded on a common time base which can be referenced to the time of the nuclear explosion.

49

TABLE 3.4 INSTRUMENTATION PLAN

EP, Electronic Pressure   ED, Electronic Deflection Gage   MDG, Mechanical Drum Gage   SG, Strain Gage   HA, Horizontal Accelerometer
SP, Self-Recording Pressure   MSC, Mechanical Scratch Gage   DSC, Diametral Scratch Gage   SSG, Shear Strain Gage   VA, Vertical Accelerometer

Structure	Nonresponding Concrete Arches		Nonresponding Concrete Domes		Responding Concrete Domes			Responding Aluminum Domes	
Structure No. and Intended Overpressure	3.6-9028.01 70 psi	3.6-9028.02 35 psi	3.6-9027.01 70 psi	3.6-9027.02 35 psi	30.1-8001.01 70 psi	30.1-8001.02 35 psi	30.1-8001.03 20 psi	3.6-9026.02 70 psi 1 inch shell	3.6-9026.01 70 psi ½ inch shell
For Location of Instrument Positions See	Figure 3.16		Figure 3.17		Figures 3.18, 3.19 and 3.20			Figure 3.21	
Gage Position a	EP	EP	EP	EP	EP	EP	EP	ED	ED
b	EP	EP	—	EP	EP	EP	EP	ED	ED
c	EP	EP	EP	EP	EP	EP	EP	ED	ED
d	EP	EP	EP	EP	EP	EP	EP	ED	ED
e	EP	EP	—	EP	EP	EP	EP	ED	ED
f	EP	EP	EP	EP	—	EP	EP	ED	ED
g	SP	SP	EP	EP	—	EP	EP	EP	—
h	SP	SP	EP	EP	ED	ED	EP	EP	—
i	SP	SP	EP	EP	ED	ED	EP	EP	—
j	SP	SP	EP	EP	ED	ED	ED	EP	—
k	SP	SP	EP	EP	ED	ED	ED	EP	—
l	SP	SP	EP	EP	ED	ED	ED	SSG(2*)	SSG(2*)
m	SP	SP	EP	EP	ED	ED	ED	SSG(2*)	SSG(2*)
n	SP	SP	SP	SP	SSG(2*)	SSG(2*)	ED	SG(4-2*)	SG(4-2*)
p	SP	SP	SP	SP	SSG(2*)	SSG(2*)	—	MSC	
q	SP	SP	SP	SP	SG(4-2*)	SG(4-2*)	—		
r	SP	SP	SP	SP	VA(2) HA(2)	VA(2) HA(2)	—		
s	SP	SP	SP	SP	MDG	MDG	MDG		
t	SP		SP	SP	MDG	MDG	MDG		
u	SP		SP	SP	—	—	—	MSC	
v	SP		SP	SP	—	—	—	MSC	
w	SP		SP		—	—	—	MSC	
x	SP		SP		—	—	—	MSC	
y	SP		SP		—	—	—	DSC	DSC
z	—		—		—	—	—	DSC	DSC
aa thru mm					Mechanical Radial-Rod Deflection Gages Located as Shown on Figure 3.19.				
pp thru ss,xx							‡		

*Numbers in parentheses refer to number of gages or, if marked by an asterisk, refer to number of recording channels per gage. Free-field EP and SP, q and overpressure gages located at 70- and 35-psi overpressure regions. One SP gage behind prototype door.

† Soil test holes.

‡ Two Fastax Cameras.

Figure 3.13 Cross section through alumirum dome and foundation.

6'-4"

3'-9"

20'-0" Dome Diameter

4'-1 11/16"
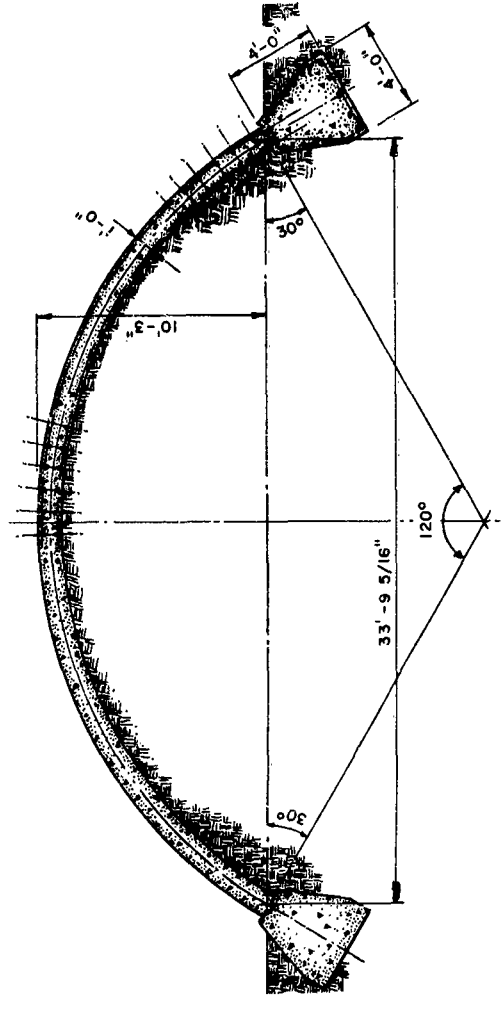
Figure 3.14 Cross section through arch and foundation.

4'-0"

4'-0"

30°

1'-0"

10'-3"

33'-9 5/16"

120°

30°

Figure 3.12 Reinforcing of concrete dome.

Great Circle Diameter

Reinforcing Bars

PLAN

Dome Diameter

Reinforcing Bars

Pole Point on Sphere Surface

Great Circle Sphere

ELEVATION

51

FRONT VIEW

SIDE VIEW

DOOR ELEVATION

SECTION A-A
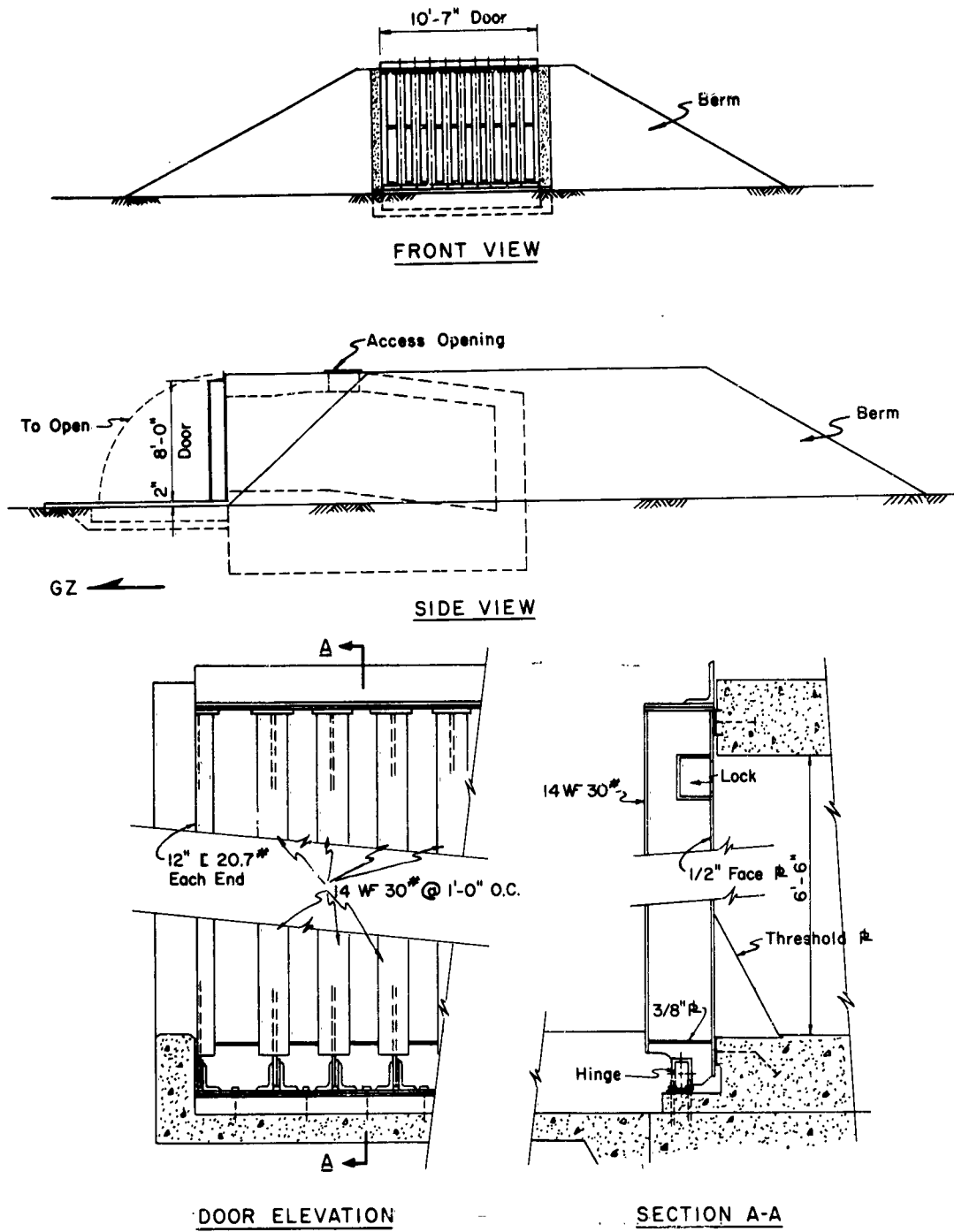
Figure 3.15 Prototype door details.

52

Figure 3.17 Location of instrumentation positions on 50-foot-diameter, 24-inch-thick, nonresponding concrete domes.

Figure 3.16 Location of instrumentation positions on nonresponding concrete arches.

53

Figure 3.19 Positions of mechanical radial-rod deflection gages in responding concrete domes.

Figure 3.18 Location of instrumentation positions on 50-foot-diameter, 6-inch-thick, responding concrete domes.

CONFIDENTIAL
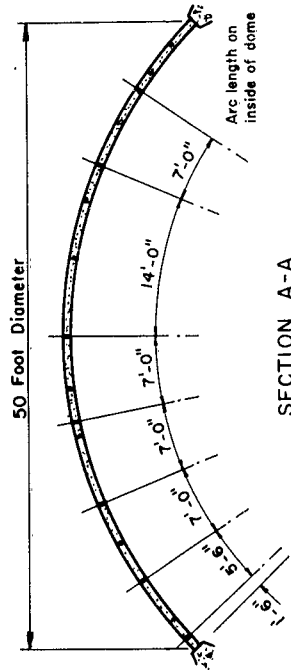
3.4.2 Self-Recording Pressure Gages. The self-recording pressure gages were installed by BRL. This type of gage (see Reference 25) was also used extensively on the dome and arch structures. The pressure record on these gages is scratched on a rotating aluminized disk by a stylus attached to a sensing diaphragm. Each gage is an independent unit containing both sensing element and recorder. Thus data obtained from this type of gage are not susceptible to mass failure due to faulty central recording or power equipment. A disadvantage of the gage is that,

Dr = Dome Radius
A = 33'-6"
a = 13'-5"
b = 1'-0"
c = 3'-0"
d = 5'-0"
e = 5'-0"
f = 6'-1"

PLAN

SECTION AA
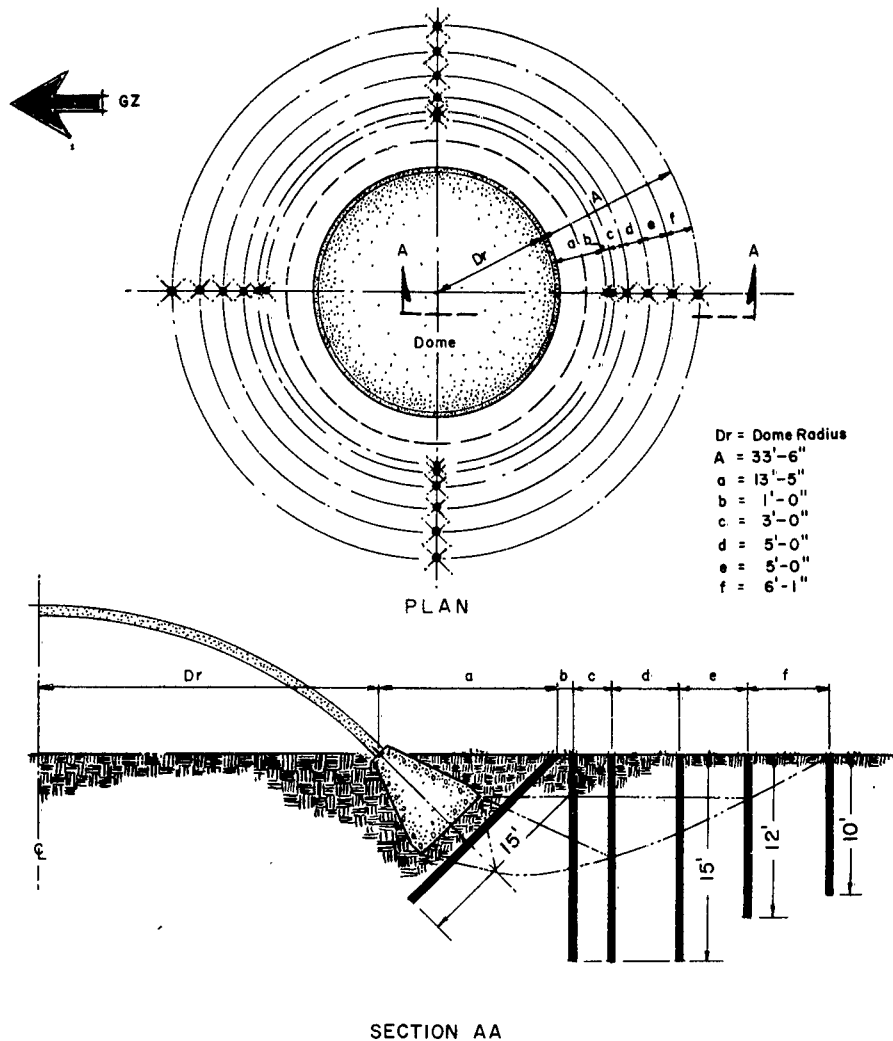
Figure 3.20 Plan of soil test holes around foundation of responding concrete dome at 70-psi overpressure region.

although the time base is linear, the time of the explosion cannot be referenced to the beginning of the record.

An examination of the instrumentation plan shows that more pressure gages were located on the sides of the domes and arches facing the blast than on the opposite side. This was done to gain a more-detailed load description on the portions of the structures where the loads were expected to be the greatest and where the loadings were expected to show the greatest change with distance on the structure. Both of these factors are important for structure design purposes.

The instrumentation plan also shows that on the nonresponding structures, which were intended primarily for loading measurements, both electronic and self-recording pressure gages were

CONFIDENTIAL

used. The gages were arranged so that the data obtained by each gage would contribute to the definition of the pressure distribution on the structure. The two types of gages were located side by side along the prime meridian of each nonresponding structure where the loading information would be most significant. The gages were also arranged so that the essential loading data would be obtained even if all the gages of a particular type should fail.

PLAN

SECTION A-A
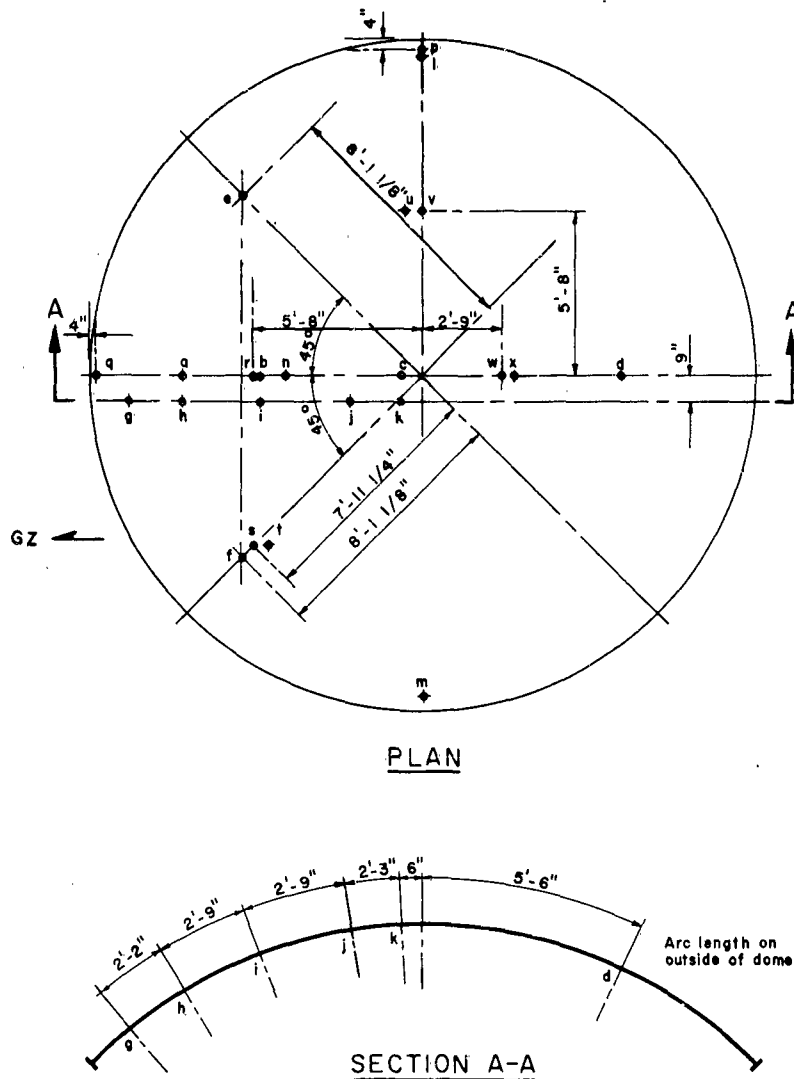
Figure 3.21 Location of instrumentation positions on 20-foot-diameter, aluminum domes.

A self-recording gage was also located behind the prototype-door structure to measure any pressure leakage by the seal.

3.4.3 Electronic Deflection Gages. The electronic deflection gages (see Figures E.7 and E.8) were installed by ARF. They consisted of linear-motion potentiometers mounted between the shell and instrument trusses, which were supported by the foundations and spanned the floor of the domes. The output of the gage was recorded electronically.

Most of the electronic deflection gages were located along the prime meridian of the dome because the most important deformations of the dome, those which would lead to eventual failure,

were expected along the prime meridian. Two deflection gages were also located off the prime meridian on each responding dome where deflection measurements were made in order to determine more accurately the response motion of the dome. The deflection-versus-time records were intended to be correlated with data obtained by the pressure gages.

The deflection-instrument support trusses were subjected to acceleration loading due to air-induced ground shock. Any deflection with respect to these supports of the instrument trusses would decrease the accuracy of the instrumentation readings, so construction to minimize such deflection was desirable.

For any given truss or girder construction, subjected to acceleration loading, the deflection is proportional to the ratio of density (γ) of truss material to modulus of elasticity (E) of truss material and inversely proportional to the square of the truss depth. Thus, doubling the size of every member of a truss will not reduce the deflection when subjected to acceleration loading. The values of γ/E for steel and aluminum are about equal and the value of γ/E for wood is 1.5 times that of steel; therefore, steel was adopted as the most economical and practical material for the responding dome trusses. They were designed to be as rigid as practical.

3.4.4 Strain Gages. SR-4 bakelite-base strain gages (see Figure E.10) were used on two of the responding concrete domes and on the aluminum domes in an attempt to measure direct stresses in the domes during the blast loading. These gages were installed by ARF. The output of the gages was recorded electronically.

The gages were mounted directly to the inside and outside of the shell on the aluminum domes. On the responding concrete domes the strain gages were mounted on the reinforcing bars at the positions shown in the instrument plan. There were four bars at the gage positions, two at right angles near the outside surface and two at right angles near the inside surface. An SR-4 strain gage was mounted to each of the bars. The output of each gage was recorded on two different oscillographic channels to increase the probability of obtaining one good record for each gage. After the gages had been mounted, the opening in the shell was sealed with a cement grout.

3.4.5 Shear Strain Gages. SR-4 bakelite-base strain gages (see Figure E.10) were used on two of the concrete domes and on the aluminum domes in an attempt to measure the shear stresses between the dome shell and the foundation. The gages were mounted at two positions on each dome as shown in the instrumentation plan. They were installed by ARF.

A Type ABFX-11 biaxial rosette gage mounted directly on the shell was used on the aluminum domes. On the responding concrete domes the shear stress was measured by mounting strain gages on two of the dowels, one near the outside surface of the shell and the other near the inside surface of the shell, which ran between the shell and foundation.

On each dome the strain gages which were used to measure shear strain were wired into a single bridge providing one output channel. The output from the gages was recorded on two different oscillographic channels to increase the probability of obtaining a good record if some of the recording equipment should fail.

After the gages were installed, the opening in the shell was sealed with a cement grout.

3.4.6 Accelerometers. Two horizontal and vertical accelerometers were located in the center of the floor of the responding concrete domes located in the 70-psi region and the 35-psi region (see Reference 25). These gages were installed by BRL. Two gages were used at each location, one with a range ten times the range of the other. This was done to cover a wide range of possible accelerations, since there was little information available from which to predict the expected accelerations.

3.4.7 Mechanical Scratch Gages. Nine Baldwin mechanical scratch gages were placed on the inside of the shell of the 1-inch, responding, aluminum dome. These gages scratch a deflection-time record that can be used to estimate strain in the material to which they are attached. The time base is nonlinear because it is caused by releasing the spring-loaded stylus when the strain occurs.

57

3.4.8 Mechanical Drum Gages. These gages (see Figure 3.22) were installed at one end of each of the instrument trusses used in the responding concrete domes. They were built by the contractor and installed by ARF. The gages were designed to measure the change in shape of the base circle of the dome during blast loading. One end of the instrument truss was mounted securely to the foundation. The other end was supported by the foundation, but it was free to move in a direction in line with the truss. A stylus was attached to the partially free end. It was adjusted to scratch a record on a spring-loaded drum which would unwind during the blast loading. This would provide a nonlinear time base for the displacement record. Each drum gage had a range of plus or minus 3 inches.

3.4.9 Diametral Scratch Gages. Diametral scratch gages (see Figure 3.23) were built by the contractor and installed by ARF on the responding aluminum domes. They were mounted at the
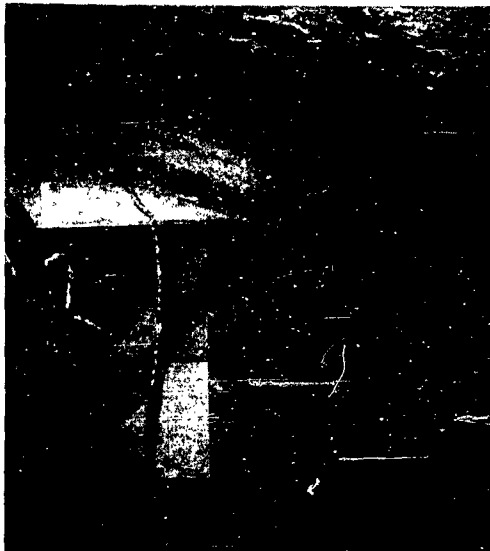
Figure 3.22 Mechanical drum gage at end of instrumentation truss.

Figure 3.23 Diametral scratch gage.

end of the instrument trusses and on pipes mounted to the foundation which spanned the floor in a direction at right angles to the instrument trusses.

These gages had a function similar to that of the mechanical drum gages. The only difference was that the scratch record was not obtained on a moving time base. These gages were used to record only maximum and minimum displacements.

3.4.10 Mechanical Radial-Rod Deflection Gages. These gages (see Figure 3.24) were built by the contractor and installed by ARF on the three responding concrete domes. They consisted of floor-mounted tripods with a hole at the apex through which a loose-fitting metal tube, fastened securely to the dome, was passed. Close-fitting nylon washers were mounted on the tube on either side of the hole. The washers were moved on the tube as the dome deflected, and thus provided a maximum and minimum record of the shell movement. The gages were located at a number of points on the dome surface. A photograph of these gages inside a responding concrete dome is shown in Figure 3.24. The instrumentation truss for the electronic deflection gages is seen in the background of this picture.

3.4.11 Soil Test Holes. Twenty-four holes were drilled around the foundation of the responding concrete dome located in the 70-psi region and filled with colored sand. The area was excavated following the blast to determine the relative motion of the soil (due to the unusually high

58

CONFIDENTIAL

foundation loads during the blast) at points along the length of each hole. This work was conducted by the Waterways Experiment Station (WES).

3.4.12 Fastax Cameras. Two Fastax cameras were installed by BRL in the 1-inch-thick, responding aluminum dome to record, if possible, deflections of the shell during the blast loading. The cameras were protected by steel boxes and surrounded by lead bricks.

3.4.13 Free-Field Instrumentation. Free-field electronic q gages and overpressure gages were located at both the 35- and 70-psi regions to obtain the free-field characteristics of the air-blast wave.

3.5 CONSTRUCTION DETAILS

A discussion of special problems encountered in the construction phase of the project and the results of concrete cylinder and core tests are given in this section.
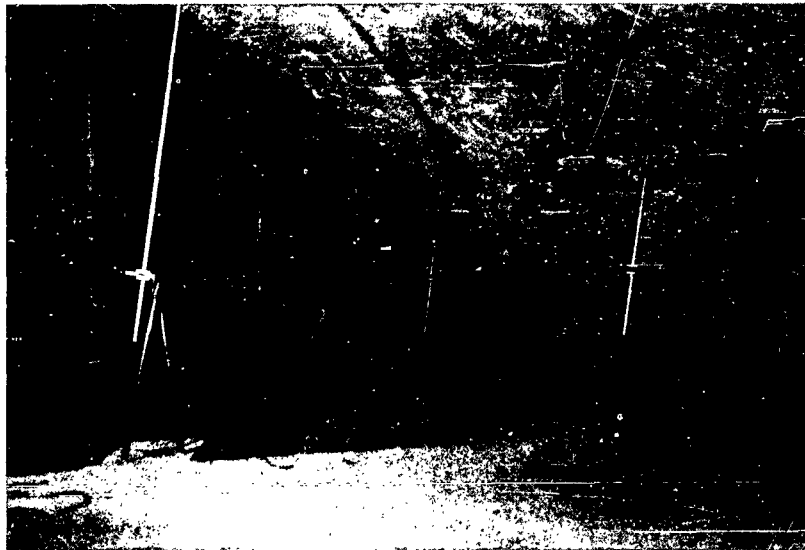
Figure 3.24 Mechanical radial-rod deflection gages on inside of responding concrete dome. Instrumentation truss supporting electronic deflection gages is shown in background.

3.5.1 Concrete Dome Construction. The responding concrete domes were poured on a shotcreted earth berm. Foundations for all domes were poured on a shotcrete-lined excavation as shown in Figure 3.25. No difficulty was experienced with the segmental wood forms used for shaping the earth berms and the outside concrete surfaces. The placing of the shotcrete on the berm is shown in Figure 3.26. The shells for the nonresponding concrete domes were poured on wood forms and satisfactory inside and outside surfaces were obtained on these shells. The shotcreted earth berms gave an unsatisfactory surface on the responding concrete domes. At the completion of each dome form, a spray of Hunt's concrete-curing compound, of variable thickness, was placed over the entire form. This was to act in the dual capacity of a curing medium and a nonbonding agent. The contractor was informed by the AMF inspector that the material used would not prevent bonding of concrete to shotcrete. First, the shotcrete surface was highly porous, and the amount of this type of material necessary to saturate would be prohibitive. Second, the heating action of the sun would cause the material to penetrate the shotcrete, thus reducing the effectiveness of the initial application. The contractor, however, en-

59

tertained a contrary view of the effectiveness of the material used. Later, extreme difficulty was experienced in removing the shotcrete from the under surfaces of the domes.

Temporary difficulty was experienced in placing the dome-shell steel. A system was eventually devised for placing the reinforcing steel so as to conform to plan. Once the idea was

Figure 3.25 Construction of foundation
for responding concrete dome.

grasped by the workmen, no further difficulty developed. The overall result of shell-steel placement was excellent.

The concrete pour of the 20-psi responding dome, the first concrete dome poured, resulted in an unsatisfactory surface. The contributing factors were as follows:

1. The concrete aggregate used was $1\frac{1}{2}$-inch maximum (government furnished) which caused considerable surface aggravation by the sweep screed, since the working area between the rein-
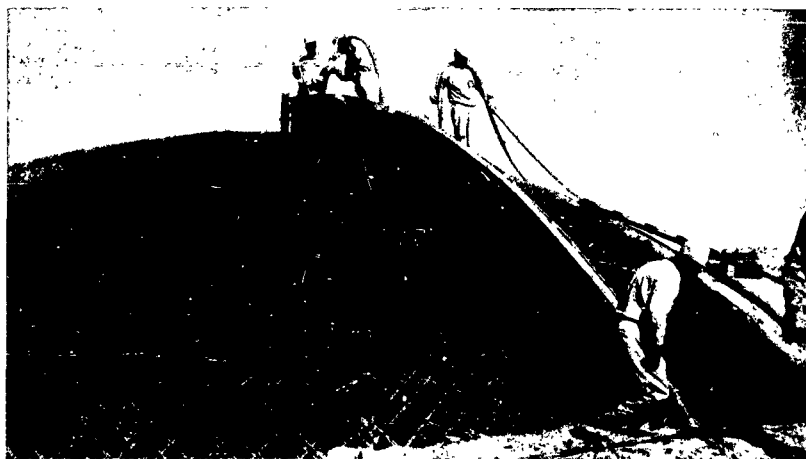
Figure 3.26 Shotcreting of earth-berm
form for responding concrete dome.

forcing steel and finished surface was only $\frac{3}{4}$ inch. This aggravation continued throughout the pour, acting upon that already poured as well as on that being poured.

2. The concrete slump limit of 2 inches further aggravated the situation in that, as interstices of steel became loaded, stiffness of mix made it difficult to crowd-aggregate, even with vibrator, without losing material to the completed portion below.

60
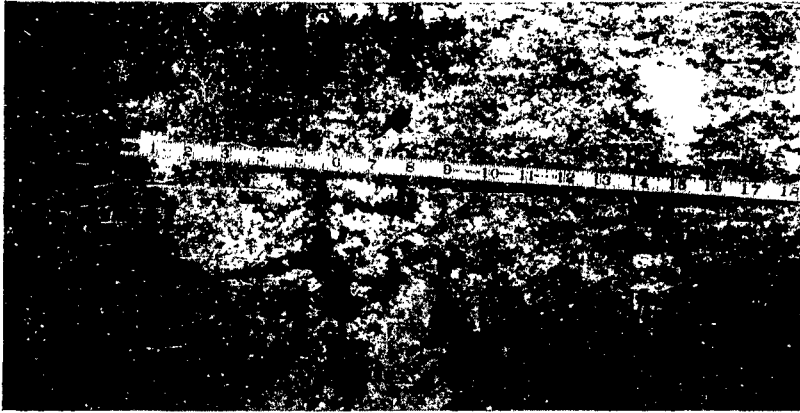
Figure 3.27 Flaws on inside surface of responding concrete dome at 20-psi overpressure region.

Figure 3.28 Flaws on inside surface of responding concrete dome at 20-psi overpressure region (close-up showing width of flaws).
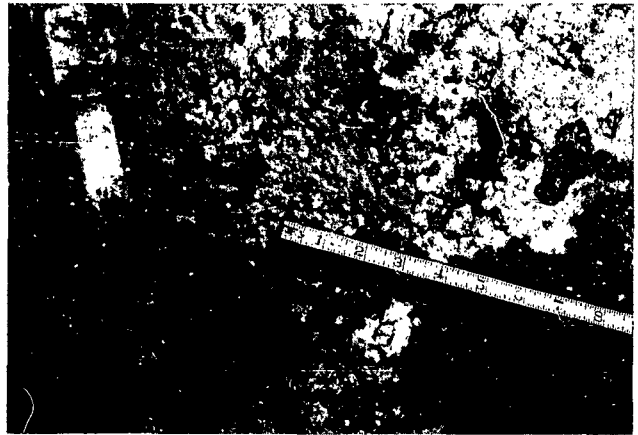
Figure 3.29 Hole on inside surface of responding concrete dome at 20-psi overpressure region.

61

3. In consequence of the above, a pocked surface resulted, which would indicate that tolerances were exceeded in places. Upon completion of the pour, a grout mix proportionate to the original concrete mix was placed as a wash and screed lubricant in an attempt to give the completed surface a better finish.

For subsequent domes, the aggregate was limited on 1-inch maximum (specification requirement) and the slump limit was increased from 2 inches to 3 inches. Furthermore, the subsequent dome-shell pours were started in early morning to take advantage of the cooler, higher-humidity atmosphere. No further difficulty was experienced in pouring the dome shells.

The removal of the shotcrete from the inside surface of the responding domes was difficult due to the improper preparation of the shotcrete surface. It adhered to the dome shells, particularly to the 20-psi shell. It was necessary to remove this shotcrete with air-driven chisels. Removal was neither complete nor satisfactory. In some places the chisels gouged the dome

Figure 3.30 Finished concrete dome. Entrance to
inside of dome shown through foundation.

shells; in others removal of shotcrete was far from complete. The more-serious gouges were patched with sand-cement mortar.

Figures 3.27 to 3.29 show typical deficiencies on the inside surfaces of the responding domes. A view of a completed concrete dome showing the entrance to the dome through the foundation is presented in Figure 3.30.

3.5.2 Arch Construction. The nonresponding arches were also poured on a shotcreted earth berm. Initially, the arch concrete was first poured at the spring lines, progressing toward the crown of the arch. However, it developed that the undulatory motion of the steel occasioned by the movement of workmen on the surface caused the top layer of steel to creep to the surface. This condition was corrected for the remainder of the work by first placing just enough concrete at the crown of the arch to lock the steel in place at that point and then switching the pour to the spring lines, working progressively upward to meet the previously placed concrete at the crown. After this method of pour was adopted, no further difficulty ensued.

Figure 3.31 shows the completed foundations and end walls of an arch before the placement of the earth berm. Figure 3.32 shows a completed arch.

3.5.3 Aluminum Dome Construction. The aluminum domes were shop-fabricated in two halves. A base plate was shop-welded around the spring line and this was secured by studs to the foundation. Figure 3.33 shows an aluminum dome foundation containing the truss for mounting the electronic deflection gages and the diametral scratch gage. The two halves of the aluminum shell are in the background. They were placed on the foundation and welded together. A completed aluminum dome is shown in Figure 3.34.

62

Figure 3.33 Foundation for aluminum dome. Two halves of shell are shown in background.

Figure 3.34 Completed aluminum dome.

Figure 3.31 Completed foundations and end walls of nonresponding concrete arch.

Figure 3.32 Completed concrete arch.

CONFIDENTIAL

Figure 3.35 Completed prototype door.
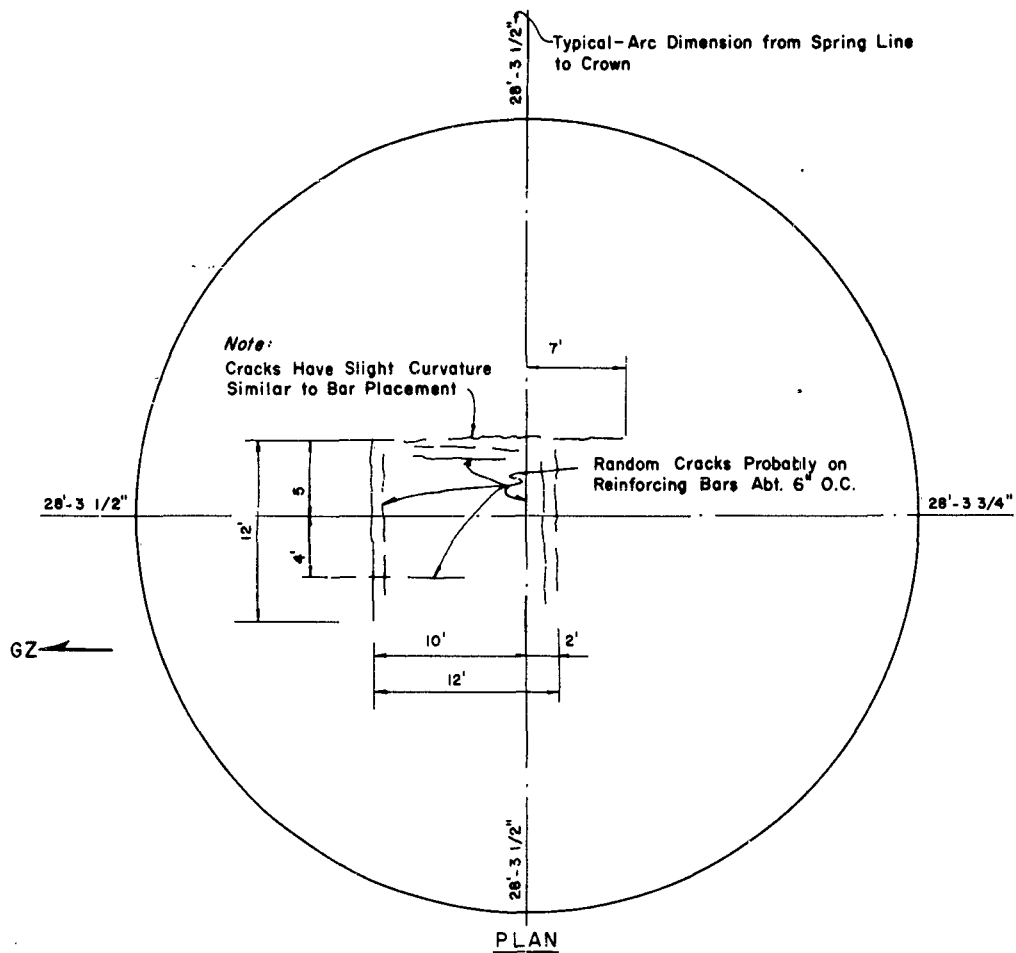
Figure 3.36 Condition of 70-psi 6-inch dome prior to test.

64

Figure 3.38 Condition of 20-psi 6-inch dome prior to test.

Figure 3.37 Condition of 35-psi 6-inch dome prior to test.

65

CONFIDENTIAL

Figure 3.40 Condition of 35-psi 24-inch dome prior to test.

Figure 3.39 Condition of 70-psi 24-inch dome prior to test.

66

CONFIDENTIAL
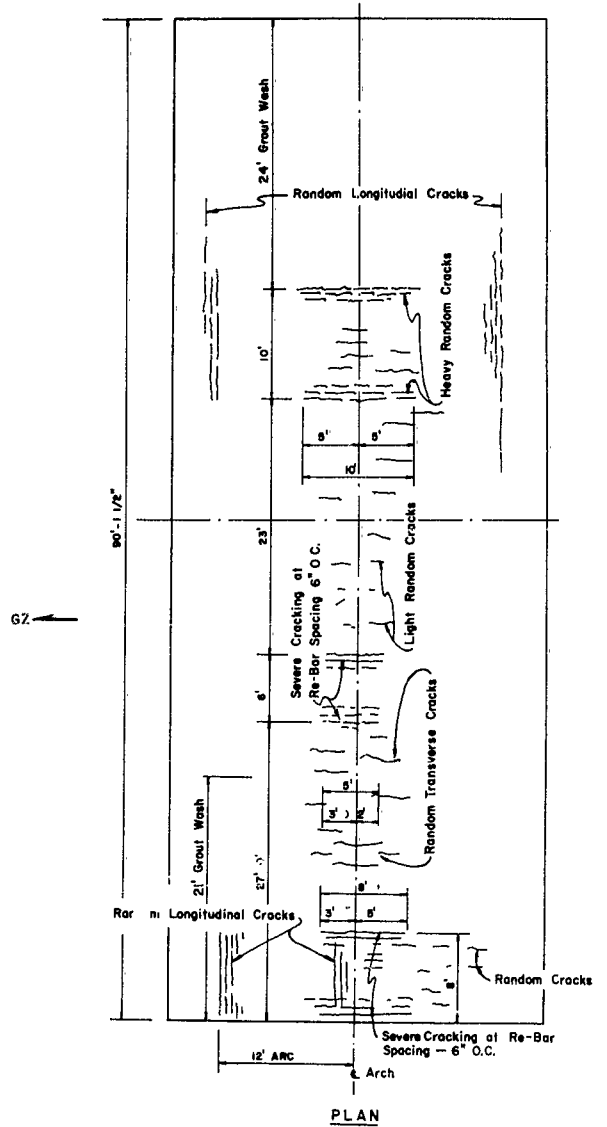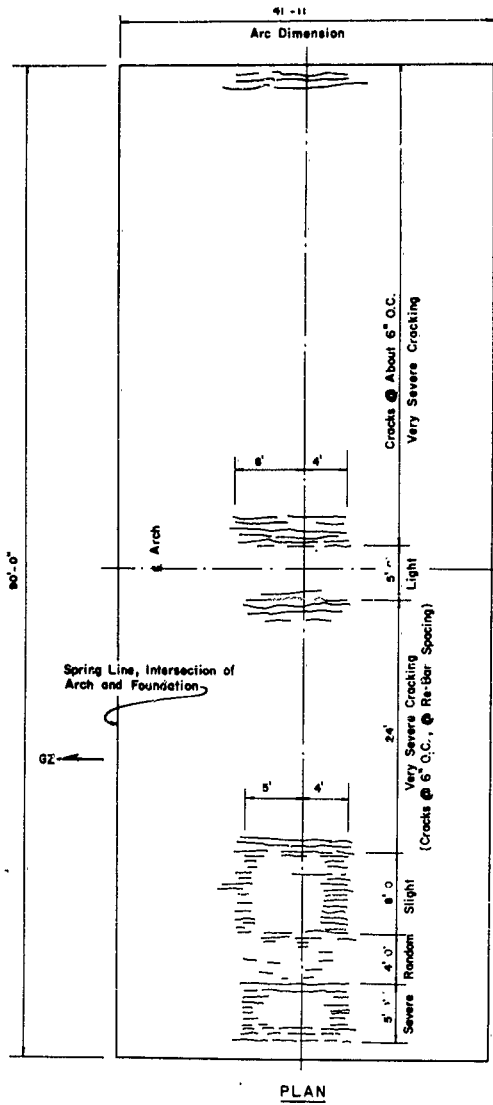
Figure 3.41 Condition of 70-psi arch prior to test.

Figure 3.42 Condition of 35-psi arch prior to test.

67

TABLE 3.5 CONCRETE CYLINDER AND CORE STRENGTH DATA, PSI

Structure	Position on Structure	Date Poured, 1957	Specification 28-Day Cylinder Strength	7-Day Cylinder Strength			28-Day Cylinder Strength			Core Strength Tested 2 August 1957	
				Maximum	Minimum	Average	Maximum	Minimum	Average	Maximum	Minimum
30.1-8001.01	Shell	17 May	4,500	—	—	2,620	3,410	3,120	3,265	—	—
70-psi, 6-in Dome	Foundation	21 April	3,500	3,210	1,500	2,355	4,730	3,650	4,115	—	—
30.1-8001.02	Shell	14 May	4,500	—	—	3,730	4,580	3,000	3,790	5,150	4,600
35-psi, 6-in Dome	Foundation	14 April	3,750	1,990	1,930	1,960	3,690	3,220	3,505	—	—
30.1-8001.03	Shell	9 May	4,500	—	—	3,000	4,280	3,970	4,125	5,370	4,550
20-psi, 6-in Dome	Foundation	14 April	3,500	—	—	—	—	—	—	—	—
3.6-9027.01	Shell	15 May	4,500	3,450	2,940	3,185	4,490	3,860	4,108	—	—
70-psi, 24-in Dome	Foundation	5 May	3,500	—	—	2,990	4,240	3,800	3,856	—	—
3.6-9027.02	Shell	16 May	4,500	3,470	3,190	3,330	4,070	3,610	3,858	—	—
35-psi, 24-in Dome	Foundation	5 May	3,500	—	—	3,230	4,460	3,570	3,936	—	—
3.6-9028.01	Shell	22 May	3,500	2,780	2,710	2,745	4,140	3,340	3,680	—	—
70-psi, Arch	Foundation	31 March	3,750	2,310	1,970	2,222	4,420	2,630	3,570	—	—
3.6-9028.02	Shell	23 May	3,500	2,830	2,160	2,495	4,220	3,730	3,942	—	—
35-psi Arch	Foundation	31 March	3,750	2,730	2,190	2,355	4,500	3,350	3,895	—	—

3.5.4 Prototype Door. No problems were encountered in the construction of the prototype door. The completed structure is shown in Figure 3.35.

3.5.5 Concrete Cylinder and Core Strength Data. Concrete test cylinders were obtained at the time the concrete was poured at each of the concrete dome and arch structures. These cylinders were tested to determine the 7- and 28-day strength of the concrete. The data from these tests are presented in Table 3.5. The table also contains the date the concrete was poured at each structure. (The weapons effects test took place 24 June 1957.)

Concrete cores were removed from the shells of two of the responding dome shells following the blast. The strengths of these cores were measured and are also given in Table 3.5.

3.5.6 Surface Condition of Concrete Structures Before Test. Many surface imperfections observed on the concrete dome and arch structures after construction work had been completed. These deficiencies are shown in Figures 3.36 to 3.42.

Chapter 4
RESULTS

4.1 DESCRIPTION OF STRUCTURE DAMAGE

4.1.1 Nonresponding Concrete Arches. The arches sustained slight structural damage. Both arches sheared at the end walls, the 70-psi arch shifting about $2\frac{1}{2}$ inches away from ground zero at the quarter points of its arc, and the 35-psi arch shifting about 1 inch. The 70-psi arch sustained a tension crack just to the "leeward" of its crown along its full length. Circumferential cracks appeared at the reinforcing bar spacing along the full length of the arc of the 70-psi arch. The damage to the arches is shown in Figures 4.1 to 4.3.

4.1.2 Nonresponding Concrete Domes. The nonresponding concrete domes survived the blast with no structural damage. A few hair cracks appeared in the 70-psi dome and its foundation. The two construction joints in the foundation on the side facing ground zero separated $\frac{1}{16}$ inch, as shown in Figure 4.4. No spalling or other damage was observed. Cracks (which had developed before the tests) over the reinforcing bars on the crowns of the nonresponding domes were not enlarged by the blast loads.

4.1.3 Responding Concrete Domes. The dome in the high-pressure region suffered total destruction, except for the lowermost crescent of its side away from ground zero, which appeared to be bent upwards and was severely damaged. In the region along the prime meridian on this side, the reinforcing rods buckled outwards and broke through the upper surface. The destroyed part of the dome was broken into pieces of concrete no larger than the mesh of the reinforcing rods. Some of the debris was scattered in the ground-zero direction. A diagram showing the damage to the dome is shown in Figure 4.5. Photographs of the damage are presented in Figures 4.6 to 4.8.

The dome in the medium-pressure region was severely damaged. A diagram showing the portion of the shell remaining after the blast is shown in Figure 4.9. The portion closest to ground zero was demolished; concrete from this portion of the dome was broken into pieces no larger than the reinforcing mesh. Two large islands of concrete remained intact on either side of the dome. Immediately after the blast, these islands were suspended in about their original position by the reinforcing bars of the undamaged half of the dome. Later (between 4 hours and 3 days after the blast) these bars yielded, and the islands drooped until their lower edges touched the ground. The half of the dome away from ground zero apparently suffered little or no permanent deformation but sustained a network of cracks matching the reinforcing mesh on both surfaces in the neighborhood of the prime meridian and two cracks on the outer surface diagonal to the mesh running from either side toward the trailing edge. Photographs of the damage to this dome are presented in Figures 4.10 to 4.12.

The dome in the low-pressure region was undamaged. No cracks could be found that were not already present before the blast.

The steel reinforcing rods from the destroyed regions of both damaged domes were stripped of practically all concrete. This condition was remarkable, because concrete bonds itself very well to steel (better, in fact, than to previously poured concrete). In any static failure of reinforced concrete, the rods always remain coated with concrete. It would be impossible to remove this concrete without elaborate scraping and grinding operations, or the like. Yet, except for about half a dozen small chunks of concrete, the rods of the domes were clean. The rods
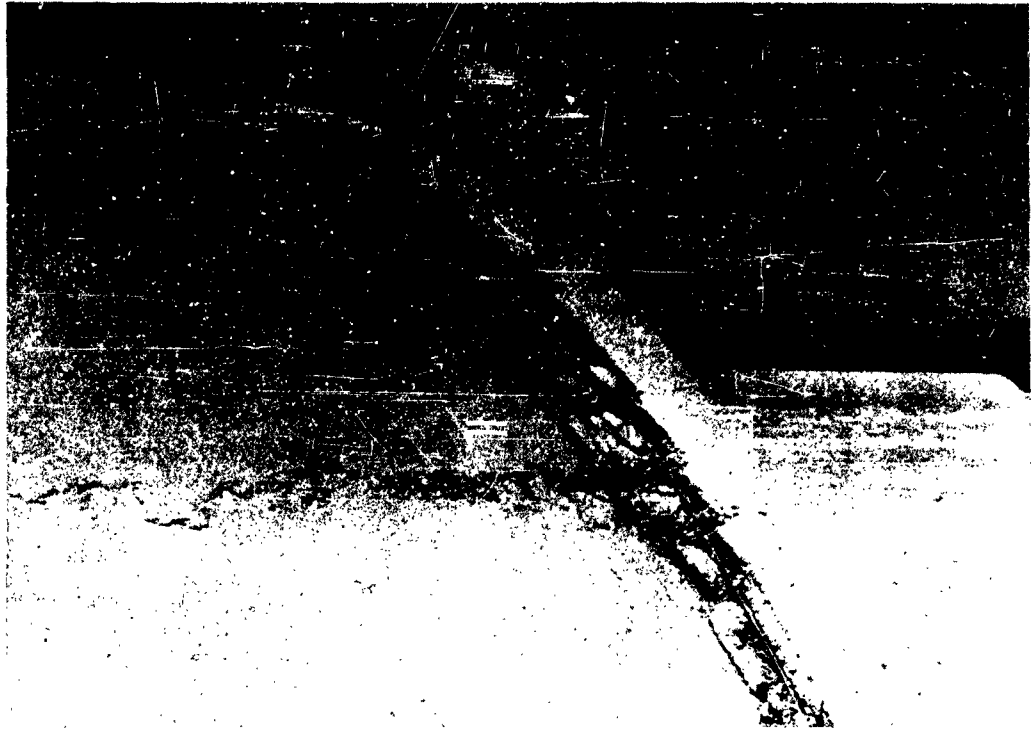
Figure 4.1 Damage to side of concrete arch facing
ground zero at 70-psi overpressure region.
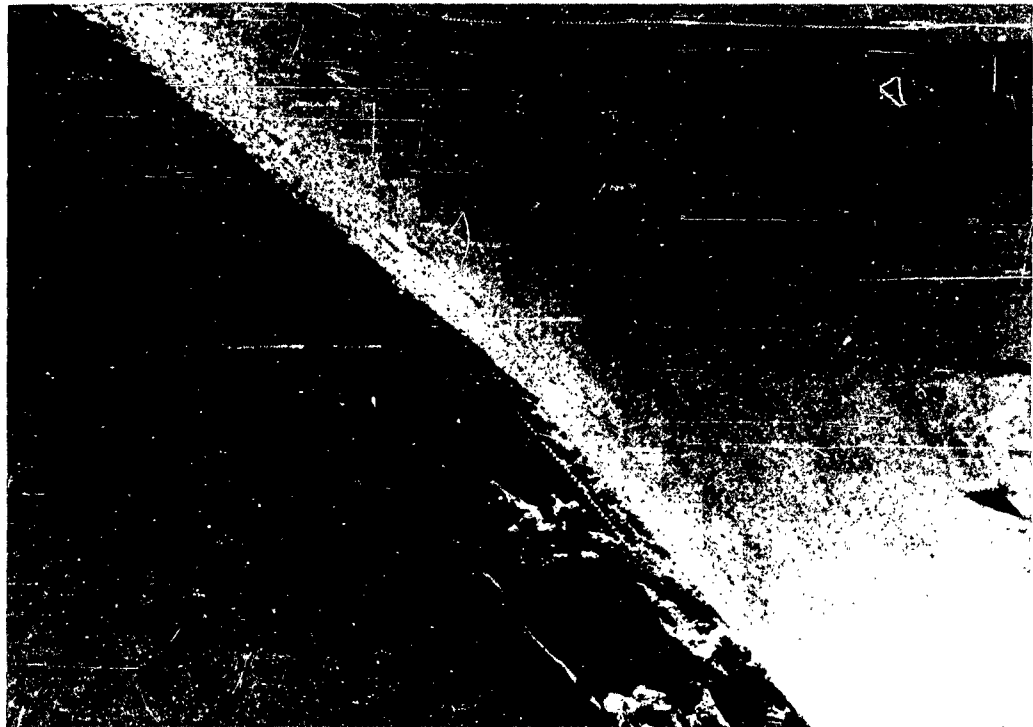
Figure 4.2 Damage to side of arch away from ground zero
at 35-psi overpressure region.

71

CONFIDENTIAL

Figure 4.3 Damage to rear side of arch at 70-psi overpressure region.

Figure 4.4 Foundation separation crack on nonresponding
concrete dome at 70-psi overpressure region.

72

CONFIDENTIAL

Figure 4.6 Responding concrete dome at 70-psi overpressure region.

Figure 4.7 View of left front of responding concrete dome at 70-psi overpressure region, looking away from ground zero.
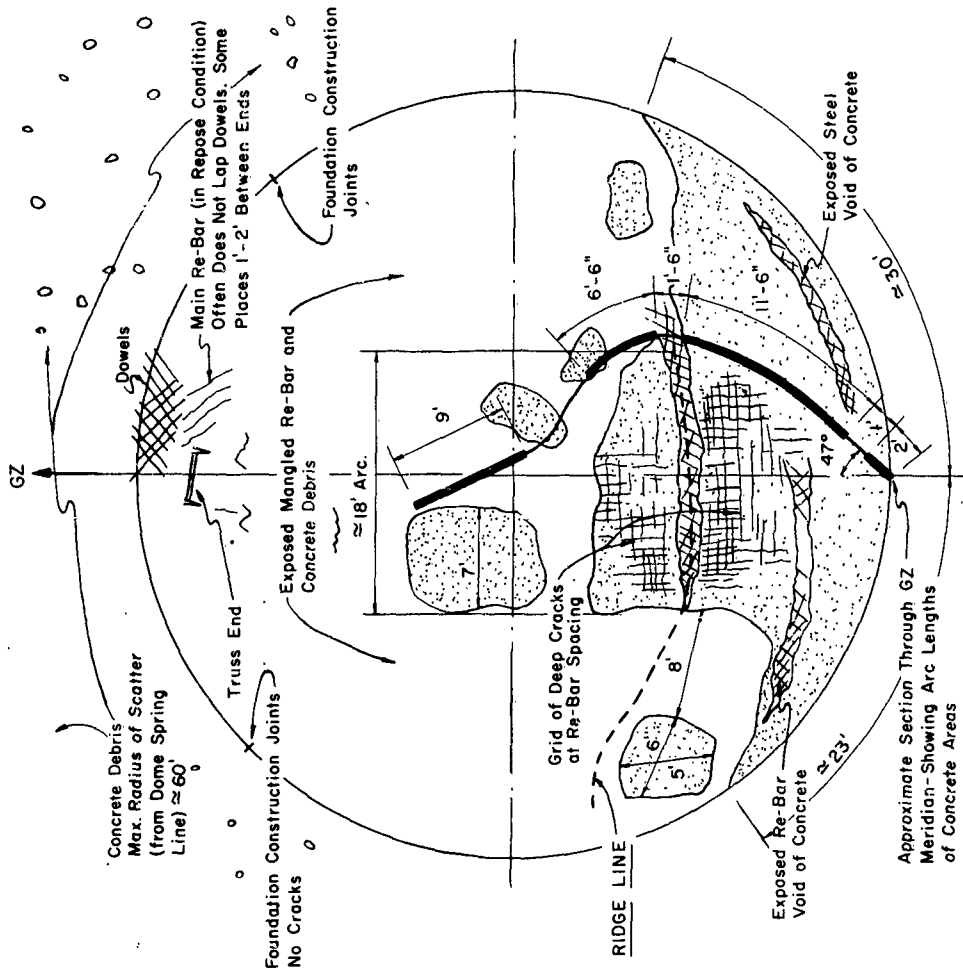
Figure 4.5 Posttest diagram of 70-psi 6-inch dome.

73

CONFIDENTIAL
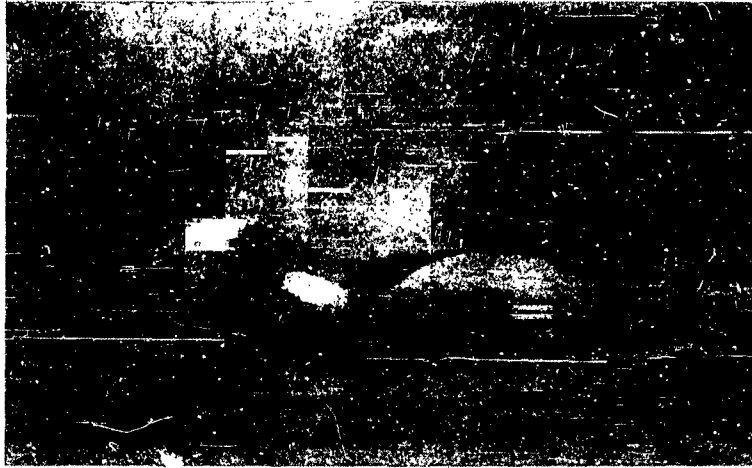
Figure 4.8 Left side of responding concrete dome
at 70-psi overpressure region.
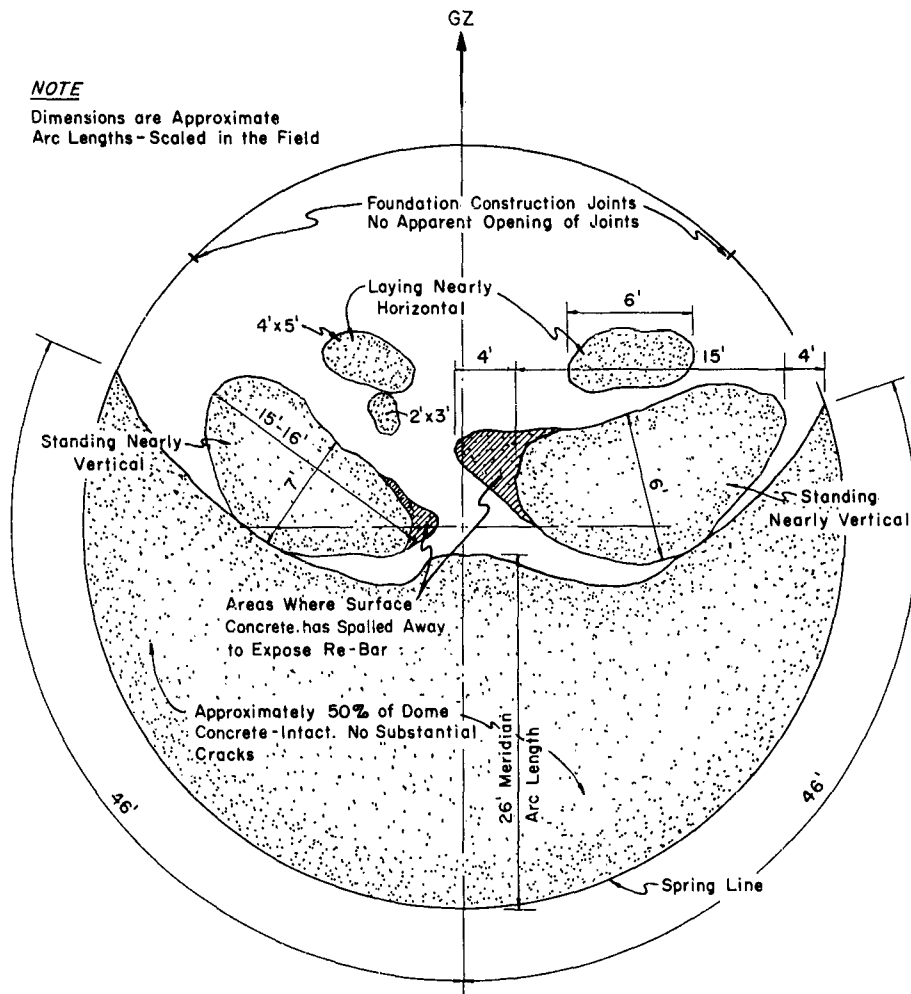
Figure 4.9 Posttest diagram of 35-psi 6-inch dome.

CONFIDENTIAL

Figure 4.12 Responding concrete dome at 35-psi overpressure region.
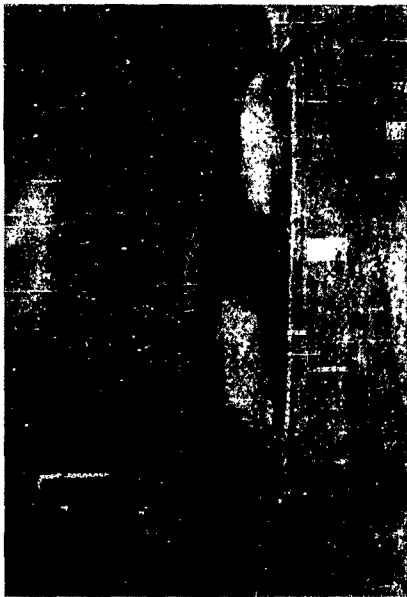
Figure 4.10 Damage to responding concrete dome at 35-psi overpressure region showing side of dome facing ground zero.

Figure 4.11 Right side of responding concrete dome at 35-psi overpressure region.

75

were pushed down and away from ground zero. Rods protruding from the footings were bent down flush with the ground. Some of the transverse rods were bent at or near the midpoint almost to a cusp, the effect being more pronounced in the medium-pressure dome. A number of reinforcing rods broke, with evidence of ductility being found at only one of the fractures.
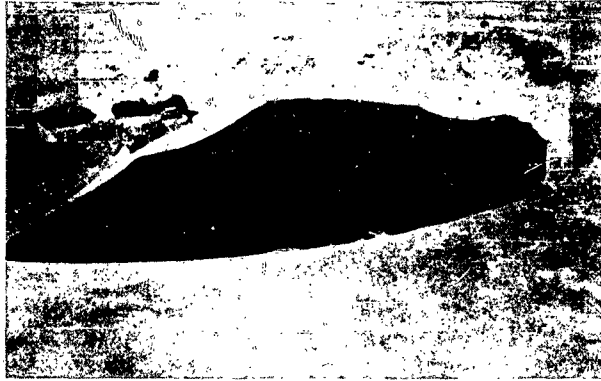
Figure 4.13 View of ½-inch-thick aluminum dome showing side of dome facing ground zero.

The trusses inside the two damaged domes, which were provided to support gages, were also demolished.

Foundations of all three domes survived without damage. The only discernible movement was a separation (about $\frac{1}{16}$ inch) of two construction joints in the high-pressure foundation.
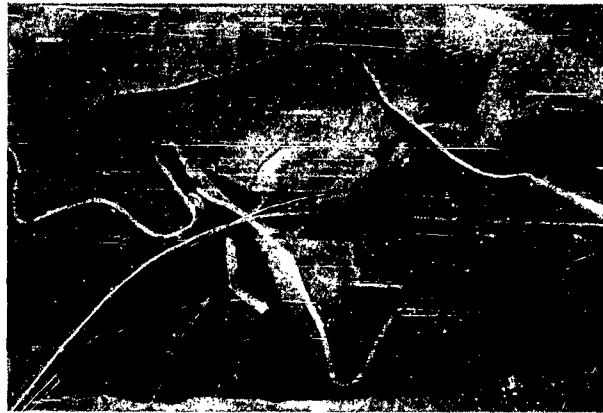
Figure 4.14 One-inch-thick aluminum dome showing side of dome facing ground zero.

Access doors showed no effects, but the trenches leading away from them were nearly filled with sand. Evidently the sandbags lining the trenches did little good.

4.1.4 Responding Aluminum Domes. Both aluminum domes were completely destroyed. The ½-inch dome was dished down into the foundation as shown in Figure 4.13. The 1-inch aluminum dome failed, apparently by separation of the circumferential welded seam between the base plate and leading edge of the dome, which was then pushed back against the side of the foundation away from ground zero. The damage is shown in Figures 4.14 and 4.15. Some of the anchor bolts which were computed to resist rebound and the negative phase were sheared off, while others were pulled out of the concrete.

Over 90 percent of the aluminum-clad asbestos provided for thermal insulation was blown off

CONFIDENTIAL

the aluminum domes. Foundations of the aluminum domes survived the blast with no apparent damage.

4.1.5 Prototype Door. No consequential damage was suffered by the prototype door. On either lateral edge of the door the upper 4 feet of edge channel were peeled down; the piece from one edge could not be found, while the piece from the other edge was not completely severed. Along the top edge of the door, the flange was bent back $\frac{1}{4}$ inch at its center and 1 inch at its ends. The entire door appeared to be bowed inward about $\frac{1}{4}$ inch.

The foam-rubber gasket apparently was not damaged at all. Its effectiveness as a seal is open to question, however. The peak overpressure recorded inside the structure behind the door was 6.6 psi.

Figure 4.15 Side of 1-inch-thick aluminum dome away from ground zero.

Part of the concrete curb in front of the door was broken loose. However, it did not fall into the door pit, where it would have obstructed the door; rather, it was pushed into the ground, which possibly was not properly tamped. It was surprising that no reinforcing bars could be seen protruding from the fractured surfaces.

After the test, the locking and hinge mechanisms functioned perfectly.

The extent of damage is illustrated by photographs of the prototype door (Figures 4.16 to 4.18).

4.2 DATA RECORDED BY INSTRUMENTS

4.2.1 Pressure Gages, Electronic and Self-Recording. The results obtained from the pressure instruments are listed in Tables 4.1 to 4.4. The performance of the pressure instrumentation was satisfactory, with 44 of the 58 electronic gages yielding useful data and all 48 of the self-recording pressure gages providing meaningful information. Several recording disks on the self-recording gages failed to rotate and provide the records with a time base, although it was possible to determine the peak pressure to which these gages had been subjected.

Pressure records were obtained for the duration of the blast load on the nonresponding concrete arches and domes, and the surviving 6-inch-thick responding concrete dome. For the 1-inch-thick aluminum dome and the two concrete domes which failed during the blast loading, partial pressure records were obtained to the point at which the domes failed. The pressure records appear to be valid for about 80 msec after the arrival of the blast wave on the aluminum and concrete domes at the 70-psi region, which indicates the probable survival time of the structures. The pressure records on the concrete dome located at the 35-psi region appear to be ac-

Figure 4.16 Prototype door, pretest view.

Figure 4.17 Prototype door, posttest view,
showing damage to edge channel.

78

curate for about 165 msec after the arrival of the blast wave, indicating the probable survival time of that structure.

Pressure-versus-time records obtained by the gages are included in Appendix D.

4.2.2 Electronic Deflection Gages.

The performance of the electronic deflection gages was generally satisfactory during the blast loading with 36 of the 42 gages operating successfully. The information obtained from most of the gages, however, is of limited value because of the early failure of four of the domes and the small response motions of the fifth dome instrumented with deflection gages. The results from each gage are summarized in Tables 4.5 and 4.6.

The deflection gages on the $\frac{1}{2}$-inch-thick aluminum dome yielded very little useful information. The movement of the deflection traces on the oscillographic paper is quite small for the

Figure 4.18 Pit in front of prototype door.

first 30 to 40 msec of dome loading. Superimposed on the small average deflection on several of the records is an oscillation, generally larger in amplitude than the average trace deflection, with a period of from 5 to 6 msec, which indicates vibration of the shell at this frequency. At about 40 msec each of the records becomes extremely noisy and undergoes a shift in position on the paper which lasts for the duration of the record, probably indicating the failure of the dome at about 40 msec.

The deflection records obtained on the 1-inch-thick aluminum dome appear reasonable for about the first 80 msec of blast-wave loading. The trace deflections on the oscillograph paper are generally small and contain a principal superimposed oscillation with a period of from 5 to 6 msec, indicating a dome vibration at this frequency. At about 80 msec the records become very noisy and undergo a large shift in position, indicating the failure of the dome at this time.

79

CONFIDENTIAL

TABLE 4.1 SUMMARY OF RESULTS FROM PRESSURE INSTRUMENTS ON NONRESPONDING CONCRETE ARCHES

All measurements in psi.

Gage Position	Structure F-3.6-9028.01, 70-psi Region					Structure F-3.6-9028.02, 35-psi Region				
	Type of Gage	Range	100 Percent Calibration Pressure	Maximum Recorded Pressure	Remarks	Type of Gage	Range	100 Percent Calibration Pressure	Maximum Recorded Pressure	Remarks
a	EP	500	400	235	—	EP	300	200	—	*
b		500	400	—	*		300	200	92	—
c		100	70	58	—		40	35	9.3	—
d		100	70	—	*		40	35	5.8	—
e		500	400	—	*		300	200	79	—
f		100	70	—	*		40	35	—	*
g	SP	400		286	—	SP	200		85	—
h		400		199	†		200		151	—
i		400		390	‡		200		120	‡
j		400		130	‡		200		53	—
k		100		80	—		50		10	‡
l		100		23	—		50		11	—
m		100		20	—		50		13	—
n		400		365	—		200		101	—
p		400		348	—		200		115	‡
q		400		317	—		200		102	—
r		100		26	—		50		12	—
s		100		20	—		50		13	—
t		100		26	‡		50		10	—

* No record.
† Only initial portion of record good.
‡ Peak pressure only.

TABLE 4.2 SUMMARY OF RESULTS FROM PRESSURE INSTRUMENTS ON NONRESPONDING CONCRETE DOMES

All measurements in psi.

Gage Position	Structure 3.6-9027.01, 70-psi Region					Structure 3.6-9027.02, 35-psi Region				
	Type of Gage	Range	100 Percent Calibration Pressure	Maximum Recorded Pressure	Remarks	Type of Gage	Range	100 Percent Calibration Pressure	Maximum Recorded Pressure	Remarks
a	EP	500	400	625		EP	300	200	—	No record
b		500	400	340		—	—	—	—	
c		500	400	325		EP	300	200	138	
d		500	400	235			300	200	78	
e		300	200	118		—	—	—	—	
f		300	200	163		EP	200	150	—	No record
g		100	70	48			40	35	15	
h		100	70	16			40	35	11	
i		100	70	14			40	35	10	
j		500	400	204			300	200	—	No record
k		500	400	—	No record		300	200	55	Zero shift at end of record
l		100	70	55			40	35	—	No record
m		100	70	55			40	35	22	
n	SP	400		561		SP	200		152	
p		400		359			200		145	
q		400		248	Poor time values		200		78	Poor time values
r		400		128	Peak pressure only		200		59	Poor time values
s		100		56			50		25	Poor time values
t		100		21			50		12	Peak pressure only
u		100		30			50		13	Peak pressure only
v		400		229			200		104	
w		400		174			200		64	
x		100		93			50		34	
y		100		66	Poor time values		50		31	

80

CONFIDENTIAL

TABLE 4.3 SUMMARY OF RESULTS FROM ELECTRONIC PRESSURE INSTRUMENTS ON RESPONDING CONCRETE DOMES

Gage Position	Structure 30.1-8001.01 70-psi Region				Structure 30.1-8001.02 35-psi Region				Structure 30.1-8001.03 20-psi Region			
	Range	100 Percent Calibration Pressure	Maximum Recorded Pressure	Remarks	Range	100 Percent Calibration Pressure	Maximum Recorded Pressure	Remarks	Range	100 Percent Calibration Pressure	Maximum Recorded Pressure	Remarks
	psi	psi	psi		psi	psi	psi		psi	psi	psi	
a	500	400	442	*	300	200	136	*	200	125	41	—
b	500	400	300	*	300	200	157	*	200	125	58	—
c	500	400	236	*	300	200	—	†	200	125	37	—
d	300	200	—	†	200	100	82	*	100	75	—	†
e	100	70	33	*	40	35	18	*	30	20	2.3	—
f	—	—	—	—	—	—	—	—	30	20	3.6	—
g	—	—	—	—	—	—	—	—	30	20	4.1	—

* Partial records only due to dome failure.
† No record.

TABLE 4.4 SUMMARY OF RESULTS FROM ELECTRONIC PRESSURE INSTRUMENTS ON RESPONDING ALUMINUM DOMES, 1-INCH SHELL, STRUCTURE 3.6-9026.02

Partial records only due to failure of dome.

Gage Position	Range	100 Percent Calibration Pressure	Maximum Recorded Pressure
	psi	psi	psi
g	500	400	55
h	500	400	75
i	500	400	165
j	300	250	95
k	100	70	29

TABLE 4.5 SUMMARY OF RESULTS FROM ELECTRONIC DEFLECTION INSTRUMENTS ON RESPONDING CONCRETE DOMES

Gage Position	Structure 30.1-8001.01 70-psi Region		Structure 30.1-8001.02 35-psi Region		Structure 30.1-8001.03 20-psi Region	
	Range	Remarks	Range	Remarks	Range	Remarks
	in		in		in	
h	24	No record	2	Each of these gages provided a good record until the time at which the dome failed. The time of dome failure is indicated by the beginning of a great deal of noise on the record. The traces continue after this point but the information is meaningless.	1	Each of these gages provided a fair record during the entire period of blast-wave loading. Trace deflections are small, on the same order as noise superimposed on deflection trace.
i	24	On these five deflection gages records were obtained throughout the blast-wave loading. However, the records are not significant because of early dome failure. Records contain a great deal of hash and are difficult to interpret at beginning of blast-wave loading because of small trace deflection.	2		1	
i	—		4		2	
j	24		2		1	
j	—		4		2	
k	24		2		1	
l	24		2		1	
l	—		4		2	
m	24		2 *		1	

* No calibration of record.

The oscillographic traces obtained from the deflection gages on the 6-inch reinforced-concrete dome located in the 70-psi region show practically no movement for about the first 80 msec of dome loading. Probably this is due to the 24-inch range of the deflection gages used on the dome, which would require a substantial movement to generate a usable signal from the gage. The gage nearest the foundation on the ground-zero side of the prime meridian, which would have been expected to register the largest deflections (based on the results obtained on the other domes) failed to operate, resulting in the loss of this important source of data. About 80 msec after the arrival of the blast load the deflection records became extremely noisy, indicating the sudden failure of the dome after this time.

Each of the gages located on the 6-inch reinforced-concrete dome at the 35-psi region provided a good deflection record for about 165 msec after the arrival of the blast load. The trace deflections on the oscillograph paper are generally free from noise and are large enough to permit accurate interpretation. The principal oscillatory component of the records has a period

TABLE 4.6 SUMMARY OF RESULTS FROM ELECTRONIC
DEFLECTION INSTRUMENTS ON RESPONDING
ALUMINUM DOMES, 70-PSI REGION

Gage Position	Structure 3.6-9026.01 1/2-inch Shell		Gage Position	Structure 3.6-9026.02 1-inch Shell	
	Range	Remarks		Range	Remarks
	in			in	
a	8	No record obtained.	a	2	For gages which func-
b	8	No record obtained.	b	2	tioned traces continued
b	16	—	b	4	for entire blast-loading
c	8	Record taken but gage	c	2	time, but they were
		calibration not given.	c	4	meaningless, because of
c	16	For gages which func-			early dome failure.
d	8	tioned traces continued			Records contain great
e	8	for entire blast-loading			deal of noise.
		time, but they were	d	2	No record obtained.
		meaningless because of	e	2	—
		early dome failure.	f	2	—
		Records contain great	f	4	No record obtained.
		deal of noise.			
f	8	No record obtained.			
f	16	Record taken but gage			
		calibration not given.			

of about 20 msec, indicating a dome vibration of this period. The records become very hashy about 165 msec after the beginning of the blast load, which probably marks the failure of the dome at this time.

All of the gages on the 6-inch reinforced-concrete dome located at the 20-psi region provided useful data throughout the period of blast-wave loading on the dome. The deflection records indicate that the movements of this shell were quite small during the loading. Most of the oscillograph traces contain a substantial amount of random noise which is of the same order of magnitude or larger than the average trace deflection.

Deflection gage records are contained in an ARF report contained in Appendix E of this report.

4.2.3 Strain Gages. Strain gages, mounted on the prime meridian of the two aluminum domes and the responding concrete domes located in the 70- and 35-psi overpressure region (in an attempt to measure the state of stress in the shell during loading), did not yield data in the case of the aluminum domes, and yielded partial data in the case of the concrete domes. The output of each gage was recorded by two amplifiers and two traces in order to increase the probability of obtaining one good record. The records are contained in the ARF instrument report.

Two of the four strain gages, located on the reinforcing bars parallel to the prime meridian, one lying near the outside surface and the other lying near the inside surface, functioned on the concrete domes until the time of the failure of the domes. The records indicate a definite vibration of the stress in the shell at a frequency of about 50 cps. No data were obtained from the gages on the bars perpendicular to the prime meridian.

82

CONFIDENTIAL

4.2.4 Shear Strain Gages. Records were obtained from the shear strain gages on the 1-inch-thick aluminum dome and the 6-inch-thick responding concrete domes located at the 70- and 35-psi regions until the time the domes failed. The strain gages measuring shear strain on each dome were wired into a single bridge providing one output channel per dome. The output of each channel was recorded on two different oscillographic channels to increase the probability of obtaining one good record. In each case where shear information was obtained both recording oscillographic channels gave good records providing a duplicate set of shear records. No shear data were obtained from the $\frac{1}{2}$-inch-thick aluminum dome. The records are shown in the ARF instrument report.

The shear record obtained on the 1-inch aluminum dome shows no perceptible movement from the time of the application of the blast load to the time of the dome failure, which is marked by the onset of a great amount of noise on the record. The shear records obtained on the concrete domes show considerable trace deflection during the blast loading and are free from noise. Superimposed on the average trace deflections are oscillations with a period of about 20 to 25 msec.

4.2.5 Accelerometers. The results from the accelerometers placed on the floor of the responding concrete domes at the 35- and 70-psi regions are summarized in Table 4.7. Records were obtained on two vertical channels on the 70-psi dome and on one vertical and one horizontal channel on the 35-psi dome. Each of the records has a substantial zero shift at the end of the blast-load period.

Since both the domes containing the accelerometers failed during the blast, it is unlikely that the accelerometers records contain much useful information. Many of the acceleration peaks are undoubtedly due to pieces of debris from the domes striking the instruments.

4.2.6 Mechanical Scratch Gages. The Baldwin mechanical scratch gages placed on the inside of the 1-inch aluminum dome did not yield any useful data. Five of the nine gages were torn from their mountings and could not be found. The remaining gages did not function.

4.2.7 Mechanical Drum Gages. The mechanical drum gages mounted at the end of each instrument truss in the responding concrete domes provided little information. The gage at the end of the lateral truss in the 70-psi region dome was not recovered. All the rest of the drum gages in each of the three domes unwound during the blast load, but indicated no change in diameter of the dome within the limit of resolution of the instrument.

4.2.8 Diametral Scratch Gages. The diametral scratch gages located in the two aluminum domes did not yield a scratch record of the change in diameter of the aluminum domes during the blast load. This indicates either that the gages did not function or that there was no measurable change in the base diameters of the domes.

4.2.9 Mechanical Radial-Rod Deflection Gages. The mechanical radial-rod deflection gages were used in the three responding concrete domes to determine the maximum and minimum shell displacement during the blast loading. No measurements were obtained in the domes at the 70- and 35-psi regions because of the destruction of these domes. The measurements obtained by the gages in the dome at the 20-psi region are listed in Table 4.8.

4.2.10 Soil Test Holes. The earth around the soil test holes filled with colored sand was excavated following the blast loading. No relative displacement was indicated along any of the holes. Horizontal cracks were found in some of the colored sand cores as shown in Figures 4.19 and 4.20. These may have been caused by the earth rebounding during the unloading phase of the blast-wave action on the ground surface or by shrinkage of the sand after being placed in the hole.

4.2.11 Fastax Cameras. No information was obtained from the two Fastax cameras placed in the 1-inch aluminum dome because of the destruction of the cameras in the failure of the dome.

CONFIDENTIAL

Figure 4.20 Separation of colored sand in soil test hole, showing horizontal crack.

Figure 4.19 Separation of colored sand in soil test hole.

TABLE 4.7 SUMMARY OF RESULTS FROM ACCELEROMETERS PLACED ON FLOORS OF RESPONDING CONCRETE DOMES

Structure 30.1-8001.01 70-psi Region				Structure 30.1-8001.02 35-psi Region			
Direction	Range, g	Maximum Recorded Acceleration	Remarks	Direction	Range, g	Maximum Recorded Acceleration	Remarks
Vertical	100	+11.4	Zero shift	Vertical	50	−6.1	Zero shift
Vertical	10	+5.4	Zero shift	Vertical	10	—	No record
Horizontal	50	—	No record	Horizontal	50	−7.9	Zero shift
Horizontal	10	+15.3	—	Horizontal	5	—	No record

TABLE 4.8 SUMMARY OF RESULTS FROM MECHANICAL RADIAL-ROD DEFLECTION GAGES IN THE 6-INCH CONCRETE DOME AT THE 20-PSI REGION

Gage Position	Deflection, inches In	Deflection, inches Out	Gage Position	Deflection, inches In	Deflection, inches Out
aa	$17/32$	$1/8$	jj	$5/32$	$3/32$
bb	$13/32$	$1/16$	kk	$3/16$	$3/32$
cc	0	1	ll	$3/16$	$1/16$
dd	$3/8$	$1/16$	mm	$3/16$	$1/16$
ee	$11/16$	$1/16$	nn	$1/4$	$3/32$
ff	$9/32$	$29/32$	pp	$3/16$	$1/16$
gg	$1/4$	$3/32$	qq	$3/16$	$3/32$
hh	$5/32$	$3/32$	rr	$3/16$	$1/32$
ii	$1/4$	$5/32$	ss	$3/16$	$1/32$
			xx	$3/16$	$13/32$

TABLE 4.9 SUMMARY OF RESULTS FROM ELECTRONIC FREE-FIELD PRESSURE GAGES

Type of Gage	Location	Range	100 Percent Calibration Pressure	Maximum Recorded Pressure	Remarks
		psi	psi	psi	
q Gage Dynamic Pressure	60 ft clockwise from 70-psi arch; 1,180 ft from ground zero	500	390	474	Good Record
	60 ft clockwise from 35-psi arch; 1,600 ft from ground zero	300	200	—	Partial Record Only
P_σ Overpressure	60 ft clockwise from 70-psi arch; 1,180 ft from ground zero	100	70	70	Good Record
	60 ft clockwise from 35-psi arch; 1,600 ft from ground zero	40	—	—	No Record

CONFIDENTIAL

4.2.12 Free-Field Gages. Results obtained from the free-field electronic pressure gages are listed in Table 4.9. The pressure-versus-time records obtained by these gages are included in the next chapter.

CONFIDENTIAL

Chapter 5
DISCUSSION

5.1 BLAST-WAVE LOADING ON ARCH AND DOME STRUCTURES

5.1.1 Characteristics of Free-Field Blast Wave.

The free-field pressure records obtained in each of the overpressure regions where the structures were located show evidence of precursor phenomena as was expected. The records do not indicate the presence of significant shock fronts, which would be characterized by a simultaneous and instantaneous rise in both static and dynamic pressure in the blast wave. Thus, it was impossible to determine reflected pressure effects such as the magnitude and duration of reflected pressure loading on any of the structures, because this loading results from the interaction of the shock front with exposed structural surfaces.

The free-field dynamic and static pressure curves at the 70-psi region, plotted as a function of time, are shown in Figure 5.1. The dynamic pressure increased rapidly following the arrival of the blast wave to a maximum value of about 474 psi in 80 msec. During this time interval the static overpressure remained quite low, never rising above 10 psi. The dynamic pressure decayed rapidly after the peak pressure had been reached, falling to a pressure one half the peak value only 8 msec after the peak pressure had been reached. As the dynamic pressure began to decrease, the static pressure increased, rising from 10 psi to a maximum of 70 psi in 30 msec. The overpressure then decayed to a value of 5 psi in 100 msec.

Because of the failure of the free-field instruments, the only data available of the characteristics of the free-field blast wave at the 35-psi region is a dynamic-pressure-versus-time curve for the first 40 msec of blast-wave loading. No free-field instrumentation was located at the 20-psi dome. Estimates of peak free-field blast-wave overpressure and dynamic pressure at these two locations may be made by referring to the pressure-distance curves presented in References 21 and 22. Maximum overpressure at the 35-psi dome is estimated at 40 psi and maximum dynamic pressure estimated at 150 psi at this location. Maximum free-field overpressure at the 20-psi dome was apparently 20 psi and maximum dynamic pressure about 65 psi at this location.

5.1.2 Arch Loading.

Since only 11 of the 19 pressure gages on the arch at the 70-psi region gave pressure-time records for the complete duration of the blast load, the loading history on this arch cannot be determined with the desired degree of certainty. Interpretation of the data is also hampered somewhat because the data obtained on the self-recording gages are not referenced to an absolute time scale as they are on the electronic pressure gages. Comparisons are made between the two types of records by assuming that the first indication of the blast wave on a self-recording pressure-gage record coincides with the first indication of the blast-wave pressure on an electronic pressure gage at the same angular position on the arch.

Reflected pressure loading of the arches was not significant because of the nonideal nature of the blast wave at both the 70- and 35-psi locations. Therefore, the primary blast load on the arch structures was a drag load due to the high flow velocities associated with the blast wave.

The characteristics of the drag loading on the arch at the 70-psi region were examined by reading the individual pressure records at a number of points and determining the local pressure coefficient as a function of time. The records were read at a 20-msec interval beginning at a time 250 msec after the detonation of the weapon, or about 17 msec after the arrival of the blast wave at the free-field gage, and ending 310 msec after detonation. The small values of most of the pressure records after 310 msec made it impractical to calculate pressure coefficients after this time.

Table 5.1 lists values of the pressure coefficients as a function of time and position on the arch. Where two or more gages were located at the same angular position on the arch, the values of the pressure coefficients are averaged. An examination of the table shows a moderate range of pressure values recorded at a given time obtained by gages located at the same point. This indicates that either the nature of the blast-wave loading or the accuracy of the instrumen-
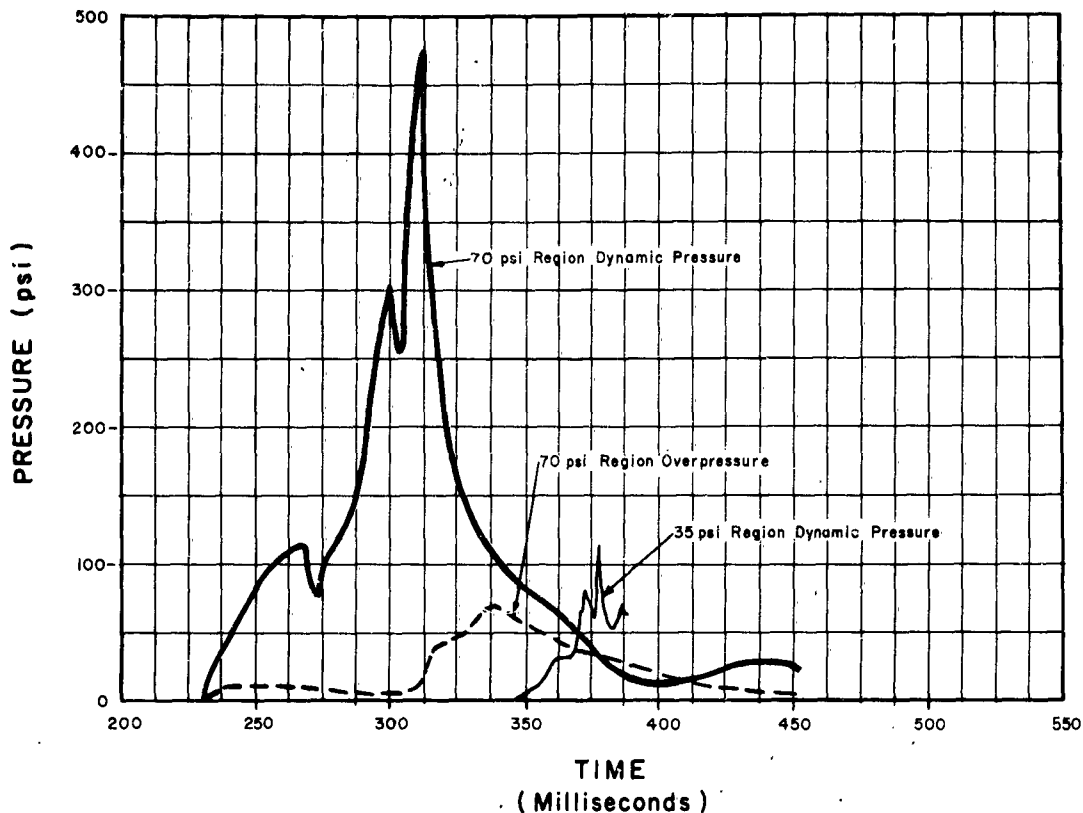
Figure 5.1 Free-field dynamic pressure and overpressure at 70-psi region and free-field dynamic pressure at 35-psi region (partial record) versus time. Time is measured from detonation of weapon.

tation and recording system are such that a moderate deviation of the recorded information from the actual loading condition may be expected on all the records.

One trend, however, does stand out in the data as presented in Table 5.1, and that is the change in the values of the pressure coefficients from the period before the arrival of the peak values of dynamic and static pressure to the period following the peak dynamic and static pressures. The phenomenon is further examined by averaging the values of the pressure coefficients at given positions on the arch obtained at 250, 270 and 290 msec and at 350 and 370 msec. During the first period the dynamic pressure was increasing from 83 to 150 psi, while the static overpressure remained almost constant at 10 psi. The variation of the average pressure coefficient with angular position on the arch during this period is plotted in Figure 5.2. It shows that the maximum pressure coefficient occurs at a region about 10 degrees above the spring line of the arch which is probably due to the boundary layer effect of the ground surface on the flow or is due to a local vortex formation at the intersection of the surface of the arch with the ground. The pressure coefficient decreases to zero at the apex of the arch and remains close to a zero value over the rear of the arch. Thus, during the initial flow associated with the precursor phase of blast wave it is unlikely that much of a wake exists on the rear half of the arch.

CONFIDENTIAL

TABLE 5.1 PRESSURE COEFFICIENTS ON ARCH AT 70-PSI REGION AS A FUNCTION OF TIME

P is measured pressure, psi; C_p is calculated pressure coefficient $(P-P_o)/q$.

Gage Location	Time of Arrival	Time from Detonation, msec 250		270		290		310		330		350		370		C_p Average of 250, 270, and 290 msec Readings	C_p Average of 350 and 370 msec Readings
		P	C_p	P	C_p	P	C_p	P	C_p	P	C_p	P	C_p	P	C_p		
a	229	30	0.24	45	0.39	30	0.16	230	0.49	180	0.88	105	0.57	85	0.88		
g	229	31	0.25	50	0.44	20	0.09	150	0.31	160	0.74	74	0.21	37	−0.04		
Average 30 deg			0.25		0.42		0.13		0.40		0.81		0.39		0.42	0.27	0.41
45 deg h	230	50	0.48	50	0.44	50	0.29	150	0.31	—	—	—	—	—	—	0.40	—
n	231	25	0.18	45	0.39	35	0.19	—	—	—	—	—	—	—	—		
p	231	35	0.30	50	0.44	95	0.59	140	0.29	60	0.03	30	−0.30	18	−0.40		
q	231	30	0.24	65	0.61	50	0.29	275	0.59	90	0.24	45	−0.13	30	−0.17		
Average 60 deg			0.24		0.48		0.36		0.44		0.14		−0.22		−0.29	0.36	−0.25
c	234	7	−0.04	13	0.03	9	0.03	2	−0.02	51	−0.04	24	−0.37	12	−0.52		
k	234	6	−0.05	15	0.06	5	−0.01	2	−0.02	50	−0.04	49	−0.08	18	−0.40		
Average 90 deg			−0.05		0.05		0.01		−0.02		−0.04		−0.23		−0.46	0	−0.35
r	237	9	−0.01	13	0.03	8	0.01	2	−0.02	12	−0.31	16	−0.46	10	−0.56		
s	237	8	−0.02	10	0	11	0.03	8	0	14	−0.30	14	−0.49	7	−0.61		
Average 120 deg			−0.02		0.02		0.02		−0.01		−0.31		−0.48		−0.59	0.01	−0.54
135 deg m	238	14	0.05	16	0.07	11	0.03	18	0.02	12	−0.31	13	−0.50	11	−0.54	0.05	−0.52
Free-Field Overpressure	234	10		10		6		10		56		56		39		—	—
Free-Field Dynamic Pressure	232	83		90		150		450		140		86		52		—	—

89

CONFIDENTIAL

The pressure coefficients following the passage of the peak pressures of the blast wave show a marked difference from the initial values. These results are also plotted in Figure 5.2. Unfortunately the gage located 15 degrees above the spring line on the side of the arch facing ground zero failed to function during this period of the loading, making it impossible to check the effect of a slightly reduced pressure coefficient at the spring line measured during the initial portion
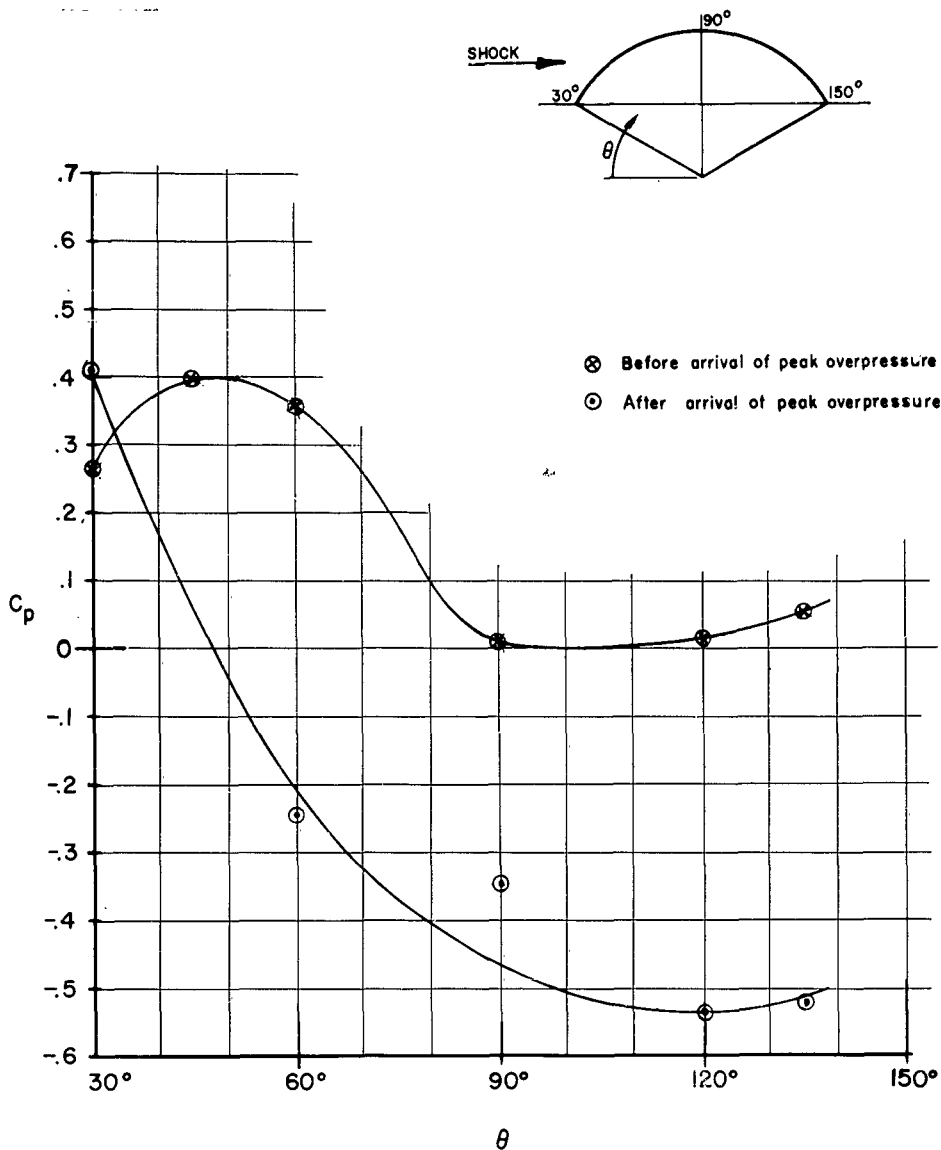
Figure 5.2 Pressure coefficient versus angle of elevation on concrete arch at 70-psi region before arrival of peak dynamic pressure and overpressure and after arrival of peak dynamic pressure and overpressure.

of the loading. The value of the pressure coefficients moved well into the negative range at a point 30 degrees above the spring line facing ground zero and remained in the negative range over the rear half of the arch. During this latter phase of the loading, then, the beginning of the wake of the flow over the arch must have moved to a point forward on the front side of the arch.

90

CONFIDENTIAL

The calculation of pressure coefficients on the arch at the 35-psi overpressure level is impossible because of the complete failure of the static-pressure gage and the early failure of the dynamic-pressure gage at this location. Although free-field self-recording gages used on another project were located about 50 feet further away from ground zero than the arch and dome
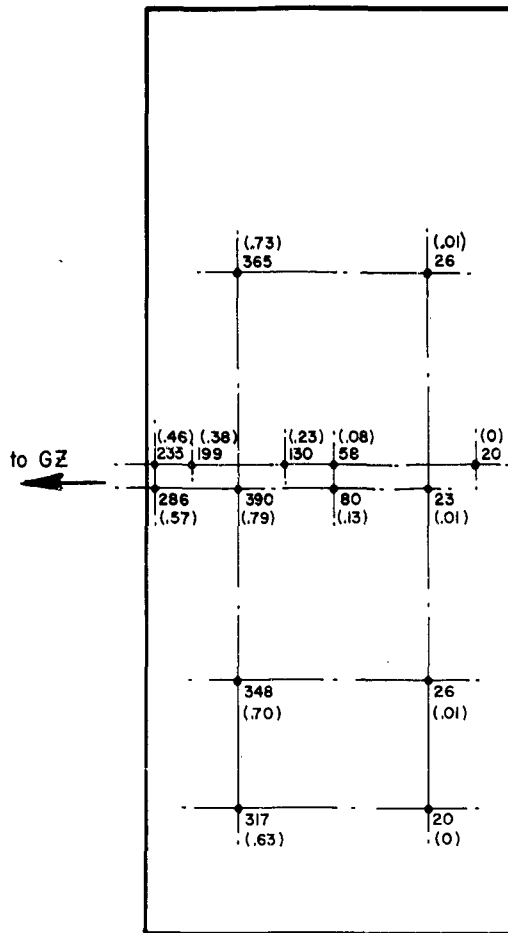
Figure 5.3 Peak pressures, psi, measured on arch at 70-psi region. Numbers in parentheses are local pressure coefficients based on peak measured pressure and peak free-field dynamic pressure.

structures at this region, the time base on these gage records is not accurate enough for calculations of pressure coefficients versus time.

The peak pressures recorded on both arches are of interest for structural design purposes. This information is shown in Figures 5.3 and 5.4 for each of the gages where peak pressures were obtained. It is interesting to observe that the pressures measured near the spring line on the sides of both arches facing ground zero were slightly less than the peak pressures measured at a higher location, indicating the same trend found in the analysis of pressure coefficients during the early portion of the blast wave.

Local pressure coefficients have been computed from the peak pressures recorded on the arches and are included in Figures 5.3 and 5.4. The pressure coefficients on the 70-psi arch are calculated by subtracting 20 psi, the overpressure value at peak dynamic pressure, from the individual peak pressures, and dividing the result by 470 psi, the peak dynamic pressure.

CONFIDENTIAL

The results are plotted in Figure 5.5 as a function of angular elevation position on the arch. The pressure-coefficient values shown in Figure 5.5 are generally larger on the front side of the arch than the values which were calculated for the portion of the flow before the arrival of peak pressure as shown in Figure 5.2. On the rear side of the arch both curves show values near zero.

Pressure coefficients cannot be calculated with as much confidence on the 35-psi arch because of the lack of free-field records at this overpressure level. Estimated maximum pres-
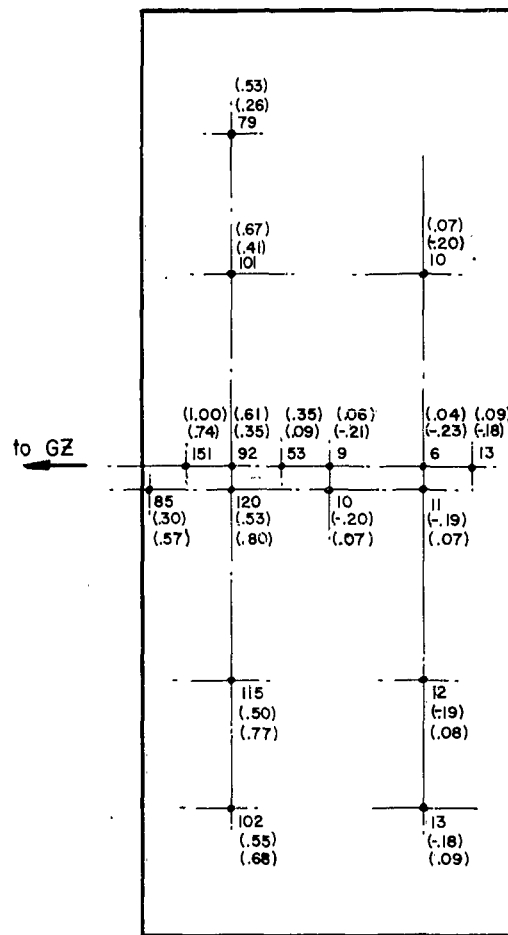
Plan

Figure 5.4 Peak pressures, psi, measured on arch at 35-psi region. Numbers in parentheses are limits of local pressure-coefficient values based on peak measured pressure and estimated peak dynamic pressure. One calculated value is based on no overpressure, the other on estimated peak overpressure.

sure values at this region were 40-psi overpressure and 150-psi dynamic pressure. Two calculations of pressure coefficients have been made, assuming the peak recorded pressures on the arch occurred at the same time as the estimated peak dynamic pressure. The first calculation assumes that the estimated 40-psi maximum overpressure existed at the time of peak dynamic pressure and the second calculation assumes the overpressure was zero at the time of peak structure pressures and peak dynamic pressure. Thus, upper and lower limits for local

92

pressure coefficients on the arch are obtained at the time of peak loading. The results of the calculations are plotted in Figure 5.5. Close agreement is indicated with the pressure-coefficient values determined for the peak pressures on the 70-psi arch.

Pressure coefficients as a function of angular position on an arch have been determined by shock-tube tests on model arches (Reference 23). These tests have yielded pressure coefficients
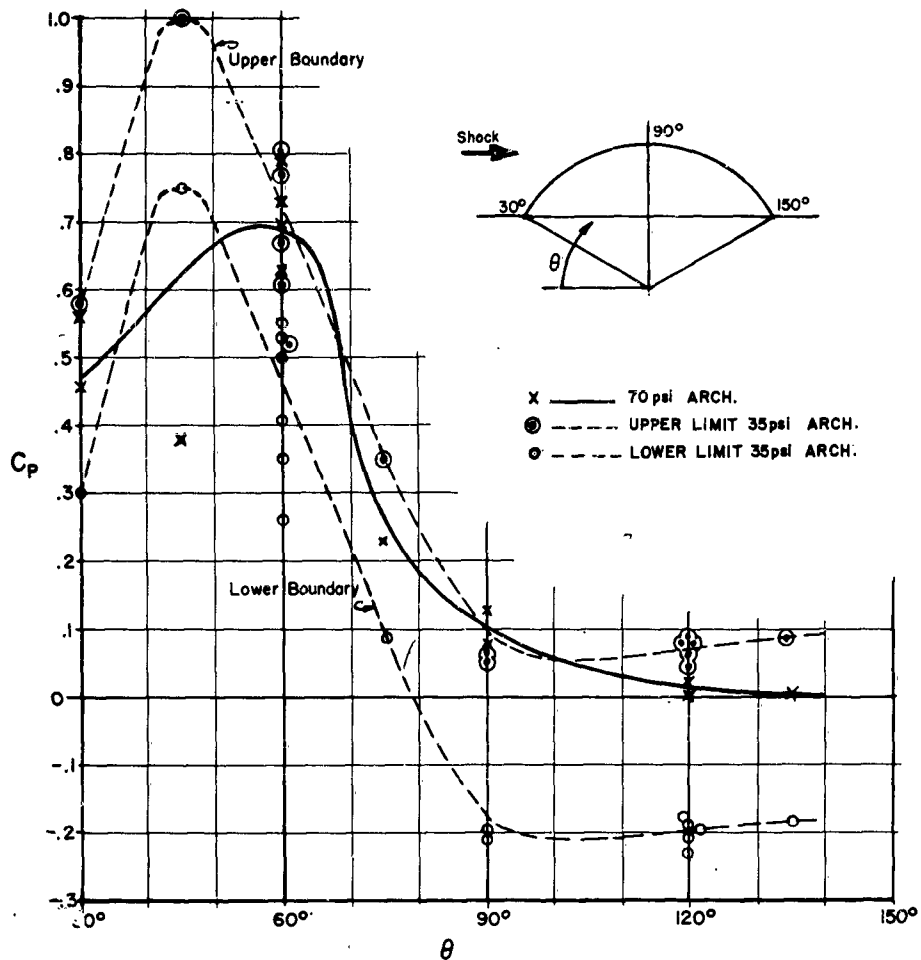
Figure 5.5 Pressure coefficient as a function of elevation angle, θ, on arches at 70- and 35-psi regions based on peak measured pressure and peak dynamic pressure. Upper and lower limits of pressure coefficient on 35-psi arch are based on assumed zero overpressure, and maximum estimated overpressure on arches at time of maximum pressure.

from as high as 0.9 at the front spring line of a 120-degree central-angle arch to about −0.9 on the apex and rear half of such an arch. The maximum pressure coefficients measured on the concrete arches are generally slightly less in absolute value on both the front and rear sides of the arch than those measured on comparable shock-tube tests.

5.1.3 Dome Loading. The successful operation of 20 of the 24 pressure gages located on the nonresponding concrete dome at the 70-psi region provided good data for the study of dome loading under severe precursor blast-loading conditions. As on the arches, diffraction loading was almost nonexistent because of nonideal blast waves. The primary dome load was due to the high

93

dynamic pressures of the flow and a study of the loading is best conducted by examining the pressure coefficients at a number of points as a function of time.

The pressure coefficients were determined at all points where pressure gages were located at 20-msec intervals beginning 250 msec after the detonation of the weapon and ending 370 msec after the blast. The results of these calculations are presented in Table 5.2. Where two or more gages were located at the same point, the results were averaged. The results were also averaged for gages located at symmetrical points off the prime meridian.

The table shows that at most locations there was a substantial change in the pressure coefficient at a point during the passage of the blast wave, similar to the changes observed on the

Figure 5.6 Pressure coefficient distribution on concrete dome
at 70-psi region before arrival of peak overpressure and peak
dynamic pressure.

arch at 70 psi. The changes are greatest between the period before the peak dynamic pressure and overpressure arrived and the period following the arrival of the peak pressures. The changes are illustrated by the plots of pressure-coefficient distribution on the surface of the dome before the peak pressures and after the peak pressures shown in Figures 5.6 and 5.7.

Figure 5.6 shows the distribution of pressure coefficients obtained by averaging the values at 250, 270 and 290 msec. It shows a high-pressure coefficient at the base of the dome facing ground zero and a very small pressure coefficient over the top and back half of the dome. There is no indication of a reduced pressure coefficient at the spring line of the prime meridian facing ground zero like the reduction indicated by the pressure instrumentation on the arches.

Figure 5.7 shows the distribution of pressure coefficients obtained by averaging the values at 350 and 370 msec. Not only are the pressure coefficients substantially reduced at the base of the dome facing ground zero, but rather large negative coefficients are indicated over the middle section and rear face of the dome. Undoubtedly this indicates that the beginning of the

94

TABLE 5.2 PRESSURE COEFFICIENTS ON DOME AT 70-PSI REGION AS A FUNCTION OF TIME

P is measured pressure, psi; C_p is calculated pressure coefficient $(P-P_\sigma)/q$.

Gage Location	Time of Detonation, msec (Time of Arrival)	250 P	250 C_p	270 P	270 C_p	290 P	290 C_p	310 P	310 C_p	330 P	330 C_p	350 P	350 C_p	370 P	370 C_p	C_p Average of 250, 270 and 290 msec Readings	C_p Average of 350 and 370 msec Readings
a	224	70	0.72	70	0.67	110	0.69	550	1.20	150	0.67	80	0.28	50	0.21		
n	224	55	0.54	60	0.56	300	1.96	500	1.09	120	0.46	50	0.07	35	-0.08		
Average			0.63		0.62		1.33		1.15		0.56		0.18		0.07	0.86	0.13
b	232	40	0.36	55	0.50	130	0.83	330	0.71	154	0.70	90	0.40	50	0.21		
c	223	30	0.24	65	0.61	130	0.83	320	0.69	140	0.60	95	0.45	75	0.69		
p	226	60	0.60	60	0.55	70	0.43	350	0.76	100	0.31	45	-0.13	20	-0.36		
Average			0.40		0.55		0.70		0.72		0.54		0.24		0.18	0.55	0.21
d	234	8	-0.02	45	0.39	60	0.36	225	0.48	125	0.49	70	0.16	45	0.12	0.24	0.14
e	230	4	-0.07	17	0.08	25	0.13	115	0.23	85	0.21	50	0.07	30	-0.17		
f	230	2	-0.10	24	0.16	38	0.21	154	0.32	100	0.31	50	0.07	25	-0.27		
Average			-0.09		0.12		0.17		0.28		0.25		0.07		-0.22	0.07	-0.08
g	232	5	-0.06	5	-0.06	3	-0.02	0	-0.02	40	-0.11	21	-0.41	11	-0.54		
s	232	9	-0.01	8	-0.02	0	-0.04	42	0.07	22	-0.24	10	-0.53	12	-0.52		
Average			-0.04		-0.04		-0.03		0.02		-0.18		-0.47		-0.53	-0.04	-0.50
h	235	10	0	8	-0.02	7	0.01	2	-0.02	6	-0.36	10	-0.53	16	-0.44		
t	235	17	0.08	9	-0.01	11	-0.03	4	-0.01	9	-0.34	21	-0.41	20	-0.37		
Average			0.04		-0.01		-0.02		-0.01		-0.35		-0.47		-0.41	0.02	-0.44
i	236	11	0.01	6	-0.04	4	-0.01	0	-0.02	6	-0.36	13	-0.50	11	-0.50		
u	236	22	0.14	10	0	10	0.03	3	-0.02	14	-0.30	24	-0.37	12	-0.35		
Average			0.08		-0.02		0.01		-0.02		-0.33		-0.44		-0.43	0.02	-0.44
j	228	30	0.24	60	0.56	60	0.36	160	0.33	140	0.60	75	0.22	60	0.40		
v	228	25	0.18	50	0.45	50	0.29	210	0.44	80	0.17	45	-0.13	30	-0.17		
Average			0.21		0.51		0.33		0.39		0.39		0.05		0.12	0.35	0.09
w	230	20	0.12	30	0.22	30	0.16	170	0.36	65	0.06	30	-0.30	18	-0.40	0.17	-0.35
l	229	1	-0.11	6	-0.04	6	0	14	0.01	50	-0.04	32	-0.28	19	-0.38	-0.05	-0.33
m	236	3	-0.08	7	-0.03	4	-0.01	12	0	55	-0.01	41	-0.17	19	-0.38	-0.04	-0.27
Overpressure	234	10		10		6		10		56		56		39			
Dynamic Pressure	232	83		90		150		450		140		86		52			

wake formation in the latter phases of the drag flow is at a point about halfway from the spring line of the dome at the prime meridian to the center line of the dome. On the other hand, wake formation is probably far back on the rear surface during the early portions of the blast loading.

The calculation of pressure coefficients on the dome at the 35-psi overpressure level is impossible because of the complete failure of the static-pressure gage and the early failure of the
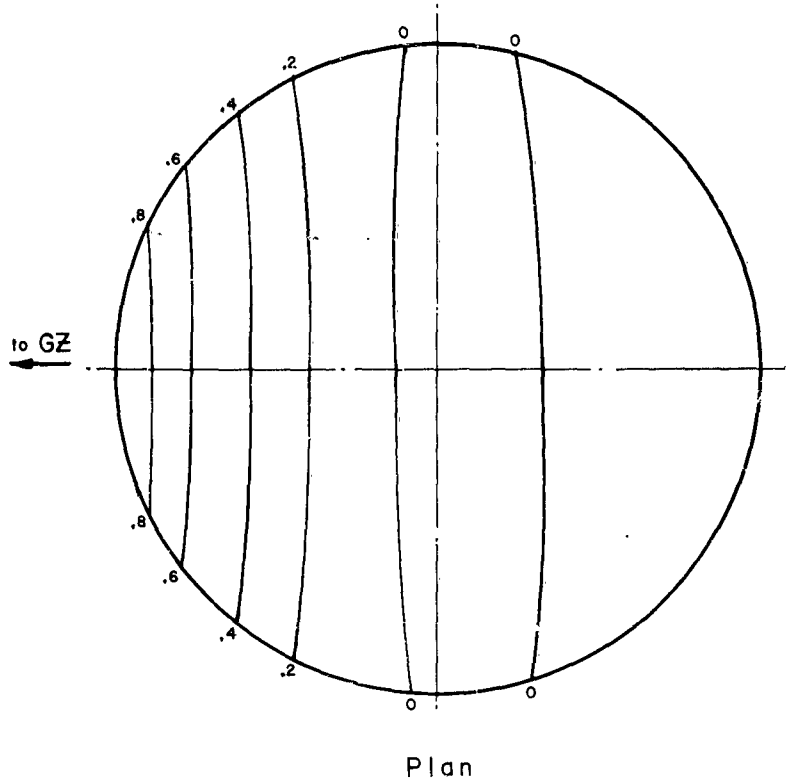

Plan
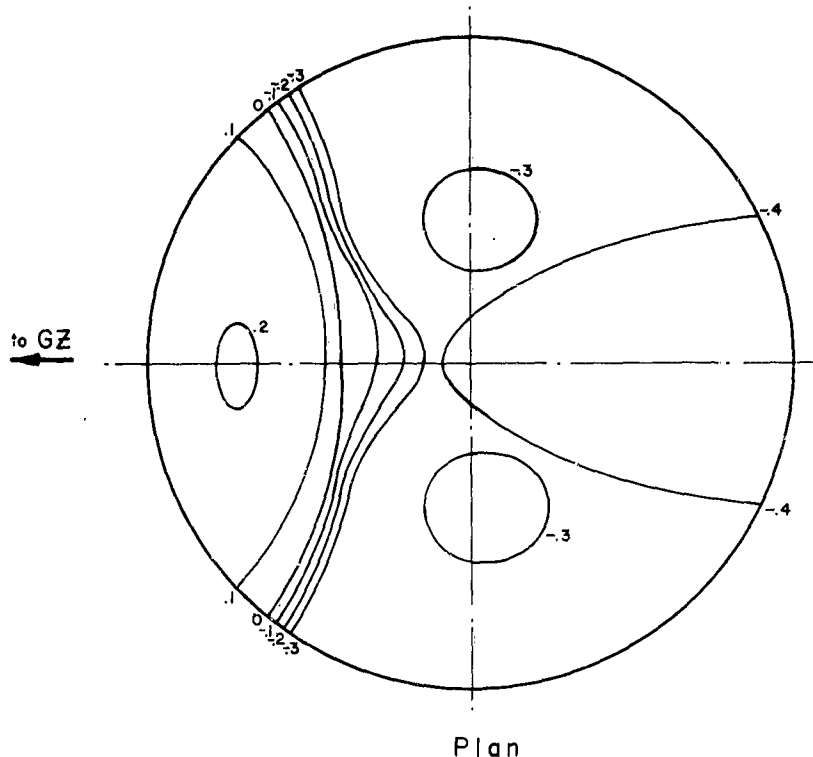
Figure 5.7 Pressure coefficient distribution on concrete
dome at 70-psi region after the arrival of peak overpressure
and peak dynamic pressure.

dynamic-pressure gage at this location. It is also impossible to calculate pressure coefficients on the dome at the 20-psi overpressure level because no free-field pressure measurements were obtained in this region.

Peak pressures measured on the dome are also of interest from a structural design standpoint. These pressures are shown in Figures 5.8, 5.9 and 5.10, at each location where the gages functioned. The highest loads are shown to be concentrated in the relatively small area around the spring line at the prime meridian facing ground zero. Local pressure coefficients have been computed from the peak pressure recorded on the 70-psi and 35-psi domes and are included in Figures 5.8 and 5.9. The pressure coefficients on the 70-psi dome are calculated by subtracting 20 psi, the overpressure value at peak dynamic pressure, from the individual peak pressures and dividing the result by 470 psi, the peak dynamic pressure. Contour lines are drawn on the figure to show the variation in pressure coefficient over the surface of the dome. The pressure-coefficient values shown in Figure 5.8 are similar to those which have been calculated for the portion of the flow before the arrival of peak pressure as shown in Figure 5.6. The values in Figure 5.8 are slightly higher than those in Figure 5.6, but this may be due partially to overshoot of the pressure gages caused by the rapid rise rate in the build-up to peak pressures. Figure 5.6, representing the average of the pressure coefficients at several time intervals before the arrival of peak pressures measured by the gages, probably gives the most accurate

CONFIDENTIAL

to GZ
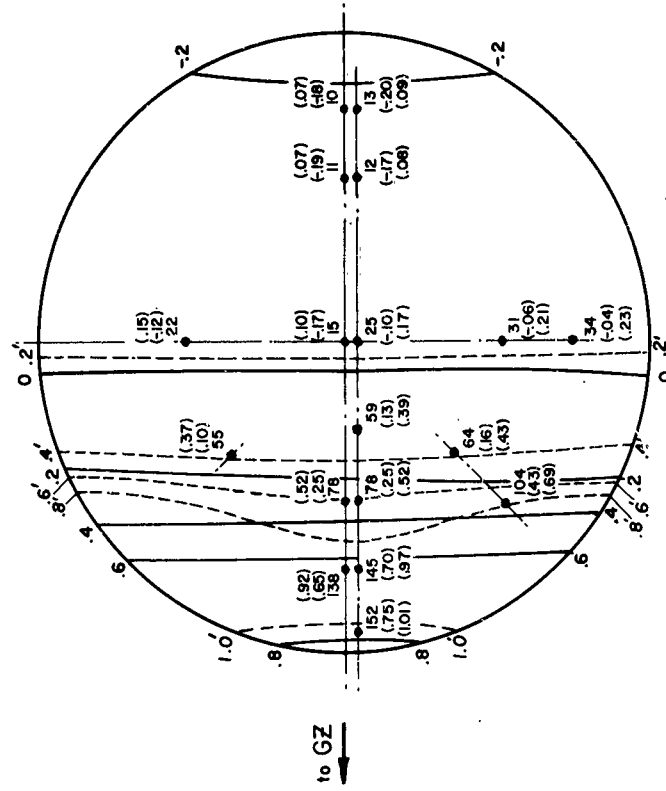
Figure 5.9 Peak pressures, psi, measured on dome at 35-psi region. Numbers in parentheses are limits of local pressure-coefficient values based on peak measured pressure and estimated peak dynamic pressure. One calculated value is based on zero overpressure, the other on estimated peak overpressure. Contour lines show distribution of pressure coefficient on dome surface, dotted lines and prime numbers for upper limit values, solid lines for lower limit values.

Plan

to GZ
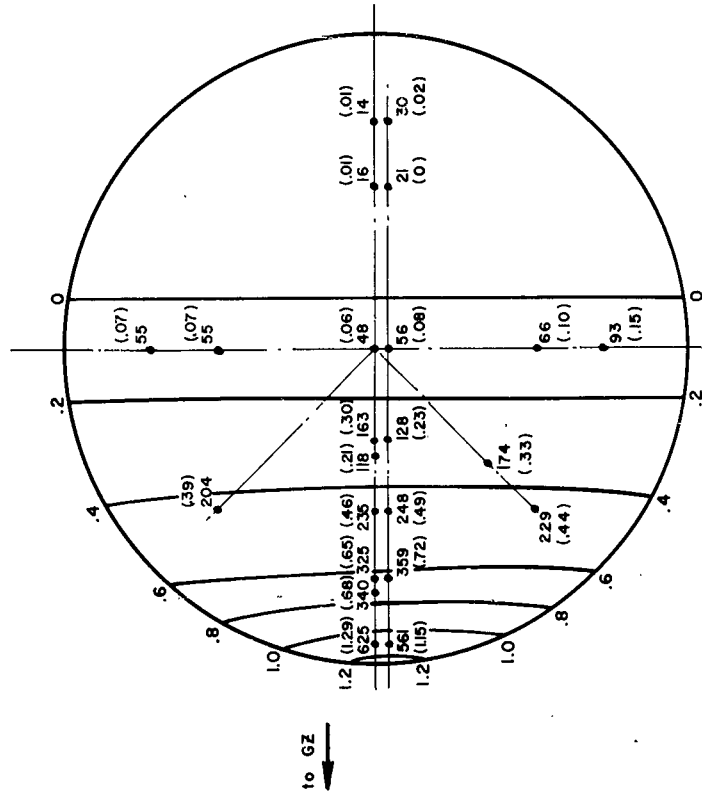
Figure 5.8 Peak pressures, psi, measured on concrete dome at 70-psi region. Numbers in parentheses are local pressure coefficients based on peak measured pressure and peak free-field dynamic pressure.

Plan

values of the maximum pressure coefficients, which would be the best values to use for the design of blast-resistant domes.

Pressure coefficients cannot be calculated with as much confidence on the 35-psi dome because of the lack of free-field records at this overpressure level. Estimated maximum pressure values at this region were 40-psi overpressure and 150-psi dynamic pressure. Two calculations of pressure coefficients have been made assuming the peak recorded pressures on the dome occurred at the same time as the estimated peak dynamic pressure. The first calculation assumes that the estimated 40-psi maximum overpressure existed at the time of peak dynamic pressure and the second calculation assumes the overpressure was zero at the time of peak structure pressures and peak dynamic pressure. Thus, upper and lower limits for local pressure coefficients on the dome are obtained at the time of peak loading. The results of the calculations are shown in Figure 5.9. Close agreement is indicated with the pressure-coefficient

Plan
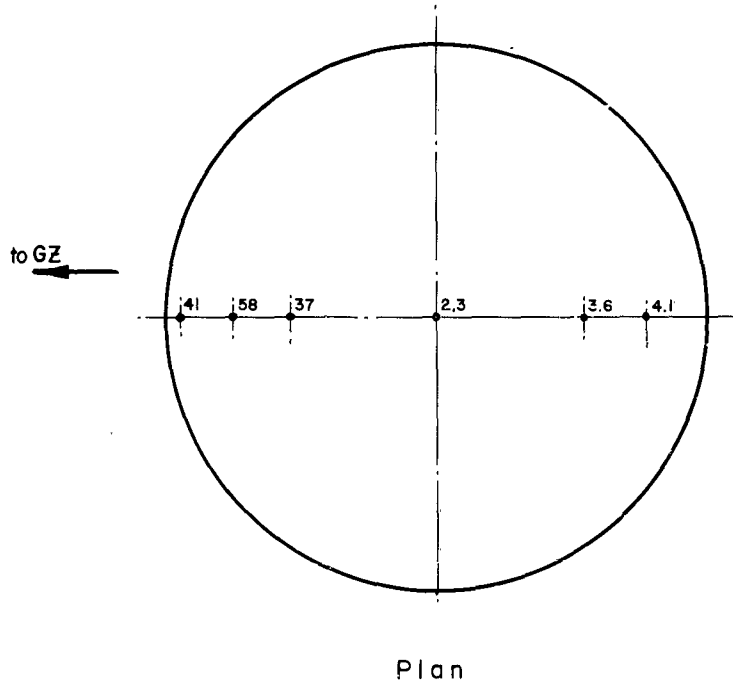
Figure 5.10 Peak pressures, psi, measured on dome at 20-psi region.

values determined on the 70-psi dome during the early portion of blast-wave loading as shown in Figure 5.6 and during the peak portion of the loading as shown in Figure 5.8.

No attempt was made to determine pressure coefficients on the 20-psi dome because of the limited amount of pressure data which was obtained on this dome and the significant effect the assumption of static overpressure would have on the calculated values.

Pressure coefficients as a function of position on a dome have been determined by shock-tube tests on model domes as described in Reference 23. The results presented for a 90-degree central-angle dome show pressure coefficients at the base of the spring line facing the oncoming blast wave about the same magnitude as the values measured in the early portions of the blast loading on the concrete test dome as shown in Figure 5.6. The shock-tube results reported for the center and rear portions of the dome compare more closely with the results obtained in the latter phases of the loading on the concrete test domes as shown in Figure 5.7.

5.2 RESPONSE OF DOME STRUCTURES TO BLAST LOADING

The extensive strain and deflection instrumentation included in these tests was provided to check the theoretical conclusions arrived at in Contract AF 33(616)-2522. There were seven

98

predictions of this theoretical investigation which it was believed could be checked both qualitatively and quantitatively by the instrumentation provided. These were:

1. The frequency of vibration of the dome structures.

2. The critical velocity concept; that is, the theoretical prediction that no radial displacement would occur ahead of the load.

3. The equivalent static load method of design. In particular, two items could be checked qualitatively; the deflection configuration of the prime meridian of the dome, and the deflection configuration of a small circle drawn in a vertical plane perpendicular to the prime meridian of the dome.

4. The ratio of the membrane stresses parallel and perpendicular to the prime meridian.

5. The ratio of the maximum membrane stress to the bending stress at one point on the dome surface.

6. The ratio of the shear stress near the foundation to the maximum membrane stress.

7. The influence of the ground surface and consequent foundation vertical acceleration and displacement on the response of the dome. Theory predicted that this influence would be small enough to neglect.

In addition to these seven predictions of the theory, it was desired to obtain the actual k_d factors for the responding domes and compare these with the limiting values established previous to the test on a theoretical basis and without the benefit of previous test information.

Reduction of the data has been hampered by loss of critical gage records and serious inconsistencies among the records obtained. There are two possible courses open in interpreting such data; one is to take the strictly scientific point of view—that the data is inconsistent and no firm conclusions can be drawn. The second, or what might be termed the engineering point of view, is to attempt to find a consistent pattern in the entire set of the information obtained and, where particular records diverge from this pattern, assume that some of the inevitable difficulties in field measurements have produced the inconsistency. The first approach would yield little usable information from the test; the second point of view would provide a probable, but not certain, means for correlation of the various data. The second point of view has been adopted in the report.

5.2.1 Smoothed Records. The 35-psi responding concrete dome survived for about 150 msec after arrival of precursor pressure; the deflections and strains recorded for this dome were of sufficient size to enable reasonable interpretation of data. Therefore, this dome has been examined in detail.

Figures 5.11 through 5.19 are smoothed records of the deflection and strain data obtained. Smoothing was accomplished by placing the photosensitive paper original of each record on a light table and drawing a fine pencil line through the center of the hash and the approximately $\frac{1}{16}$-inch-wide trace appearing on the original record. Coordinates of the pencil line were accurately measured with a Gerber expanding scale. Since a time of 1 msec corresponded to a distance of only 0.016 inch, the times measured can be considered as accurate only to 3 or 4 msec. In particular, inasmuch as the initial slope of practically all of the records was quite small, the times of arrival listed on the smoothed records are open to some question. However, the difference between the onset of motion at gages h and k was about 13 msec. This distance was clearly discernible on the records. Since these gages were separated by a distance of 40 feet, it would indicate that the precursor was moving at around 3 ft/msec, a not unreasonable value.

5.2.2 Loading and Equivalent Static Loads. When the tests were planned it was hoped that there would be sufficient correlation between corresponding gages on the nonresponding and responding domes at a given overpressure level to establish a loading pattern for the responding domes from the records obtained on the more-heavily pressure-instrumented nonresponding domes. Examination of the records discloses that this aim was not achieved on the 35-psi domes. There is little correlation between the records at corresponding points on the responding and nonresponding domes at 35 psi other than the peak pressures attained.

CONFIDENTIAL
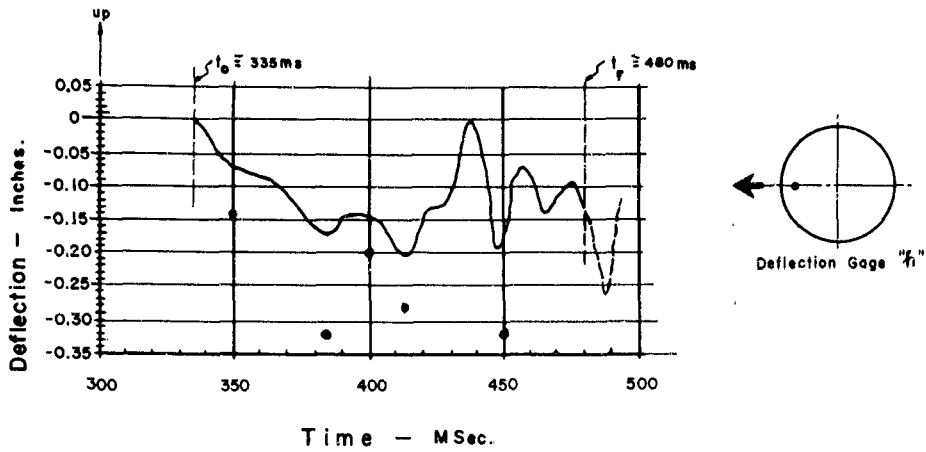
Figure 5.11 Smoothed deflection-versus-time record obtained at Position h on 50-foot-diameter, 6-inch-thick, concrete dome at 35-psi region. Dots show deflection positions computed from dome loading records.
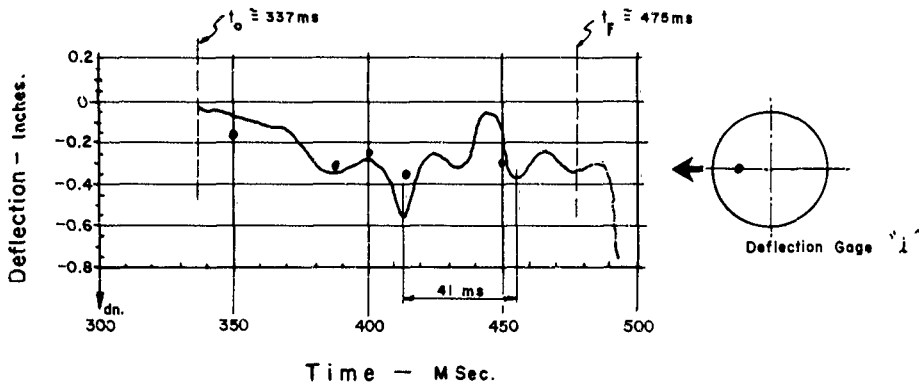
Figure 5.12 Smoothed deflection-versus-time record obtained at Position i on 50-foot-diameter, 6-inch-thick, concrete dome at 35-psi region. Dots show deflection positions computed from dome loading records.
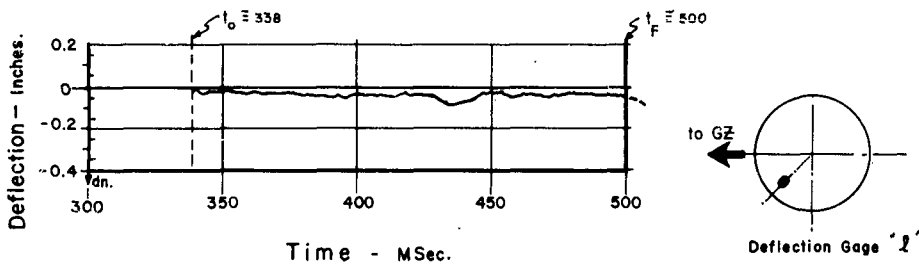
Figure 5.13 Smoothed deflection-versus-time record obtained at Position l on 50-foot-diameter, 6-inch-thick, concrete dome at 35-psi region.

100

CONFIDENTIAL
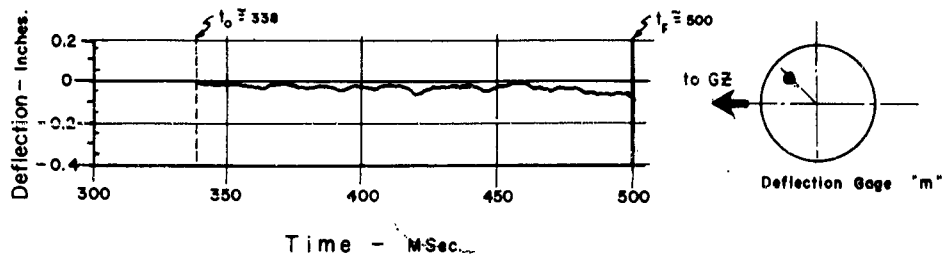
Figure 5.14 Smoothed deflection-versus-time record obtained at Position m on 50-foot-diameter, 6-inch-thick, concrete dome at 35-psi region.
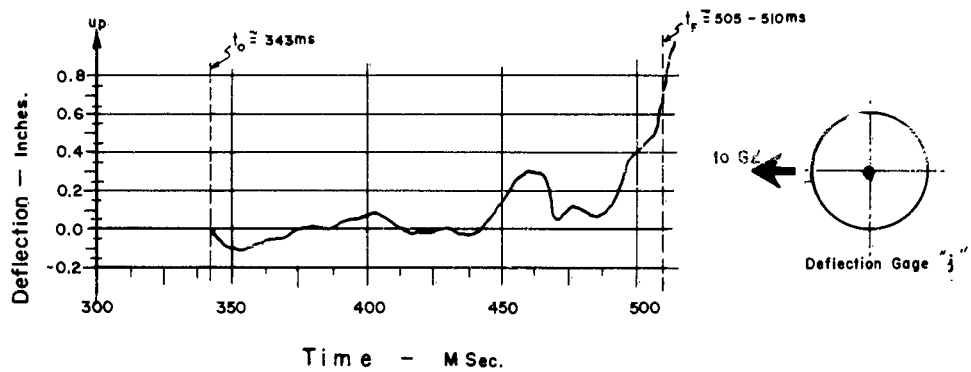
Figure 5.15 Smoothed deflection-versus-time record obtained at Position j on 50-foot-diameter, 6-inch-thick, concrete dome at 35-psi region.
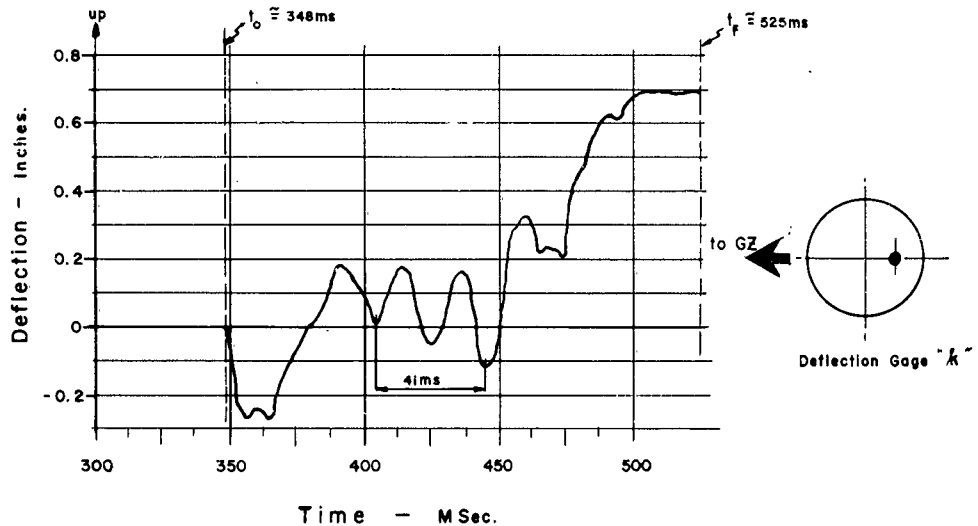
Figure 5.16 Smoothed deflection-versus-time record obtained at Position k on 50-foot-diameter, 6-inch-thick, concrete dome at 35-psi region.

CONFIDENTIAL
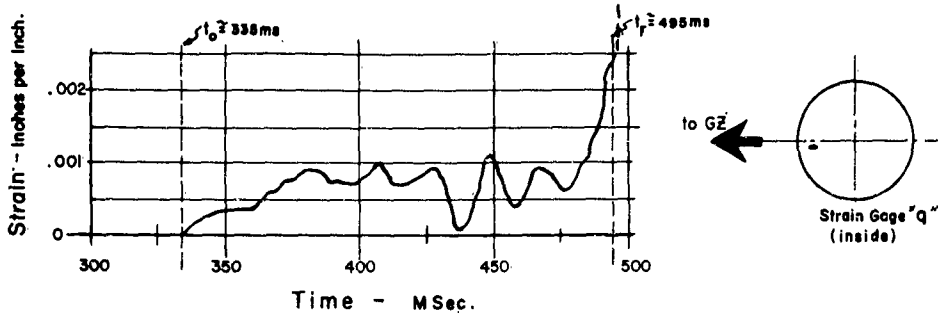
Figure 5.17 Strain-versus-time record obtained at Position q on 50-foot-diameter, 6-inch-thick, concrete dome at 35-psi region. Gage was mounted on reinforcing bar parallel to prime meridian near inside surface of dome.
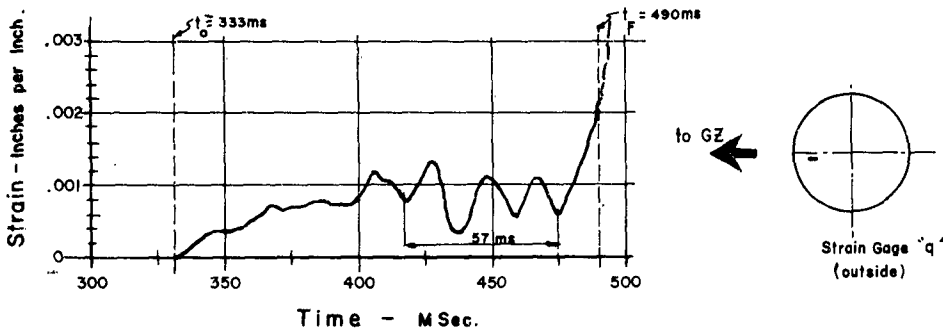
Figure 5.18 Strain-versus-time record obtained at Position q on 50-foot-diameter, 6-inch-thick, concrete dome at 35-psi region. Gage was mounted on reinforcing bar parallel to prime meridian near outside surface of dome.
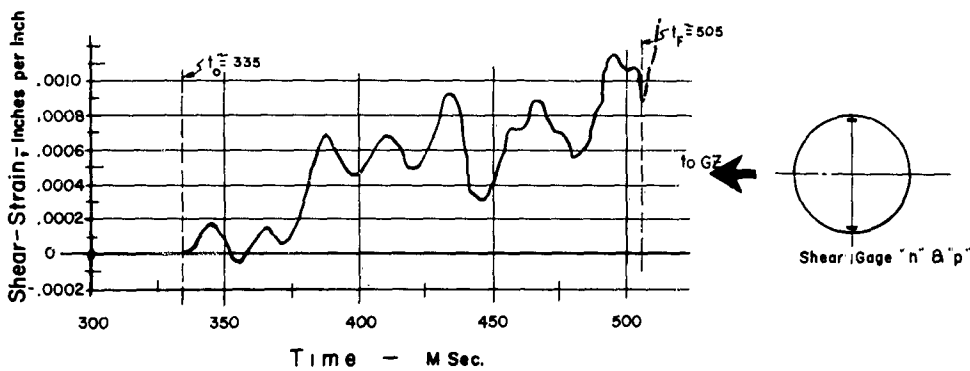
Figure 5.19 Shear strain-versus-time record obtained on 50-foot-diameter, 6-inch-thick, concrete dome at 35-psi region.

102

CONFIDENTIAL

The equivalent static loads at gages a, b, d and e were determined by the graphical method given in Appendix C. There was no pressure record obtained at Point c and it was believed that there was insufficient correspondence between pressures obtained on the responding and nonresponding domes to justify determination of the equivalent static load at c from the pressure measured on the nonresponding dome. The equivalent static loads are given in Figures 5.20 through 5.25.

5.2.3 Comparison of Measured Frequency with Theory. Figures 5.12 and 5.16 show two clearly discernible two-period-of-vibration intervals of 41 msec each. Figure 5.18 shows a
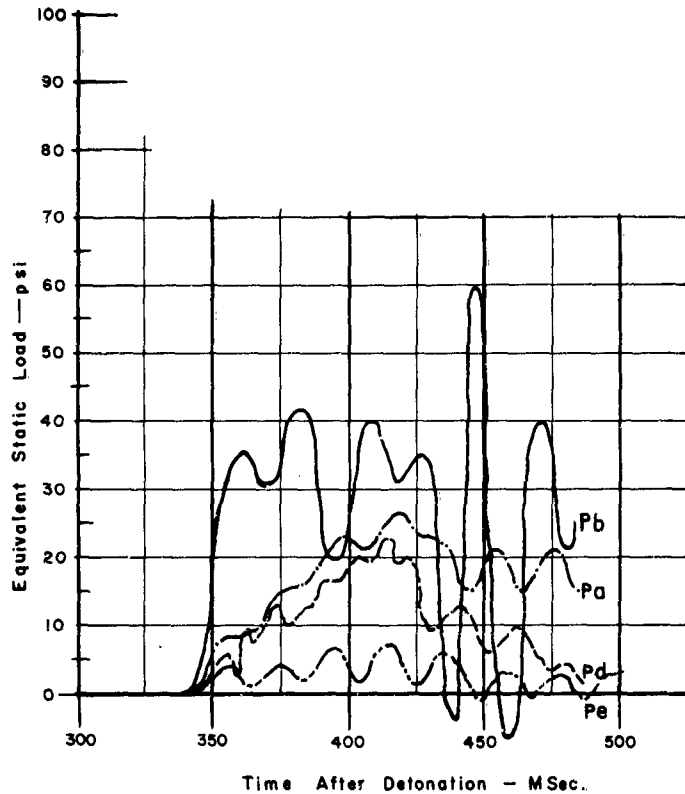
Figure 5.20 Equivalent static load versus time at Positions a, b, d and e on 50-foot-diameter, 6-inch-thick, concrete dome at 35-psi region.

three-period-of-vibration interval of 57 msec. Thus it appears that one period of vibration is in the vicinity of 19 to 20½ msec. The period of vibration of the dome computed from assumed physical constants was 21 msec. The period of vibration of the dome computed from the experimentally determined shell constants is 19.8 msec.

5.2.4 Critical Velocity Concept. In view of the uncertainty in establishing the time of arrival of the blast wave at each of the gages, the critical velocity phenomenon cannot be considered to be conclusively checked; however, the trend exhibited is compatible with the existence of such a phenomenon, and there is no contrary evidence.

5.2.5 Comparison of Measured Deflections with Posttest Predictions by Equivalent Static Load Method. It is extremely unfortunate that the pressure gage at the c position on the 35-psi responding dome failed. The position of this gage corresponds to the deflection gage at Point i,

103
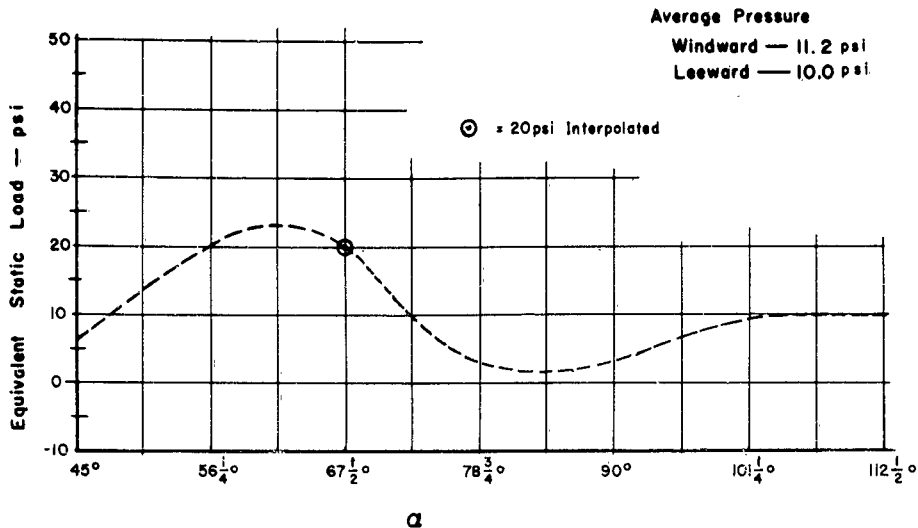
Figure 5.21 Equivalent static load versus α on 50-foot-diameter, 6-inch-thick, concrete dome at 35-psi region 350 msec after detonation of weapon. The average pressures listed are averages over one half of the dome surface of the equivalent static load assuming that the equivalent static loads do not vary with β .
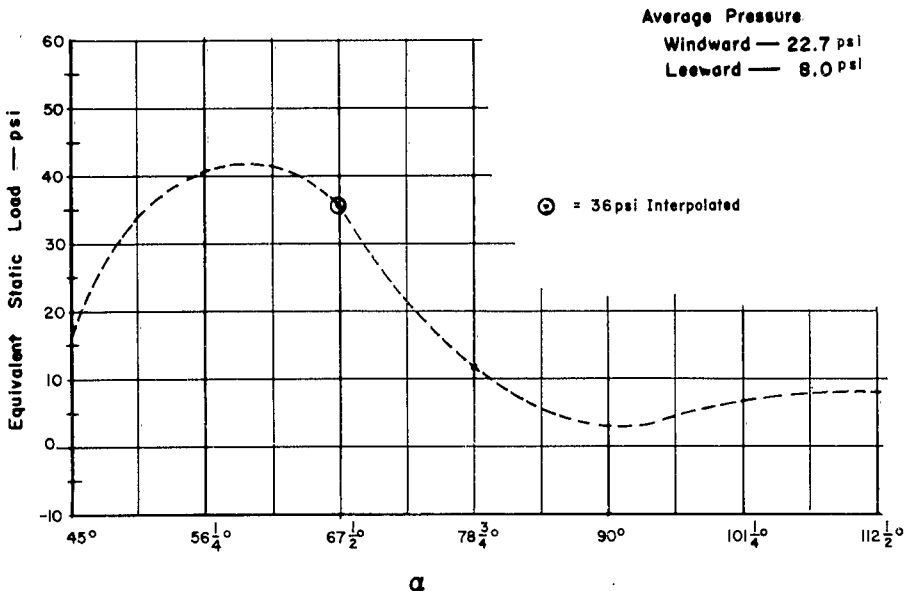
Figure 5.22 Equivalent static load versus α on 50-foot-diameter, 6-inch-thick, concrete dome at 35-psi region 380 msec after detonation of weapon. The average pressures listed are averages over one half of the dome surface of the equivalent static load assuming that the equivalent static loads do not vary with β .

104
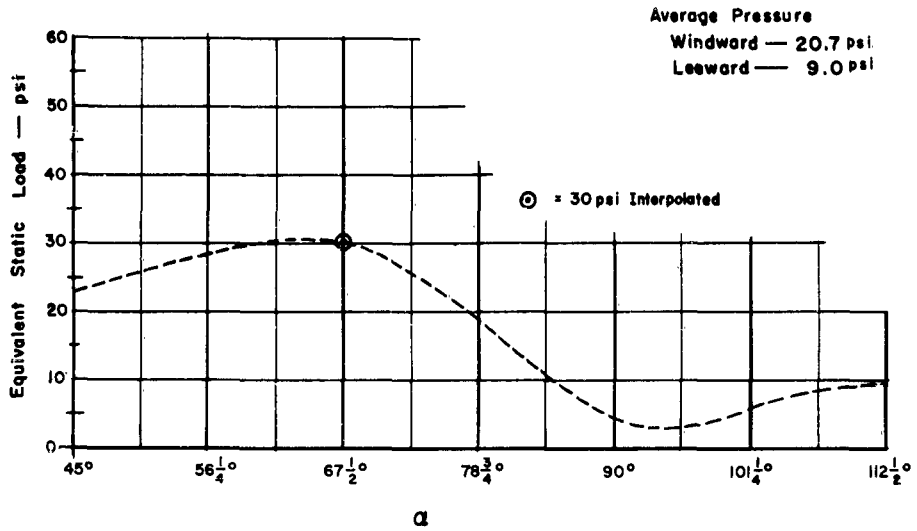
Figure 5.23 Equivalent static load versus α on 50-foot-diameter, 6-inch-thick, concrete dome at 35-psi region 400 msec after detonation of weapon. The average pressures listed are averages over one half of the dome surface of the equivalent static load assuming that the equivalent static loads do not vary with β.
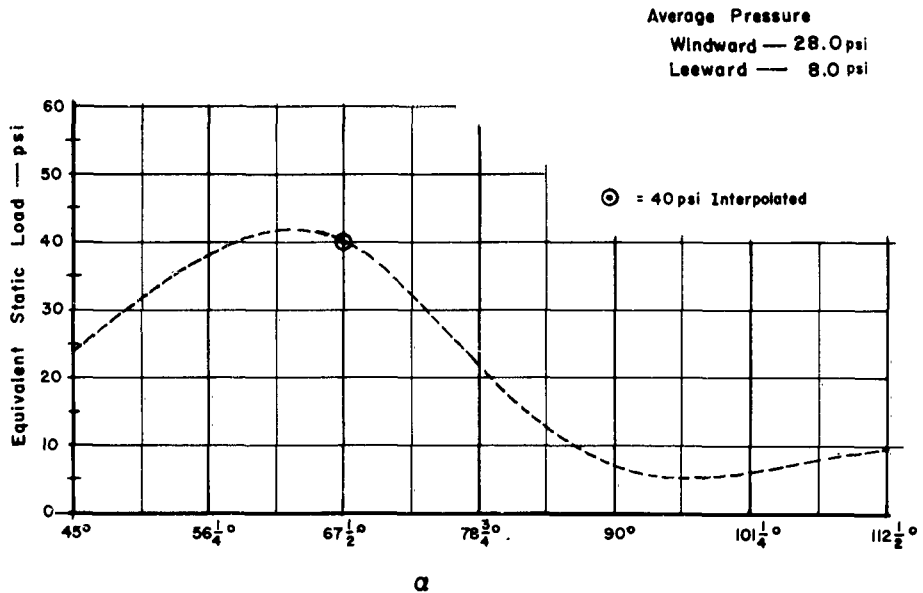
Figure 5.24 Equivalent static load versus α on 50-foot-diameter, 6-inch-thick, concrete dome at 35-psi region 413 msec after detonation of weapon. The average pressures listed are averages over one half of the dome surface of the equivalent static load assuming that the equivalent static loads do not vary with β.

CONFIDENTIAL

the point at which maximum deflections were measured, and also is the point at which the deflection-instrumented small circle intersects the prime meridian. Peak deflection at Point i before failure was about 0.55 inch. At the next gage to the windward, Point h, peak deflection before failure was only 0.2 inch. Therefore, in checking the equivalent static load method of design, the loads at Point i were interpolated graphically from the computed loads at other points along the prime meridian for which data were obtained. Deflections at both Points i and h have been computed from the measured pressure data for an interval of 100 msec after time

Average Pressure
Windward — 21.2 psi
Leeward —— 6.0 psi
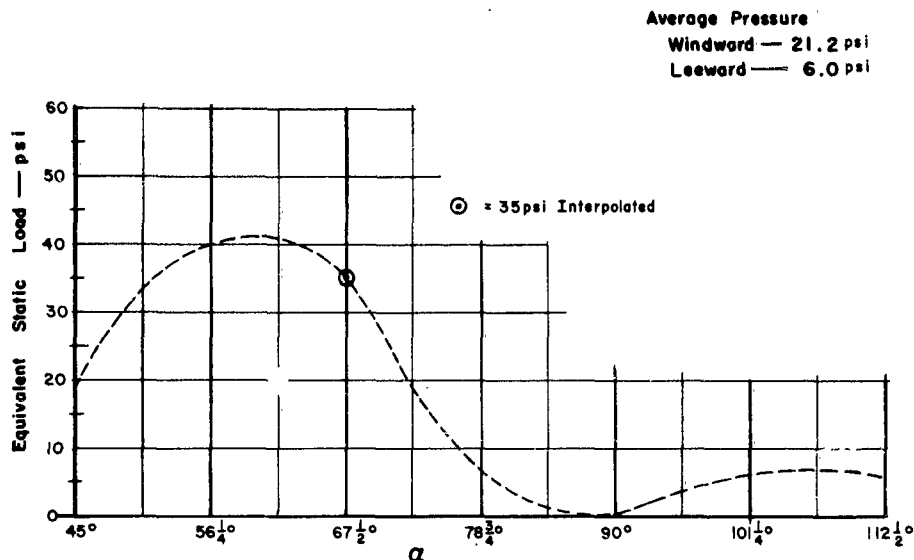
Figure 5.25 Equivalent static load versus α on 50-foot-diameter, 6-inch-thick, concrete dome at 35-psi region 450 msec after detonation of weapon. The average pressures listed are averages over one half of the dome surface of the equivalent static load assuming that the equivalent static loads do not vary with β.

of arrival of the precursor. The posttest-computed deflections are shown by points in Figures 5.11 and 5.12.

The deflections at these two points were computed as follows:

1. For the time instants 350, 380, 400, 413 and 450 msec after detonation, the equivalent static loads were plotted as functions of position (Figures 5.21 through 5.25).

2. Based on the pressure-coefficient pattern reported in Section 5.1.3, it was assumed that at any instant the pressure along a small circle of constant α was constant.

3. The partition of stress between the σ_α stress along the prime meridian and σ_β stress along the small circles of constant α was estimated as discussed in detail in Section 5.2.9.

4. Under the influence of the σ_β compression stress the small circle arc of constant α was assumed to contract uniformly and to remain circular.

5. The deflection at the prime meridian was then computed from the geometric relations between the initial and contracted arc. Geometric considerations lead to the following formula relating the deflection, w, to the membrane stress, σ_β.

$$w = \frac{\sin \alpha (1 - \cos \beta_0)}{(\sin \beta_0 - \beta_0 \cos \beta_0)/\beta_0} R(\sigma_\beta/E_c)$$

(5.1)

Where: β_0 = half-central angle of small circle of constant α
R = spherical radius
E_c = modulus of elasticity of the shell material

106

E_C was computed from the formula

$$E_C = (4 \pi^2/T^2) R^2 \rho \qquad (5.2)$$

Where: T = the period of vibration of the shell
  ρ = the unit mass of the shell material

In performing the calculations the observed value of 20 msec was used for T. The unit weight and consequent unit mass of the shell material was obtained by the water displacement method us-

TABLE 5.3 POSTTEST COMPUTATION OF DEFLECTIONS

P_{ESL} = equivalent static load, psi
  P_W = average windward pressure, psi
  P_L = average leeward pressure, psi
  $f = \frac{1}{4} \sec^4 \phi/2$
  $g = 10^6 \times \left[\dfrac{\text{vers } \beta_0 \sin \alpha}{\dfrac{\sin \beta_0}{\beta_0} - \cos \beta_0} \right] \dfrac{R}{E_c}$ Factors defined for brevity of equations.

		Time, in milliseconds	350	380	400	413	450
Point h	$\alpha = 56\frac{1}{4}°$	P_{ESL}	20	41	28	38	40
	$\phi = 33\frac{3}{4}°$	P_W	11.2	22.7	20.7	28.0	21.2
	$\beta_0 = 31\frac{1}{2}°$	P_L	10	8	9	8	6
	$f = 0.30$	$f\,P_W$	3.35	6.8	6.2	8.4	6.4
	$g = 138$	$(0.5 - f)\,P_L$	2.00	1.60	1.8	1.6	1.2
		$\sigma_\alpha P_{ESL}\,(h/R)$	0.27	0.20	0.28	0.26	0.19
		$\sigma_\beta P_{ESL}\,(h/R)$	0.73	0.79	0.72	0.74	0.81
		$\delta = g \times \sigma_\beta \times 10^{-6}$	0.14"	0.320"	0.20"	0.28"	0.32"
Point i	$\alpha = 67\frac{1}{2}°$	P_{ESL}	20	36	30	40	35
	$\phi = 22\frac{1}{2}°$	P_W	11.2	22.7	20.7	28.0	21.2
	$\beta_0 = 40°$	P_L	10	8	9	8	6
	$f = 0.27$	$f\,P_W$	3.0	6.1	5.6	7.6	5.7
	$g = 150$	$(0.5 - f)\,P_L$	2.3	1.8	2.1	1.8	1.4
		$\sigma_\alpha\,P_{ESL}\,(h/R)$	0.27	0.22	0.26	0.23	0.20
		$\sigma_\beta\,P_{ESL}\,(h/R)$	0.73	0.79	0.74	0.77	0.80
		$\delta = g \times \sigma_\beta \times 10^{-6}$	0.16"	0.30"	0.24"	0.34"	0.30"

ing one of the cores taken from the dome after test. The core chosen contained short pieces of reinforcing steel. The computed unit weight obtained was 145 ± 0.1 lb/ft^3.

When these values were substituted into the above formula, the computed value of the modulus of elasticity obtained was 3,950,000 psi. A value of 4×10^6 psi was used for computation.

A summary of the computations of posttest predicted deflections is given in Table 5.3. The explanation and formulas used to compute this table are given in Figure 5.26.

Comparison of the measured and posttest computed deflections shows that there appears to have been more equal distribution of the total stress between the σ_α and σ_β components than has been assumed. Further, for domes as small as those tested, the shells are quite sensitive to resonances with peaks in the net pressure. In computing the equivalent static load at Point h, a peak of 40 psi occurred at about 410 msec after detonation. A phase shift of the equivalent static load of about 80 degrees, corresponding to a time of only $4\frac{1}{2}$ msec would have increased

CONFIDENTIAL

this peak to over 60 psi. At 413 msec after detonation, the peak deflection computed at Point i is 0.34 inch, while the measured deflection at the peak occurring at this point is about 0.55 inch. Thus the phase shift would account for the peak measured deflection quite adequately.

For a larger dome, perhaps 300 or 400 feet in diameter, the random pressure spikes developing would have a duration considerably less than a quarter period of vibration and would, therefore, have less pronounced effect on the net displacement.

Comparison of the deflection records of Figures 5.12 and 5.13 (Points i and l, respectively) indicated that the theoretical prediction that small-circle arcs of constant α would remain cir-
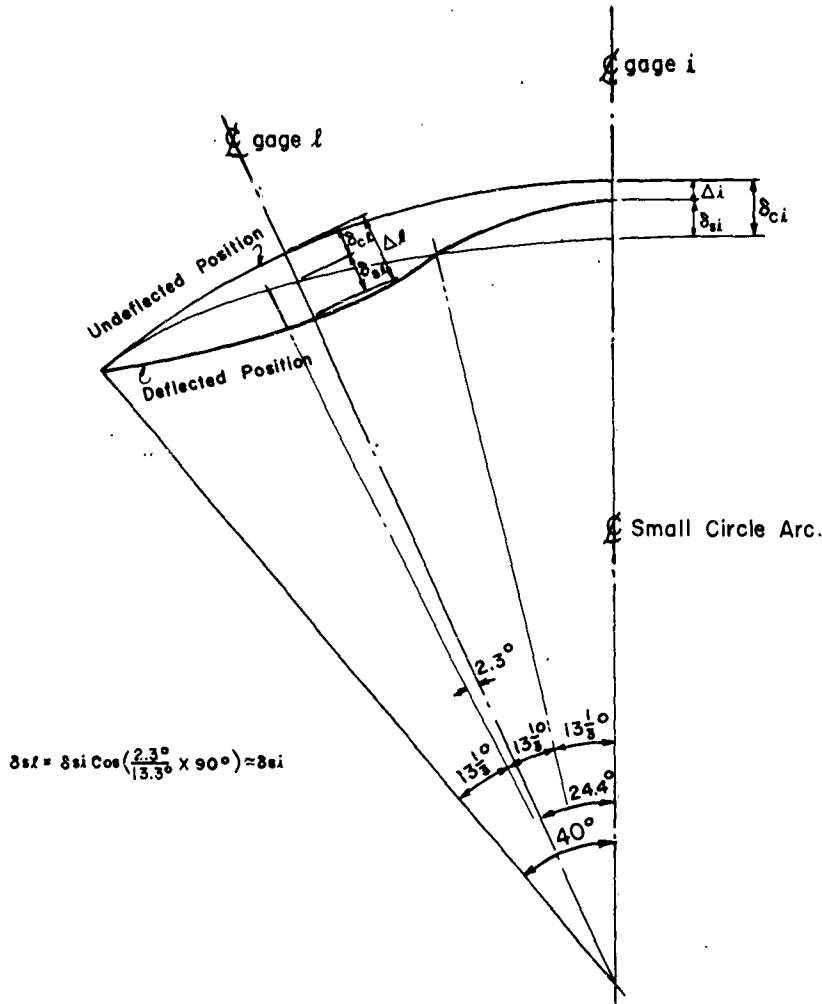
Figure 5.26 Assumed geometry of instrumented small-circle deflection.

cular during deflection was grossly correct but also that departures from circularity were significant.

An index of this departure from circularity which could be used in evaluating the test data was desired. Now, whatever the deflected curve of the small circle, the curve can be represented by a Fourier series. Further, we expect intuitively that the major fraction of the departure from true circularity is represented by the first term of the series. Also, since we have only two points on the small circle to describe the curve, no more than one correction term can be evaluated. Figure 5.26 shows diagrammatically the deflection configuration of the instru-

108

CONFIDENTIAL

mented small circle based on the assumption that the deflection consists of two components, a circular deflection δ_c, and a sinusoidal deflection of three lobes, δ_s. Measured deflections are denoted Δ_i and Δ_l at Points i and l respectively.

From the geometry of the small-circle deflection assumed, it can be shown that at the instrumented small circle:

$$\delta_{cl} = 0.63 \, \delta_{ci}$$

$$\delta_{sl} \cong \delta_{si}$$

$$\delta_{ci} = 0.615 \, (\Delta_l + \Delta_i)$$

$$\delta_{si} = 0.614 \, \Delta_l - 0.386 \, \Delta_i$$

$$\frac{\delta_{si}}{\delta_{ci}} = \frac{\Delta_l - 0.63 \, \Delta_i}{\Delta_l + \Delta_i}$$

Also, it can be shown on application of the elementary stress formulas that at the instrumented small circle

$$\frac{\sigma_b}{\sigma_c} = \frac{0.73 \, c}{R} \, (\delta_{si}/\delta_{ci}) \tag{5.3}$$

Where: σ_b is the bending stress parallel to the small circle a distance c from the neutral axis

σ_c is the compression stress

R is the spherical radius

The values of δ_{si}/δ_{ci} and σ_b/σ_c were computed for five time instants. Results are given in Table 5.4.

From an examination of the values in Table 5.4, it is evident that the maximum departure from circularity of the instrumented small-circle deflection curve exceeded 50 percent of the circular component of deflection. However, for the 6-inch dome shell this introduced a bending stress into the reinforcing steel of less than 1 percent of the direct stress.

5.2.6 Measured Membrane Stresses. It is extremely unfortunate that all of the strain gages mounted to measure strains parallel to small circles of constant α failed. Thus, though clear records of the strains on both the inside and outside bars parallel to the prime meridian were obtained on both the 70-psi and 35-psi responding concrete domes, no measured value for the partition of membrane stress between the α and β directions can be established.

The strains on the inside and outside bars on the 35-psi dome are given in Figures 5.17 and 5.18, respectively, from time of precursor arrival to dome failure. For all but a 75-msec interval between times 400 and 475 msec after detonation, the records are practically identical. Within this interval some bending of the prime meridian could be inferred from the graphs, the maximum bending strain occurring at about 425 msec after detonation with about 20 percent of the magnitude of the membrane strain. In view of the questionability of the records, however, no conclusion should be drawn since this value departs so much from the theoretical predictions.

The records obtained on two domes are quite clear up to the time of failure. Yet the strains indicated cannot possibly have existed across the total area of the measured bars. The reasoning leading to this statement is given in some detail.

The deflections and consequent strains for any dynamically loaded structure can be considered to be composed of two components, a quasi-static component and an oscillatory dynamic component. The quasi-static component is the deflection or strain that would exist at a particular instant if the loading existing at the same instant were to be applied to the structure as a static load. The dynamic component is oscillatory and has a net value near zero when integrated over a cycle of vibration of the structure. It is due to the inertia effects of the structure. Thus the

109

average value of strain or displacement integrated over a cycle or so is very nearly the strain or displacement that would be developed if the loading existing during the vibration interval considered were applied as a static load.

The average value of the net pressure at the strain gages on the 35-psi responding dome was about 29 psi during the interval from 400 to 450 msec after detonation. During the same interval the average value of indicated strain was about 0.00095.

TABLE 5.4 DEPARTURE OF INSTRUMENTED SMALL CIRCLE
FROM CIRCULARITY

Time after Detonation, msec	350	380	400	413	450
$\dfrac{\delta_{si}}{\delta_{ci}}$	−0.22	−0.48	−0.47	−0.55	−0.40
$\dfrac{\sigma_b}{\sigma_c}$ (c = $2\frac{1}{2}''$)	0.001	0.002	0.002	0.002	0.002

Now, although the partition of membrane stress between the α and β directions is not known, their sum can be computed without ambiguity. Thus:

$$\sigma_\alpha + \sigma_\beta = PR/h \tag{5.4}$$

Where: P is a static pressure
R is the dome spherical radius
h is the dome thickness

For 29 psi, the computed value is

$$\sigma_\alpha + \sigma_\beta = 2,070 \text{ psi} \tag{5.5}$$

Taking the computed value of 4×10^6 psi for the modulus of elasticity of the shell concrete, the strain recorded would indicate an average concrete stress in the meridianal direction of

$$\sigma_\alpha = 3,800 \text{ psi} \tag{5.6}$$

Thus an average σ_β stress of 1,730-psi tension is indicated.

Neither theory nor the deflection records obtained admit this tension stress. Further, the theory indicates that the average compression stress, σ_α, should be on the order of 200 to 300 psi.

The strains measured on the 70-psi dome indicate apparent errors of the same order of magnitude.

Four possible explanations for the high apparent strains were considered:

1. A strain concentration factor introduced by the cavity left in the concrete for installation of gages on the bars. The cavity was subsequently grouted.

2. Erroneous calibration factor.

3. Erroneous identification of the records; that is, that the records were actually of the gages placed parallel to small circles of constant α.

4. A local bending of the bars within the grouted cavity.

The first three explanations can easily be eliminated from consideration. Even if the extreme circumstances of zero grout resistance (open hole) and infinite bond stress between the bar and concrete at the edge of the cavity are assumed, the theory of elasticity gives a maximum strain concentration factor of two in the bar. This is considerably smaller than required to reconcile the data.

110

The calibration equipment was carefully checked before and after test; also, the calibration resistor values have been checked and found to be correct.

The ranges within which the several strain gages actually recorded were as agreed on before test. Thus, it must be concluded that the strain gages were correctly calibrated.

Complete field notes were kept of the placement of each gage. If it be assumed that the strains recorded were actually developed parallel to the instrumented small circle, the values obtained are higher by a factor of 60 percent than the maximum values which could have been developed by the external pressure. The weight of evidence indicates that the strain records were correctly identified.

It appears that the only likely explanation for the high apparent strains is that a column action occurred in the bars which produced a high local bending stress superimposed on the axial stress. The method of mounting the strain gages was conducive to development of local bending stresses; the flat spot milled on the bar for attachment of the strain gages introduced a slight eccentricity which would result in bending-induced compression stress at the gage. Also, a two- or three-inch length of bar at the gage was wrapped with electrical insulation. The insulation was soft enough to allow the bar to deflect laterally a slight amount without meeting appreciable resistance.

Assuming the bar to be a fixed end column of length l, and diameter d, the deflection δ_0, due to a bending strain ϵ_b is given by

$$\delta_0 = \frac{1}{\pi^2} \epsilon_b \frac{l^2}{d} \tag{5.7}$$

If the length of the bar is taken as 6 inches and the bending strain as the maximum measured total strain, about 0.001, the necessary lateral deflection is only about 0.007 inch. For a more realistic assumed effective length of bar, about 3 inches, the necessary lateral displacement is about 0.002 inch.

Milling the flat spot on the bar introduced an eccentricity on the order of 0.02 inch. Thus the deflection in the short length would have to be only a fraction of the eccentricity introduced by milling to account for the high measured stress. However, it also can be shown that for small eccentricities

$$\frac{\epsilon_b}{\epsilon_c} = \frac{\pi^2}{2} \ (e/d) \tag{5.8}$$

Where: ϵ_b is the unit strain due to bending
       ϵ_c is the unit strain due to direct compression
       e is the eccentricity of loading
       d is the bar diameter

This formula is valid for cases where

$$\sec \sqrt{\epsilon_c} \ \frac{l}{d} \simeq 1 + \frac{\epsilon_c l^2}{2d^2} \tag{5.9}$$

Substitution of the appropriate parameters into the formula yields

$$\frac{\epsilon_b}{\epsilon_c} \simeq 0.2 \tag{5.10}$$

which is far too low to account for the observed effects. Thus, we can conclude only that we do not know the causes of the high apparent strains and attempt to determine the magnitude of the error by indirect means.

111

Since all bars were milled with the same jig, the error introduced was fairly constant for all gages. However, since the error is extremely sensitive to the geometry of the milled flat, it cannot be estimated with any accuracy. Had only a single gage mounted parallel to the instrumented small circle functioned, it would be possible to determine both the partition of membrane stress and to make an accurate estimate of the magnification factor introduced by the eccentricity.

An estimate of the magnification factor will be useful in interpreting the shear strain data. Referring to Table 5.3 it is seen that during the interval between 400 and 450 msec after detonation the average of the estimated partition of membrane stress is 23 percent in the σ_α direction and 77 percent in the σ_β direction. The average value of posttest predicted deflection at Point i is quite good in the interval between 400 and 450 msec after detonation. Therefore, the 23 percent factor can be used with a fair degree of confidence. Taking the previously computed value of $(\sigma_\alpha + \sigma_\beta)$, 2,070 psi, we estimate the actual σ_α stress as 480 psi. Then, since the average stress indicated by the strain gages during the same interval is 3,800 psi, we obtain an estimated magnification factor of 7.9.

5.2.7 <u>Measured Shear Strains at Foundation.</u> The shear strain records suffer from the same shortcomings as the axial strain records discussed in Section 5.2.6. No definite conclusions can be drawn. However, by making use of the magnification factor estimated in Section 5.2.6, an approximate comparison of interest can be made. The loading experienced by the domes differed markedly from the anticipated loading. In particular, there was a fairly high sustained average load on the windward half of the dome and only a small sustained average load on the leeward half. It is shown in Section 5.2.9 that under these conditions ideally the maximum shear occurs at $\theta = \pm 45$ degrees while ideally the shear at $\theta = \pm 90$ degrees, the gage locations, is zero. For a load similar to a wind load, maximum shear occurs at $\theta = \pm 90$ degrees.

The gage records obtained enable a comparison of the shear stress developed at $\theta = \pm 90$ degrees with the estimated shear stress at $\theta = \pm 45$ degrees. To measure shear strain, four gages connected in a bridge circuit were used, two mounted on tension bars and two mounted on compression bars. If it is assumed that the eccentricity induced by the milled surface would not increase the measured tension strain, the net magnification factor would be $(m + 1)/2$, where m is the magnification factor for the compression bar. However, we have seen in the previous section that the lateral displacement was only a fraction of the initial eccentricity. Under these conditions the magnification factor for tension would be nearly equal to that in compression. Accordingly, we use the factor of 7.9 estimated for compression unchanged for shear.

During the interval between 400 and 450 msec after detonation, the average shear strain at Points n and p was about 0.0006. Taking the shear modulus for the concrete as one half the modulus of elasticity, the apparent shear stress is computed to be 1,200 psi. Applying the magnification factor of 7.9, the estimated actual shear stress is computed to be $\tau_{90} = 152$ psi.

In Section 5.2.9 it is shown that, based on the assumption that the windward half of the dome is uniformly loaded and that the leeward half is unloaded, the shear stress at $\theta = \pm 45$ degrees is given with less than 5 percent error by

$$\tau = \frac{PR}{h} \frac{\sec^4(\phi/2)}{4} \tag{5.11}$$

At the foundation this becomes

$$\tau = 0.18 \, PR/h \tag{5.12}$$

During the interval of interest the average value of net pressure on the windward half of the dome was 29 psi. Thus the average value of shear stress at $\theta = \pm 45$ degrees during this interval is estimated to be

$$\tau_{45} = 370 \text{ psi} \tag{5.13}$$

112

and the ratio of stress at $\theta = 90$ degrees to that at 45 degrees is computed to be

$$\frac{\tau_{90}}{\tau_{45}} = 0.41 \tag{5.14}$$

This appears somewhat high but not unreasonable. The ratio indicates that within the range -90 degrees $\leq \theta \leq 90$ degrees, the shear component varying along the foundation as $\sin \theta$ is 41 percent of that varying as $\sin 2\theta$.

One further comparison can be made to emphasize that the indicated shear strain is nearly an order of magnitude too high. For the dome uniformly loaded on its windward half and unloaded on its leeward half, the net component of foundation shear in the direction of blast is given by:

$$V = \frac{\sqrt{2}}{\sqrt{3}} \sec^4 (\phi_0/2)\ PR^2 \tag{5.15}$$

$$V = 0.340\ PR^2 \tag{5.16}$$

For P taken as 29 psi

$$V = 1,330,000 \text{ pounds} \tag{5.17}$$

At the indicated shear value of 1,200 psi, the 6-inch-thick shell has a shear resistance of 7,200 lb/in of circumference. Thus at this stress level the entire horizontal component of force resisted by shear could be carried in two bands 7 feet 3 inches wide, one centered on each side of the dome at the points where the $\theta = \pm 90$ degrees meridians intersected the foundation. This is only 10 percent of the foundation circumference.

5.2.8 <u>Foundation Acceleration Effects</u>. The acceleration records obtained showed little more than a random series of acceleration pulses of short duration. Peak values were about eight gravity units at the 70-psi dome. Even if these accelerations were transmitted through the foundation to the dome shell undiminished in intensity, they would produce inertia force effects on the order of 4 psi maximum. This effect is small enough to neglect in design.

5.2.9 <u>Estimate of Partition of Membrane Stresses Along the Prime Meridian</u>. Reference 24, Section 79 gives a method which is applicable for determination of the partition of membrane stresses along the prime meridian for the case of a dome uniformly loaded over its windward half and unloaded over its leeward half. The solution obtained is in the form of an infinite series but less than 5 percent error is introduced for domes of 90-degree central angle if only the first term is retained. Along the prime meridian the simplified formula is most conveniently expressed in terms of the angle ϕ. Thus:

$$\sigma_\alpha = \frac{PR}{h} \frac{\tan^2 (\phi/2)}{\sin^2 \phi} = \frac{PR}{h} \frac{\sec^4 (\phi/2)}{4} \tag{5.18}$$

Where: P = uniform pressure on windward half of dome
R = spherical radius
h = shell thickness

A reasonable estimate for the magnitude of the σ_α stress for nonuniform loading over half the dome can be made by averaging the pressure over the dome and computing the stress induced by the average pressure. Investigations carried out on Contract AF 33(616)-2522 (Reference 1) showed that the difference between the actual point pressure and the average pressure was carried almost entirely by the σ_β stress, the σ_α stress resisting less than 5 percent of this pressure.

113

CONFIDENTIAL

Reference 24 shows also that for 90-degree central angle domes the shear stress at the spring line for a dome uniformly loaded over its windward half and unloaded over its leeward half is given with less than 5 percent error by:

$$\tau = \frac{PR}{h} \frac{\tan^2 (\phi_0/2)}{\sin^2 \phi_0} \sin 2\,\theta \tag{5.19}$$

Thus for $\theta = \pm 90$ degrees, the points at which the shear gages were mounted, this formula indicates zero shear, the maximum occurring at $\theta = \pm 45$ degrees.

5.2.10 Estimates of k_d Factor. The survival and failure data of the reinforced-concrete domes exposed to this test permit establishment of definite limits on the value of the k_d factor for a 50-foot spring-line-diameter 90-degree reinforced-concrete dome exposed to the type of

TABLE 5.5 POSTTEST COMPUTATION OF k_d FACTORS

Dome, all 50 foot ϕ		Average σ_c 24 June 1957	P_σ Actual	P_d Actual	Performance	k_d		k_{dd}	
inches	psi	psi				<	>	<	>
24	70	4,400	70	470	Survived	6.85	—	1.02	—
24	35	4,100	40	150	Survived	10.6	—	2.91	—
6	70	3,550	70	470	Failed	—	1.42	—	0.21
6	35	4,050	40	150	Failed	—	2.83	—	0.76
6	20	4,550	20	65	Survived	6.30	—	1.95	—

blast waves obtained in a nuclear explosion over soil similar to that existing at the Nevada Test Site.

The relationship defining k_d is

$$h = k_d \frac{P_\sigma R}{2\sigma_c} \tag{5.20}$$

Where: P_σ is peak overpressure
h is the shell thickness
R is the spherical radius
σ_c is the ultimate strength of the concrete

Thus we can write

$$k_d = \frac{2\sigma_c h}{P_\sigma R} \tag{5.21}$$

The preponderance of the dynamic pressure effects on the test structures leads to an alternate definition:

$$k_{dd} = \frac{2\sigma_c h}{P_d R} \tag{5.22}$$

Where: k_{dd} = dynamic factor based on peak dynamic pressure
P_d = actual peak dynamic pressure

k_d and k_{dd} factors computed with these formulas are given in Table 5.5.
The ultimate concrete strengths on the day of test have been estimated from the data contained in Table 3.5. Estimated strengths are tabulated in Table 5.5.

114

CONFIDENTIAL

5.2.11 Aluminum Dome Failures. The failure of the 1-inch-thick aluminum ɔ ιe was not predicted, although an examination of several factors influencing the behavior of ᴉ ɔ dome shows that the failure could have been expected. The first reason is the undisputable eʋ ɔnce of poor workmanship shown by the failure. Although the dome was badly deformed by the ιast, all ruptures in the shell, except for one relatively short tear, followed along the shop- ʋ led seams. Also, the 7-inch-diameter spuds butt-welded into the shell to support the pressuᴙ ;ages failed by punching shear. The welding was obviously improperly done. For example, oꞎ ᴛhe circumferential seam joining the shell to the base plate, there was one section, about a y: ·d long, where the weld penetration was no more than 50 percent of the plate thickness. The orꞌgʋ ιl vee of the plate was plainly visible for the center half of its thickness in this region. At ɔᴛᴎᵉ points along the shop welds, including one complete radial seam, the welds apparently separaꞌ ꞓ between the individual beads. On the other hand there were no failures along any of the field ʋ ·ds.

A second factor which could have influenced the behavior of the 1-inch-thick ;ᴉᵤ.. ɪnum dome was the nearness of the probable maximum blast loads to the critical buckling pᵢ ᴇꞩ. ɪre. The critical buckling pressure of the 1-inch dome was predicted by the classical bucꞌꞁɪꞅ ; formula for spheres as 416 psi. However, small departures from true sphericity result in ꞁuch lower critical pressures.

Pressures in excess of 416 psi were measured on the nonresponding concrete do. ιe at the 70-psi region and it is likely that pressures of this order of magnitude would havᵉ a ted on the aluminum domes had they remained standing for the entire blast-loading period. ꝛꝭ ᐟ highest pressure measured on the 1-inch aluminum dome, ᵣecorded as the dome failed earꝉ in the blast loading, was 165 psi. The nominal stress in the shell where this pressure was ᴂꝕ꜠ied may ʰᵉ computed at 14,000 psi, assuming equal biaxial stresses and ᴛhe load applied statically. ꞌʰe static load application is not too bad an assumption because of the high natural ꝼrequᵉꞏncᵧ of the dome. This calculation places the nominal stress in the dome aboᵥᵉ the 13,000 ꝧꞅi yield point of the aluminum plate used for construction and it is a sufficient reaꞩon for the ꞌꜳꞁuᵣe of the dome. Initial fracture appears to have occurred by transverse shear in poorlᵧ ꞷᴂde shop welds.

5.3 FOUNDATION RESPONSE

The 70-psi nonresponding dome had a tangent foundation 6 feet wide. Aveᵪ_ net pressure on the windward half of this dome ranged from about 250 psi to 75 psi during thᴇ 50-msec interval between 315 msec to 365 msec after detonation.

During this period the average soil pressure varied between at least 55 ksᵢ ᴂ ꝺ 16.4 ksf and the estimated peak soil pressure varied between 115 ksf and 35 ksf. These valu ꞩ are at least ten times higher than ordinarily used for conventional design in soils somewhat ꞁmilar to Frenchman Flat soil and three times higher than used previously in nuclear test .,

The modified Meyerhof theory indicates that at an angle of internal friction oꞌ 42 degrees (average for Frenchman Flat) and concentric load at 70-psi overpressure, the ᴜ ꞁmate ꞩoil-bearing value should be 210 ksf.

Since the 70-psi nonresponding dome showed no evidence of settlement nor ꞩᴇᵣᵤous distress, it is concluded that the indicated safety factor of between 1.8 and 6 actually exiꞅꞌ ꝺd.

The foundations for the tesᴛ structures cost more than the superstructure. ꞁ ᴜꞧ it is evident that further research and testing of the modified Meyerhof theory is clearly indᵢ꜠.ᴛed. There can be no doubt that potentially great dollar savings for domes and other strucᴛᵣ᷿ ᴜꞩ are offered by establishment of the limits of reliability of the modified Meyerhof theory.

Chapter 6
CONCLUSIONS and RECOMMENDATIONS

Conclusions from the Operation Plumbbob tests of dome and arch structures have been separated into two groups, the conclusions relating to loading, and those relating to response. Recommendations have also been separated into two groups: (1) recommendations for further development of dome and arch design data; and (2) recommendations relating to field testing.

6.1 LOADING CONCLUSIONS

All loading conclusions apply only to NTS terrain conditions except where stated otherwise.

1. For precursor-type blast waves, where the peak dynamic pressure is significantly greater than that given by classical theory, dome and arch design should be based on dynamic pressure rather than overpressure.

2. Pressure-versus-time records measured at corresponding positions on identical domes in the 70-psi region were quite similar. Pressure-versus-time records measured at corresponding positions on identical domes in the 35-psi region, where precursor conditions were more severe, differed significantly although the gages recorded comparable peak pressures before the failure of the thinner dome.

3. No reflection effects were observed on the precursor-loaded domes and arches.

4. During the precursor phase of loading on the domes, the net pressure along a small circle of constant α was nearly uniform at any given instant.

5. During the period of dome loading following the arrival of peak overpressure, the net pressure along a small circle of constant α departed somewhat from a uniform pressure.

6. End effects had a negligible influence on arch loading.

6.2 RESPONSE CONCLUSIONS

1. The nonresponding arches responded sufficiently to indicate the validity of the theoretically obtained conclusion that, compared with domes, arches are inefficient structurally in resisting high drag loading.

2. The cracking at the end walls of the nonresponding arches verified the theoretically obtained conclusion that this joint would have to be ruggedly proportioned and highly reinforced to prevent serious cracking.

3. The theoretical frequency of vibration of dome structures as given in Reference 1 was verified with better accuracy than that to which the physical properties of the construction materials are ordinarily known. Measured frequency varied within ± 4 percent of the frequency computed from measured physical properties.

4. The critical velocity phenomenon was not conclusively verified. The trend exhibited by the data is compatible with the phenomenon.

5. The equivalent static load method of design was verified qualitatively but not quantitatively, that is, the deflection-versus-time curves observed had the same general geometry as those predicted by the equivalent static-load method but the peak values of deflection observed differed significantly from those predicted.

6. The deflection curve of the prime meridian was verified qualitatively.

7. Departure of small circles of constant α from uniform circular displacement was on the order of 50 percent of the circular displacement component. The resulting bending stresses were negligible on the 6-inch-thick, 50-foot-diameter, responding domes.

CONFIDENTIAL

8. The partition of membrane stress appears to have been more nearly equal than predicted in Reference 1, particularly during the short peak dynamic pressure on the 70-psi nonresponding dome.

9. No firm conclusion can be drawn on the ratio of bending to membrane stresses. Probably, the ratio for domes of the radius-to-thickness ratio tested (71.5) is small ($<$ 20 percent). This ratio may have been considerably exceeded just before failure.

10. The test did not subject the domes to a clean shock front and the considerable dynamic effects (factor of 2) associated therewith on the basis of theoretical investigations. No conclusions can be drawn on the reality of the theoretically predicted effects.

11. Ground surface acceleration at overpressure levels of 70 psi and below has negligible influence on dome response.

12. Fortuitous pressure peaks of duration on the order of one half period of dome vibration can induce serious resonance deflections and stresses in domes. This phenomenon will be significant primarily for small domes of the size tested.

13. The 1-inch-thick, 20-foot-diameter, aluminum dome did not fail primarily by buckling, although buckling phenomena undoubtedly contributed significantly to the failure. More research on very thin domes is indicated.

14. The foundation design was conservative as predicted, even though the peak and average bearing values were extremely high by conventional standards. The modified Meyerhof theory appears sound (on the basis of this single test) when applied to friction soil.

15. The prototype door structure design was adequate and not excessive.

16. The simple, yielding hinges provided for the prototype door were quite adequate.

17. The seal between the prototype door and tunnel structure was inadequate. The problem of door seals, in general, deserves further specialized study.

6.3 RECOMMENDATIONS FOR FURTHER DEVELOPMENT OF DOME AND ARCH DESIGN DATA

1. The loading of domes and arches by blast waves is only incompletely understood. Since the thickness and cost of these structures is approximately proportional to the net pressures developed on the structures, it is recommended that loading studies, both experimental and theoretical, be continued by every available means.

2. The phenomenon of buckling of domes under dynamic load should receive a complete theoretical development. It is pointed out in this connection that at the time the investigations were started on the thicker reinforced-concrete domes there existed a substantial number of papers by renowned authorities which indicated that response of domes could be predicted by normal-mode methods and that the normal-mode frequencies would be widely separated as they are in most other structures. After considerable research effort misdirected on the authority of the previous papers, the investigation reported in Reference 1 arrived at the conclusion that dynamically loaded domes vibrated at a single frequency and that normal-mode methods were inadequate for design. The results of the Plumbbob tests conclusively prove the correctness of this conclusion.

Therefore, since thin domes offer a potential solution to the currently pressing problem of missile silo cover design, they should be investigated without too much reliance on previously obtained solutions which, in general, neglect the important factors of dynamic response and initial nonsphericity which is inevitable in actual construction.

3. Response tests of dome structures loaded by clean, sharp-rise blast waves are recommended. Theory predicts that a sharp rise will require an increase of the shell thickness (by a factor approaching 2). These could be conducted, preferably at EPG, using large-diameter domes (the necessary diameter would be a function of the expected rise time) or possibly in the shock tube using optical methods for displacement measurement. At the present state of the art, mechanical and electrical displacement methods are inadequate, even in the 6-foot shock tube.

Further tests, either full scale or properly designed shock-tube tests to measure the partition of membrane stresses, are recommended. If the partition of stress inconclusively indicated by the Plumbbob tests actually exists under a range of loading conditions, the costs of dome structures could be considerably reduced from those indicated by the investigations reported in Reference 1.

5. It is strongly recommended that the modified Meyerhof foundation-capacity theory (which was developed specifically for the tests herein reported) receive a complete theoretical and experimental investigation. If the theory is correct, some of the vaguely defined "dynamic soil properties" previously used to explain high observed foundation capacity can be placed on a sound theoretical basis with consequent dollar savings for actual construction. Further, the introduction of the theoretically important foundation-load, angular-eccentricity factor qualitatively explains wide scatter obtained in previous bearing tests which neglected this important factor.

6. The continuation of basic laboratory and theoretical investigations into the dynamic properties of reinforced concrete is recommended. The very clean separation between the concrete and reinforcing bars observed in the fractured 70-psi and 35-psi domes in the Plumbbob tests has yet to be explained on a rational basis. The exposed bars at the end walls of the arch structures were not similarly clean.

6.4 RECOMMENDATIONS RELATING TO FIELD TESTING

The tests of the reinforced-concrete domes reported herein were based on an adequate, previous theoretical investigation. On the other hand, the very thin aluminum domes were hastily designed on the basis of inadequate theory in order to meet the test-schedule requirements. The results of the tests clearly point out the net results of the two approaches.

Furthermore, the instrumentation provided was inadequate and had to be designed in an extremely short period in order to meet the test schedule. Some of the difficulties that developed certainly could have been avoided had more time been allowed for investigation and reflection on the possible effects of various instrumentation techniques.

Field tests are extremely expensive. They are conducted to obtain information that cannot be obtained in any other way. Ultimately, the only precise data obtained are the instrumentation records. Thus, though field instrumentation is expensive, it is the real reason for the tests and should not be slighted in favor of concrete and steel.

The following recommendation is based on these observations.

1. Future field tests should be designed well in advance of the actual tests. Time, an excess of time, should be allowed for instrumentation design. It if is a military fact that we cannot wait for design before test, it is most certainly an engineering fact that a hastily designed and conducted structure test will result in little usable engineering data regardless of military necessity. It is recommended that the present moratorium on field testing be used to carefully plan and design the next series of tests.

It is pointed out that the entire theoretical investigations conducted prior to the tests reported herein cost the Government less than the cost of field instrumentation and that the success of the tests was due in large degree to this previous research.

2. In future tests of concrete reinforcing, strain gages connected in series should be mounted one on each side of each bar tested, even at the expense of reduction of bar section.

3. All of the strain gages that failed were mounted in the same aspect with respect to the bars. The possibility that polarized electromagnetic effects produced the failures should be investigated and possible shielding methods developed.

Appendix A
NOMENCLATURE

A number of symbols used in this report have more than one meaning. To keep these meanings clear and to simplify location of the definition of the symbols, the symbols have been grouped in four sections:

1. Blast-Wave and Air-Pressure Nomenclature.
2. Dome-Shell-Theory Nomenclature.
3. Foundation-Theory Nomenclature.
4. Miscellaneous Nomenclature.

Units given are those used unless specified otherwise in text.

A.1 BLAST-WAVE AND AIR-PRESSURE NOMENCLATURE

P_σ, peak overpressure, psi

P_d, peak dynamic pressure, psi

P_a, ambient atmospheric pressure, psi

$P_n(\phi, \theta, t)$, net pressure on structure, psi

n_r, Reynolds number

U, shock front velocity, ft/sec

c_d, drag coefficient

c_p, pressure coefficient

c_r, reflection coefficient, clean shock wave

c_r', reflection coefficient, pressure wave

ξ, shock strength $(P_\sigma + P_a)/P_a$

A.2 DOME-SHELL-THEORY NOMENCLATURE

Spring line. The small circle line of contact where the dome shell rests on the foundation.

Prime Meridian. The meridian connecting the crown of the dome with the point on the spring line at which blast pressure first touches dome.

P, uniform static pressure, psi

P_0, a reference pressure, psi

P_σ, peak overpressure, psi

P_d, peak dynamic pressure, psi

$\left.\begin{array}{l}P_s \\ P_s(\alpha,\beta)\end{array}\right\}$ distributed static pressure, psi

$\left.\begin{array}{l}P \\ P(\alpha,\beta,t)\end{array}\right\}$ distributed pressure, time dependent, psi

$\left.\begin{array}{l}P_n, \\ P_n(\phi,\theta,t)\end{array}\right\}$ net pressure on surface of structure, time and space dependent, psi

$\left.\begin{array}{l}F(\phi,\theta;t^*) \\ F(\alpha,\beta;t^*) \\ F(\alpha,t^*) \\ F\end{array}\right\}$ equivalent static load at instant t^*, psi

P_{ESL}, equivalent static load, psi

$\overline{F}$, peak value of equivalent static load, psi

P_W, average pressure, windward face of dome, psi

P_L, average pressure, leeward face of dome, psi

P_{cr}, static critical buckling pressure, psi

R, spherical radius of dome, inches

h, dome-shell thickness, inches

h_s, dome-shell thickness required for static load, inches

D, dome spring-line diameter, feet

w, radial displacement of dome, inches

$w(\alpha,\beta)$, radial displacement of dome due to static load, inches

$w(\alpha,\beta,t)$, radial displacement of dome due to time varying load, inches

$\left.\begin{array}{l}\delta_c \\ \delta_s \\ \Delta_i \\ \Delta_\ell\end{array}\right\}$ radial displacement components defined in Figure 5.26, inches

$H_s(\alpha,\beta)$, harmonic displacement function, static, inches

$H_d(\alpha,\beta,t)$, harmonic displacement function, dynamic, inches

$\left.\begin{array}{l}\phi \\ \theta \\ \alpha \\ \beta\end{array}\right\}$ dome coordinates, see Figure 2.1

ϕ_0, half central angle of spherical dome

β_0, half central angle of small circle of constant α

E, modulus of elasticity, psi

ρ, mass density, lb-sec^2/in^4

C, sound velocity in dome material, in/sec

ν, Poisson's ratio

ω, circular frequency of dome vibration, rad/sec

t, time, variable, seconds

t^*, time, particular instant, seconds

t_a, time of arrival, seconds

t_c, clearing time, seconds

T, period of dome vibration, seconds

τ, time, dummy variable, seconds

U, shock front velocity, ft/sec

U_{cr}, critical velocity of bending waves, ft/sec

σ, unit stress, psi

σ_α, membrane stress along meridian of constant β, psi

σ_β, membrane stress along parallel of constant α, psi

σ_b, bending stress parallel to parallel of constant α, psi

σ_c, compression stress parallel to parallel of constant α, psi

σ_t, rebound tension membrane stress, psi

τ, shear membrane stress, psi

u_c, elastic strain energy per unit volume of concrete, psi

$N_\theta = \frac{1}{2} PR$, unit membrane force, lb/in

N_α, static unit membrane force in direction parallel to prime meridian at points along prime meridian, lb/in

N_β, static unit membrane force in direction perpendicular to prime meridian at points along prime meridian, lb/in

$N_{\alpha/\beta}(\alpha)\max$, the larger value of N_α or N_β occurring at point on prime meridian having coordinate α, lb/in

∇^2, Laplacian operator

V, shear force, pounds

k_s, dimensionless factor appearing in nonuniform statically loaded dome formulas

k_d) dynamic factor. Dimensionless factor appearing in dynamically loaded dome formulas
$k_d ( )$

k_{dd}, dynamic load factor based on peak dynamic pressure

$\left.\begin{matrix} f \\ g \end{matrix}\right\}$ factors defined for brevity in Table 5.3

A.3 FOUNDATION-THEORY NOMENCLATURE

P_σ, overpressure, psi

P_b, ultimate bearing pressure, psi

$\left.\begin{matrix} P_n \\ P_p \end{matrix}\right\}$ normal pressure (see Figure B.1), psi

$\left.\begin{matrix} \tau_b \\ \tau_n \\ \tau_p \end{matrix}\right\}$ shear stress in soil (see Figure B.1), psi

γ, soil density, lb/in^3

ϕ, soil angle of internal friction

Γ, angular eccentricity of foundation loading (see Figure B.1)

$\left.\begin{matrix} \alpha_o \\ \alpha_i \\ \beta \\ \theta \\ \theta_o \\ \theta_i \\ \epsilon \\ \delta \end{matrix}\right\}$ angles, see Figure B.1

r, radius coordinate of logarithmic spiral, inches

Δr, small increment of r, inches

e, base of natural logarithms

$\dfrac{P_b}{P_{bo}}$, factor defined by Equation 2.25 and B.24

A.4 MISCELLANEOUS NOMENCLATURE

l, column length, inches

d, circular column diameter, inches

e, column eccentricity, inches

δ_0, maximum lateral deflection of column, inches

ϵ_c, column axial compression strain

ϵ_b, column maximum bending strain

120

Appendix B
INCLINED-FOUNDATION BEARING CAPACITY

This analysis was conducted to determine reasonable values for foundation bearing capacity. It is a pressure-field theory applicable to statically applied loading. Essentially, it is based on the theories of Meyerhof (References 9 and 10). However, the Meyerhof theory has been extended to include angular eccentricity of the applied load.

The various pressures and angles used in the analysis are defined in Figures B.1 through B.4. The angle of internal friction of the soil, as given by triaxial test, is denoted by ϕ. Cohesion of the soil is neglected in this analysis.

B.1 RELATION BETWEEN P_σ AND P_p

Referring to Figure B.2:

$$\tau_p = P_p \tan \phi \tag{B.1}$$

The summation of the vertical forces must vanish

$$0 = P_\sigma + \tau_p \sec \alpha \sin \alpha - P_p \sec \alpha \cos \alpha \tag{B.2}$$

$$0 = P_\sigma + P_p \tan \phi \tan \alpha - P_p \tag{B.3}$$

$$P_p = \frac{P_\sigma}{1 - \tan \phi \tan \alpha} \tag{B.4}$$

This reduces to:

$$P_p = P_\sigma (1 + \sin \phi) \tag{B.5}$$

B.2 RELATION BETWEEN P_p, P_n, AND θ_o

Referring to Figure B.3 and Reference 20:

$$r = r_o e^{\theta \tan \phi} \tag{B.6}$$

Therefore:

$$\Delta r = \Delta r_o e^{\theta \tan \phi} \tag{B.7}$$

The resultants of the normal forces and shear forces on Arch ab and cd pass through Point O. The shears on Δr_o and Δr_i have no moments about Point O. Since the resultant moment of forces about Point O must vanish:

$$0 = P_n \Delta r_o r_o - P_p \Delta r_i r_i \tag{B.8}$$

$$0 = P_n \Delta r_o r_o - P_p \Delta r_o e^{\theta_o \tan \phi} r_o e^{\theta_o \tan \phi} \tag{B.9}$$

$$P_n = P_p e^{2\theta_o \tan \phi} \tag{B.10}$$

B.3 RELATION BETWEEN θ_o, δ, AND ϕ

From Figure B.1:

$$\alpha_o = 45° + \frac{\phi}{2} - \frac{\delta}{2} \tag{B.11}$$

$$\theta_o = 180 - \epsilon - \alpha_o - (45° - \frac{\phi}{2}) \tag{B.12}$$

$$\theta_o = 90° - \epsilon + \frac{\delta}{2} \tag{B.13}$$

B.4 RELATION BETWEEN P_b AND P_n

Referring to Figure B.4:

$$P_b = P_n \sec^2 \phi + \tau_n \sec \phi \cos \delta \tag{B.14}$$

$$\tau_n = P_n \tan \phi \tag{B.15}$$

$$P_b = P_n \sec^2 \phi (1 + \sin \phi \cos \delta) \tag{B.16}$$

$$\tau_b = P_n \sec \phi \tan \phi \sin \delta \tag{B.17}$$

$$\Gamma = \tan^{-1} \frac{\tau_b}{P_b} \tag{B.18}$$

$$\Gamma = \tan^{-1} \left(\frac{\sin \phi \sin \delta}{1 + \sin \phi \cos \delta} \right) \tag{B.19}$$

or: $\tan \Gamma = \dfrac{\sin \delta}{\csc \phi + \cos \delta}$ (B.20)

B.5 RELATION BETWEEN P_b, P_σ, AND δ

$$\frac{P_b}{P_\sigma} = \left(\frac{P_b}{P_n} \right) \left(\frac{P_n}{P_p} \right) \left(\frac{P_p}{P_\sigma} \right) \tag{B.21}$$

$$\frac{P_b}{P_\sigma} = \sec^2 \phi (1 + \sin \phi \cos \delta) e^{(\pi - 2\epsilon + \delta) \tan \phi} (1 + \sin \phi) \tag{B.22}$$

$$\frac{P_b}{P_\sigma} = \frac{(1 + \sin \phi \cos \delta)}{(1 - \sin \phi)} e^{(\pi - 2\epsilon) \tan \phi} e^{\delta \tan \phi} \tag{B.23}$$
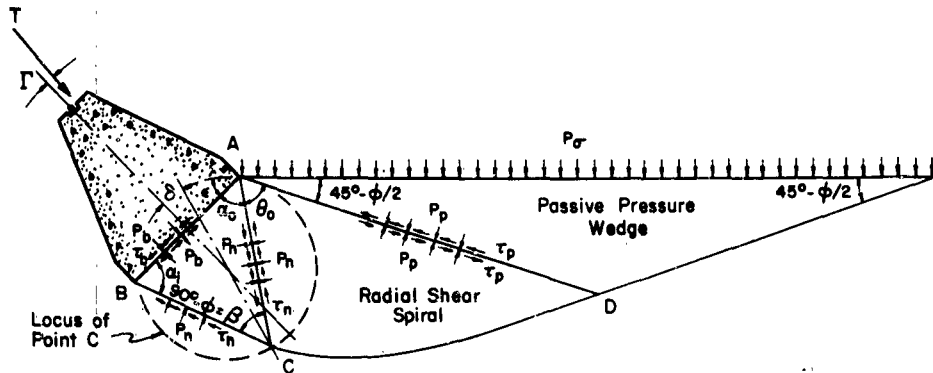
121

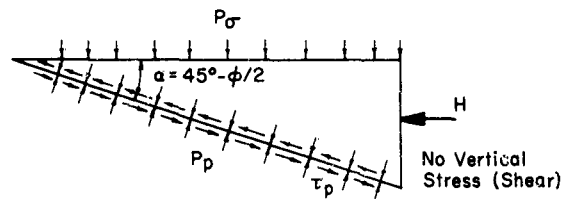Figure B.1   Boundaries of zone of plastic equilibrium.
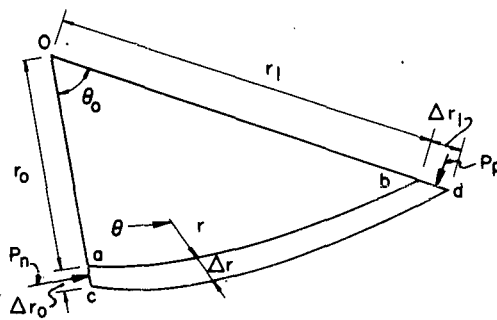

Figure B.2   Passive pressure wedge.

Figure B.3   Radial shear spiral.

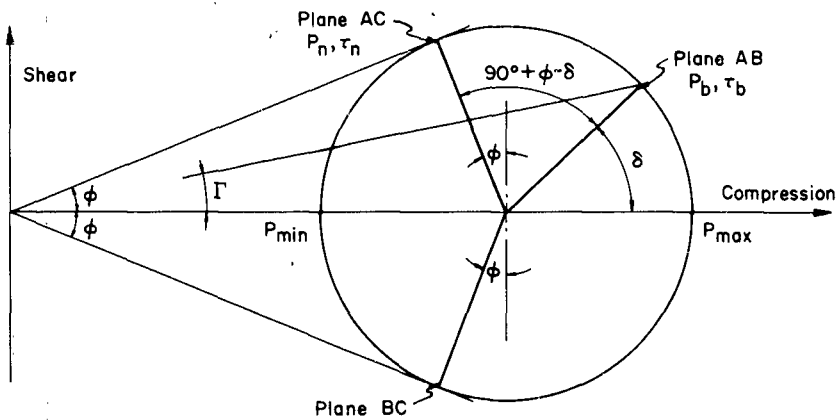Figure B.4   Mohr's circle.

CONFIDENTIAL

B.6 PREPARATION OF FIGURE 2.5

The value of ϕ at the site was believed to range between 40 and 45 degrees. Therefore, a conservative design value of 35 degrees was assumed. Then for a range of values of δ and ϵ, corresponding values of Γ and P_b/P_σ were computed and plotted against each other.

An inspection of Equation B.23 shows that the ratio

$$\frac{P_{b\Gamma}}{P_{bo}} = \frac{P_b(\Gamma)/P_\sigma}{P_b(0)/P_\sigma} \tag{B.24}$$

is independent of ϵ.

123

CONFIDENTIAL

Appendix C
COMPUTATION of k_d

Computation of k_d for the 20-psi responding concrete dome includes all of the effects which must be considered; therefore, this structure has been chosen for illustrative purposes.

The reflection coefficient was originally defined for phenomena measured in a shock tube. The larger portion of data on reflection coefficients was obtained by shock-tube measurements. In a shock tube the relation between static overpressure and dynamic pressure is very nearly the theoretical value.

At the test site the dynamic pressure has been measured at values about six times the theoretical. Though particle velocities within the precursor may be considerably higher than the theoretical value behind the main shock, a considerable portion of the dynamic pressure measured undoubtably has been due to the kinetic energy of the entrained dust.

For purposes of computation, the net pressure during the diffraction phase is taken to be the theoretical value of diffracted pressure plus five sixths of the dynamic pressure (see Section 3.2.1 for more discussion of this point).

A method for computing diffraction pressure due to pressure waves having a linear, finite rise time recently has been presented by Schiffman (Reference 12). This method was used to compute the peak reflected pressure.

Since Formula 2.21 is of the same functional form as the response of a mass-spring system, advantage can be taken of the simplicity of the system to develop simplified methods for solving Formula 2.21. The equivalent mass-spring system can be represented (here F is analogous to the displacement of the mass and $P(\alpha, t)$ is analogous to the so-called static displacement):

$$\ddot{F} + \omega^2 F = \omega^2 P(\alpha, t) \tag{C.1}$$

Taking $P(\alpha, t)$ to be of the form:

$$P(\alpha, t) = P_1 + P_2 \frac{\omega t}{2\pi} \tag{C.2}$$

where P_1 and P_2 are constants (P_1 being the magnitude of the pressure at the instant $t = 0$, and P_2 being the magnitude of the pressure increase during a complete cycle of vibration), a solution of Equation C.1 is:

$$F = P_1 + P_2 \frac{\omega t}{2\pi} + R \sin(\omega t + \phi) \tag{C.3}$$

where R and ϕ are constants. Now,

$$\frac{\dot{F}}{\omega} = \frac{P_2}{2\pi} + R \cos(\omega t + \phi) \tag{C.4}$$

If at time $t = 0$, F and $\dot{F}$ have the values

$$\begin{aligned} F(0) &= F_0 \\ \dot{F}(0) &= \dot{F}_0 \end{aligned} \tag{C.5}$$

the functions F and $\frac{\dot{F}}{\omega}$ have the simple graphical interpretation of Figure C.1.

Thus, if the driving function $P(\alpha, t)$ consists of a series of straight-line elements, the response of the system can be determined graphically by the use of the terminal conditions for each element as the initial conditions for the next.

Figure C.2 shows the computed diffracted form of the rise of the main wave of Figure 3.4 added to half of the static precursor pressure plus five sixths of the dynamic pressure (see Section 3.2.1). The precursor pressure is divided by two, because at the time of the main rise, the static precursor pressure is applied to the entire dome, which is about twice as efficient in resisting this pressure as it is in resisting the diffracted and the dynamic pressures.

Schiffman presented (Reference 12) a formula for computing the reflection coefficient for compression waves impinging on a vertical wall:

$$c_r' = \frac{(2 \xi^{1/7} - 1)^7 - 1}{\xi - 1} \tag{C.6}$$

Where: ξ is the ratio of absolute peak pressure to ambient pressure.

For values of ξ between six and seven, it gives practically the same results as the classical steep shock reflection formula:

$$c_r = \frac{6 + 8\xi}{6 + \xi} \tag{C.7}$$

Therefore, for design of the domes, it was assumed that the reflection coefficients for steep shock fronts could be used for c_r'.

Figure C.2 shows graphically Schiffman's method for constructing the profile of diffraction pressure
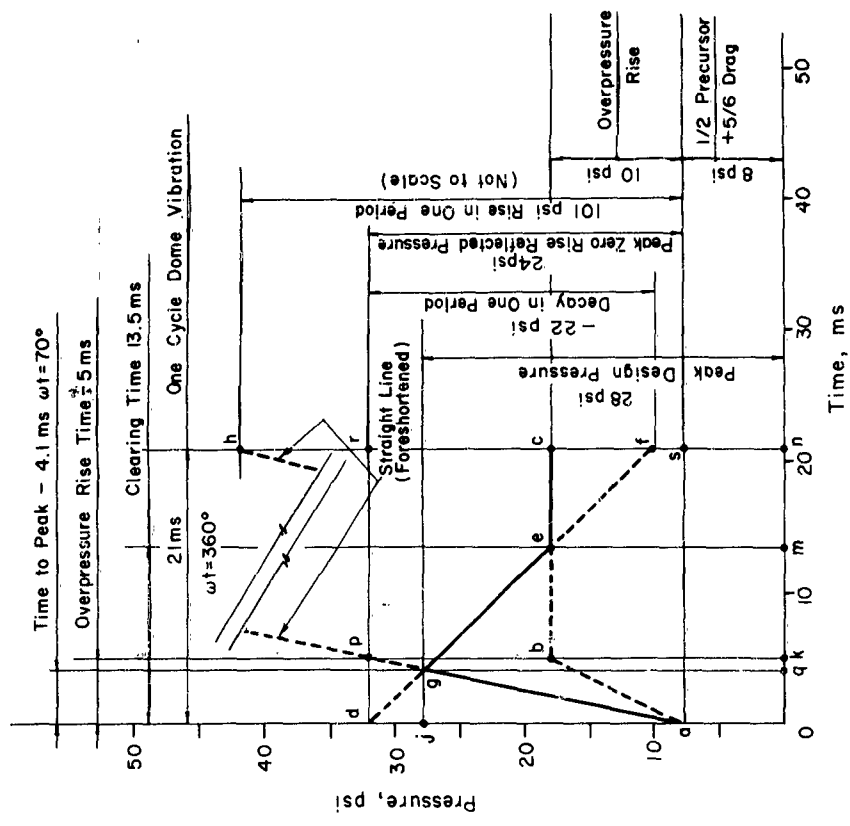
124

Figure C.2 Graphical determination of design wave form. Precursor overpressure, 10 psi; overpressure wave rise, 10 psi; overpressure rise time, 5 msec; dynamic pressure, 53 psi; drag pressure at $\alpha = 50$ degrees, 3.6 psi.
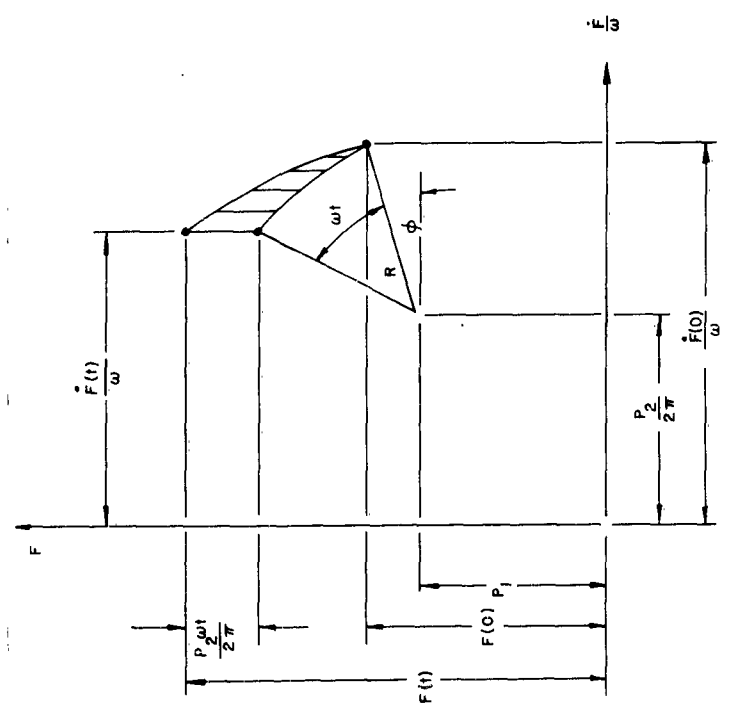

Figure C.1 Graphical representation of Equations C.3 and C.4.

CONFIDENTIAL

versus time. The thickness was computed at $\alpha = 50$ degrees, about 3 feet from the spring line of the dome. This value was adopted throughout the project. It corresponds to about six shell thicknesses for the responding domes and $1\frac{1}{2}$ shell thicknesses for the nonresponding domes. For the latter shells, the design value of α might have been increased to 55 or 60

was omitted as being negligible during the interval of interest.

3. The clearing time (m) and rise time (k) and period (n) were laid off, and the product of sharp rise reflection coefficient and overpressure rise (d−a = 24 psi) was laid off on the pressure axis and the rise-time ordinate above the 8-psi level.

Figure C.3 Gyrogram for determination of k_d.

degrees without seriously reducing the conservatism of the design.

Figure C.2 was constructed as follows:
1. The initial data was:
    Precursor overpressure, 10 psi
    Overpressure wave rise, 10 psi
    Overpressure rise time, 5 msec
    Dynamic pressure, 53 psi (six times ideal)
    Drag pressure at $\alpha = 50$ degrees, 3.6 psi
2. The value of half the precursor pressure plus five sixths of the drag pressure (8 psi) was plotted (0, a). The overpressure rise was plotted above this (a, b, c). Wave decay might have been plotted but

4. The diagonal lines defining peak design pressure were drawn (d, e and a, p) and extended to the one-cycle ordinate (Points f and h).

5. The time (0, q) to peak design pressure (q, g = 28 psi) was measured and converted to degrees, one cycle of vibration being 360 degrees.

6. The pressure differentials corresponding to one cycle of vibration for the pressure peak rise rate (s, h) and decay rate (f, r) were measured.

Figure C.3 shows the gyrogram for determining the maximum value of F, which was found to be 48.5 psi. The significant data obtained from Figure C.2 is shown on Figure C.3. Figure C.3 can best be under-

126

stood by comparison with Figure C.1 and the values obtained from Figure C.2. It was constructed as follows:

1. The initial pressure 8 psi and initial rise note of 101 psi per period or 16.1 psi per radian were laid off as Point A.

2. An arc of 70 degrees was swung about Point A, the radius being length 0A. Seventy degrees is equal to the rise time (4.1 msec, 0 to q of Figure C.2) expressed as a fraction of the dome vibration period (21 msec).

3. The initial rise of the reflected pressure wave, 20 psi (a to j of Figure C.2) was laid off from Point B parallel to the 0F axis. This located Point C.

4. The initial pressure 28 psi and the initial decay note of 22 psi per period or 3.5 psi per radian of the line segment g to e of Figure C.2 were laid off. These coordinates located Point D.

5. Using Point D as the center an arc of radius DC was swung until it intersected the F axis at Point E. The angle EDC was measured and found to be 123 degrees.

6. The angle 123 degrees is equal to wt* expressed in degrees where t* is the time subsequent to time q of Figure C.2 at which the equivalent static load maximizes. The decay during this interval of the peak reflected pressure along the line from g to e of Figure C.2 was computed from the formula

$$\text{decay} = 22 \times \frac{123}{360} = 7.5 \text{ psi}$$

where 22 psi per period was the decay note of the reflected overpressure during the interval q to m of Figure C.2. The decay of 7.5 psi was laid off on the F axis downward (decay is a negative rise) from Point E of Figure C.3, locating Point G.

7. Point G locates the maximum value of the equivalent static load. This was measured (0 to G) and found to be 48.5 psi.

At the instant that the unit force along small circles of $\alpha = 50$ degrees (N_β) reaches its maximum, the unit force, along great circles of constant β, (N_α) is assumed to be 10 percent of the determinate sum $N_\alpha + N_\beta$. Therefore, the unit force N_β is 90 percent of the total.

Denoting the peak overpressure by P_σ, the peak equivalent static load by $\bar{F}$, the dome spherical radius by R, the allowable unit stress by σ, the dome thickness by h, and using the subscripts s and d to represent uniform static and dynamic loading, respectively, and recalling that:

$$N_{\alpha d} + N_{\beta d} = \bar{F}R \tag{C.8}$$

$$N_{\alpha s} + N_{\beta s} = P_\sigma R \tag{C.9}$$

we have

$$h_s = \frac{P_\sigma R}{2\sigma} \tag{C.10}$$

$$h_d = \frac{0.9 \, \bar{F}R}{\sigma} \tag{C.11}$$

Thus

$$k_d = \frac{h_d}{h_s} = \frac{1.8 \, \bar{F}}{P_\sigma} \tag{C.12}$$

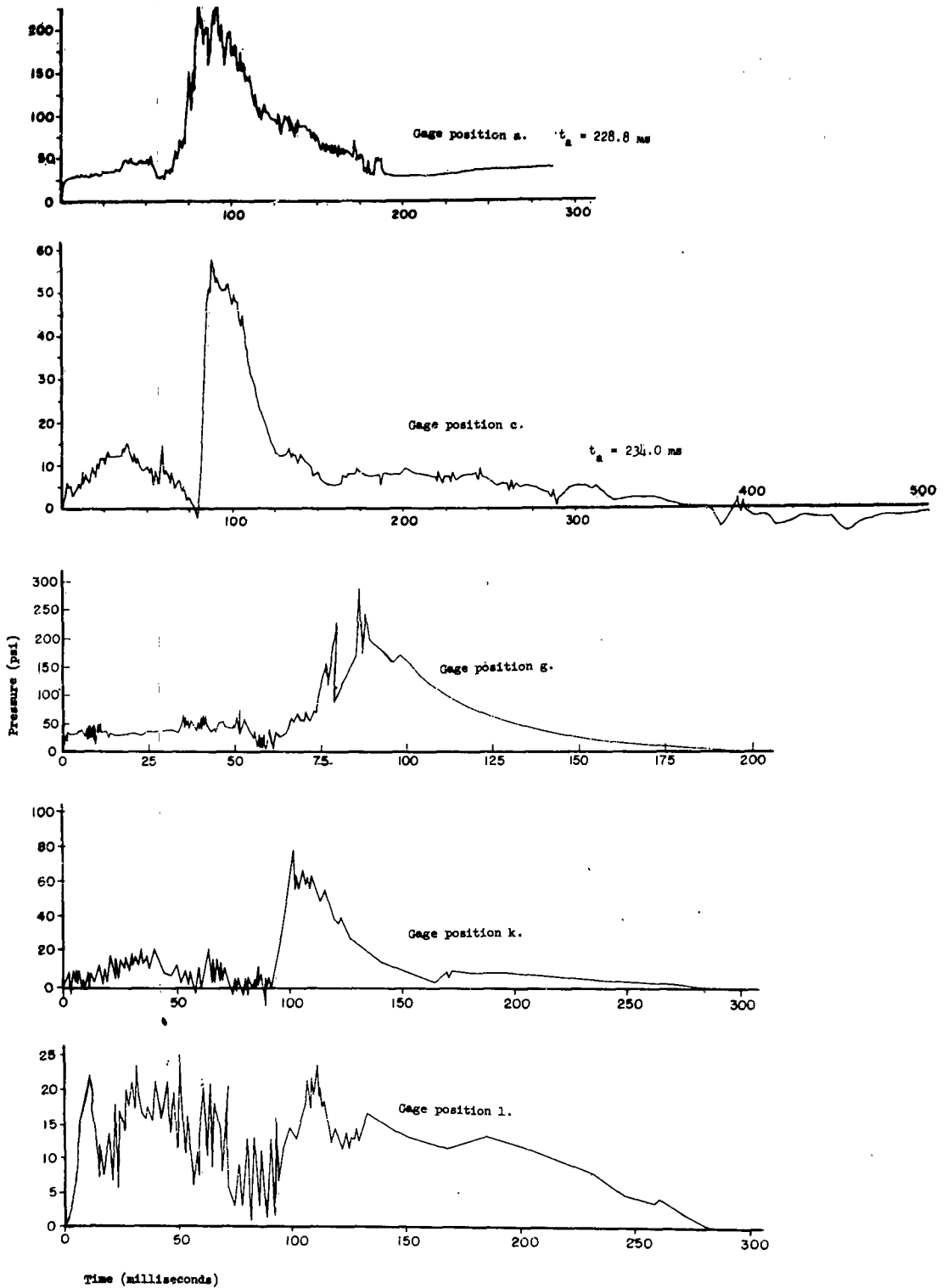For the 20-psi responding concrete dome, k_d was computed

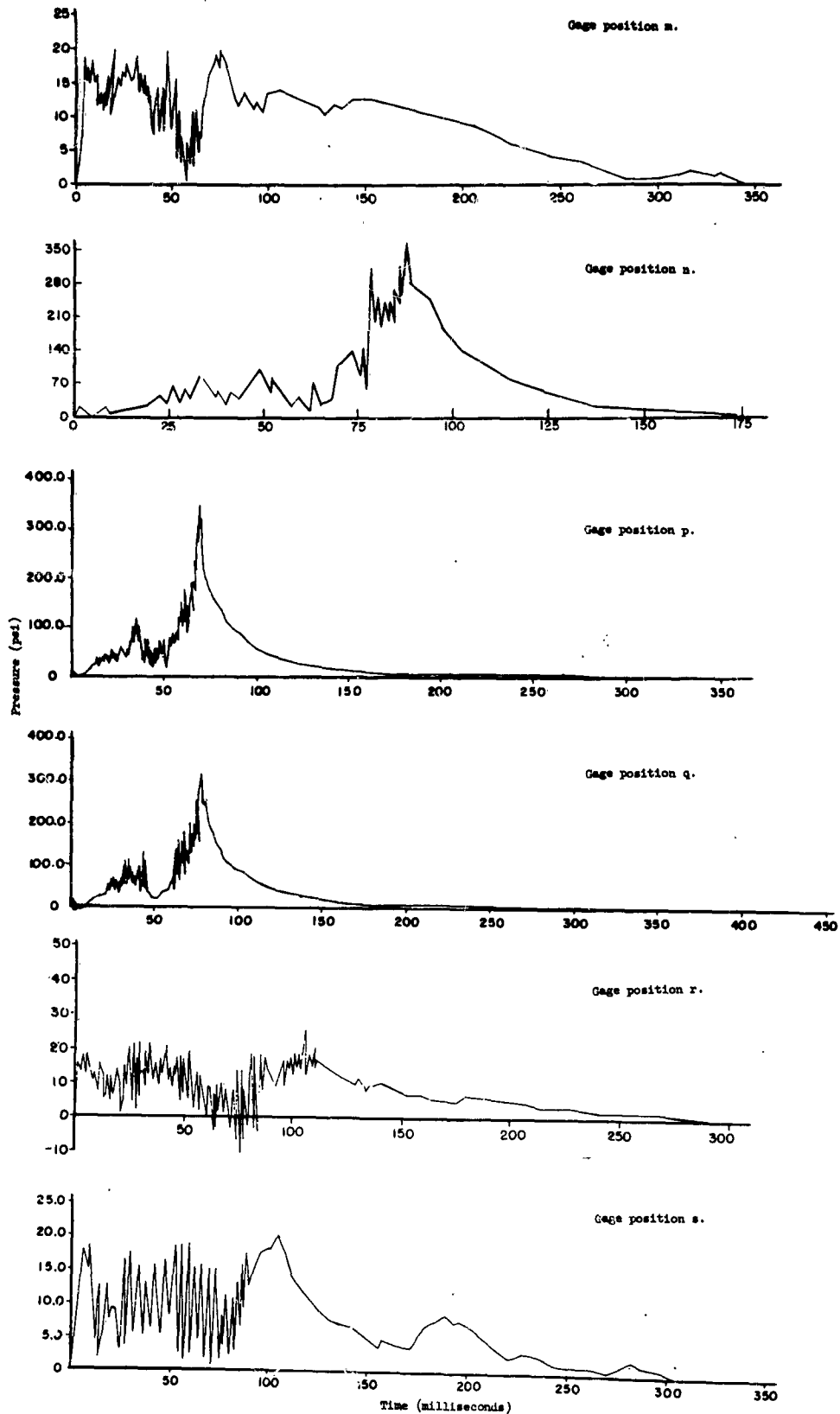$$k_d = \frac{1.8 \times 48.5}{20} = 4.35$$

127

Appendix D
PRESSURE RECORDS

The pressure-versus-time records obtained on the nonresponding domes and arches, the responding concrete domes, and the one-inch-thick aluminum dome are presented in this appendix. Records are listed according to the gage position on each structure and are given for both electronic and self-recording pressure gages. All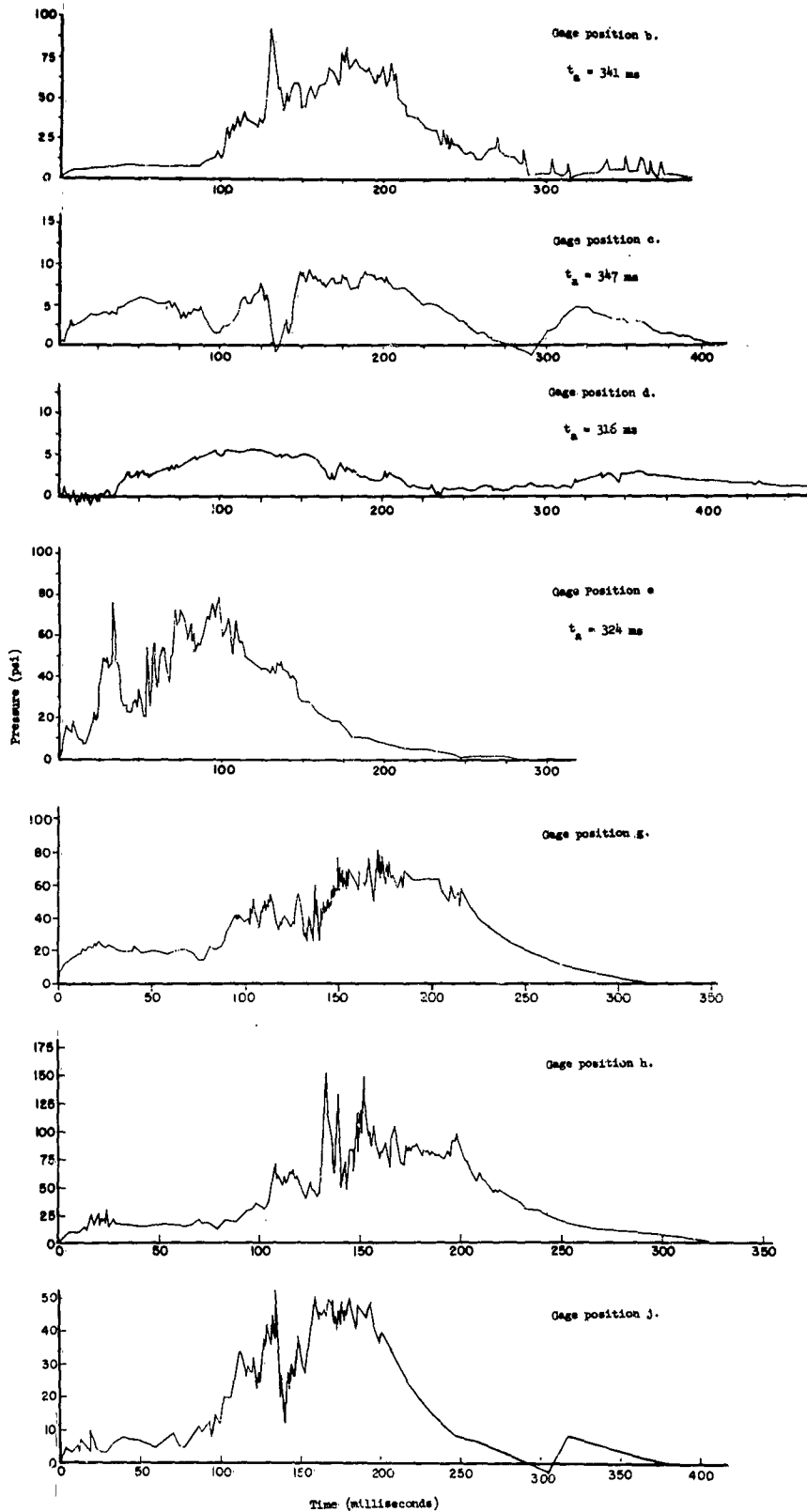 records are plotted on a time base which begins with a zero reference at the first indication of blast-wave pressure on the gage. Zero time on the records from the electronic gages is referenced to the time of detonation of the weapon by t_a, which is the time in milliseconds from detonation to zero time on the pressure record. These records were obtained by the Ballistic Research Laboratories.

128

CONFIDENTIAL

Pressure versus time records obtained on Structure F-3.6-9028.01,
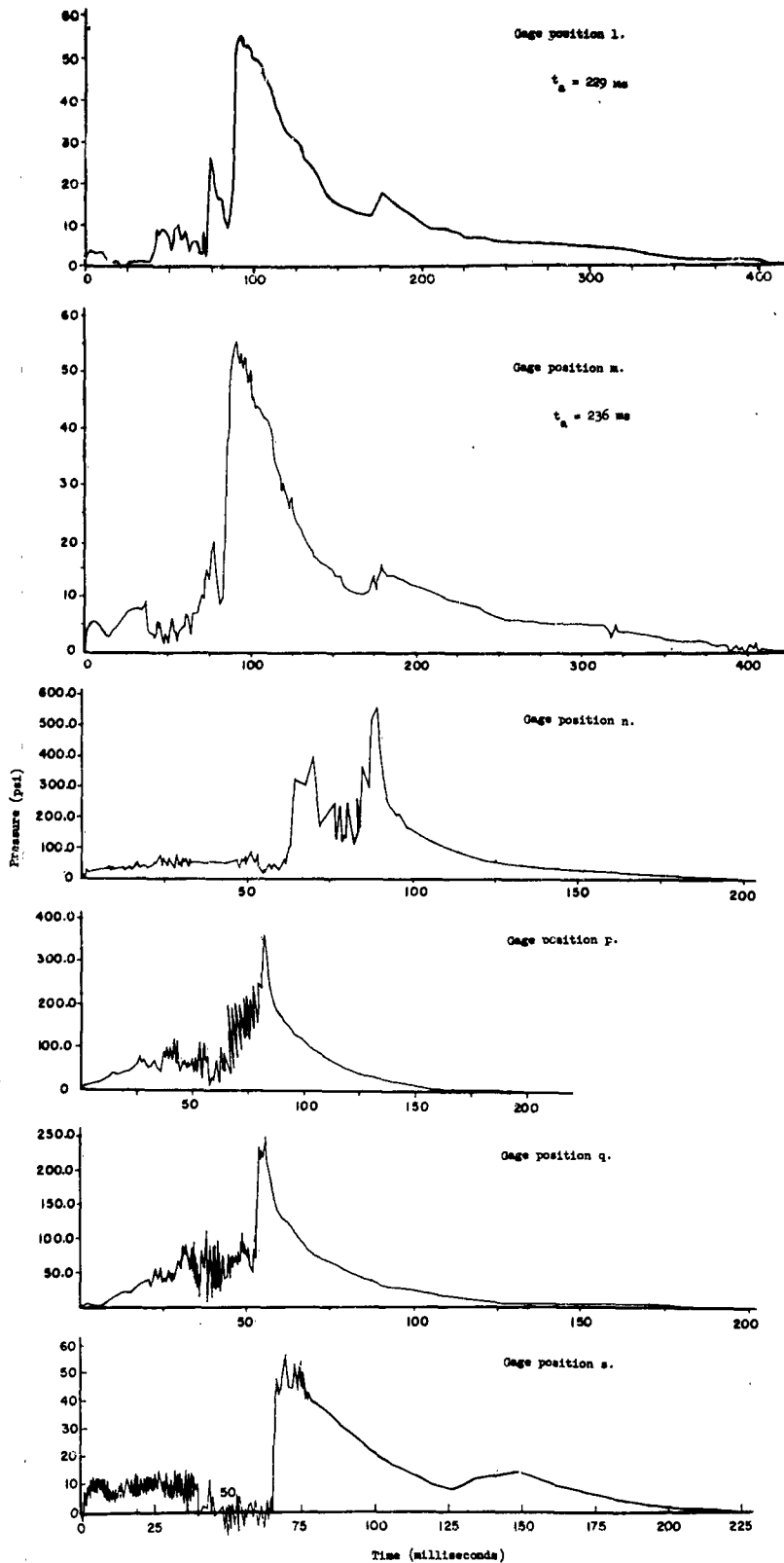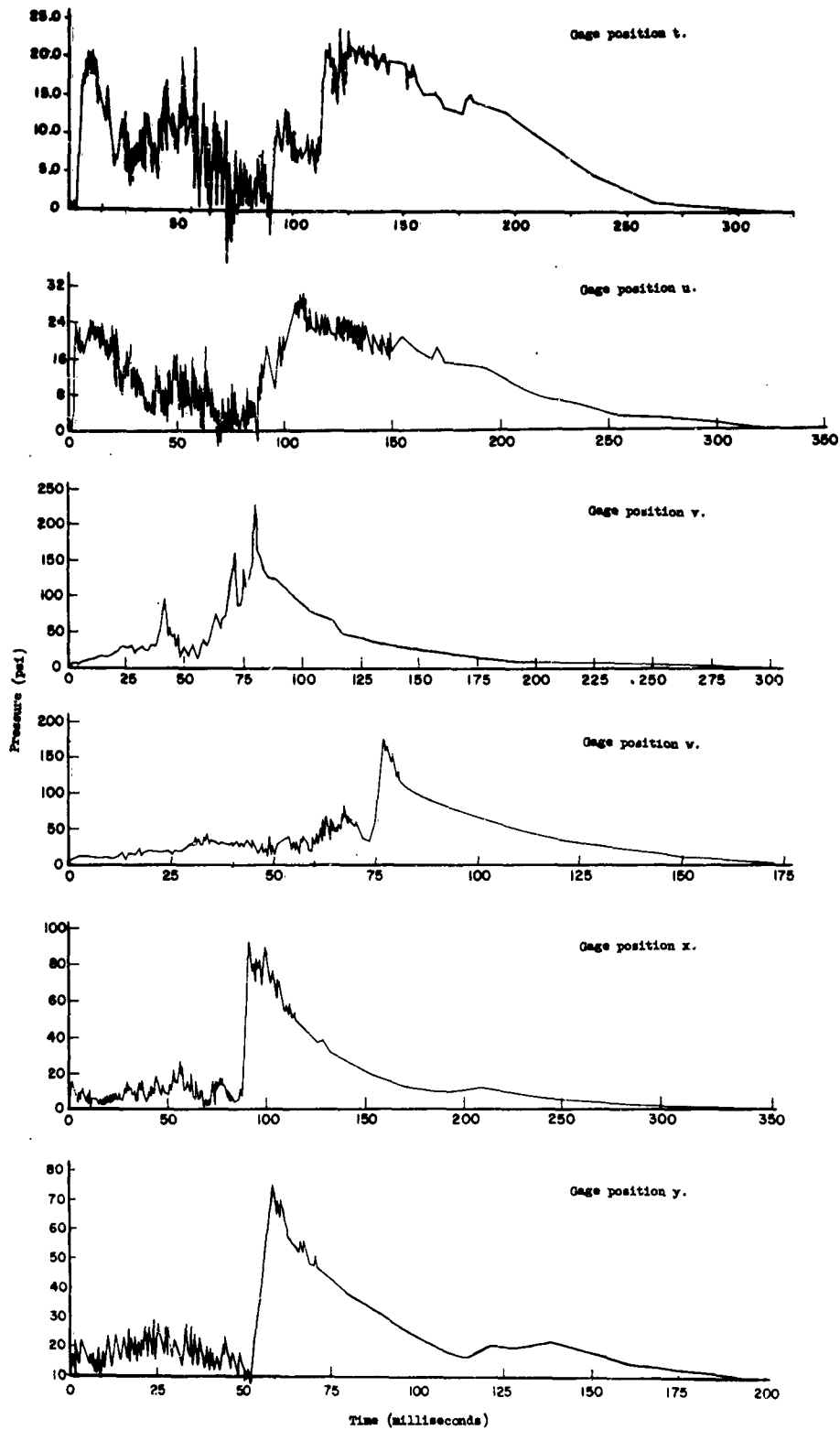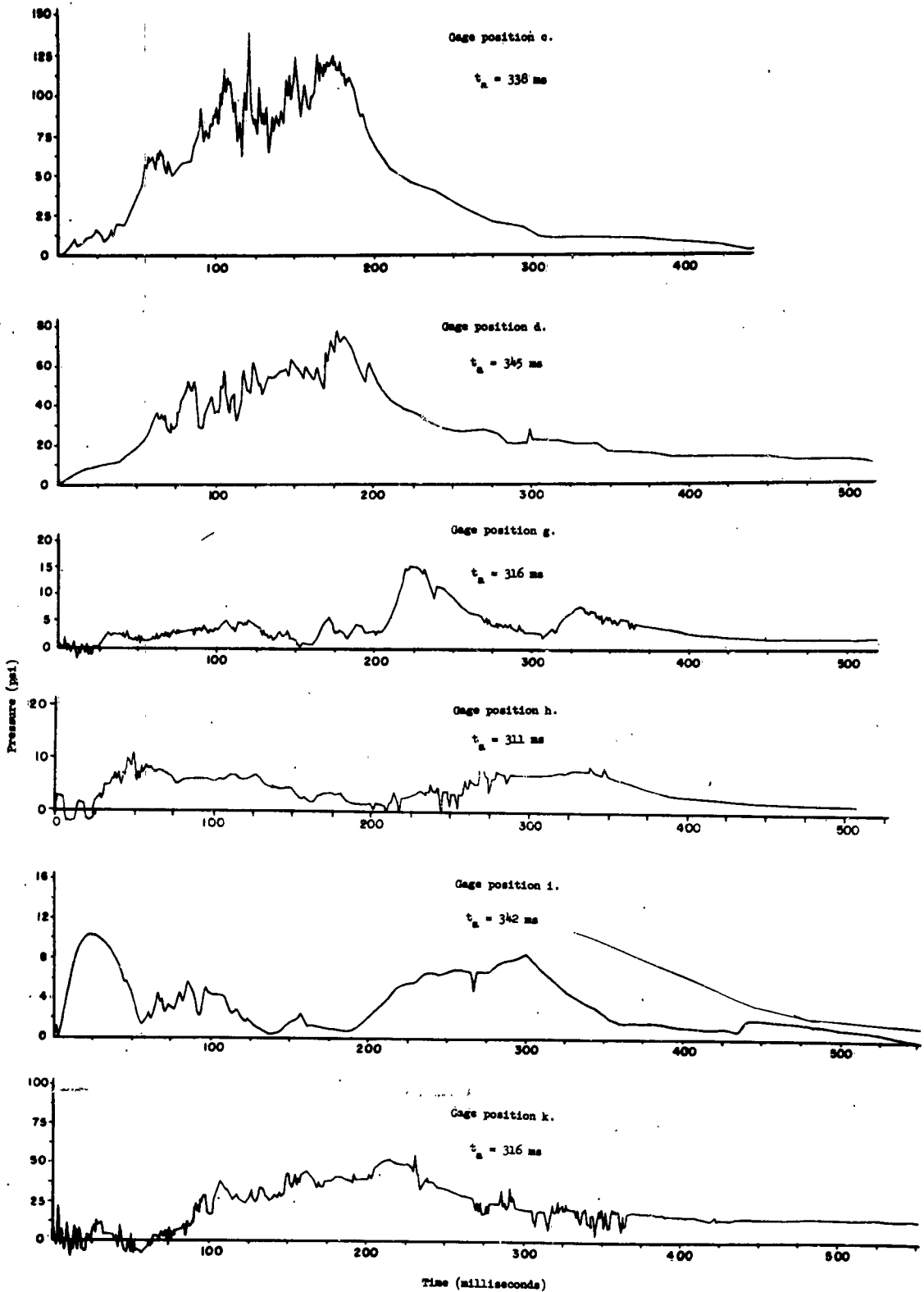reinforced concrete arch, located at the expected 70-psi overpressure
region.

129

CONFIDENTIAL

Gage position m.

Gage position n.

Gage position p.

Gage position q.

Gage position r.

Gage position s.

Pressure versus time records obtained on Structure F-3.6-9028.01,
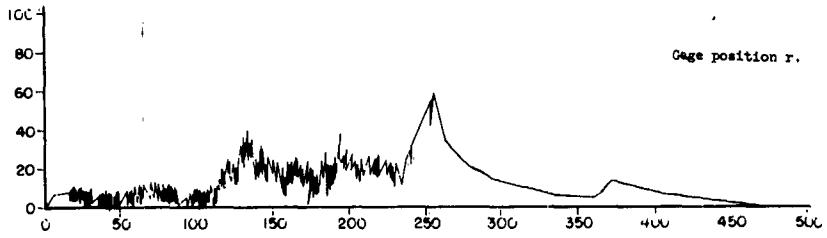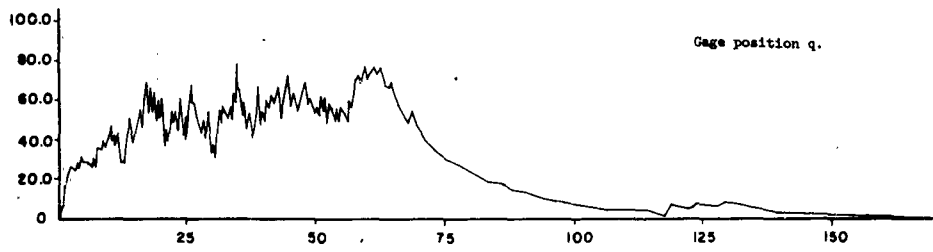reinforced concrete arch, located at the expected 70-psi overpressure
region.

130

CONFIDENTIAL

Gage position b.

$t_a = 341$ ms

Gage position c.

$t_a = 347$ ms

Gage position d.

$t_a = 316$ ms

Gage Position e

$t_a = 324$ ms

Gage position g.

Gage position h.

Gage position j.

Time (milliseconds)

Pressure versus time records obtained on Structure F-3.6-9028.02,
reinforced concrete arch, located at the expected 35-psi overpressure
region.

131

CONFIDENTIAL

Gage position l.

Gage position m.

Gage position n.

Gage position q.

Gage position r.

Gage position s.

Gage position t.

Time (milliseconds)

Pressure versus time records obtained on Structure F-3.6-9028.02,
reinforced concrete arch, located at the expected 35-psi overpressure
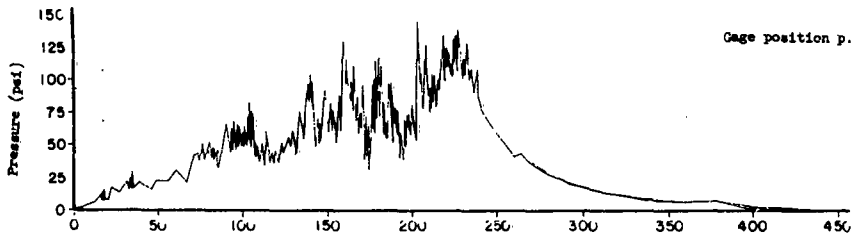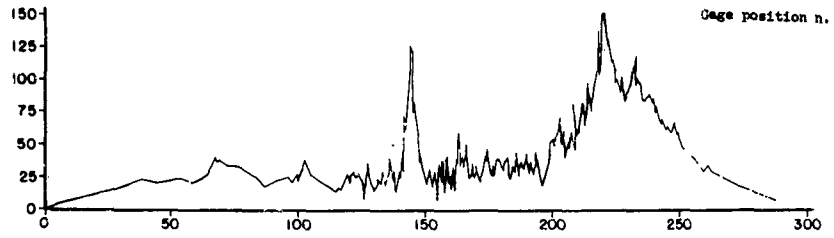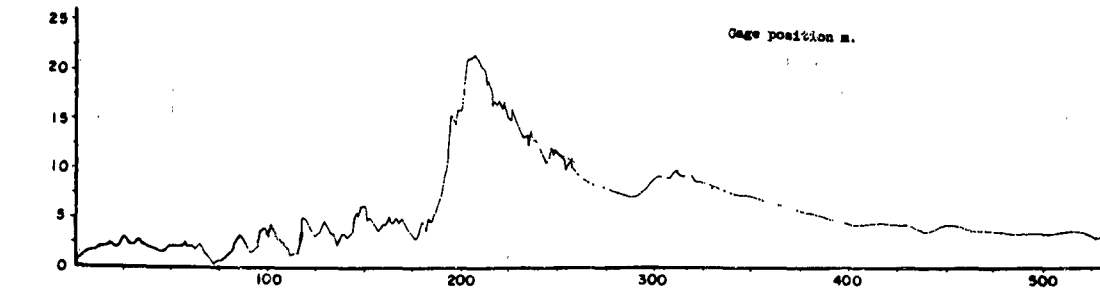region.

132

CONFIDENTIAL

Pressure versus time records obtained on Structure F-3.6-9027.01, 24-inch-thick, reinforced concrete dome, located at the expected 70-psi overpressure region.
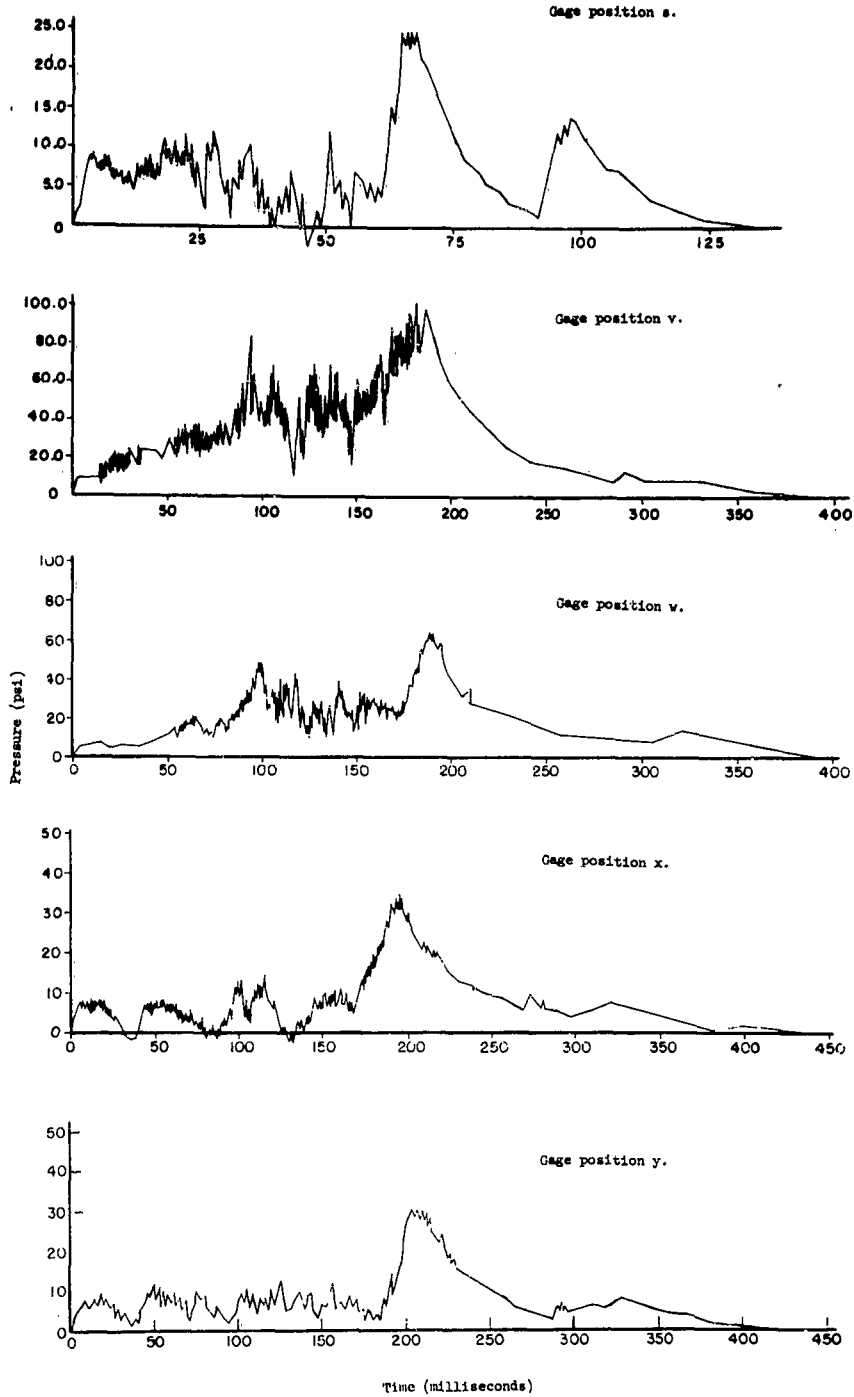
133

Gage position e.

$t_a = 230$ ms

Gage position r.

$t_a = 230$ ms

Gage position g.

$t_a = 232$ ms

Gage position h.

$t_a = 235$ ms

Gage position i.

$t_a = 236$ ms

Gage position j.

$t_a = 228$ ms

Pressure (psi)

Time (milliseconds)

Pressure versus time records obtained on Structure F-3.6-9027.01, 24-inch-thick, reinforced concrete dome, located at the expected 70-psi overpressure region.
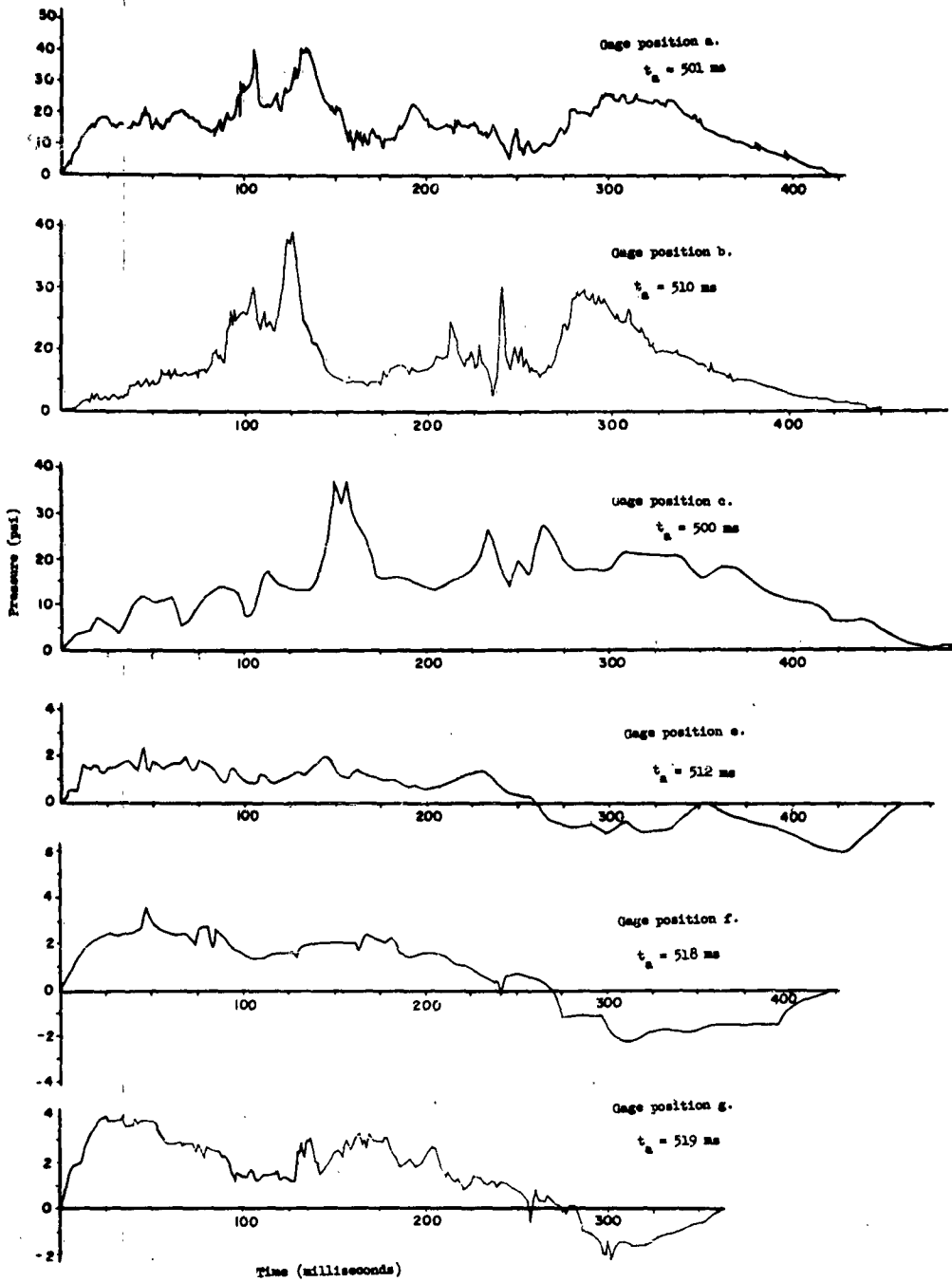
134

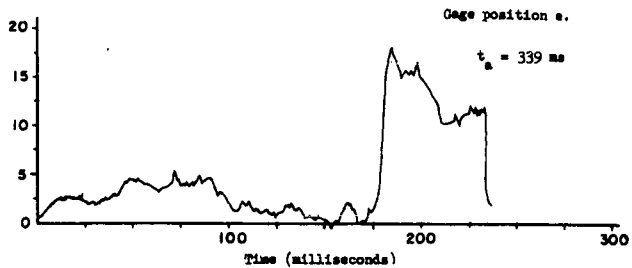CONFIDENTIAL

Pressure versus time records obtained on Structure F-3.6-9027.01,
24-inch-thick, reinforced concrete dome, located at the expected
70-psi overpressure region.

135

Pressure versus time records obtained on Structure F-3.6-9027.01, 24-inch-thick, reinforced concrete dome, located at the expected 70-psi overpressure region.
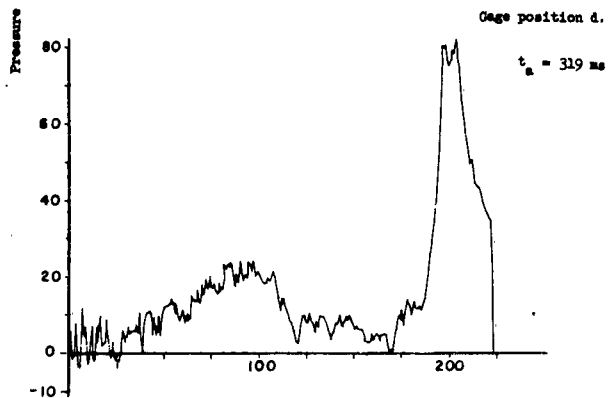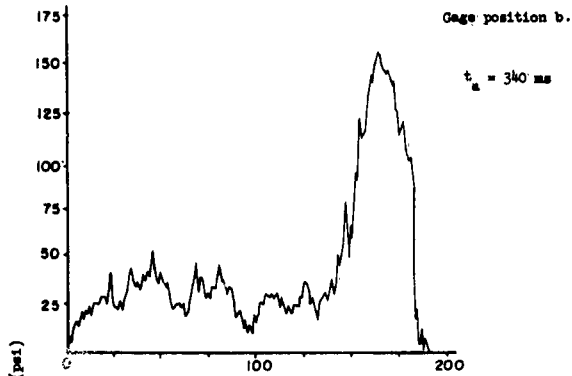
136

Pressure versus time records obtained on Structure F-3.6-9027.02,
24-inch-thick, reinforced concrete dome, located at the expected
35-psi overpressure region.

137

Gage position m.

Gage position n.

Gage position p.

Gage position q.

Gage position r.
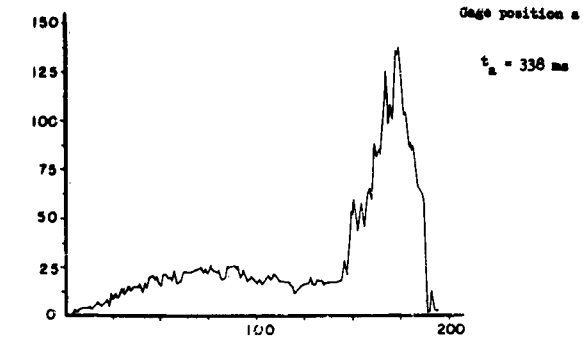
Time (milliseconds)

Pressure versus time records obtained on Structure F-3.6-9027.02,
24-inch-thick, reinforced concrete dome, located at the expected
35-psi overpressure region

138

CONFIDENTIAL

Gage position s.

Gage position v.

Gage position v.
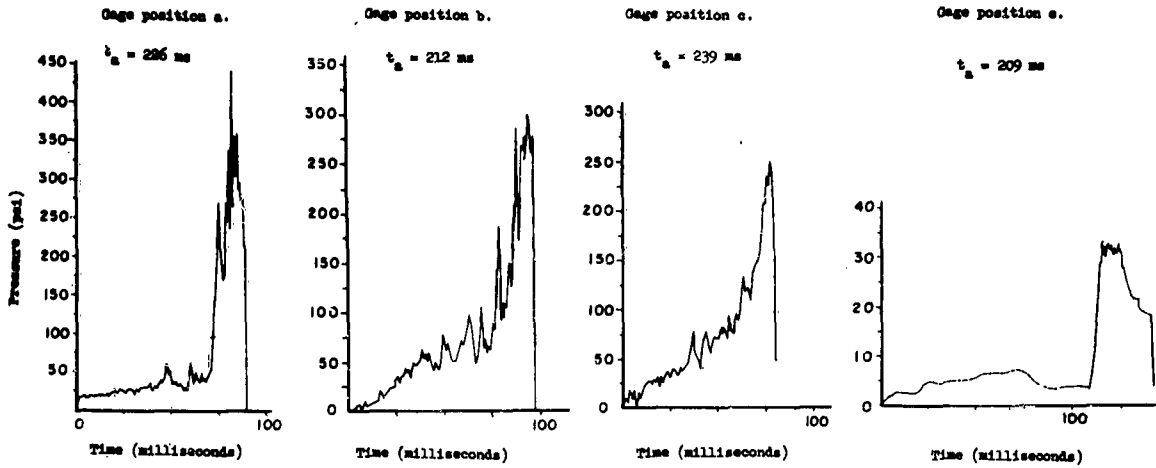
Gage position x.

Gage position y.

Time (milliseconds)

Pressure versus time records obtained on Structure F-3.6-9027.02,
24-inch-thick, reinforced concrete dome, located at the expected
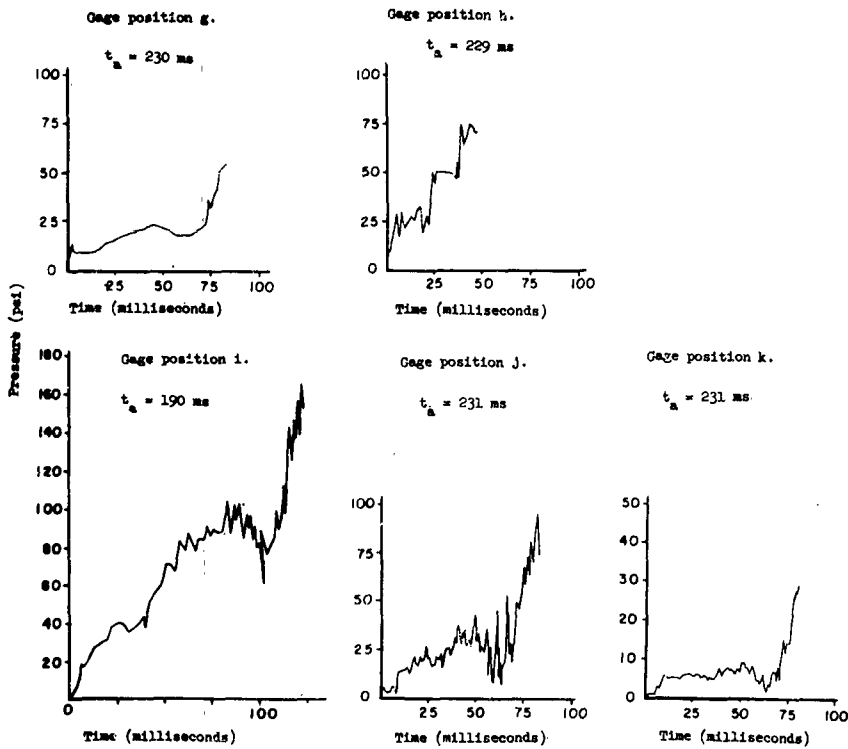35-psi overpressure region

139

CONFIDENTIAL

Pressure versus time records obtained on Structure P-30.1-8001.03, six-inch-thick, reinforced concrete dome, located at the expected 20-psi overpressure region.

140

Pressure versus time records obtained on Structure F-30.1-8001.02, six-inch-thick, reinforced concrete dome, located at the expected 35-psi overpressure region.

Gage position a.

$t_a = 226$ ms

Gage position b.

$t_a = 212$ ms

Gage position c.

$t_a = 239$ ms

Gage position e.

$t_a = 209$ ms

Pressure (psi)

Time (milliseconds)

Pressure versus time records obtained on Structure F-30.1-8001.01, six-inch-thick, reinforced concrete dome, located at the expected 70-psi overpressure region.

Gage position g.

$t_a = 230$ ms

Gage position h.

$t_a = 229$ ms

Pressure (psi)

Time (milliseconds)

Gage position i.

$t_a = 190$ ms

Gage position j.

$t_a = 231$ ms

Gage position k.

$t_a = 231$ ms

Time (milliseconds)

Pressure versus time records obtained on Structure F-3.6-9026.02, 1-inch-thick, aluminum dome, located at the expected 70-psi overpressure region.

142

CONFIDENTIAL

Appendix E
FIELD INSTRUMENTATION for RESPONSE MEASUREMENTS of DOME-TYPE STRUCTURES UNDER HIGH-STRENGTH SHOCK LOADING

Gilbert H. Brittain and Edward H. Scharres, Armour Research Foundation,
Illinois Institute of Technology, Technology Center, Chicago, Illinois

This report describes the instrumentation plan and results for the measurement of deflections and strains in the 6-inch-thick concrete and $\frac{1}{2}$-inch- and 1-inch-thick aluminum dome-shaped structures.

This plan provided for the construction of two recording instrumentation shelters, each to be located inside a nonresponding concrete dome. Since one of these was to be located approximately 1,180 feet from ground zero, the radiation problem was of prime importance. The Armed Forces Special Weapons Project (AFSWP) equipment which was available for this task consisted of Consolidated Electrodynamics Corporation (CEC) oscillograph recorders, and carrier amplifiers manufactured by CEC and the William Miller Corporation.

Since these oscillographs required the use of photographic recording media, extensive tests were made on both Micro-File film and Lino-Writ paper to evaluate the amount of radiation which could be tolerated without obliterating the record. The Lino-Writ paper made it possible to obtain the desired frequency response. It was felt that this recording medium should not, if possible, be exposed to more than 1 r of gamma radiation. An exposure of 10 r of gamma radiation could be tolerated, and the instrumentation shelters were designed by Weapons Effects Tests to reduce the expected radiation to meet the 10 r maximum requirement.

Ruggedized linear potentiometers, manufactured by Colvin Laboratories, were selected for the displacement transducers. These potentiometers covered the range of deflections from 1 inch to 24 inches. Baldwin SR-4 strain gages of the AB-7 and ABFX-11 types were chosen to measure strain and shear. These gages have a bakelite base, and therefore a much higher breakdown potential than the conventional paper-base strain gages.

Special circuitry was designed and fabricated to provide electrical calibration of all the transducers prior to zero time. A sequence timer was designed and built to initiate certain events at times not supplied by the standard timing system. Power transferring equipment was designed and fabricated to change over from field power service to battery power. During the tests the batteries supplied power to the motors driving 110-volt, 60-cps single-phase alternators of sufficient capacity to operate all the instrumentation.

Timing on the records was obtained from secondary frequency standards located in each of the instrument shelters.

At shot time, 73 channels of response instrumentation were in operation. One recorder failed operationally just before zero time, resulting in a loss of six channels not duplicated on other recorders. In addition, one deflection and seven strain channels failed to record at zero time because of gage or circuit failures.

After the main air shock arrival, some high-frequency oscillations, not attributable to vibration of the structures, occurred on many of the record traces. These oscillations were present to a reduced degree in the records from the rear shelter (F731), probably due to the greater distance from ground zero.

No radiation fogging was apparent on the oscillograms. Film dosimeters placed in the instrument shelters showed a maximum of 18 r just below the access hatch in Shelter F730. Dosages at the recorder positions, however, were considerably less than 1 r in both shelters.

Postshot examination of the instrument shelters indicated that the recording instruments and associated control and power equipment withstood the shock phenomena.

E.1 OBJECTIVES

The overall objective of this research program was to determine the effects of high-strength shock waves on several reinforced concrete and fabricated aluminum domes. These structures were designed by the American Machine and Foundry Company (AMF).

The program was part of Operation Plumbbob at the NTS. The testing of the aluminum domes was sponsored by the U. S. Air Force under Operation Plumbbob Project 3.6, and the testing of the three concrete domes was sponsored by the Federal Civil Defense Administration (FCDA) under Operation Plumbbob Project 30.5a.

The specific objective of the work of the Mechanics Instrumentation Section of the Armour Research Foundation (ARF) was to measure certain strains and deflections on these structures when subjected to blast loading. The knowledge of these parameters as they were manifested under full-scale blast conditions will form a basis for the future design of protective structures.

E.2 BACKGROUND

On August 10, 1956, a meeting was held at the Armed Forces Special Weapons Project (AFSWP) offices in Washington, D. C., to discuss the response measurements which were desired on a number of structures to be erected for testing under full-scale blast conditions. Attending this meeting were Lt. Col. Pickering and Mr. E. H. Wang, representing AFSWP and AFSWC, and Messrs. R. W. Bull and G. H. Brittain of Armour Research Foundation. At this meeting the ARF representatives advised AFSWP and AFSWC of its capabilities for this program. It was agreed that ARF would install and operate instrumentation for measuring and recording deflections and strains in certain structures to be tested at the Nevada Test Site during Shot Priscilla of Operation Plumbbob.

Since it was imperative that the preliminary planning be started as soon as possible, and since AMF already had a contract with FCDA and AFSWC for the design of these structures, it was decided that this plan be undertaken as a subcontract from AMF. This preliminary study had as its objective the planning of a suitable instrumentation system, and the determination of the condition and adequacy of available government-owned equipment.

The result of this preliminary study was a proposal which outlined the overall instrumentation plan and presented estimates of the effort and cost of its implementation. This proposal is contained in "Instrumentation for Operation Pilgrim (Plumbbob)", Final Report, Armour Research Foundation Project K106, May, 1957.

The structures to be instrumented were two fabricated aluminum domes for DOD Structures Project 3.6, and three concrete domes for FCDA Structures Project 30.1. The physical layout of both projects was in close proximity, and the anticipated availability of recording equipment was such that it was deemed advisable that joint utilization of this instrumentation for both projects would provide a maximum overall economy of manpower, material, and money.

Accordingly, a Memorandum of Understanding was entered into between Weapons Effects Tests, Field

Command, AFSWP, and the Civil Effects Test Group (CETG) of FCDA, which established two separate subprojects, AFSWP Project 3.6, and CETG (FCDA) Project 30.5a. This memorandum outlined the objectives of both subprojects and the responsibilities and field support to be provided by each sponsoring agency.

E.3 THE TEST PROGRAM

E.3.1 Pretest Operations. The preliminary program outlined an overall instrumentation plan for the field tests. In preparation for the actual testing, it was necessary to obtain the required equipment, design the specific control circuitry, and generally check out the system in the laboratory. Most of the amplifier systems and recorders were obtained on loan from the AFSWP supplies. Special control circuits were designed and constructed for the project by ARF. Transducers, cables, and other expendable items were purchased as needed from project funds. Where possible, circuits were set up and checked out completely for operation in the laboratory.

E.3.2 Pretest Field Operations. The field operations consisted of the installation of the complete instrumentation and control equipment at the test site. Except in a few instances, all field workers and necessary equipment were furnished through ARF.

The labor and construction equipment for digging the trenches and laying cables was provided through the AFSWP program director in the field. Where possible, these services were requested well in advance of the actual required date.

E.3.3 Posttest Operations. In the field, the posttest operations consisted of recovering the oscillographic records from the instrument shelters and photographically processing them. In preparation for the recovery operation, two members of the ARF field crew had received training and were certified as official rad-safe (radiation safety) monitors.

When nuclear radiation levels subsided sufficiently to allow personnel to work in the area safely, an appraisal was made, where possible, of the operation of transducers and other equipment. After completion of the posttest investigations, the instruments and other equipment were returned to the ARF laboratory.

E.4 DESCRIPTION OF STRUCTURES TESTED

The five structures instrumented consisted of dome-shaped protective structures arranged at various distances from ground zero. A chart (Table E.1), showing the structures tested and their characteristics, is shown on the next page. The location of these structures with respect to ground zero is depicted in Figure E.1.

E.5 QUANTITIES MEASURED AND METHOD USED

The physical quantities measured on the domes

CONFIDENTIAL

TABLE E.1 TABULATION OF INSTRUMENTED DOME STRUCTURES

Structure Number	Diameter	Thickness	Distance from Ground Zero	Expected Overpressure	Predicted Range	
					Deflection	Unit Strain
	ft	in	ft	psi	in	
F3.6-9026.01*	20	½	1,180	70	8	5×10^{-3}
F3.6-9026.02*	20	1	1,180	70	2	5×10^{-3}
F30.1-8001.01†	50	6	1,180	70	24	5×10^{-3}
F30.1-8001.02†	50	6	1,600	35	2	5×10^{-3}
F30.1-8001.03†	50	6	2,030	20	1	2×10^{-3}

* Aluminum type structure.
† Reinforced-concrete type structure.
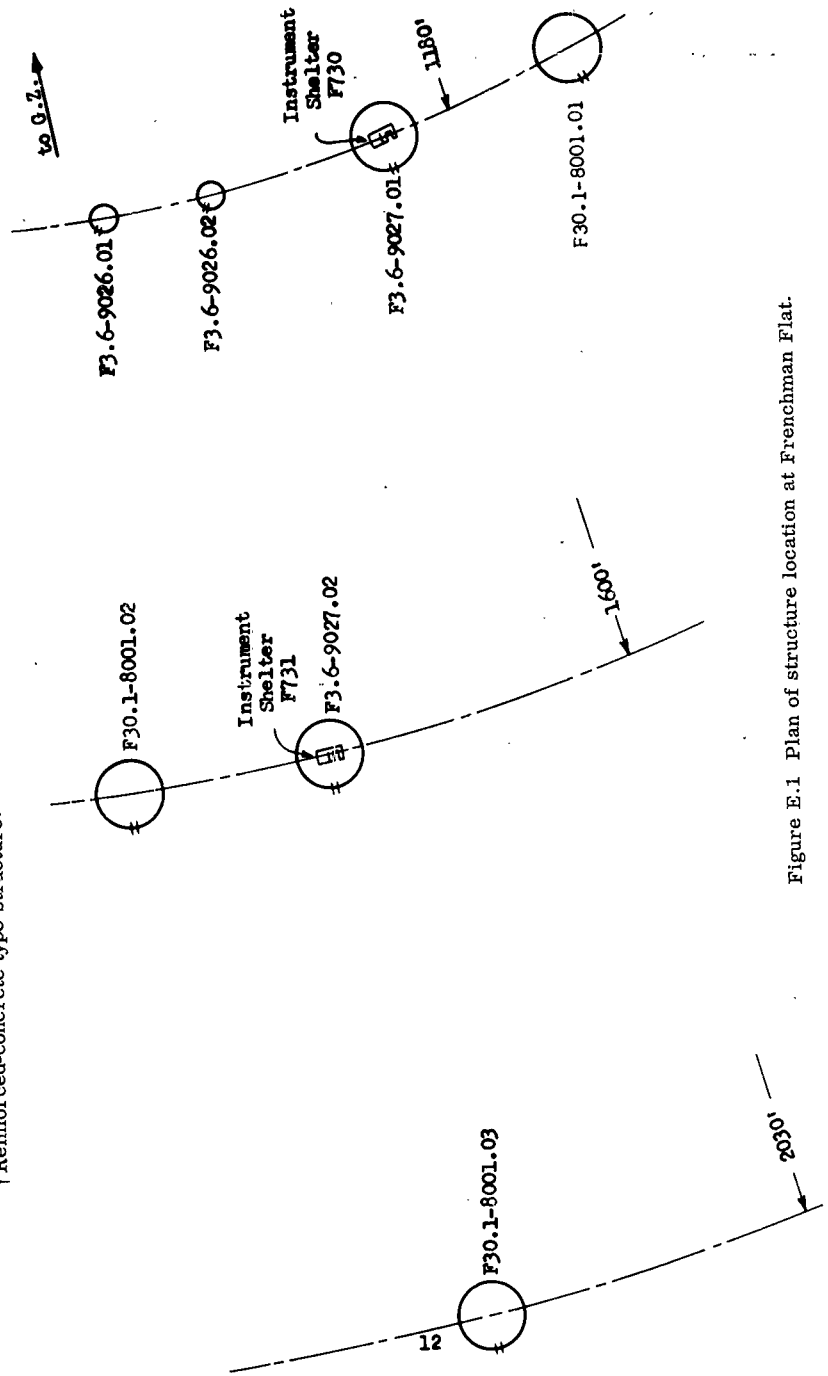
Figure E.1 Plan of structure location at Frenchman Flat.

consisted of strains and deflections at various locations on the dome structures. Six deflection measurements were made on each of the five domes. Unit strain was measured in the structures at a point approximately on the prime meridian, $22\frac{1}{2}$ degrees from the vertical axis of the dome. Strain gages located near the base of the domes were used to determine

stalled by ARF, and the specific points of measurement are shown in Figures E.2, E.3, and E.4.

E.6 INSTRUMENTATION SYSTEM

E.6.1 General Description. The basic instrumentation and control center layout as used is depicted in
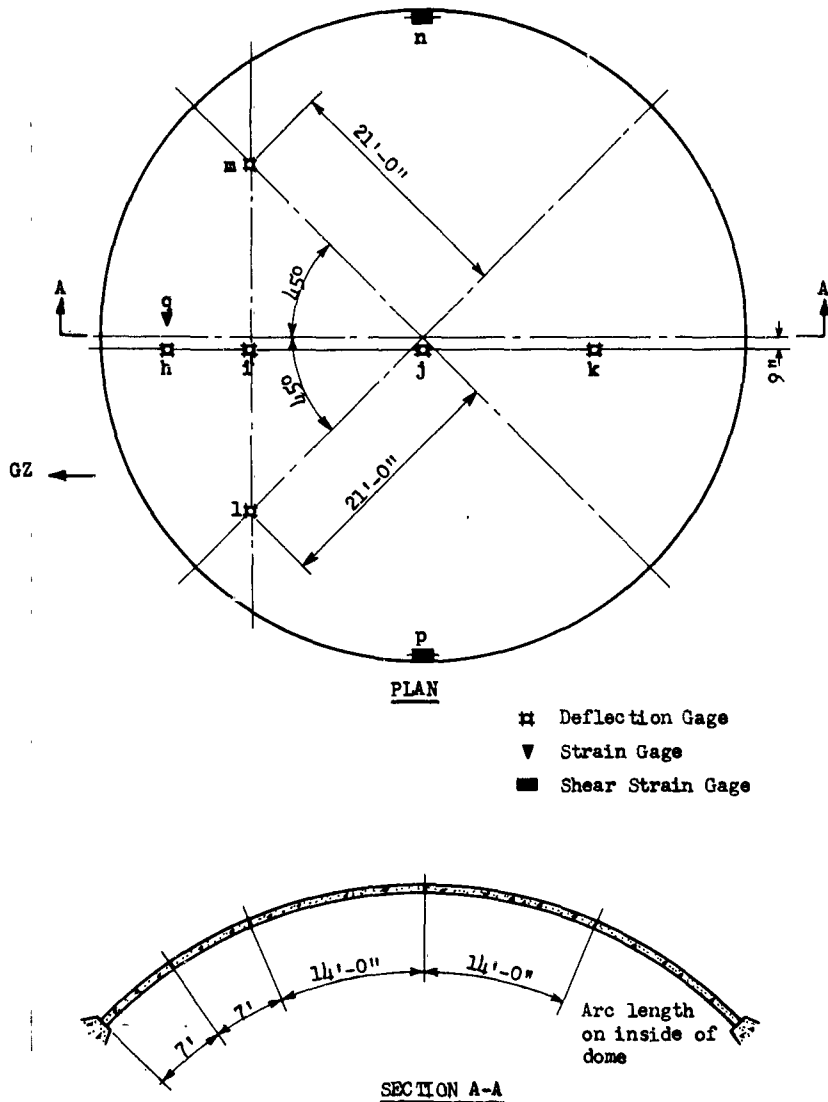
Figure E.2 Diagram showing location of gages in 6-inch-thick concrete domes.

the shear strains. Expected values of these quantities, as estimated by AMF, are listed in Table E.1.

In addition to the electronic instrumentation channels, nine Baldwin mechanical scratch gages were placed on the inner surface of the 1-inch-thick aluminum dome (F3.6-9026.02).

Table E.2 is a complete schedule of sensors in-

the block diagram of Figure E.5. Essentially, the recording system consists of strain and displacemment transducers, carrier amplifiers, and magnetic oscillographs. However, in order to prepare the recording circuits for the measurement of physical quantities, a number of auxiliary circuits were necessary for providing calibration and control functions. Typical

146

TABLE E.2 SCHEDULE OF SENSOR LOCATIONS

Structure			Sensor				
Number	Type	Thickness	Number	Position	Type	Primary Range	Backup Range
		in				in	in
F3.6-9026.01	Aluminum	½	D70DL1	a	linear motion	8	—
			D70DL2	b	potentiometer	8	16
			D70DL3	c		8	16
			D70DL4	d		8	—
			D70DL5	e		8	—
			D70DL6	f		8	16
			V70DL7	l	SR-4 strain	$5,000 \times 10^{-9}$	
			V70DL8	l	rosette		
			V70DL9	m			
			V70DL10	m			
			S70DL11	n	SR-4 strain	$5,000 \times 10^{-6}$	
			S70DL12	n	rosette		
			S70DL13	n			
			S70DL14	n			
F3.6-9026.02	Aluminum	1	D70DH1	a	linear motion	2	—
			D70DH2	b	potentiometer	2	4
			D70DH3	c		2	4
			D70DH4	d		2	—
			D70DH5	e		2	—
			D70DH6	f		2	4
F3.6-9026.02	Aluminum	1	V70DH12	l	SR-4 strain	$5,000 \times 10^{-6}$	
			V70DH13	l	rosette		
			V70DH14	m			
			V70DH15	m			
			S70DH16	n			
			S70DH17	n			
			S70DH18	n			
			S70DH19	n			
			MS70DH1	p	Baldwin		
			MS70DH2	q	mechanical		
			MS70DH3	r	scratch gage		
			MS70DH4	s			
			MS70DH5	t			
			MS70DH6	u			
			MS70DH7	v			
			MS70DH8	w			
			MS70DH9	x			
F30.1-8001.01	Concrete	6	D70DF10	h	linear motion	24	
			D70DF11	i	potentiometer	24	
			D70DF12	j		24	
			D70DF13	k		24	
			D70DF14	l		24	
			D70DF15	m		24	
			S70DF6	q	SR-4 strain	$5,000 \times 10^{-6}$	
			S70DF7	q	gage		
			S70DF8	q			
			S70DF9	q			
			V70DF16	n			
			V70DF17	n			
			V70DF18	p			
			V70DF19	p			
F30.1-8001.02	Concrete	6	D35DF10	h	linear motion	2	—
			D35DF11	i	potentiometer	2	4
			D35DF12	j		2	4
			D35DF13	k		2	—
			D35DF14	l		2	4
			D35DF15	m		2	—
			S35DF6	q	SR-4 strain	$2,500 \times 10^{-6}$	
			S35DF7	q	gage		
			S35DF8	q			
			S35DF9	q			
			V35DF16	n	SR-4 strain	$2,500 \times 10^{-6}$	
			V35DF17	n	gage		
			V35DF18	p			
			V35DF19	p			
F30.1-8001.03	Concrete	6	D20DF8	h	linear motion	1	—
			D20DF9	i	potentiometer	1	2
			D20DF10	j		1	2
			D20DF11	k		1	—
			D20DF12	l		1	2
			D20DF13	m		1	—

147

CONFIDENTIAL

Figure E.4 Diagram showing location of mechanical scratch gages in 1-inch thick aluminum dome.

Figure E.3 Diagram showing location of gages in aluminum domes.

CONFIDENTIAL

control functions were the switching of local power, switching of recorder chart transport, calibration sequence, and transducer protection functions. These functions were provided by a specially designed se-

other at 2,030 feet from ground zero, it was necessary to house the instrumentation in two separately located instrumentation shelters. This would reduce the length of cable runs to the shelters, particularly in the high-
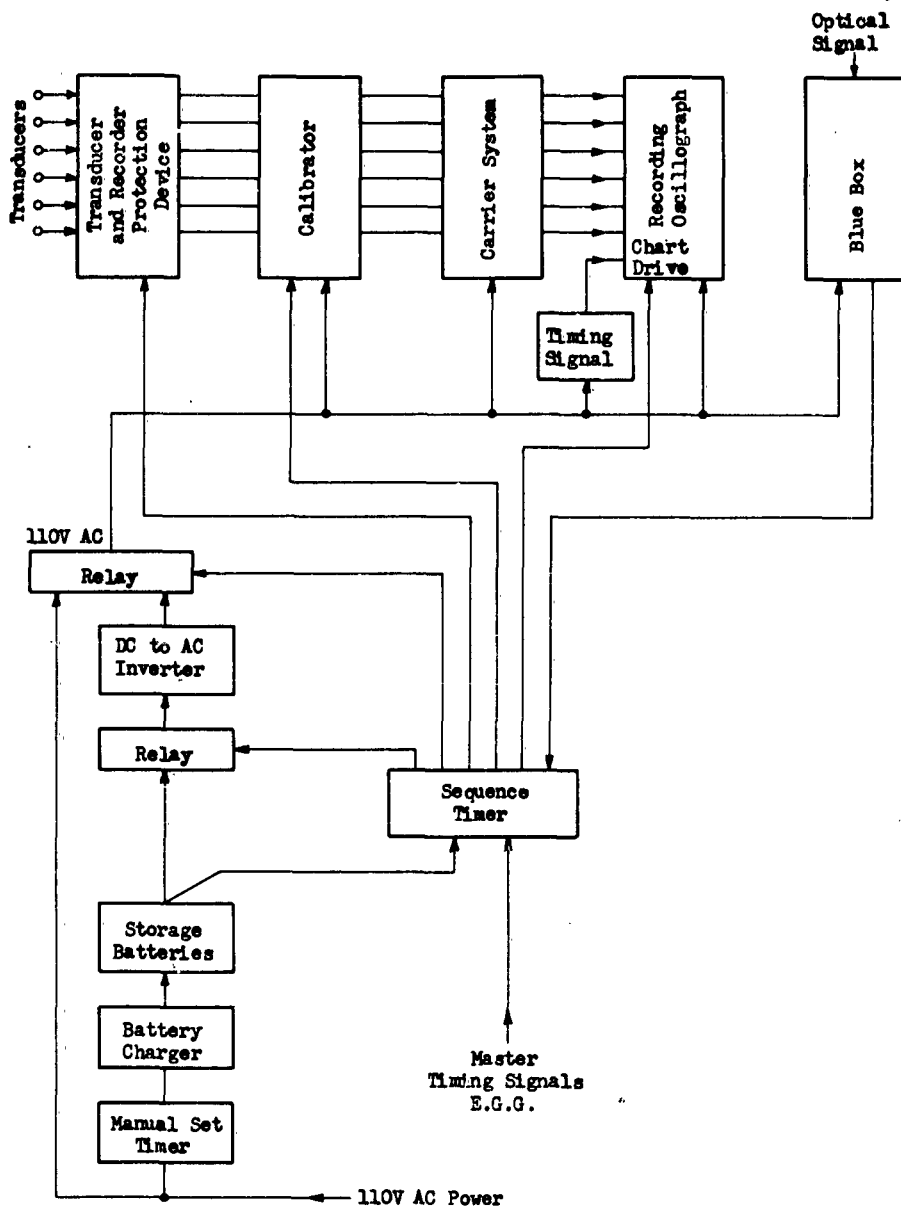
Figure E.5 Block diagram of typical instrumentation system.

quence controller which receives its impetus from the master Edgerton, Germeshausen & Grier (EG&G) timing systems.

E.6.2 Instrumentation Shelter Requirements.
Since the ARF instrumentation was concerned with three structures at a radius of 1,180 feet from ground zero, and two structures, one at 1,600 feet and the

overpressure regions, and thus reduce the electromagnetic interference effect on the instrumentation. One of these shelters would serve the structures in the higher pressure region (1,180 feet from ground zero). The other would serve the remaining two structures in the lower-pressure regions.

The estimated yield of the weapon was such that the calculated unshielded radiation dosage expected

CONFIDENTIAL

at the 1,180-foot radius was approximately 2,500 r. Since none of the existing portable instrument shelters could provide a radiation attenuation factor of at least 500, it seemed advisable to proceed with plans for new instrument shelters. It was decided to locate the shelters beneath the nonresponding concrete domes and thus take advantage of the additional shielding provided by their 2 feet of wall thickness. A shelter was specified having 3-foot-thick concrete walls and roof. Additional earth cover, to a depth of 5 feet, was specified to reduce the total radiation to a level of 1 r.

The space requirements to accommodate the instrumentation were as follows.

Instrument room	9 by 12 feet by 8 feet high.
Battery room	4 by 6 feet by 8 feet high.
Escape hatch	36 by 36 inches, with built-in ladder.

The hatch cover was to provide adequate shielding and require no more than 2 minutes for opening after being sealed.

Additional requirements for the shelters were for adequate lighting and power distribution, adequate ventilation, provision for cable ports and power capability for operation of instrumentation of a 10-kva single-phase load at 110 volts, 60 cps.

Although the shelters would have resulted in a total radiation level of approximately 1 r, the construction would have been very costly. Personnel from Operation Plumbbob Program 3 re-evaluated the shielding requirements consistent with a maximum radiation dosage of 10 r which could be tolerated by the photographic medium used for recording. On this basis, the wall thickness and roof thickness which were evolved for this shelter were reduced to 18 inches of reinforced concrete. The earth cover of 5 feet was maintained. It was decided to make both shelters identical, even though the radiation level expected in the lower-pressure region was much lower than in the higher-pressure region.

Figure E.6 is an interior view of the instrument shelter (F730) installations.

E.6.3 Sensors. The sensors which were selected for the measurements of displacements and strains were linear-motion potentiometers and SR-4 strain gages, respectively.

The linear-motion potentiometers ranged from a 1-inch stroke to a 24-inch stroke. The resistances of these potentiometers were 5,000 ohms for the Type 226, which includes strokes from 1 inch to 8 inches. The Type 223 potentiometers, with strokes of 16 inches and 24 inches, had resistances of 2,000 ohms.

These potentiometers were fabricated with ball and socket swivel joints on both the main body of the unit and the shaft. This type of construction was ideally suited to the deflection measurements to be encountered on the dome-type structures, since the direction of the response to the blast phenomena was not known.

Typical installations of the deflection sensors are shown in Figures E.7 and E.8. As shown, the shaft of the potentiometer was attached to the structure, which was provided with a threaded hole at the point to be instrumented. The body of the potentiometer was supported by a reference truss constructed inside the structure solely for the purpose of supporting the deflection instrumentation. The ends of these reference trusses were supported by the foundation of the dome structure. In the aluminum domes especially, where clearance between the truss and the dome was appreciably greater than the anticipated deflection, cylindrical aluminum pedestals were utilized to support the potentiometers. These pedestals are shown in Figure E.8.

The strains and shears to be determined were sensed by means of bakelite-base SR-4 strain gages. The Type AB-7 gage is a gage with a nominal length of $\frac{1}{4}$ inch, and it was used for the measurement of strains occurring in the reinforcing bars of the concrete domes and, with proper electrical circuitry, permitted the measurement of horizontal shear of the dome and its foundation. The Type ABFX-11 gage is a biaxial rosette, and it was used for the measurement of shear in the aluminum domes at their foundations. Specific gage locations are shown in Figures E.2 and E.3. A view of the strain gages mounted on the reinforcing bars in a concrete dome is shown in Figure E.10.

As previously stated, about 50 percent of the measurement channels were backed up by duplicate channels. For the deflection measurements, duplicate sensors, as well as amplifiers and galvanometers, were utilized. It was decided not to duplicate the strain sensors for the backup, so two amplifiers and recording channels were driven by a single strain gage bridge.

Prior to mounting the strain gages, the surfaces were prepared in the usual manner to provide a smooth plane surface onto which the gage would be cemented. The reinforcing bars were machined to a sufficiently flat surface to receive the gage without undue reduction of the cross section of the bar. This machining was accomplished using a $\frac{1}{2}$-inch-diameter carbide-tipped burr driven by a portable flexible shaft grinder mounted in a special jig, as shown in Figure E.9.

Strain gages were cemented on the prepared surfaces using Armstrong A-6 cement. After the cement was cured, the gages and leads were sealed with Scotchkote electrical coating. The reinforcing bars with the mounted strain gages were then embedded in a sand and Cal Seal mixture which completely sealed the small access holes in the structures.

E.6.4 Amplifiers. Excitation voltages for both the strain gage transducers and the linear-motion potentiometers were provided by 3,000 cps carrier supplied by the CEC oscillator-power supply combinations and the common carrier oscillator of the William Miller multichannel oscillograph amplifiers.

The transducers modulated the carrier voltage which was then amplified by individual alternating-
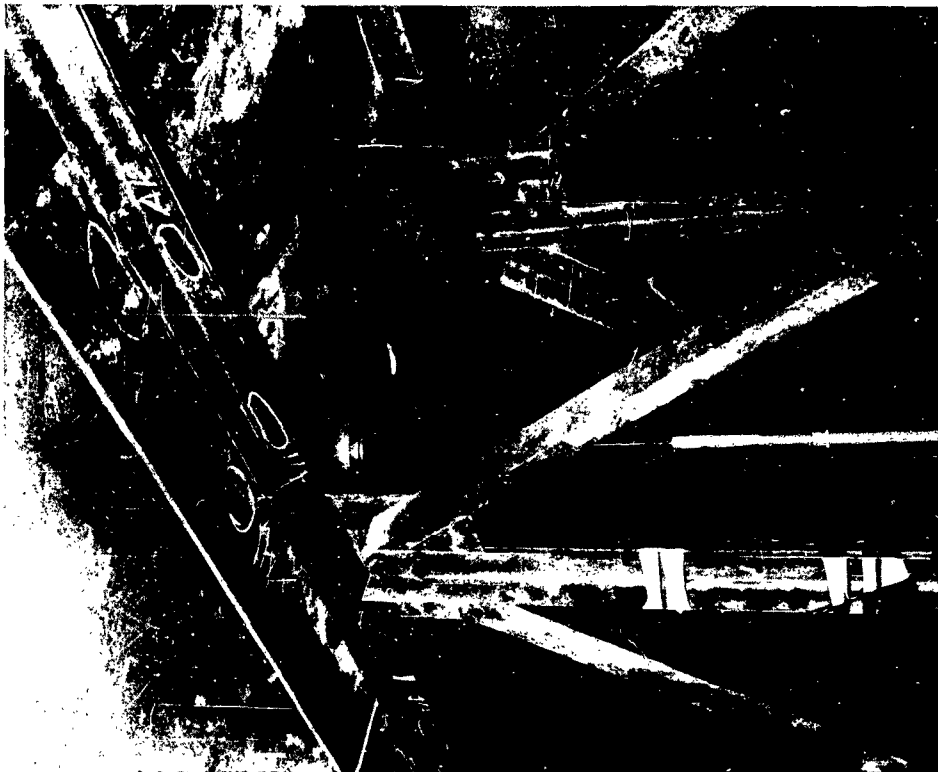
150

Figure E.7 Deflection gage (24-inch range) at center of concrete dome structure, mounted on reference truss.
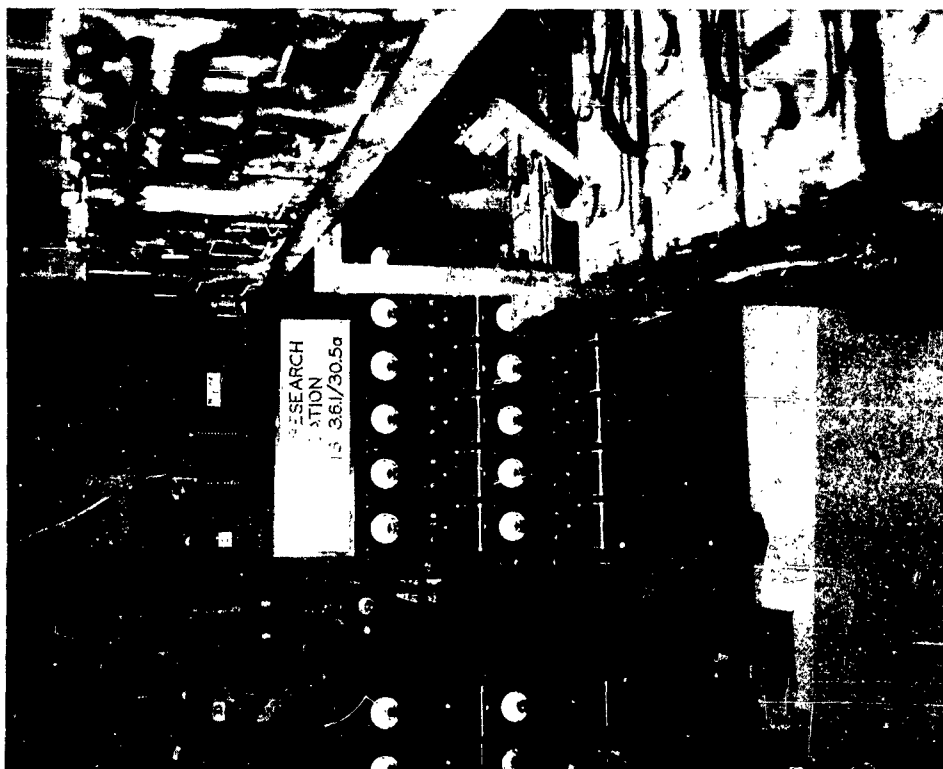

Figure E.6 Interior view of Instrument Shelter F730, showing the Miller carrier amplifiers and CEC recorders.
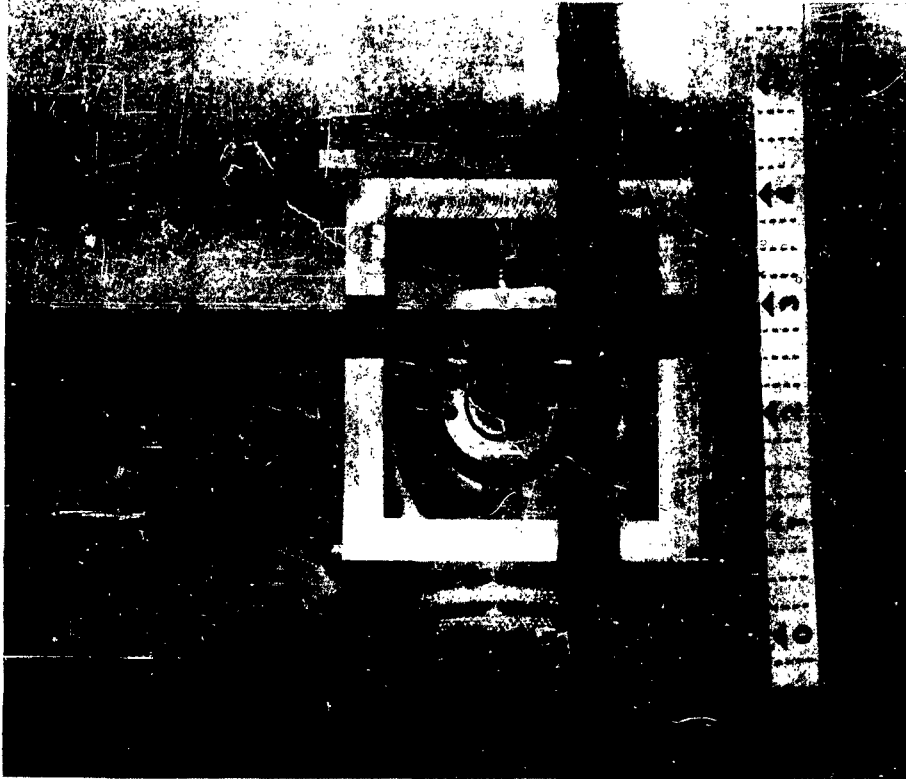
151

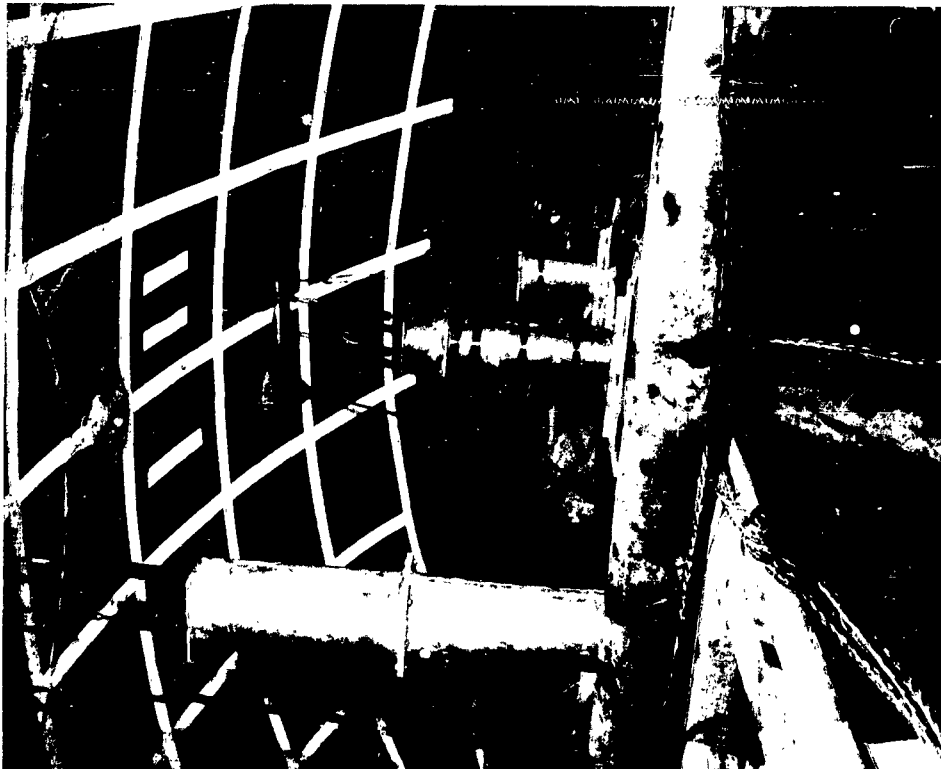Figure E.9 Jig for machining surfaces of reinforcing bars preparatory to mounting strain gages.

Figure E.8 Deflection gages (2-inch and 4-inch ranges) in 1-inch aluminum dome, mounted on reference truss.

152

current amplifiers for each channel. Alternating-current amplifiers were used because of their high gain and stability. The amplifier signal was then demodulated in a phase-sensitive detector and applied to a galvanometer in the recorder. The resulting deflection was proportional to the original modulating signal.

Of the total of 93 channels of amplifiers which were obtained through the AFSWP catalog of available equipment, 60 channels were Miller and 33 channels were Consolidated amplifiers.

obliterated for a small but finite time. Since such a condition could not be tolerated, the trace identifiers of all the recorders were made inoperative and identification of traces was accomplished by means of sequentially calibrating all the channels.

The amplifiers and recorders were shock-mounted to isolate them from the ground disturbance due to the detonation. Shock mounts provided on the Consolidated recorders and carrier amplifiers were adequate. The Miller systems, however, were not provided with shock mounts. For these, a shock-mounted rack,
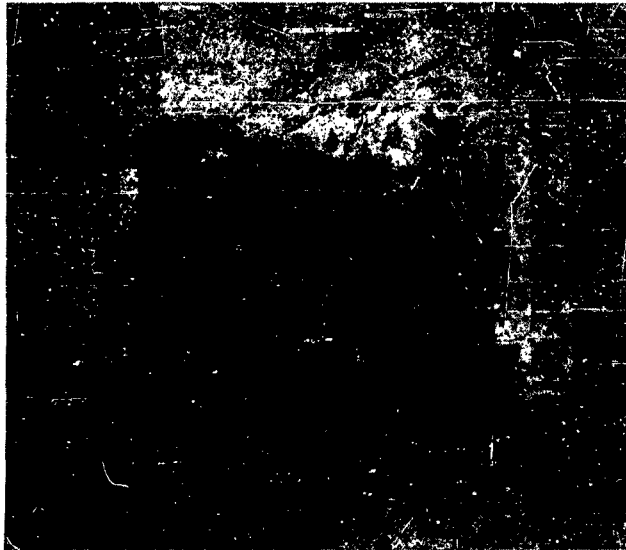
Figure E.10 SR-4 strain gages mounted on reinforcing bars in concrete dome, prior to grouting access opening.

E.6.5 Recorders. All of the recorders used on this program were Consolidated equipment. Of the eight recorders, five were obtained from available AFSWP equipment lists, two from the Ballistic Research Laboratories (BRL), and one from ARF. The chart widths for these recorders were 12 inches, 5 inches, and 7 inches, respectively. This is a total chart width of 77 inches. Since 75 channels were used, this allowed approximately 1 inch of chart width for each channel without overlap.

The recorder operation is such that a light beam is caused to illuminate a mirror suspended on a galvanometer movement. The reflection of this beam is focused on photosensitive paper or film. A current flowing through the galvanometer produces a deflection of the suspension and causes the reflected light beam to deflect across the moving photosensitive media contained in a removable record magazine. Record speeds are controlled by selection of proper gear ratios in the transmission. The record number is photographed automatically at the end of each run.

The method of trace identification used on these recorders blanks each trace in sequence. Thus, part of the intelligence contained in each channel would be

constructed of Unistrut channels, on which the Miller amplifiers were clamped, provided adequate isolation. A view of this mount is shown in Figure E.6.

In arranging the various transducer channels with amplifiers and recorders, it was deemed advisable to record the data from one structure on two or more recorders utilizing amplifiers from several amplifier groups. Using this scheme, should a complete amplifier group or recorder malfunction, data from one whole structure would not be lost. Thus, a plan was put into effect whereby data channels from a given structure were distributed among at least three recorders and amplifier groups.

E.6.6 Recording Materials. The Consolidated recorders used on this program can accommodate either film or photosensitive paper as the recording medium. Numerous tests were conducted to determine which of these would be most suitable under the field operating conditions. Among the factors considered were writing rate and radiation sensitivity.

The medium selected was the Lino-Writ 3 Type W photo recording paper. This paper has a relatively high tungsten sensitivity. It is extra thin and has a

153

semimatte finish. The thin base of this paper permits each roll to contain approximately 50 percent more length than standard weight papers. Thus, for a given diameter roll of paper, the recording time is increased approximately 50 percent.

E.6.7 Calibration Unit. The calibration unit provides two principal functions. One of these is to insert calibrating resistors to the transducer circuits

ground at this time. The time duration for this protection was approximately 40 msec.

Four calibrating relays, each capable of calibrating 13 separate channels, are located in this unit. They were energized at slightly different times in order to provide a sequential calibration procedure for trace identification. These relays were controlled from four agastat time-delay relays located in the timer unit. Each of these was set for a different time delay.
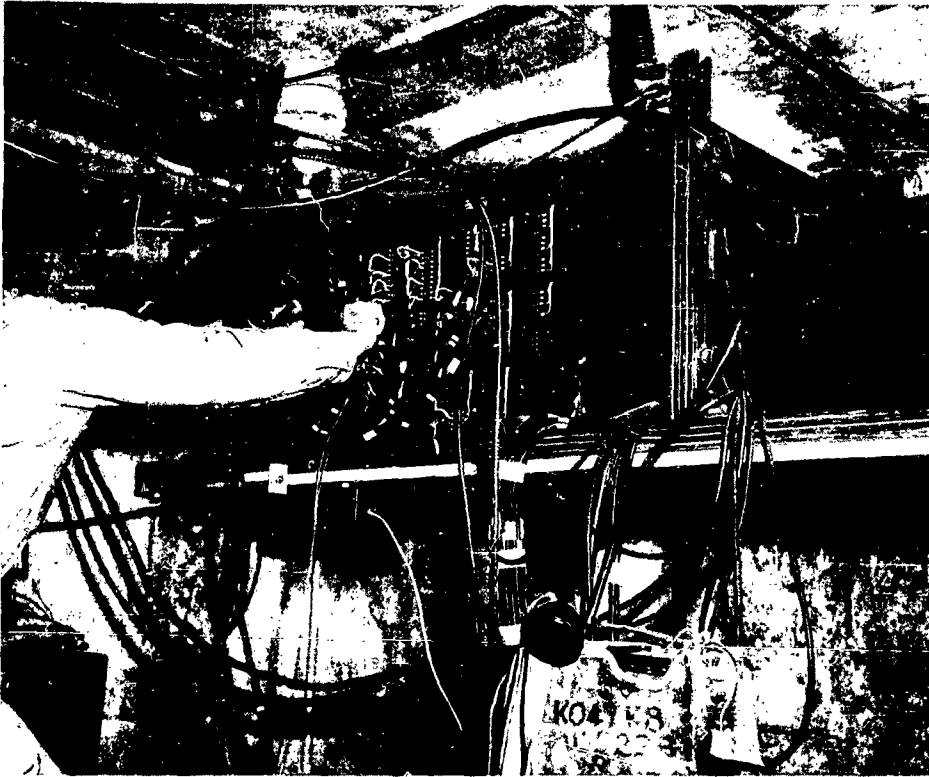
Figure E.11 Delicate calibration equipment slung on springs from ceiling of shelter.

during the three calibrating operations prior to zero time. The second main function is to short to ground each amplifier input for a predetermined time interval.

The strain gages which were used for the determination of strain and shear were connected in Wheatstone bridge circuits. During calibration, a calibrating resistor was connected across one of the active arms of each of the bridge circuits. The deflection measurements were made with linear-motion potentiometers as the sensors, and, in this case, the calibration was affected and a signal was produced which was 110 percent of that resulting from full deflection.

The purpose of short-circuiting the input to each carrier amplifier was to prevent damage to the sensors and amplifier input circuits resulting from the electromagnetic effect occurring at zero time (Reference 26). The carrier supply voltages were also shorted to

Since the calibration unit, along with the timer and time base oscillator (described in Sections E.6.8 and E.6.10), could be adversely affected by the ground shock, they were slung on soft spring mounts from the shelter ceiling. This is shown in Figure E.11.

E.6.8 Timer Unit. The timer unit was designed and built to supplement the timing signals provided by the EG&G network. This unit received all of the EG&G relay signals available, as well as the signals from the Blue Box. In operation, this unit controlled the protective shorting relays located in the calibrator unit, the calibration relays, and the operation of the recorder chart motors.

E.6.9 Power System. The source of power for one shelter consisted of twenty 12-volt batteries connected in series-parallel to supply 120 volts dc at 400 amp-hr

154

capacity. The source of power for the other shelter consisted of twelve 12-volt batteries and sixteen 6-volt batteries connected in a series-parallel arrangement to give 120 volts dc at 400 amp-hr capacity.

Each power system consisted of a specially designed power controller, a commercial motor starter, and a motor-generator set. This power controller contained two large power contactors and a number of smaller relays. At H −1 hour the EG&G timing signal initiated the motor starter, which, in turn, started the inverter providing ac power to the bulk of the recording and associated equipments. The remaining operations were controlled by the timer unit, and all equipment was turned off at H + 3 minutes.

E.6.10 Time Base. The time base provided on the Consolidated oscillograph recorders operates from synchronous motors, and therefore requires a power source of a stable and accurately known frequency.

Since all power for operation of the instrumentation during the shot was derived from storage batteries and from alternators driven from motors operating from those batteries, the frequency of this alternating voltage could not be regulated too well without more elaborate speed-control equipment. This method of timing was therefore not used, and the timing lamps in the oscillographs were removed.

Instead, two Hewlett-Packard Model 100D low-frequency standards were used to provide timing signals. One was located in each instrument shelter, and its output supplied the excitation to a galvanometer in each recorder in that shelter.

This instrument is a highly stable secondary frequency standard producing standard frequencies of 100 kcps, 10 kcps, 1 kcps, 100 cps, and 10 cps, with a stability of 2 parts/million/week, or a short-term stability of 1 part/million after 24-hour warm up. The 100D may be conveniently standardized with a primary frequency standard by using the front panel cathode-ray tube and adjustment to set the internal oscillator "on frequency".

The frequency standards were calibrated prior to their installation in the shelter, and with a 1-hour warm-up period before the shot, should have reached a stable operating condition. Although the stability probably was not 1 part/million, should the frequency have been off 5 cps in 10,000, this would only be an error of 0.05 percent, and should not be of great concern.

E.6.11 Cables. The signal cables used on the program were manufactured by the Ohm Wire and Cable Corporation of Brooklyn, N. Y., to the same specifications as the cable which BRL personnel ordered for their instrumentation on Operation Plumbbob. This four-conductor cable consisted of two twisted pairs, each of which was separately shielded and laid parallel and covered with 0.032-inch thick thermoplastic insulation rated at 90 C. Each pair of conduc-

tors conformed to the following specifications: two conductors were No. 22 (7/30 T.C.), 0.040-inch-thick polyethylene insulated hook-up wire, twisted, shielded No. 36 T.C., 85 percent minimum coverage, conductor insulation was solid colored, one conductor red and one conductor green. Two conductors were No. 18 (16/30 T.C.), 0.040-inch-thick polyethylene insulated hook-up wire, twisted, shielded No. 34 T.C., 85 percent minimum coverage, conductor insulation solid color, one white and one black.

It was found that a number of the reels of cables tested showed shorted, grounded, or open conductors in the cable. This luckily did not hamper the operation seriously, because cable runs were comparatively short so that one reel provided at least three runs. Thus cable runs between faults could be assigned to provide the most economical use, and no splicing at the test field was necessary.

E.7 PLAN OF OPERATION

The plan of operation of the recording system was as follows. At H −1 hour the motor generators were started from local battery power. All ac and dc equipment was energized. At H −15 minutes the recorder chart motors were initiated, and automatic calibration of all channels was accomplished. When this was completed the chart motors were shut off. At H −1 minute the recorder chart motors were turned on again. Automatic calibration of all channels was initiated. The chart motors remained on. At H −5 seconds the transducer cables and amplifier inputs were short-circuited. At H −1½ seconds backup of this previous step was accomplished; in addition, a parallel relay contact was closed in the chart motor circuit as a further backup measure. At H −0 the nuclear device was detonated. The Blue Boxes responded to the flash of the detonation, initiating a 40-msec time-delay circuit. At H + 0.04 second the transducers and amplifier inputs were unshorted and ready to receive the response signals from the various sensors. At H + 3 minutes all power to the instruments was turned off.

E.8 EVALUATION TESTS

E.8.1 Recording Materials. Two types of recording materials were evaluated for use on this program. The evaluations were conducted on the basis of ability of the material to record oscillographic traces of certain frequencies and amplitude and the sensitivity of the material to gamma radiation.

The recording materials tested were Lino-Writ 3 Type W photo recording paper and Kodak Micro-File film. The Lino-Writ paper is a thin base material with a very high tungsten rating. The Micro-File film is a film which was developed specifically for microfilming purposes and has a very poor tungsten rating. However, it has been used successfully for photographing the flash from atomic weapons, and it has been shown to be very insensitive to gamma radiation.

155

Identical tests were performed on both materials. Thus, on each material a 100-cps sine wave signal was recorded with a peak-to-peak amplitude of approximately 1 inch. The speed of the recording medium was the same for all tests, approximately 20 in/sec. After the materials were exposed to this signal, small sections of the records were mounted in a specially designed film holder. These were then exposed to gamma radiation from a calibrated Cobalt 60 source. They were subjected to radiation dosages from 10 r to 1,000 r. The materials were then processed by conventional techniques, and it became very apparent that the Lino-Writ paper would be the most satisfactory material of the two, provided the radiation intensity was kept below 14 r.

Subsequent tests were performed on both materials with various combinations of exposure and development. By overexposing both materials and underdeveloping them it was possible to bring out a higher degree of contrast than previously. It was felt that the preferable approach to be taken on this program would be to use the faster of the recording media and rely upon external shielding to keep the radiation level at the recording instruments below 10 r. Thus the possibility of losing the high frequency response of the desired phenomena was minimized.

E.8.2 Sensors. An evaluation program was conducted on two types of strain gages to determine which might be more suitable for this field test program. The two types were the Baldwin bakelite base SR-4 strain gage and the weldable strain gage manufactured by the Micro Test Co.

These tests were designed to determine how effective both types of gages were when operating in high-radiation fields, both electromagnetic and electrostatic. On the first series of tests typical gages were installed on a section of steel reinforcing bar similar to the type to be used on the concrete domes. This bar was then inserted in the ARF reactor, where it was exposed to both gamma and neutron radiation. Records were taken on an Edin two-channel recorder to determine the effect, if any, resulting from these radiations. It was not possible to determine any extraneous effects resulting from the imposed radiations.

The reactor was operating at approximately 10 kw. In order to simulate a sudden change in radiation level, since it was not possible to bring the reactor up to its rating rapidly, the simulation was obtained by "scramming" the control rods (dropping them at their fastest rate), thus effectively shutting down the reactor.

Electrostatic induction tests were conducted by placing a similarly mounted pair of gages close to the high-energy spark. The amount of energy released was approximately 5,000 joules, obtained by discharging a 1-mfd condenser which had been charged to 100,000 volts. No noticeable pickup could be observed on an oscillograph during this discharge from either of the two gages.

It was decided to use the bakelite-base strain gages, since their installation in the field would not present unusual difficulties. The weldable-type gage must be spot-welded at very close intervals in order to obtain a proper bond. This would have been extremely difficult under existing field conditions.

E.8.3 Thyratrons. For the timer unit controlling the sequence of operations required by the instrumentation plan, the use of thyratrons in the time-delay circuits was contemplated. It was considered of the utmost importance that the effect of radiation on the premature ionization of the thyratrons be determined. Consequently, the thyratrons (2D21) were connected in a typical timing circuit and inserted in the ARF reactor to determine the effect of both gamma and neutron radiation. Neither of these types of radiation caused the thyratrons to ionize, thus establishing the reliability of this circuit for timing purposes in the instrumentation shelter.

E.9 RESULTS

The original plans called for a total of 77 channels of electronic instrumentation, as outlined in Table E.2. Of these, 50 were primary channels and 27 were for backup. Due to delays in delivery of some displacement sensors, three backup channels were omitted from the responding concrete dome in the high-pressure region. In addition, one of the strain gages in the responding concrete dome in the medium-pressure region was damaged during grouting, an operation performed to seal the access opening at the gage location. There was insufficient time available to repair or replace this gage. Thus, the total number of channels at shot time was 73.

Upon processing of the records it was discovered that one recorder had malfunctioned, resulting in a loss of six measurements not duplicated on other recorders. Although the recording paper had completely run through the magazine, the galvanometer lamp and its spare had burned out during the final calibration before shot time. However, the response measurements from a given structure were distributed among the various recorders as described in Section E.6.5. This scheme proved its worth with the failure of one recorder.

Records indicate that one deflection gage and seven strain gages failed at zero time.

Posttest inspection of the two instrument shelters in the nonresponding dome indicated that the recording instruments and associated equipment, such as batteries, motor-generator sets, timers and controls, all withstood the shock phenomena associated with the detonation. Nothing appeared to have shifted position in the shelters due to the ground shock.

Oscillographic records indicate no radiation fogging, and all data traces were dense and had good contrast. Film dosimeters placed in the shelters showed dos-

156

CONFIDENTIAL

ages of 18 r just below the access hatch in the instrument Shelter F730. Dosage at a corresponding position in Instrument Shelter F731 was approximately 8 r. Dosages recorded at the instruments, however, were considerably less than 1 r.

The oscillographic response records are reproduced in Figures E.12 through E.18. Structure and position identifications correspond to those listed in Table E.2 and Figures E.2, E.3, and E.4.

Deflection calibration constants are in terms of inches deflection of the structure per inch displacement of the oscillograph trace. A downward motion of the structure is indicated by the direction of the arrow shown behind the appropriate calibration constant.

Strain calibration constants are in terms of unit strain in the structure element per inch displacement of the oscillograph trace. The arrow indicates trace displacement corresponding to compression.

Shear strain calibration constants are in terms of unit shear strain in the structure per inch of displacement of the oscillograph trace. The arrow indicates trace displacement corresponding to shear produced by a horizontal force displacing the top of the structure away from ground zero.

Time signal is at a rate of 100 cps, providing a scale of 10 msec between adjacent signal peaks.

E.10 DISCUSSION

The oscillograms obtained in the field tests were delivered to AMF for analysis of the structures. No analysis of the records was to be done on Project 3.6.1/30.1a. However, there are some characteristics of the instrumentation which show up in the oscillograms which are discussed below.

E.10.1 General Operation. Oscillograms indicate considerable amounts of high-frequency oscillation on the traces beginning at the arrival of the main air shock wave. This phenomenon occurs to a greater extent on the records from the front-line structures where the electrical and mechanical disturbances are greater. These sharp spikes occur on the deflection channels; whereas, they do not, in most of the records, appear on the corresponding strain channels. This indicates the probability of these disturbances being due to mechanical oscillations in the gage parts or its mounting structures.

The strain and shear signals generally produced very clean traces up until the time of actual physical gage failure.

The carrier instruments and oscillographs performed adequately for these tests, except for one difficulty. The CEC amplifier system utilizes a common carrier supply for all eight transducers in an amplifier group. Thus, if one transducer should short or ground at some point, all the other channels supplied from the common carrier supply are affected. Evidence of this type of failure appears in the oscil-

lograms of the lower-pressure structures where the CEC systems were used.

E.10.2 Deflection Measurements. In a number of instances the data shows greater upward than downward deflection of the dome points. At some points this type of distortion is the reverse of that which might be expected. It is to be noted that the deflection sensors were installed according to the pretest plan, which provided 10 to 20 percent of the deflection range for upward travel. In some positions this was inadequate, and the actuator rod was pulled from the body of the sensor, resulting in failure of the channel for further recording. In positions such as Position j (Figure E.2) on the domes, horizontal deflections of either the dome or the truss supporting the instruments would result in an equivalent negative deflection signal for the dome. Gross destruction of the domes generally prevented any postshot evaluation of sensor operation.

E.10.3 Strain Measurements. The failure of the strain gages at zero time is attributed to insulation breakdown. Postshot examination of these gages was not possible because they could not be found.

E.10.4 Mechanical Scratch Gages. The mechanical scratch gages in the aluminum structures yielded no usable data from the targets that could be recovered. Five of the nine gages were torn from their mountings and could not be found. The remainder had not functioned.

E.11 RECOMMENDATIONS

In an operation of the magnitude and importance of Shot Priscilla, maximum instrument reliability can best be obtained through checkout and calibration of the complete instrumentation system in the home laboratory of the contracting agency. When instrumentation equipment has to be purchased or obtained from AFSWP equipment stocks, sufficient extra time must be available for obtaining, checking and calibrating this equipment. It is, therefore, recommended that contracts for field instrumentation be let well in advance of the scheduled shot date.

In the field, instrumentation installation can be efficiently accomplished only when the structures are free of construction forms and personnel. When construction is behind schedule, it is recommended that sufficient time be allotted to the instrumentation agencies in order to permit a thorough check of the equipment after installation.

In addition to protection of the transducers by shorting the input cables, it is recommended that spark gaps be installed at the transducer between the cable shield and local ground to limit the induced voltage.

If an instrument reference structure is utilized, such as the reference trusses used in these tests,
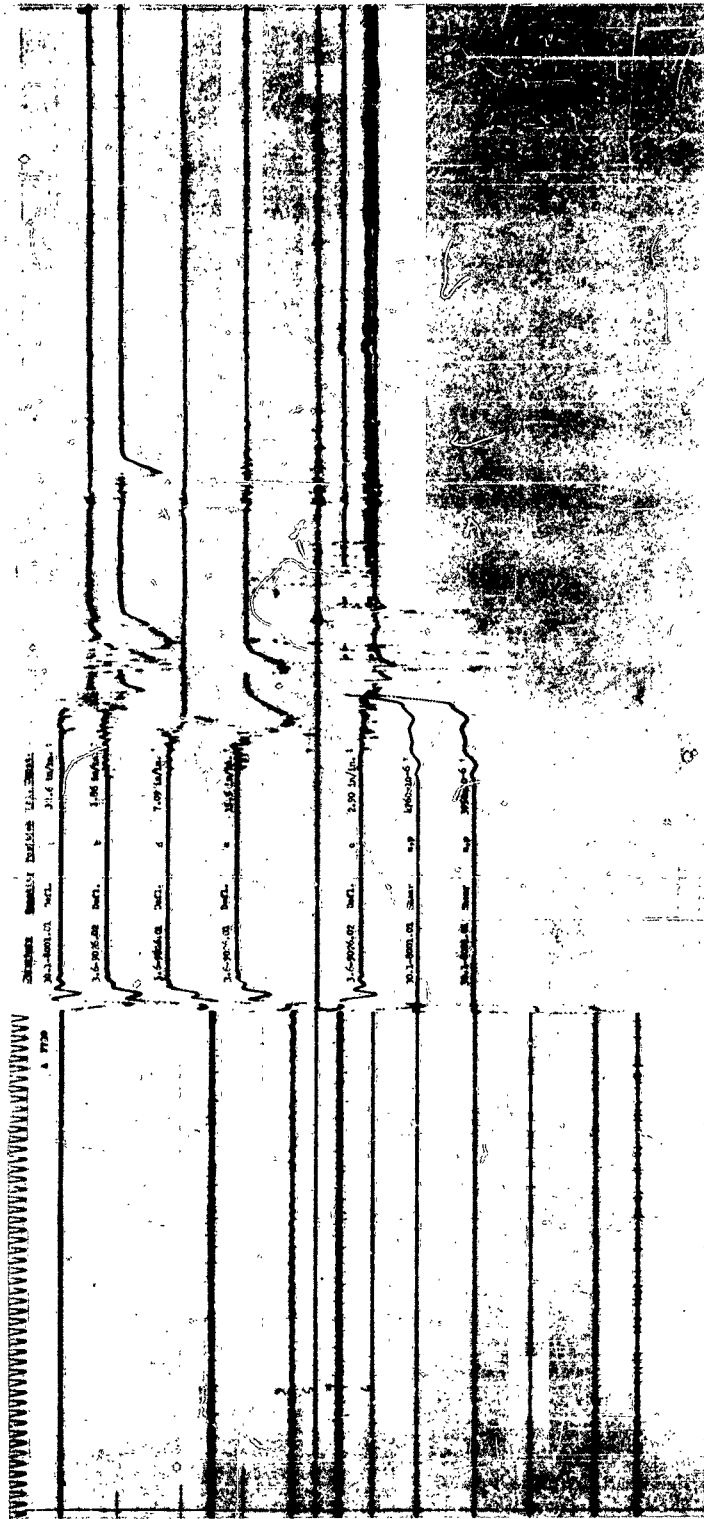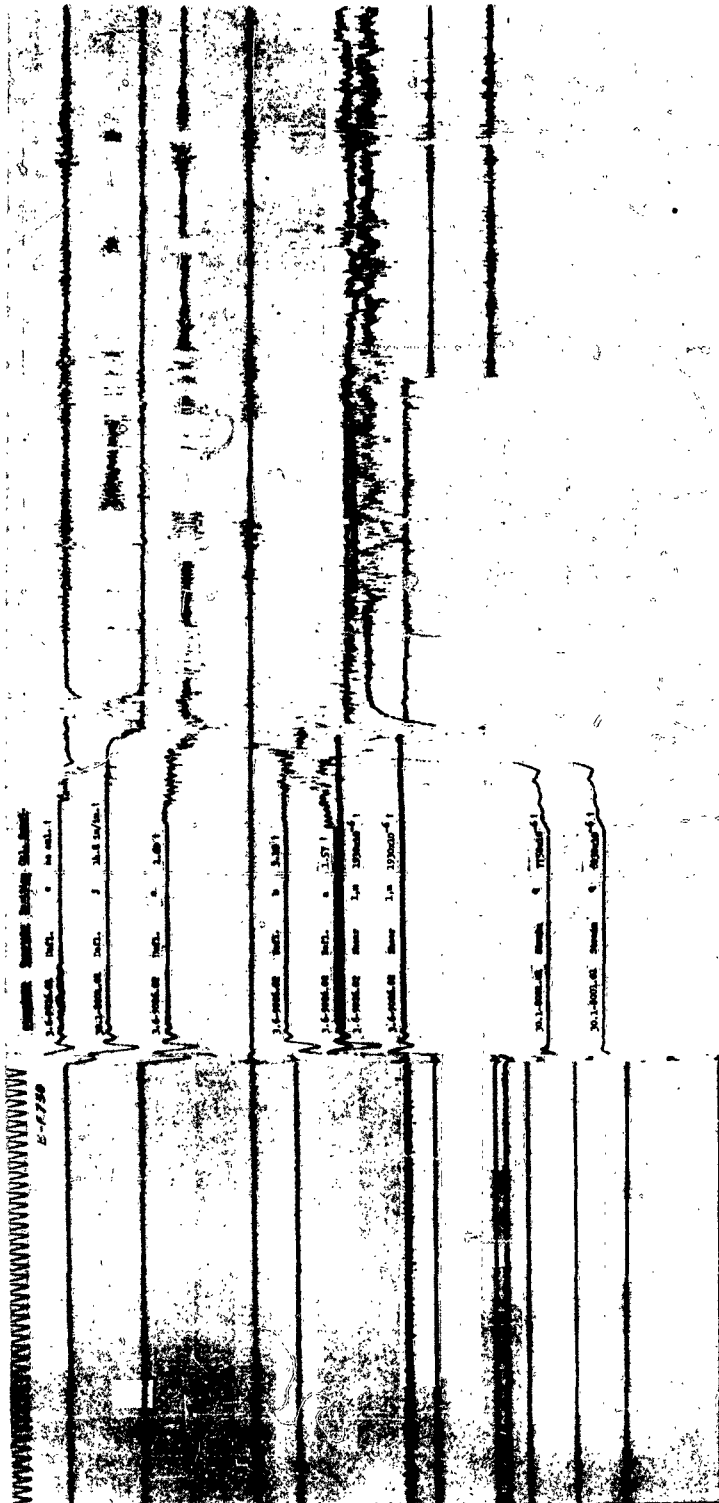
157

Figure E.12 Oscillogram of structure response.

CONFIDENTIAL

Figure E.13 Oscillogram of structure response.

159

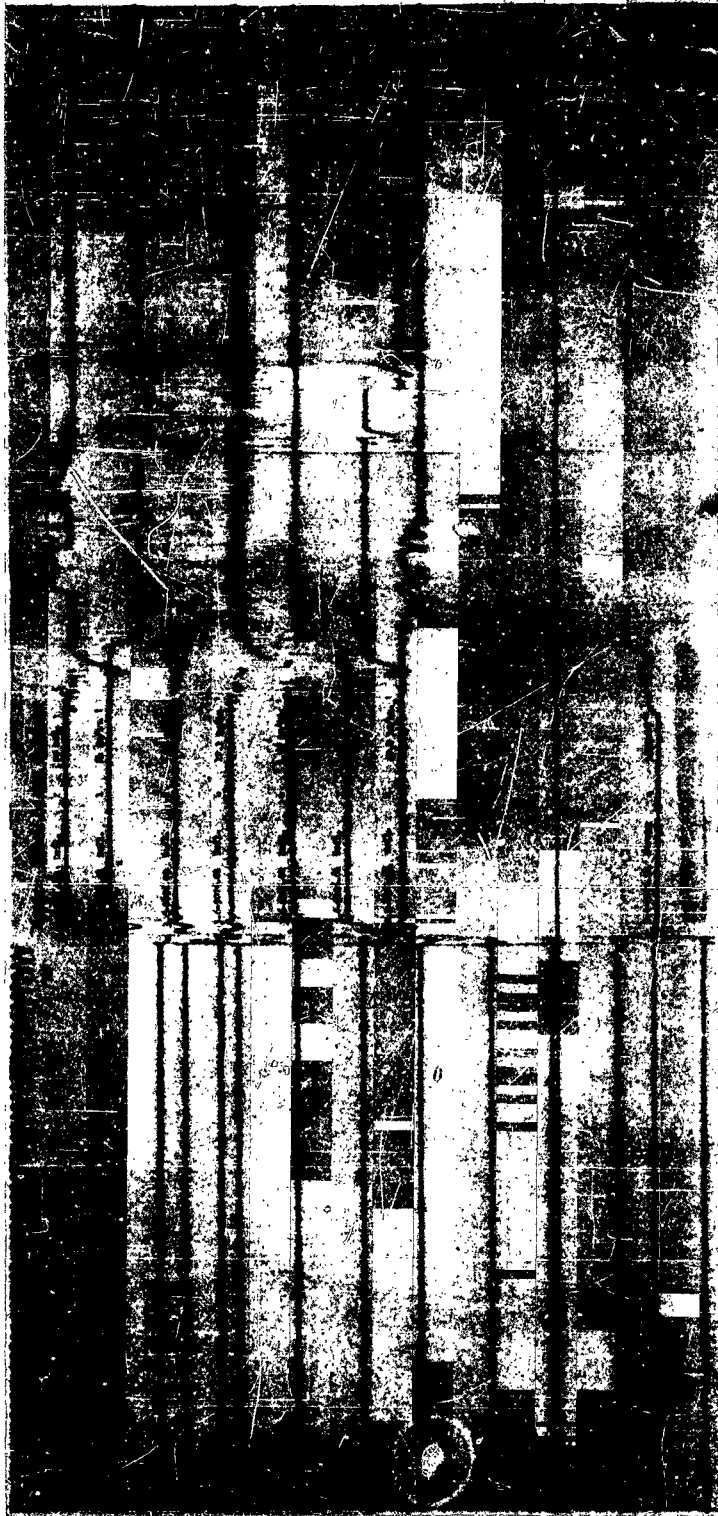Figure E.14 Oscillogram of structure response.

CONFIDENTIAL

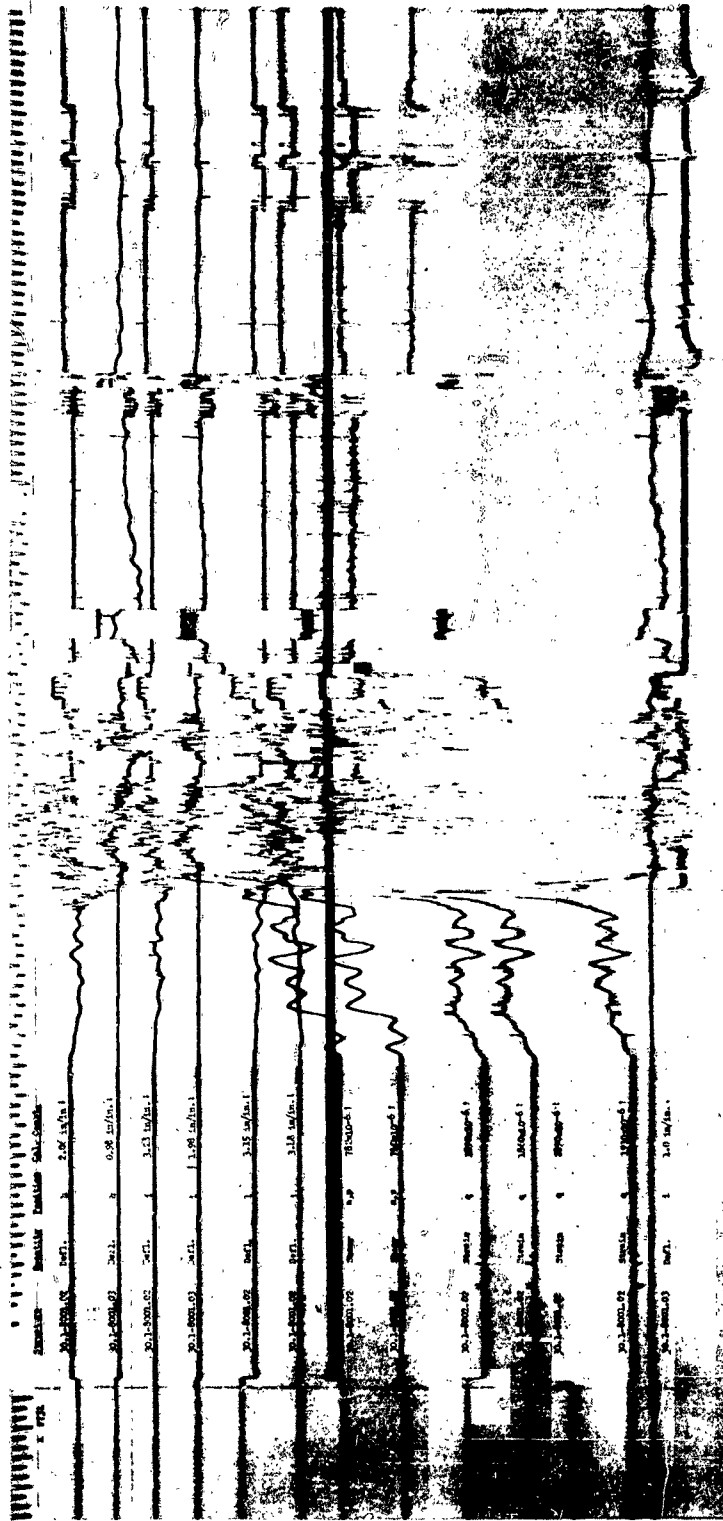Figure E.15 Oscillogram of structure response.

161
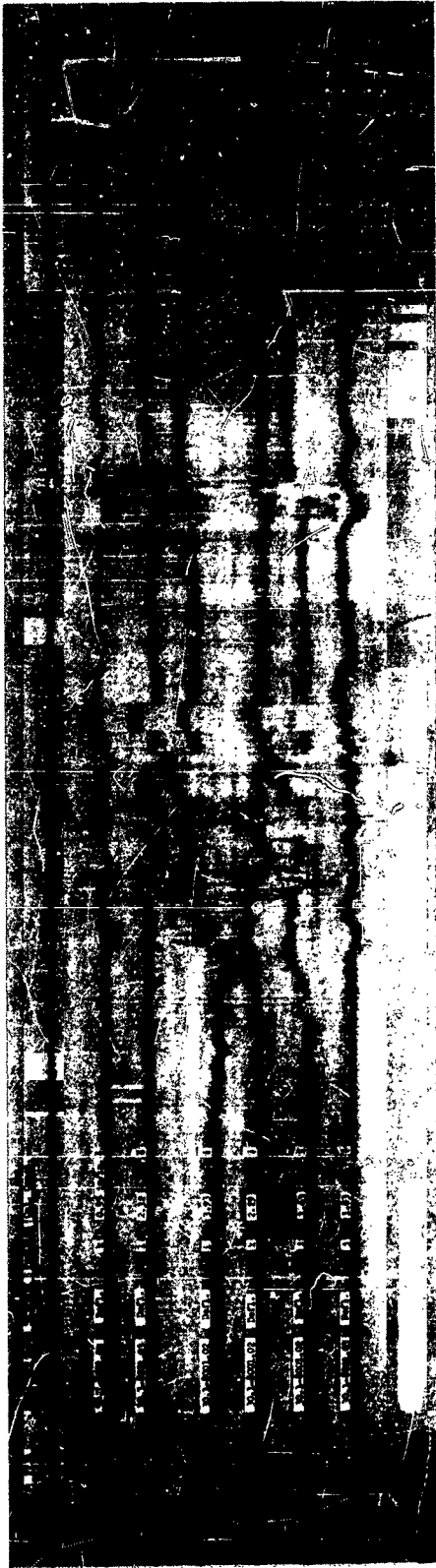
Figure E.16 Oscillogram of structure response.
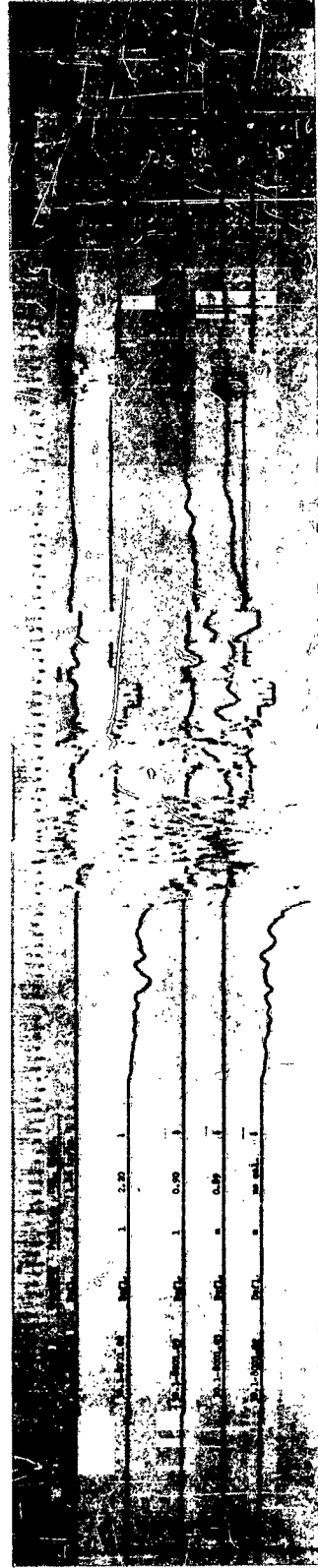
162

Figure E.17 Oscillogram of structure response.

Figure E.18 Oscillogram of structure response.

163

this structure should be monitored, if at all possible. An accelerometer mounted on each reference truss could have aided in the interpretation of records.

As an aid in separating the disturbances from the actual signals, a control channel for each type of sensor should be installed and mechanically isolated from the structure. These channels would record any electrical disturbance which might infiltrate the system, without recording any mechanical effects.

REFERENCES

1. T. G. Morrison; "Protective Structures"; Final Report, Contract No. AF 33(616)-2522, November 1958, American Machine and Foundry Company, AFSWC TR 59-2; Special Weapons Center, Kirtland Air Force Base, New Mexico; Vol I and Vol II classified Secret, Vol III Unclassified.

2. "Summary Report of the Technical Director"; Operation Greenhouse; Secret Restricted Data.

3. R. M. Longmire and L. D. Mills; "Navy Structures"; Projects 3.11−3.16, Operation Upshot-Knothole, WT−729, May 1955; Bureau of Yards and Docks, Department of the Navy, Washington 25, D. C.; Confidential Restricted Data.

4. "Technical Summary of Military Effects Programs 1−9"; Operation Teapot, WT−1153, February 1960; Office of Deputy Chief of Staff for Weapons Effects Tests, Headquarters Field Command, Defense Atomic Support Agency, Sandia Base, Albuquerque, New Mexico; Secret Restricted Data.

5. E. Rines, M. Ferguson and C. Kingery; "Air Blast Loading on Three-Dimensional Scale Models of Dome Shape"; Memorandum Report No. 889, AFSWP No. 773, April 1955; Ballistic Research Laboratories, Aberdeen Proving Ground, Maryland; Unclassified.

6. J. E. Fitzgerald; "Basic Design of Protective Structures for the Far East Air Force"; Contract No. AF 33(616)-2457, Call No. 6, 14 September 1956, American Machine and Foundry Company; Special Weapons Center, Kirtland Air Force Base, New Mexico; Appendix A classified Secret, all other portions of report are Unclassified.

7. K. Terzaghi; "Theoretical Soil Mechanics"; John Wiley and Sons, Inc., 1943; Unclassified.

8. K. Terzaghi and R. B. Peck; "Soil Mechanics in Engineering Practice"; John Wiley and Sons, Inc., 1948; Unclassified.

9. G. G. Meyerhof; "The Ultimate Bearing Capacity of Foundations; Geotechnique"; Vol 2, Page 301, 1951; Unclassified.

10. G. G. Meyerhof; "The Bearing Capacity of Foundations Under Eccentric and Inclined Loads"; Proc. Third Int. Conf. Soil. Mech. and Found. Engrg, Vol 1, Page 440, 1953; Unclassified.

11. W. C. Huntington; "Building Construction"; Second Edition, John Wiley and Sons, Inc., 1941; Unclassified.

12. T. H. Schiffman; "Numerical Solution for the Reflection of a Compressive Wave"; AFSWC Shock Tube Symposium, MIT, Cambridge, Massachusetts, February 26 - 27, 1957; Unclassified.

13. L. M. Swift and D. C. Sachs; "Air Pressure and Ground Shock Measurements"; Project 1.1b, Operation Upshot-Knothole, WT−711, January 1955; Stanford Research Institute, Stanford, California; Secret Formerly Restricted Data.

14. J. O. V. Irminger and C. Nøkkentved; "Wind Pressure on Buildings Experimental Researches"; First Series, Danmarks Naturovidenskabelige Samfund København, 1930; Unclassified.

15. S. F. Hoerner; "Aerodynamic Drag"; Sighard F. Hoerner, Midland Park, New Jersey, 1951; Unclassified.

CONFIDENTIAL

16. R. J. Heyman; "Transient Drag and Its Effect on Structures"; Final Report, Contract No. AF 33(616)-2285, 25 February 1955, American Machine and Foundry Company; Wright Air Development Center, Wright-Patterson Air Force Base, Ohio; Confidential.

17 "Alcoa Aluminum Handbook"; Aluminum Company of America, 1956; Unclassified.

18. R. J. Roark; "Formulas for Stress and Strain"; Second Edition, McGraw-Hill Publishing Co., Inc., 1943; Unclassified.

19. "Capabilities of Atomic Weapons"; October 1953, AFSWP; Secret Restricted Data.

20. L. Prandtl; "Über die Härte Plastischer Körper"; Nachr. kgl. Ges. Wiss. Göttingen, Math. Phys. Klasse; Unclassified.

21. E. J. Bryant, J. H. Keefer and J. G. Schmidt; "Basic Air-Blast Phenomena, Part I"; Project 1.1, Operation Plumbbob, ITR-1401, October 1957; Explosion Kinetics Branch, Terminal Ballistics Laboratory, Ballistic Research Laboratories, Aberdeen Proving Ground, Maryland; Confidential Formerly Restricted Data.

22. L. M. Swift, D. C. Sachs and F. M. Sauer; "Air-Blast Phenomena in the High-Pressure Region"; Project 1.3, Operation Plumbbob, ITR-1403, October 1957; Stanford Research Institute, Menlo Park, California; Confidential Formerly Restricted Data.

23. E. V. Gallagher; "Air Blast Loading on Arches and Domes"; Armour Research Foundation, September 1958; Unclassified.

24. S. Timoshenko; "Theory of Plates and Shells"; McGraw-Hill Book Co., Inc., 1940; Unclassified.

25. J. J. Meszaros, H. S. Burden and J. D. Day; "Instrumentation of Structures for Air-Blast and Ground-Shock Effects"; Project 3.7, Operation Plumbbob, ITR-1426, December 1957; Ballistics Research Laboratories, Aberdeen Proving Ground, Maryland; Confidential.

26. L. M. Swift; "Instrument Disturbances Due to the 'Induction Signal'"; Interim Technical Memorandum No. 1, Stanford Research Institute, February 6, 1957.

CONFIDENTIAL

DISTRIBUTION

Military Distribution Category 32

ARMY ACTIVITIES

1   Deputy Chief of Staff for Military Operations, D/A, Washington 25, D.C. ATTN: Dir. of SW&R
2   Chief of Research and Development, D/A, Washington 25, D.C. ATTN: Atomic Div.
3   Chief of Engineers, D/A, Washington 25, D.C. ATTN: ENGNB
4   Chief of Engineers, D/A, Washington 25, D.C. ATTN: ENGEB
5   Chief of Engineers, D/A, Washington 25, D.C. ATTN: ENGTB
6- 7   Office, Chief of Ordnance, D/A, Washington 25, D.C. ATTN: ORDTN
8   Chief of Transportation, D/A, Office of Planning and Int., Washington 25, D.C.
9- 11   Commanding General, U.S. Continental Army Command, Ft. Monroe, Va.
12   Director of Special Weapons Development Office, Headquarters CONARC, Ft. Bliss, Tex. ATTN: Capt. Chester I. Peterson
13   President, U.S. Army Artillery Board, Ft. Sill, Okla.
14   President, U.S. Army Air Defense Board, Ft. Bliss, Tex.
15   Commandant, U.S. Army Command & General Staff College, Ft. Leavenworth, Kansas. ATTN: ARCHIVES
16   Commandant, U.S. Army Air Defense School, Ft. Bliss, Tex. ATTN: Command & Staff Dept.
17   Commandant, U.S. Army Armored School, Ft. Knox, Ky.
18   Commandant, U.S. Army Artillery and Missile School, Ft. Sill, Okla. ATTN: Combat Development Department
19   Commandant, U.S. Army Aviation School, Ft. Rucker, Ala.
20   Commandant, U.S. Army Infantry School, Ft. Benning, Ga. ATTN: C.D.S.
21   Commanding General, Chemical Corps Training Comd., Ft. McClellan, Ala.
22   Commandant, USA Transport School, Ft. Eustis, Va. ATTN: Security and Info. Off.
23   Commanding General, The Engineer Center, Ft. Belvoir, Va. ATTN: Asst. Cmdt, Engr. School
24   Director, Armed Forces Institute of Pathology, Walter Reed Army Med. Center, 625 16th St., NW, Washington 25, D.C.
25   Commanding Officer, Army Medical Research Lab., Ft. Knox, Ky.
26   Commandant, Walter Reed Army Inst. of Res., Walter Reed Army Medical Center, Washington 25, D.C.
27- 29   Commanding Officer, Chemical Warfare Lab., Army Chemical Center, Md. ATTN: Tech. Library
30   Commanding General, Engineer Research and Dev. Lab., Ft. Belvoir, Va. ATTN: Chief, Tech. Support Branch
31   Director, Waterways Experiment Station, P.O. Box 631, Vicksburg, Miss. ATTN: Library
32- 33   Commanding General, Aberdeen Proving Grounds, Md. ATTN: Director, Ballistics Research Laboratory
34   Commanding General, Ordnance Ammunition Command, Joliet, Ill.
35   Director, Operations Research Office, Johns Hopkins University, 6935 Arlington Rd., Bethesda 14, Md.
36   Commander-in-Chief, U.S. Army Europe, APO 403, New York, N.Y. ATTN: Opot. Div., Weapons Br.

NAVY ACTIVITIES

37   Chief of Naval Operations, D/N, Washington 25, D.C. ATTN: OP-03EG
38   Chief of Naval Operations, D/N, Washington 25, D.C. ATTN: OP-75
39- 40   Chief of Naval Research, D/N, Washington 25, D.C. ATTN: Code 811
41   Chief, Bureau of Naval Weapons, D/N, Washington 25, D.C. ATTN: DLI-3

42   Chief, Bureau of Ordnance, D/N, Washington 25, D.C.
43   Chief, Bureau of Ships, D/N, Washington 25, D.C. ATTN: Code 423
44   Chief, Bureau of Yards and Docks, D/N, Washington 25, D.C. ATTN: D-440
45   Director, U.S. Naval Research Laboratory, Washington 25, D.C. ATTN: Mrs. Katherine H. Cass
46- 47   Commander, U.S. Naval Ordnance Laboratory, White Oak, Silver Spring 19, Md.
48   Director, Material Lab. (Code 900), New York Naval Shipyard, Brooklyn 1, N.Y.
49   Commanding Officer and Director, Navy Electronics Laboratory, San Diego 52, Calif.
50- 51   Commanding Officer, U.S. Naval Radiological Defense Laboratory, San Francisco, Calif. ATTN: Tech. Info. Div.
52- 53   Commanding Officer and Director, U.S. Naval Civil Engineering Laboratory, Port Hueneme, Calif. ATTN: L31
54   Commanding Officer, U.S. Naval Schools Command, U.S. Naval Station, Treasure Island. San Francisco, Calif.
55   Superintendent, U.S. Naval Postgraduate School, Monterey, Calif.
56   Officer-in-Charge, U.S. Naval School, CEC Officers, U.S. Naval Construction Bn. Center, Port Hueneme, Calif.
57   Commanding Officer, Nuclear Weapons Training Center, Atlantic, U.S. Naval Base, Norfolk 11, Va. ATTN: Nuclear Warfare Dept.
58   Commanding Officer, Nuclear Weapons Training Center, Pacific, Naval Station, San Diego, Calif.
59   Commanding Officer, U.S. Naval Damage Control Tng. Center, Naval Base, Philadelphia 12, Pa. ATTN: ABC Defense Course
60   Commanding Officer, U.S. Naval Medical Research Institute, National Naval Medical Center, Bethesda, Md.
61   Commanding Officer and Director, David W. Taylor Model Basin, Washington 7, D.C. ATTN: Library
62   Officer-in-Charge, U.S. Naval Supply Research and Development Facility, Naval Supply Center, Bayonne, N.J.
63   Commander, Norfolk Naval Shipyard, Portsmouth, Va. ATTN: Underwater Explosions Research Division
64   Commandant, U.S. Marine Corps, Washington 25, D.C. ATTN: Code A03H
65   Director, Marine Corps Landing Force, Development Center, MCS, Quantico, Va.
66   Commanding Officer, U.S. Naval CIC School, U.S. Naval Air Station, Glynco, Brunswick, Ga.
67   Chief, Bureau of Naval Weapons, Navy Department, Washington 25, D.C. ATTN: RR12

AIR FORCE ACTIVITIES

68   Hq. USAF, ATTN: Operations Analysis Office, Office, Vice Chief of Staff, Washington 25, D. C.
69   Director of Civil Engineering, HQ. USAF, Washington 25, D.C. ATTN: AFOCE
70- 71   Air Force Intelligence Center, HQ. USAF, ACS/I (AFCIN-3V1) Washington 25, D.C.
72   Deputy Chief of Staff, Plans and Programs, HQ. USAF, Washington 25, D.C. ATTN: War Plans Division
73   Director of Research and Development, DCS/D, HQ. USAF, Washington 25, D.C. ATTN: Guidance and Weapons Div.
74   The Surgeon General, HQ. USAF, Washington 25, D.C. ATTN: Bio.-Def. Pre. Med. Division
75- 76   Commander, Tactical Air Command, Langley AFB, Va. ATTN: Doc. Security Branch

167

CONFIDENTIAL